

DUMPSTER DYNAMICS

Space Trash De-Orbiter System

EMA 569: Senior Design
Engineering Mechanics and Astronautics
University of Wisconsin-Madison
April 30, 2025

Authors

Kyle Adler
Dominic Morand-Rivers
Martin Du Jardin
Gavin Day
Bryce Quinton

Supervisors

Sonny Nimityongskul
Travis Sheperd
Scott Russell

1 Executive Summary

The escalating accumulation of space debris in Low-Earth Orbit (LEO) presents a significant and growing threat to space sustainability, operational spacecraft, and future missions, necessitating proactive Active Debris Removal (ADR) solutions beyond passive mitigation. Dumpster Dynamics addresses this critical challenge through the design of an innovative, multi-target Space Trash De-Orbiter (STD) System.

The proposed system employs a robust two-stage architecture. A dedicated kick stage, utilizing a high-performance MMH/NTO bipropellant system, serves as the carrier and deployment platform. Launched via a SpaceX Falcon 9, the kick stage precisely delivers seven individual Space Trash De-orbiters (STDs) to multiple designated operational orbits targeting defunct Starlink satellites.

Each STD is a self-contained unit equipped with a reliable monopropellant hydrazine propulsion system (3100 N thrust), attitude control systems for managing tumbling targets (up to $10^{\circ}/\text{s}$), and advanced GNC for autonomous operation. Upon release, STDs perform phasing maneuvers to rendezvous with their assigned target. Capture is achieved using a robust four-point armature gripping mechanism, analyzed to withstand operational loads. A key requirement is the rapid de-orbiting of the captured satellite within one week, minimizing orbital risk. Both the STD and captured debris are designed for complete atmospheric burn-up, adhering to stringent safety standards (NASA-STD 8719.14) and eliminating ground impact hazards.

Comprehensive analysis validates the system's feasibility. Orbital mechanics calculations determined mission delta-V requirements (3.02 km/s for the kick stage, max 183 m/s per STD). Component sizing yielded an estimated STD fueled mass of approximately 400 kg. Rigorous structural analysis confirmed the kick stage and STD frames withstand demanding launch loads (up to 6g axial, 3.5g lateral) and operational stresses, incorporating NASA safety factors. Thermal analysis verified the atmospheric burn-up strategy.

The Dumpster Dynamics project successfully establishes the design and operational concept for a capable and efficient ADR system. By leveraging a multi-deployment strategy, it offers a scalable approach to mitigating the space debris problem, contributing to the long-term safety and sustainability of the LEO environment for future technological advancement and exploration.

Table of Contents

1	Executive Summary	1
2	Introduction	6
3	Applicable Designs	8
3.1	ClearSpace-1	8
3.2	NASA's ADRV	9
3.3	Astroscale's ELSA-M	9
4	Regulations and Standards	11
4.1	FCC: CFR-2015 Title 47, Volume 2, Part 25	11
4.2	NASA-STD 8719.14	11
4.3	NASA-STD-5002A	11
4.4	NASA-STD-6016	12
4.5	NASA-HDBK-1005	12
4.6	NASA-STD-5001B	12
5	Design Specifications and Criteria	13
6	Mission Profile	16
6.1	Qualitative Mission Overview	16
6.2	Orbital Mechanics Calculations	19
6.3	Total Mission Delta-V	27
6.4	Mission Verification using Simulation	28
7	Design Concepts	33
7.1	Overall Design	33
7.2	Propulsion System	35
7.3	Gripping Mechanism	37
8	Equipment	42
8.1	Propulsion System	42
8.2	Docking Mechanism	42
8.3	Attitude Control System	42
8.4	Inertial Measurement Unit	42
8.5	Flight Computer	42
8.6	GNSS Receiver	42
8.7	Star Tracker	43
8.8	S-band Communications	43
8.9	Radar Tracking	43
8.10	LiDAR	43
9	STD Sizing	44
9.1	Fuel tank	44

9.2 Propulsion	48
9.3 Attitude Control	49
9.4 Angular Momentum	54
9.5 Power Requirements	66
9.6 Gripping Mechanism Sizing	66
10 Gripping Mechanism Sizing	68
11 Kick Stage Sizing	72
11.1 Propellant Selection	72
11.2 Mass Predictions	72
12 Analysis Introduction	76
12.1 Material Properties and Yield Stresses	76
12.2 Safety Factors	76
12.3 Launch and Global Load Conditions	77
13 Kick Stage Propulsion Analysis	78
13.1 Material Selection	78
13.2 Propulsion Parameters	81
13.3 Injector Design	85
13.4 Combustion Chamber Design	95
13.5 Nozzle Design	100
13.6 Thermal Analysis	104
13.7 Finite Element Model	107
14 Kick Stage Structural Analysis	114
14.1 Analytic Calculation	114
14.2 Finite Element Analysis	122
14.3 Reduced Cross Section	133
14.4 Summary	135
15 STD Structural analysis	136
15.1 Preliminary Design of STD Structure	136
15.2 Launch Forces on STD	136
15.3 Cross-Sectional Area of STD Frame Bars	142
15.4 Simple Finite Element Model	146
15.5 Complete Finite Element Model	154
16 STD Engine Analysis	163
16.1 Decomposition Analysis and Gas Properties	163
16.2 Pressure Analysis	164
16.3 Thermal Analysis	166
16.4 Injector Area Specifications	168
16.5 Finite Element Work	170
16.6 Reflection and Future Work	176

17 Gripping Mechanism Analysis	177
17.1 Gear Reduction	177
18 Re-entry Analysis	182
18.1 Trajectory Analysis	182
18.2 Thermal Analysis	188
19 Design	200
19.1 Kick Stage	201
19.2 STD	205
19.3 Final Assembly	212
20 Future Work	213
20.1 Orbital Mechanics	213
20.2 Kick Stage Propulsion	214
20.3 Kick Stage Structure	214
20.4 Flight Computer	215
20.5 Gripping Mechanism Refinement	215
21 Conclusion	216
22 References	219
A Product Design Specification (PDS)	228
B STD fuel tank sizing code	236
C Orbital Mechanics Calculations	238
C.1 Hohmann Transfer	238
C.2 Split-plane Change	239
C.3 Phasing	241
C.4 De-orbit	243
C.5 Satellite Orbit Figures	244
C.6 Convergence Analysis	246
C.7 Re-entry Analysis	249
D Nozzle Geometry and State Calculations	263
E Attitude Control Calculations	268
F Kick Stage Propulsion Python Code	273
F.1 CEA	273
F.2 Kick stage propulsion sizing	274
G Kick Stage Propulsion EES Code	290
G.1 Initial Approximation	290
G.2 Film Cooling and Bartz Model	290

H STD Simple Model APDL Code	293
I STD Engine Pressure Distribution	297
J Orbital Mechanics Calculations	300
J.1 Main Script	300
J.2 tauSTD.m	301
J.3 eom _s atquat.m	302

2 Introduction

The increasing accumulation of space debris presents a growing threat to the sustainability of space activities. Space debris consists of defunct human-made objects, such as decommissioned satellites, spent rocket stages, and fragments from collisions or explosions in orbit. These objects, ranging from millimeter-sized paint chips to large satellite remnants, travel at extreme velocities—often exceeding 10 km/s in low-Earth orbit (LEO) [1]—posing a significant risk of collision to operational spacecraft, crewed missions, and space-based infrastructure. LEO, defined as the region of space within 2,000 km orbital altitude, is the most densely populated orbital region, containing the majority of operational satellites and space debris. The high traffic in LEO, the majority of which is space debris, creates external costs for other space missions, as nearly all spacecraft must enter or traverse this region. These costs arise from the increased risk of collision and the need for evasive maneuvers.

As humanity’s reliance on satellite technology expands, so does the urgency of addressing the space debris problem. Critical orbit density refers to the density of space debris in LEO when it reaches a level that makes the orbit unusable. This occurs when the density of debris becomes so great that collisions between debris and satellites cause a chain reaction that destroys space infrastructure—a cascading effect that is known as the Kessler syndrome. D. Kessler finds that the rate of increase for collision fragments below 1,000 km is currently low, but would surge rapidly with growth of the intact population [2]. As SpaceX is planning to launch up to 42,000 Starlink satellites—with 7,000 of them already in orbit [3]—it will contribute to an increasingly congested LEO at around 550 km orbital altitude, making collision risks more pronounced.

Current mitigation efforts, such as collision avoidance maneuvers and end-of-life de-orbiting strategies, have helped manage the issue to some extent. However, studies indicate that passive measures alone are insufficient to prevent further escalation [4, 5, 6]. The lifespan of debris varies significantly; some objects in LEO may de-orbit within a few years due to atmospheric drag, while others can remain in orbit for centuries. Figure 2.1 displays how long it takes on average for space debris to naturally decay in LEO, depending on its altitude. Without proactive intervention, the problem of space debris will continue to worsen, increasing the cost and complexity of space operations.

The hazards posed by space debris are not limited to satellites alone; crewed missions, such as those aboard the International Space Station (ISS), regularly conduct avoidance maneuvers to mitigate collision risks. In some cases, debris has punctured spacecraft, highlighting the severity of the issue. Ensuring the safety of future space endeavors necessitates more effective debris removal strategies, including active debris removal (ADR). By physically retrieving or de-orbiting hazardous debris, ADR offers a potential long-term solution to mitigate the risk of uncontrolled collisions and safeguard space for future generations.

This report explores the design of a payload with multiple active space debris de-orbiters aimed at mitigating the space debris crisis. By developing an effective solution to remove hazardous debris from LEO, this project contributes to the broader goal of preserving space as an accessible environment for future technological advancements and exploration.

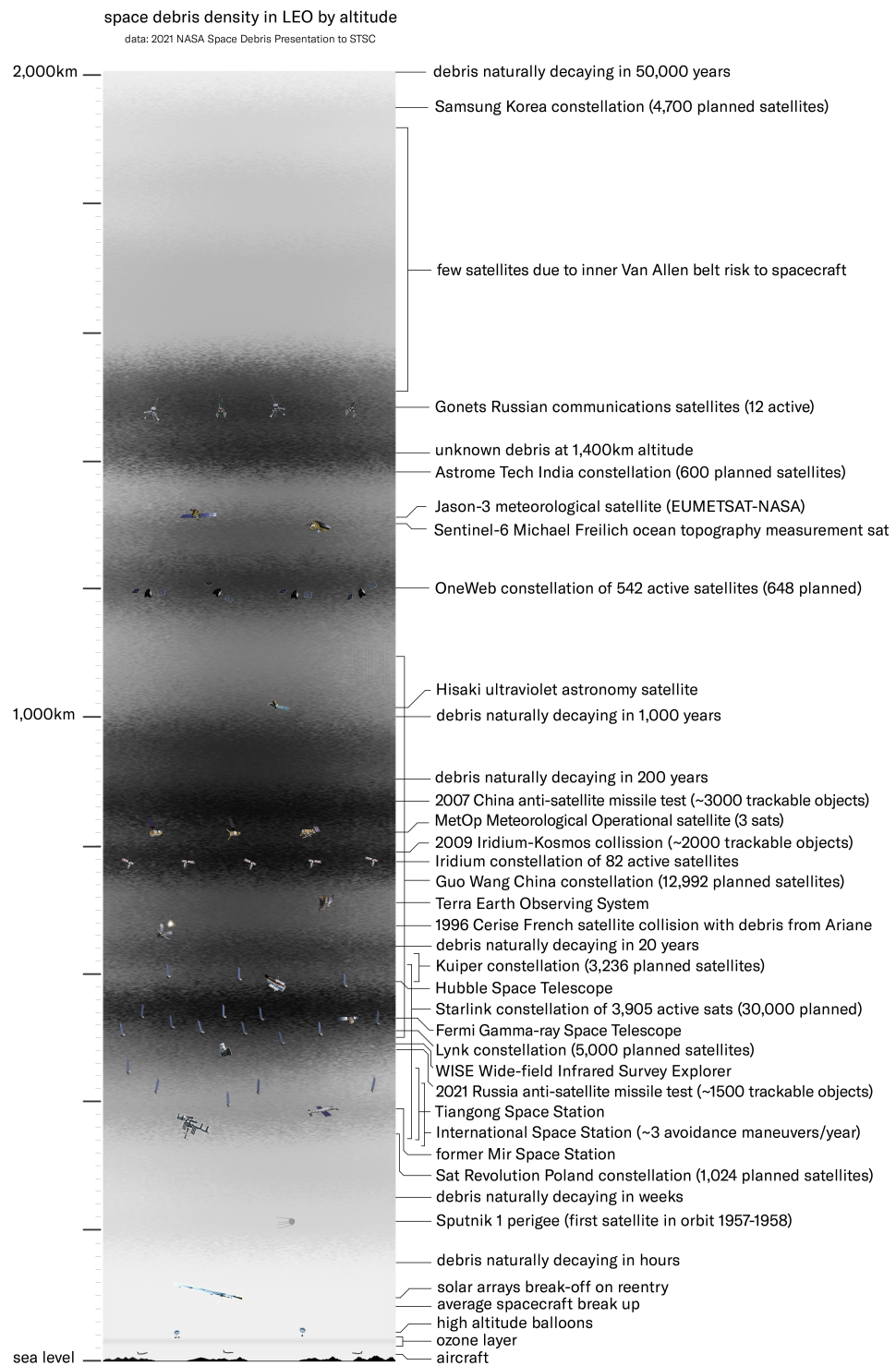


Figure 2.1: Natural decay of debris in LEO [7].

3 Applicable Designs

Since the issue of space debris is not new, numerous designs and concepts have already been proposed to actively remove debris from orbit. While none have been fully deployed and are operational as of this writing, these designs provide valuable insights and technological foundations for future innovations. Concepts such as ClearSpace-1, NASA's ADRV, and Astroscale's ELSA-M each offer different approaches to debris removal, from robotic arm capture to a patented capture and release system and magnetic docking.

3.1 ClearSpace-1

ClearSpace-1 is a joint mission developed by the European Space Agency (ESA) and OHB SE, designed to remove a specified object from LEO. Scheduled for launch by 2028, the mission will target and de-orbit the PROBA-1 satellite, a 95 kg spacecraft launched in 2001. ClearSpace-1 will mark the first-ever attempt to remove an unprepared and uncooperative object from orbit, relying on highly precise and complex close-proximity operations [8].

The mission is designed to act as a demonstration of active debris removal, using four robotic arms to latch onto PROBA-1 and guide both itself and the satellite into Earth's atmosphere, where they will burn both up upon re-entry. The target dimensions are roughly fixed at $0.6\text{ m} \times 0.6\text{ m} \times 0.8\text{ m}$, however, ESA also plans to use ClearSpace-1 for future debris removal efforts, including de-orbiting the Vega Secondary Payload Adapter (VESPA), a leftover payload adapter from a 2013 Vega launch, which resides in a much higher orbit. VESPA is a conical object with a diameter of approximately two meters and a mass of around 112 kg [9]. A conceptual render of ClearSpace's secondary mission to de-orbit VESPA can be seen in Figure 3.1.



Figure 3.1: ClearSpace-1 capturing VESPA [8].

While this mission represents a crucial step in space sustainability, its single-use design poses a significant limitation. The spacecraft is not reusable, it is designed for a specific piece of

space debris, and can only remove that one piece of space debris during its mission. This makes large-scale cleanup efforts costly and inefficient.

3.2 NASA’s ADRV

NASA’s MSC-TOPS-90 is a lightweight, low-cost Active Debris Removal Vehicle (ADRV) designed as an affordable alternative to other proposed orbital debris removal systems. It autonomously captures and de-orbits large, tumbling debris in low-Earth orbit, using a Spacecraft Control System (SCS) for maneuvering, a Debris Object Characterization System (DOCS) to assess target motion, and a Capture and Release System (CARS) for secure docking [10]. The CARS snare design can adaptively capture a variety of uncooperative targets that were not originally intended for docking. However, the effectiveness of this system in capturing objects lacking compatible structural features remains uncertain. While NASA states that CARS can adaptively capture various debris types [10], its real-world applicability may depend on the specific characteristics of the target.

The ADRV can handle debris between 1,000–4,000 kg at altitudes of 200–2,000 km. Due to its compact design, up to eight ADRVs can be launched in a single payload, enabling high impact orbital debris removal missions within the same inclination group. Despite reaching Technology Readiness Level 6—meaning that the system or sub-system prototype has been successfully demonstrated in a relevant operational environment—the ADRV has not yet been licensed for commercial use. This may be due to the high development costs, uncertain market demand, and regulatory challenges associated with space debris removal. Additionally, while NASA offers the ADRV patent for licensing through its Technology Transfer Program, no publicly available information confirms any active licensing agreements.

3.3 Astroscale’s ELSA-M

End-of-Life Services by Astroscale-Multiple (ELSA-M) uses servicer spacecraft to actively remove defunct satellites and other debris from orbit. Designed to service multiple objects in a single mission, ELSA-M features a magnetic capture mechanism that enables it to dock with satellites equipped with compatible docking plates [11]. Astroscale secured a contract with satellite internet services provider Eutelsat OneWeb. Each OneWeb satellite measures approximately 1 m × 1 m × 1.3 m, has a mass of around 150 kg, and operates in a 1,200 km orbit above Earth [12]. The ELSA-M mission will be launched into LEO and perform extensive technical checkouts, before raising itself using its thrusters to the OneWeb altitude. After docking with the selected satellite, it will drag its cargo down to about 350 km orbital altitude, where it will leave the satellite to naturally de-orbit over a period of three years [13]. The docking phase of the mission profile is conceptually displayed in Figure 3.2.

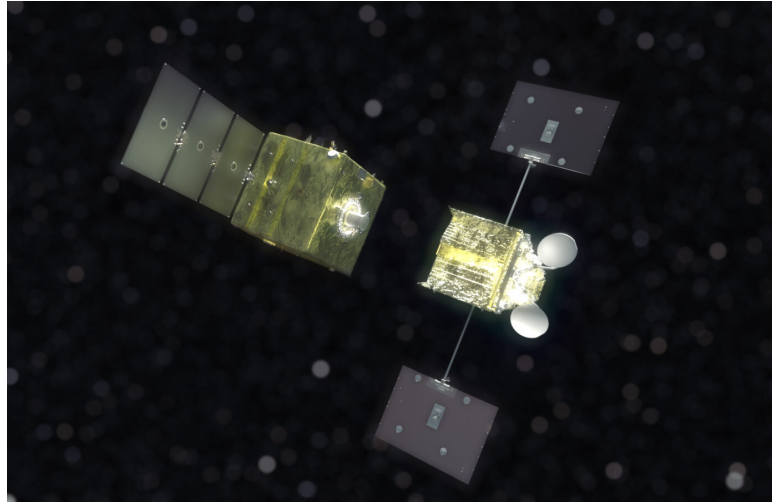


Figure 3.2: ELSA-M ([left](#)) docking to OneWeb ([right](#)) [11].

One of the key innovations of ELSA-M is its ability to autonomously navigate, capture, and de-orbit multiple pieces of debris during a single deployment. The system integrates advanced guidance, navigation, and control (GNC) technologies to safely approach and attach to tumbling target satellites before directing them toward uncontrolled re-entry. Unlike single-use debris removal missions like ClearSpace-1, ELSA-M represents a shift toward reusable and cost-effective solutions for long-term space sustainability.

While ELSA-M presents a significant advancement in active debris removal, it has some limitations. One major drawback is that it only lowers defunct satellites to an altitude of 350 km, relying on natural atmospheric drag for final de-orbiting over several years. This extended timeline leaves the debris in orbit for a longer period, during which it could still pose a collision risk. Additionally, ELSA-M can only remove satellites equipped with a compatible docking plate, meaning it cannot target older or unprepared debris. This restricts its effectiveness in addressing the vast majority of existing space junk, much of which lacks standardized interfaces for removal. Alternative universal capture methods, such as robotic arms or net-based systems, could broaden the range of debris active de-orbiters can service. Furthermore, the magnetic nature of the docking plate introduces additional constraints, as several science missions are undertaking extensive efforts to make their spacecraft magnetically neutral, which could challenge the effectiveness of magnetic docking methods.

4 Regulations and Standards

The design of a de-orbiting satellite is guided by a set of rigorous standards that span regulatory compliance, mission planning, and engineering design. Although this project is unique in its approach to satellite de-orbiting, it relies on a comprehensive framework of industry standards to ensure operational safety and mission success. The primary standards that govern this work include CFR-2015 [14], NASA-STD 8719.14 [15], NASA-STD-5002A [16], NASA-STD-6016 [17], NASA-HDBK-1005 [18], and NASA-STD-5001B [19]. Each of these standards addresses a critical aspect of the mission.

4.1 FCC: CFR-2015 Title 47, Volume 2, Part 25

This project seeks to design a satellite that has a mass of over 180 kg, the wet mass limit from FCC 19-18 to qualify for the streamlined process of FCC 19-81. Therefore, the satellite must adhere to CFR-2015 Title 47, Volume 2, Part 25, which establishes regulations for satellite communications and orbital operations. This Compliance ensures that the [satellite](#) does not interfere with existing satellite networks and maintains proper orbital coordination. Given its mission to dock with and de-orbit a dysfunctional Starlink satellite, the [satellite](#) must meet the legal requirements for orbital debris mitigation by minimizing the risk of debris generation, implementing collision avoidance strategies, and ensuring a controlled end-of-life disposal.

Additionally, Part 25 mandates that the satellite's radio frequency transmissions comply with spectrum management policies to prevent harmful interference with operational satellites and ground stations. The satellite must adhere to power limits, frequency coordination, and telemetry regulations to maintain secure and uninterrupted communication throughout its mission. By following these regulatory guidelines, the [satellite](#) ensures legal compliance, which is critical for mission success [14].

4.2 NASA-STD 8719.14

NASA-STD 8719.14[Process for Limiting Orbital Debris](#) provides technical requirements and methodologies for minimizing orbital debris and the risks associated with the debris. This standard is the basis for the goal of the de-orbiting mission, but it also provides key benchmarks to the design such as atmospheric reentry requirements. In the assessment of debris surviving atmospheric reentry, it must be proven that the risk of human casualty from surviving debris shall be less than 1:10,000. Additionally, any surviving debris must impact no closer than 370 km from foreign landmasses [15].

4.3 NASA-STD-5002A

NASA-STD-5002A,[Load Analyses of Spacecraft and Payloads](#), provides the methodologies, practices, and requirements for conducting comprehensive load analyses. This establishes a consistent framework for evaluating structural integrity. NASA-STD-5002A provides requirements to have a 50 percent confidence that the structural integrity will not fail 99.87

percent of the time (3-sigma). This includes, but does not exhaust, the following tests [16]:

- Static Loading
- High-Frequency Vibration
- Low-Frequency Vibration
- Cyclic Loading
- Shock Loading.

4.4 NASA-STD-6016

NASA-STD-6016, [Standard Materials and Processes Requirements for Spacecraft](#), will help ensure Dumpster Dynamics determines appropriate material choices for each component. It will address potential issues such as flammability, compatibility, toxicity, and outgassing, ensuring that all materials perform reliably in the space environment. For structural components, materials such as aluminum alloys (e.g., 7075-T6, 6061-T6), titanium, or carbon fiber-reinforced polymers (CFRP) may be considered based on factors like strength-to-weight ratio, mechanical strength, thermal stability, and resistance to radiation. By following NASA-STD-6016, the team can mitigate risks associated with material failures, contamination, and degradation, ultimately enhancing the satellite's effectiveness in safely de-orbiting space debris [17].

4.5 NASA-HDBK-1005

The overall mission architecture and project execution for the de-orbiting satellite is guided by NASA-HDBK-1005, SMAF Handbook for Uncrewed Missions. This handbook provides a comprehensive guide for developing the mission profile—from initial concept and design to integration, testing, and operations. It emphasizes the importance of systems engineering, clear objectives, defined requirements, and lifecycle cost management, ensuring that the entire project is coordinated and executed in a structured manner. By aligning with NASA's established policies and processes, this standard not only facilitates a coherent mission architecture but also fosters an environment of continuous improvement throughout the project's lifecycle [18].

4.6 NASA-STD-5001B

NASA-STD-5001B, [Structural Design and Test Factors of Safety for Spaceflight Hardware](#), will provide the primary guideline for ensuring structural integrity and mission reliability of the satellite. This standard was applied throughout the design and verification process to establish appropriate design and test factors of safety, based on the criticality, loading environment, and verification method of each structural component. Key characteristics of NASA-STD-5001B that were applied to the design will be defined in the Analysis chapter.[19]

5 Design Specifications and Criteria

The design specification and criteria will provide a high level guideline to the goal of de-orbiting dysfunctional satellites. These requirements will be crucial in completing the mission overview in Figure 5.1. A kick stage will carry seven individual Space Trash De-orbiters (STDs) and deploy STDs at circular orbits of 525 km, 530 km, and 535 km. Each STD will de-orbit one satellite. A more in-depth look at the mission profile will follow in Section 6.

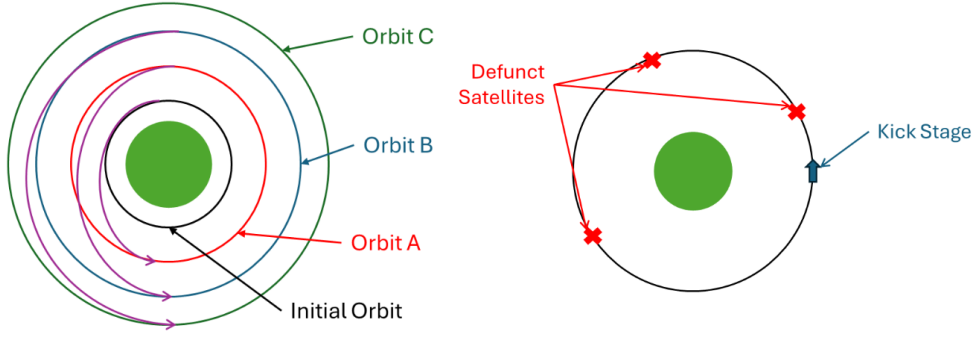


Figure 5.1: Visual overview of the design requirements of the STD mission.

As mentioned, the mission will require two main systems, the kick stage and the STDs. The kick stage must carry seven STDs. The kick stage will be taken to orbit via a contracted medium launch provider. As of April of 2025, viable medium lift contracts includes SpaceX’s Falcon 9, ULA’s Atlas V and Vulcan, Russia’s Soyuz-2, and ESA’s Ariane 6. Table 5.1 provides an objective comparison of cost and capabilities of each of the options.

Table 5.1: Comparison of available launch vehicles

Vehicle	Payload to LEO (Mg)	Launch Facility	Fairing Diameter (m)	Fairing Height (m)	Cost (M)	\$/Kg to LEO	No. Launches	No. Successful	Manufacturer
Falcon 9 (Block 5)	22.8	KSC, VAFB	5.2	13.2	\$67	\$2,700	450+	450+	SpaceX
Atlas V (401)	8.7	KSC, VAFB	4.2	12.2	\$110	\$13,000	80+	80+	ULA
Vulcan Centaur	16.4	CCSFS	5.4	15.5	\$100	\$6,000	2	2	ULA
Soyuz-2.1b	11.0	GSC, BC	3.35	7.7	\$48.5	\$4,400	100+	95+	Roscosmos
Ariane 6 (A62)	15.0	GSC	5.4	17	\$75	\$5,000	2	1	Arianespace

By examining Table 5.1, the Falcon 9 emerges as the most favorable launch option. Although its launch cost is slightly higher than the Russian Soyuz, Falcon 9 offers significantly greater accessibility and lower logistical costs for ground transit. Its ability to launch from both California and Florida provides flexible orbital insertion opportunities, enhancing mission versatility. Falcon 9 also offers generous mass and volume margins, supporting robust design options for the Kick Stage and STDs. Most notably, its reliability is proven, with over 450 successful missions completed as of April 2025. Based on these factors, SpaceX’s Falcon 9 is selected as the launch vehicle for Dumpster Dynamics.

The integrated kick stage and Space Trash De-orbiters (STDs) must be fully compatible with SpaceX’s Falcon 9 launch vehicle [20], adhering to payload fairing constraints, mass limits, and rideshare deployment interfaces as shown in Figure 5.2. This compatibility enables efficient deployment through rideshare opportunities or dedicated multi-unit launches, ensuring

mission flexibility and cost-effectiveness. Additionally, the STDs will experience loads due to vibrations and acceleration at launch. Load factors for Falcon 9 can reach 6 g for vertical acceleration and 2 g for lateral which will be discussed further in the analysis chapter [20].

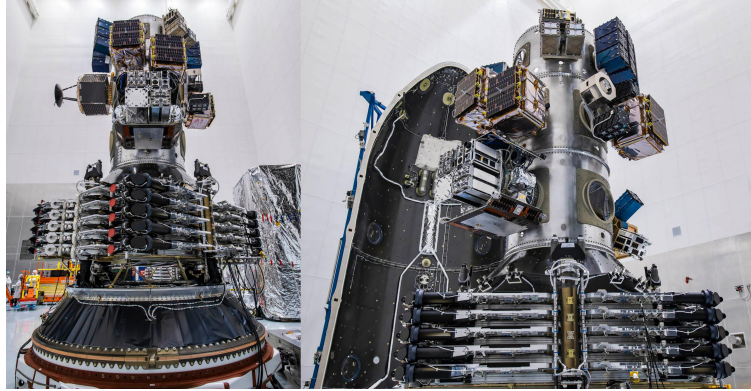


Figure 5.2: Payloads interfaced with Falcon 9 for SpaceX’s rideshare [20].

After launch, to ensure reliability in the environment of space, both the kick stage and STDs must be designed to withstand extreme thermal cycling, vacuum conditions, and prolonged exposure to radiation. All electronic components must be radiation-hardened. The structural materials must maintain integrity under micro-meteoroid and orbital debris impacts and mitigate temperature fluctuations ranging from -150°C to 150°C . Additionally, all propulsion and actuation systems must be vacuum-rated to ensure reliable performance in the absence of atmospheric pressure.

The kick stage must deliver sufficient delta-V to place each STD into the required altitude, inclination, and orbital plane dictated by the mission parameters. Specifics on the orbital maneuvers will be explained in detail in Section 6. Once the kick stage deploys an STD it must autonomously rendezvous and dock with the target debris without generating additional debris. This will require a secure, non-destructive capture mechanism. The docking maneuver must also account for variations in angular velocities due to dysfunctional attitude control on the target satellite.

A key operational requirement is that the STD must de-orbit its target debris within one week of launch. This rapid timeline minimizes risks associated with prolonged orbital maneuvers, ensuring de-orbit operations are conducted in a controlled and predictable manner. To achieve this, propulsion systems must be designed to meet the delta-V requirements calculated in Table 6.6 and Table 6.7. Similarly the attitude control system must meet maneuver requirements defined in Section 9.3.

Additionally, both the target debris and the STD must fully burn up upon reentry, ensuring no surviving fragments pose a risk to populated areas or other spacecraft. This necessitates the careful selection of materials and structural components to guarantee complete atmospheric destruction. The de-orbit trajectory must also be optimized to prevent partial debris survival, aligning with international space sustainability guidelines. Lastly, any remaining

hypergolic propellants must also be vented prior to re-entry to ensure none make it into the atmosphere.

By integrating Falcon 9 compatibility, precise orbital maneuvering, a non-destructive docking system, and a reliable de-orbit mechanism, this system offers a scalable and effective solution for mitigating space debris. Its implementation contributes to long-term orbital sustainability, reducing collision risks and ensuring the safe, controlled removal of hazardous debris from LEO.

6 Mission Profile

Dumpster Dynamics aims to de-orbit defunct V3 Starlink satellites in the altitude range 525–535 km at inclinations in the range 33°–53°. The mission profile can be broken down into various stages. The subsequent sections will explore the mission in-detail, backed by orbital mechanics equations found in [21] and [22]. Numerical calculations, figures, and simulations were done using MATLAB [23]. All orbital mechanics calculations will be done assuming impulsive maneuvers and ignoring orbital drift due to J2 perturbations [24].

The team will explore the scenario in which there are three different target orbits, each at different altitudes, inclinations, and all being circular. The target orbits were taken from [25], a SpaceX filing to the FCC that details the planned orbits for Starlink Gen2 satellites, which will closely reflect those of the current V3 satellites. For a given altitude and inclination, there exists a ring of spaced Starlink satellites. It will be assumed that within a ring of satellites, they will all be at the same altitude so all STDs can be released simultaneously and no micro-corrections in altitude will need to occur. Table 6.1 shows the target orbits and their differing parameters.

Table 6.1: Target Orbits of Defunct Starlink Satellites

Orbit Tag	Altitude [km]	Inclination [°]	# Defunct Satellites
A	525	33	2
B	530	43	2
C	535	53	3

From Table 6.1, Dumpster Dynamics' mission will show that the popular bands of Starlink satellites can be serviced. Additionally, across all target orbits, the defunct satellites will be spread out [arbitrarily](#) to show the full capabilities of the STDs when phasing.

6.1 Qualitative Mission Overview

This section explores the mission in a qualitative way, demonstrating what types of maneuvers are required for both the STDs and kick stage at each step of the mission. [The mother ship, referred to as the "kick stage" deploys the STDs in their target orbits.](#) The STDs are the smaller, individual ships that perform phasing maneuvers and attach to the defunct satellites to de-orbit.

6.1.1 Injection Orbit to Orbit A

The mission begins with a kick stage catching a ride on a Falcon 9 rocket. Falcon 9 will take off from Cape Canaveral, Florida at a designated azimuthal angle, releasing the kick stage into a circular low-Earth orbit with a known orbital radius and inclination matching Orbit A. The kick stage will then perform a Hohmann transfer to Orbit A.

Once in Orbit A, the kick stage will release two STDs to de-orbit the defunct satellites. The STDs will then split up, performing a phasing maneuver to rendezvous with the satellites. Seen in Figure 6.1, designated by $\Delta\theta$, the true anomaly relative to the kick stage can be seen for each defunct satellite.

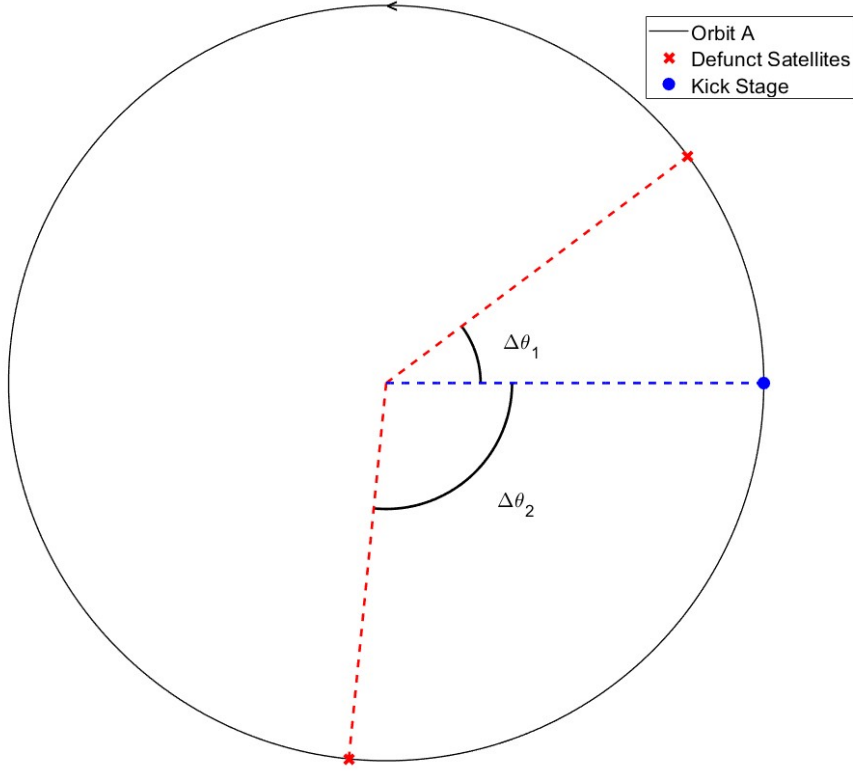


Figure 6.1: Relative position of the defunct satellites to the kick stage in Orbit A.

From Figure 6.1, for an STD to rendezvous with the defunct satellite at $\Delta\theta_1$, the STD will need to drop its orbit to catch up. For an STD to rendezvous with the defunct satellite at $\Delta\theta_2$, the STD must raise its orbit, slowing down to meet the satellite. To raise the orbit, the STD must produce a Δv in same direction it is moving in, indicated by the arrow in the figure. To lower its orbit, the STD must produce a Δv in the opposite direction it is moving in, called a retrofire. Once the STDs arrive at the defunct satellites, they will attach and burn into an elliptical orbit with a perigee altitude of 100 km. This is the point which satellites begin to burn up [26].

6.1.2 Orbit A to Orbit B

After the STDs have been released into Orbit A, the kick stage will perform a split-plane change and Hohmann transfer to arrive in orbit B. Once in Orbit B, the kick stage will

release two STDs to de-orbit the defunct satellites. Seen in Figure 6.2, the location of the satellites relative to the kick stage can be found.

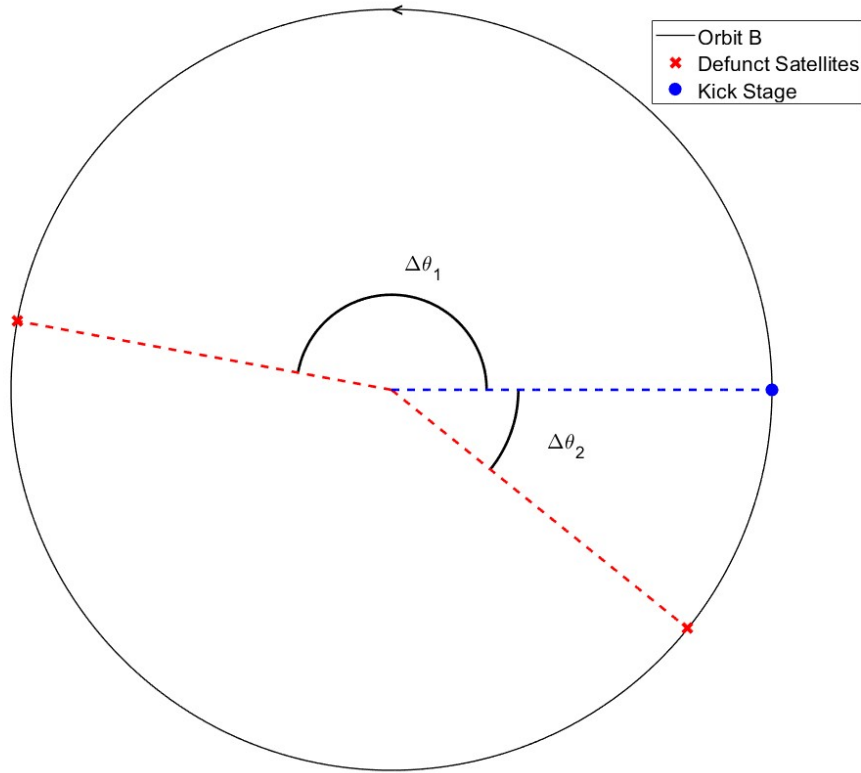


Figure 6.2: Relative position of the defunct satellites to the kick stage in Orbit B.

From Figure 6.2, the defunct satellites lie at different points than those in Orbit A. For the first STD to catch the first defunct satellite at $\Delta\theta_1$, it will need to drop its orbit, speeding it up. For the second STD to catch the second satellite at $\Delta\theta_2$, it will need to raise its orbit, slowing it down. Once at the defunct satellites, the STDs will attach and burn into an elliptical orbit with a perigee altitude of 100 km.

6.1.3 Orbit B to Orbit C

After the STDs have been released into Orbit B, the kick stage will perform another split-plane change and Hohmann transfer to arrive in Orbit C. Here, three STDs will be released and will perform phasing maneuvers to rendezvous with the defunct satellites. The location of the defunct satellites relative to the kick stage can be found in Figure 6.3.

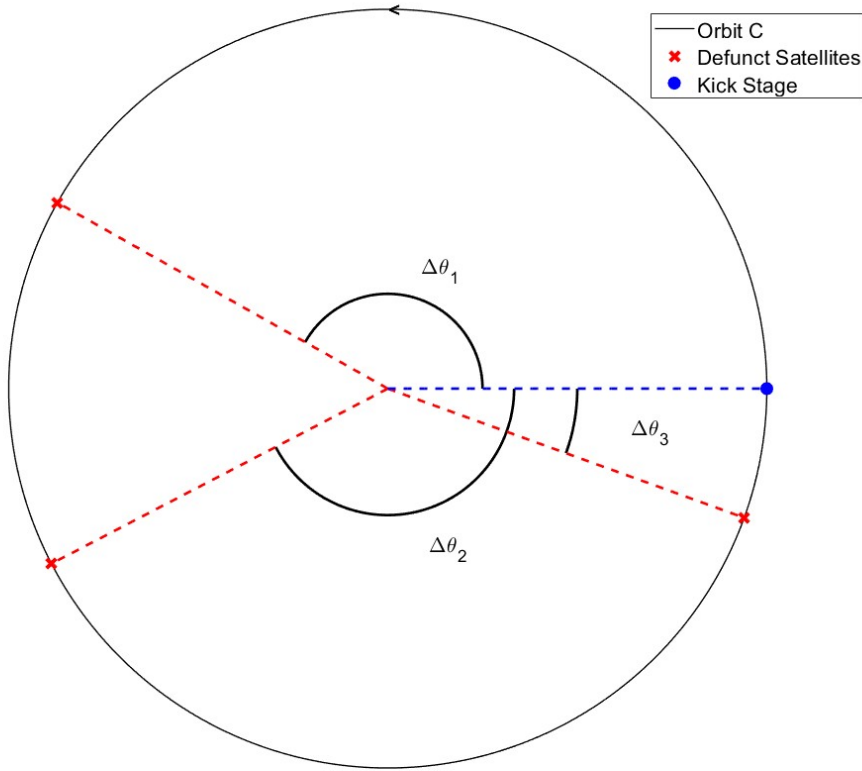


Figure 6.3: Relative position of the defunct satellites to the kick stage in Orbit C.

From Figure 6.3, the remaining three defunct satellites span a wide range of values, requiring precise timing in the phasing maneuvers. For the first STD to catch the first satellite at $\Delta\theta_1$, it will need to lower its orbit, speeding up. For the second STD to reach the second satellite at $\Delta\theta_2$, it will need to raise its orbit, slowing it down. Lastly, for the third STD to catch the third satellite, it will need to raise its orbit, slowing it down.

6.1.4 Orbit C to End-of-mission

After releasing the last of the STDs, the kick stage will burn into an elliptical orbit with a perigee altitude of 100 km. This ensures Dumpster Dynamics does not contribute to the accumulation of space debris.

6.2 Orbital Mechanics Calculations

This section performs the orbital mechanics calculations for each step of the mission. The results of these calculations will scope the sizing requirements of both the STDs and the kick stage.

6.2.1 Launch Configuration

Although the kick stage will be catching a ride on Falcon 9, the launch configuration can be specified such that Falcon 9 released the kick stage in the inclination matching Orbit A. This eliminates the need for the kick stage to perform a plane change, saving fuel for the kick stage. The spherical triangle used to calculate the azimuthal launch angle A_z can be seen in Figure 6.4

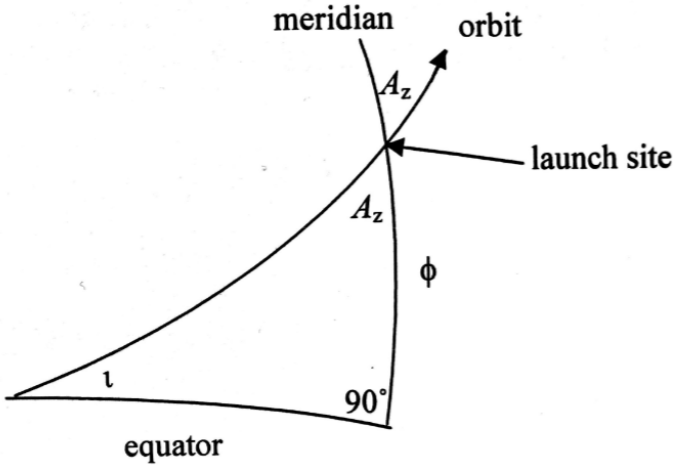


Figure 6.4: Spherical triangle showing the relationship between inclination i , latitude ϕ and azimuth A_z [22].

From Figure 6.4, using law of cosines, the relationship between the inclination i and azimuth A_z is given by

$$\cos(i) = \sin(A_z) \cos(\phi) \quad (6.1)$$

For the launch site of Cape Canaveral, Florida, the latitude ϕ is fixed at 28.533° [22]. Equation 6.1 can be solved for the required launch angle A_z such that the inclination of the initial orbit i is 33° , consistent with orbit A. Solving this yields a required azimuthal angle of 72.7° , which is within the site's safe range of 35° – 120° [22].

6.2.2 Injection Orbit to Orbit A Transfer

From the launch configuration determined in Section 6.2.1, the kick stage will be released into an orbit matching the inclination of the Orbit A. All that is required is to perform a Hohmann transfer into Orbit A. To visualize a Hohmann transfer, Figure 6.5 was created.

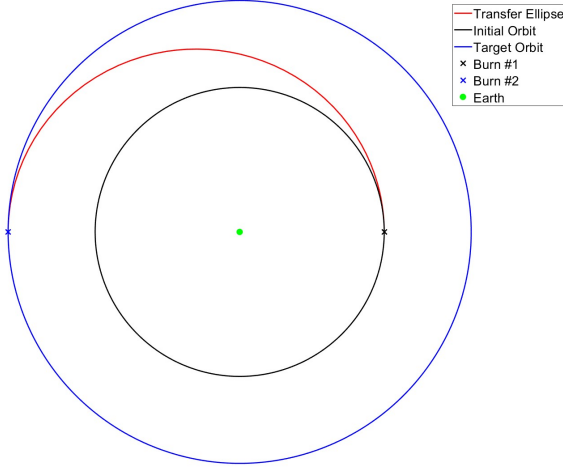


Figure 6.5: Hohmann transfer example.

Seen in Figure 6.5, a Hohmann transfer utilizes two burns. The first, seen by the black X, puts the ship on a transfer ellipse chosen such that the ship reaches the target orbital radius at apogee. The second burn, seen by the blue X, puts the ship into the desired orbit. In this case, a circular orbit. The governing equation for the transfer is the *Vis-viva* equation, derived from the conservation of energy for a particle in a gravitational field, given by

$$v_o = \sqrt{\mu_e \left(\frac{2}{r_o} - \frac{1}{a} \right)} \quad (6.2)$$

where v_o is the speed at point o , r_o is the radial distance from the center of Earth to point o , and a is the semi-major axis of the orbit. μ_e is the gravitational parameter for Earth and, from [27], is $0.3986 \times 10^6 \text{ km}^3/\text{s}^2$. Equation 6.2 gives the instantaneous speed for any point in an orbit characterized by semi-major axis a at the radial distance r_o from its focal point. The semi-major axis is given by

$$a = \frac{r_p + r_a}{2} \quad (6.3)$$

where r_a and r_p are the apogee and perigee radii, respectively. The apogee is the furthest point in the orbit while the perigee is the closest point in the orbit. For a circle, the apogee and perigee are the same value so a for a circular orbit is simply the radius r . Figure 6.6 shows an elliptical orbit with labeled parameters.

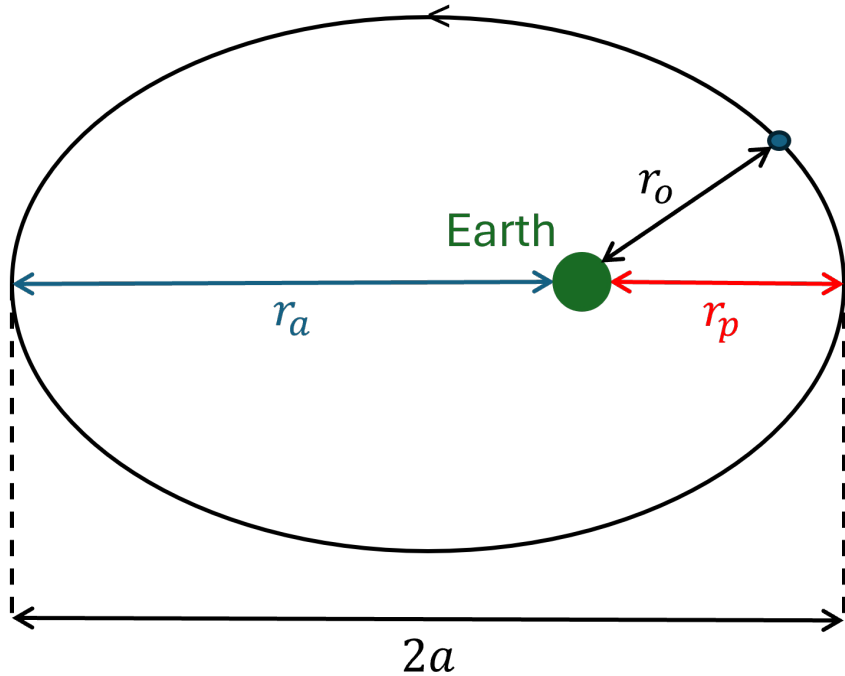


Figure 6.6: Elliptical orbit example.

From Figure 6.6, the orbital parameters can be visualized and it is clear where Equation 6.3 comes from. Shown in Figure 6.6 is an exaggerated size of Earth. This is just for visual purposes. All of the equations from the employed standard orbital mechanics references [21] and [22] assume negligible radii of orbital bodies.

The burns are characterized by a Δv —a change in velocity to move the ship into a designated orbit characterized by Equation 6.2. The general equation for the Δv is

$$\Delta v = v_f - v_i \quad (6.4)$$

where v_f is the final orbital velocity and v_i is the initial orbital velocity. It is important to note that Δv can be negative. The negative sign indicates that the burn is a retrofire while a positive sign indicates a Δv in the direction of motion. For this Hohmann transfer, the kick stage is moving from the initial orbit at an altitude of 100 km to Orbit A at an altitude of 525 km. From [27], the equatorial radius of Earth is approximately 6,378 km. For the transfer ellipse, the semi-major axis a , using Equation 6.3, is the average of the perigee and apogee radii. For a Hohmann transfer, the transfer ellipse perigee is the initial orbital radius 6,478 km and the apogee radius is the destination orbital radius 6,903 km. For this transfer ellipse, a is 6,691 km.

Using Equation 6.2 and 7.1, the first burn Δv_1 to go into the transfer ellipse was found to be 0.124 km/s. The second burn Δv_2 takes the kick stage from the transfer ellipse into Orbit A and was found to be 0.122 km/s. For this mission, impulsive maneuvers are assumed. This means that the Δv is instantaneously applied in the desired direction. In reality, there is a nonzero burn time provided by the rocket.

6.2.3 Orbit A to Orbit B Transfer

To go from Orbit A to Orbit B, the inclination will need to change alongside the altitude. To be most efficient, this will require a split-plane change combined with a Hohmann transfer. The split-plane change allows the inclination change to be split optimally between the two burns. The split change is defined by

$$\alpha_1 + \alpha_2 = \Delta i \quad (6.5)$$

where α_1 is the first burn inclination change (at perigee of the transfer ellipse) and α_2 is the second (at apogee of the transfer ellipse). Seen in Figures 6.7 and 6.8, the vector diagram of the split-plane change at the first and second burn, respectively, is shown.

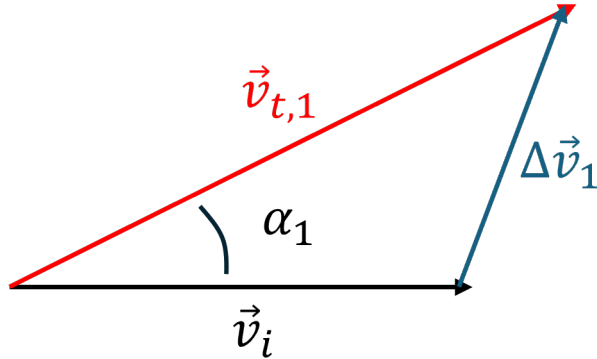


Figure 6.7: Split-plane change diagram for first burn.

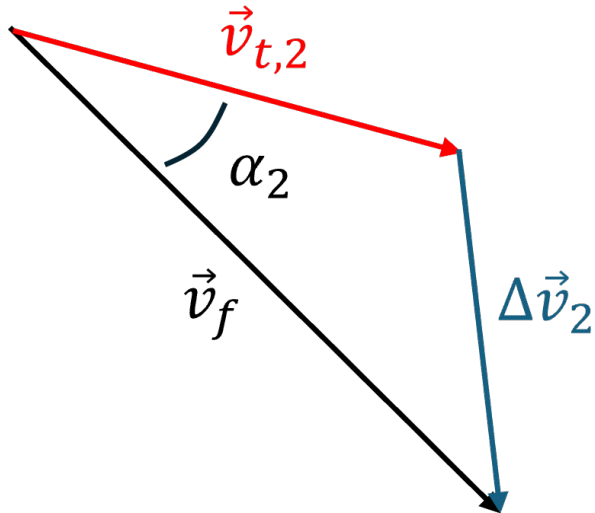


Figure 6.8: Split-plane change diagram for second burn.

From Figures 6.7 and 6.8, Δv_1 and Δv_2 can be found using law of cosines. The resultant equation for Δv_1 is

$$\Delta v_1^2 = v_{t,1}^2 + v_i^2 - 2v_{t,1}v_i \cos(\alpha_1) \quad (6.6)$$

where $v_{t,1}$ is the transfer ellipse velocity at the first burn, v_i is the velocity of the initial orbit. Similarly, Δv_2 can be written as

$$\Delta v_2^2 = v_{t,2}^2 + v_f^2 - 2v_{t,2}v_f \cos(\alpha_2) \quad (6.7)$$

where $v_{t,2}$ is the transfer ellipse velocity at the second burn, v_f is the velocity of the final orbit. The total Δv for the mission is

$$\Delta v_{total} = \Delta v_1 + \Delta v_2 \quad (6.8)$$

To minimize Δv_{total} , substitute Equation 6.5 into Equation 6.7 then substitute Equations 6.6 and 6.7 into 6.8 and solve for what α_1 value satisfies

$$\frac{\partial \Delta v_{total}}{\partial \alpha_1} = 0 \quad (6.9)$$

and the second-derivative test

$$\frac{\partial^2 \Delta v_{total}}{\partial \alpha_1^2} > 0 \quad (6.10)$$

Since this is still a Hohmann transfer, $v_{t,1}, v_{t,2}, v_i, v_f$ were calculated using Equation 6.2 and the same process outlined in Section 6.2.2.

Using MATLAB to solve Equation 6.9 and to check the second-derivative condition yielded an optimal α_1 and α_2 of 0.11° and 9.89° , respectively. The results can be seen graphically in Figure 6.9

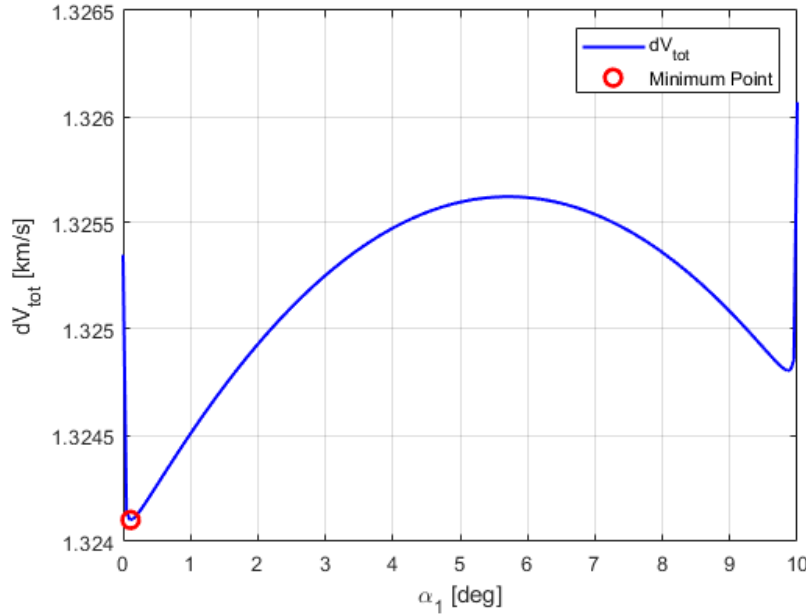


Figure 6.9: Split-plane change Δv vs α_1 .

From Figure 6.9, the minimum value can be very close to 0° . The overall magnitude of

the Δv saved from this split-plane change is small. However, such small splits may seem unnecessary, but every bit of saved fuel is important when sending things into space. Using these α_1, α_2 values, Δv_1 and Δv_2 can be calculated using Equation 6.6 and 6.7. These values are 0.015 km/s and 1.309 km/s, respectively. The total Δv for the transfer from Orbit A to Orbit B is 1.324 km/s, also seen by Figure 6.9.

To find how much Δv is saved by using the split-plane change, the Δv required for a standard plane change combined with a Hohmann transfer should be calculated. This is found by solving Equations 6.6 and 6.7 when α_2 is Δi and α_1 is 0° . For the standard plane change combined with a Hohmann transfer, the Δv required is 1.325 km/s. This saves roughly 1 m/s in fuel.

6.2.4 Orbit B to Orbit C Transfer

Following the same methodology outlined in Section 6.2.3, the Δv required for the kick stage to perform a split-plane change and Hohmann transfer can be calculated. Using the orbit data from Table 6.1, the Δv for this combined maneuver is 1.324 km/s. The first burn Δv_1 and α_1 are 0.015 km/s and 0.11° , respectively, while the second burn Δv_2 and α_2 are 1.309 km/s and 9.89° , respectively. These numbers match the exact calculations for the A–B transfer. This is expected since the inclination change Δi is the same and the altitudes are approximately the same given the scale of Earth, the gravitational body.

6.2.5 Phasing and De-orbits

Since these satellites need to be de-orbited within one week of launch, the phasing should be timed perfectly as to use the full amount of time remaining in the mission. Recall that the allotted time for the mission is one week from launch. This will give the most fuel-efficient de-orbit. From [21], the Δv required for a phasing maneuver is given by

$$|\Delta v| = \frac{|\Delta\theta|}{2\pi} \frac{\mu_e}{3v_0 a_0 N} \quad (6.11)$$

where v_0 is the initial velocity, a_0 is the original orbit semi-major axis, and N is the number of original orbital periods needed for the interceptor to move $\Delta\theta$. The time that can be allotted to these phasing maneuvers will depend on how much time has elapsed in the mission until the point before phasing.

From the time of launch until Falcon 9 has reached an altitude of 100 km, roughly 200 seconds will have passed [28]. The transfer time between orbits can be calculated by using Kepler's Third Law. From the time of launch until Falcon 9 has reached an altitude of 100 km, roughly 200 seconds will have passed [28]. From [22], the transfer time between orbits can be calculated by using Kepler's Third Law

$$T_0 = 2\pi \sqrt{\frac{a_0^3}{\mu_e}} \quad (6.12)$$

where T_0 and a_0 are the full orbital period and the orbit's semi-major axis. From Figure

6.5, it can be seen that a Hohmann transfer traverses half of the transfer ellipse. To find the transfer time, one should half the full orbital period. The transfer ellipses' semi-major axes can be calculated using the approach outlined in Section 6.2.3. The transfer times were calculated using Equation 6.12 and compiled into Table 6.2.

Table 6.2: Transfer Times Between Target Orbits

Transfer	Transfer Time (s)
Inject-A	2723
A-B	2853
B-C	2859

The next thing to calculate is the de-orbit time. This is well-defined for each orbit since the de-orbit trajectory is simply a Hohmann transfer to an altitude of 100 km. Using the approach shown above, the de-orbit times for each orbit altitude are shown in Table 6.3

Table 6.3: De-orbit Times for Various Altitudes

Altitude	De-orbit Time (s)
525	2723
530	2724
535	2726

From Table 6.3, the de-orbit times are essentially the same. Again, this is due to the small change in altitude relative to the Earth's gravitational parameter, seen in Equation 6.12. To calculate the allowable phasing time for each STD, the total mission time T can be written

$$T = T_l + T_t + T_p + T_d \quad (6.13)$$

where T_l, T_t, T_p, T_d are the launch time (from ground to 100 km), transfer time(s), phasing time, and de-orbit time, respectively. In Equation 6.13, T_t will change depending on which target orbit the STD is released into. Considering this, the maximum allowable phasing time for each target orbit can be found in Table 6.4

Table 6.4: Maximum Allowable Phasing Time for Target Orbits

Target Orbit	Maximum Phasing Time (s)
A	599000
B	596300
C	593400

From Table 6.4, each of the maximum allowable phasing times are less than 6 solar days (518400s). This will be the allotted time for phasing since this gives the mission one day of

extra time in case additional loitering is required. From Equation 6.11, N is defined as

$$N = \begin{cases} \frac{2\pi - \Delta\theta}{2\pi} + m & \Delta\theta \geq 0 \\ \frac{|\Delta\theta|}{2\pi} + m & \Delta\theta < 0 \end{cases} \quad (6.14)$$

where m , an integer, is the number of original orbit periods that must elapse before meeting. This is directly related to the timing. m can be calculated by solving

$$T_p = N \times T_0 \quad (6.15)$$

where T_0 is the original orbital period and T_p is the desired phasing time. All that is required to solve for the phasing Δv are the $\Delta\theta$ values for each defunct satellite. For reference, these angles can be seen in Figures 6.1, 6.2, and 6.3. Table 6.5 has the numerical values.

Table 6.5: Relative True Anomalies for Defunct Satellites

Orbit Tag	$\Delta\theta_1$	$\Delta\theta_2$	$\Delta\theta_3$
A	37.0°	-95.7°	-
B	169.0°	-38.8°	-
C	150.0°	-152.0°	-19.9°

Using all known orbital parameters for each target orbit and Equation 6.11, the maximum Δv for phasing is 0.06 km/s. The 6-day phasing maneuver makes this value incredibly small, explained by the fact that $\Delta v \propto \frac{1}{T_p}$.

6.3 Total Mission Delta-V

Section 6.2 demonstrated the process used to perform the orbital mechanics calculations. This section serves as a collection of all total mission Δv -values.

6.3.1 Kick Stage

For the kick stage, Table 6.6 has the required total Δv broken down by each maneuver.

Table 6.6: Total Kick Stage Δv

Maneuver	Δv [km/s]
Injection–Orbit A	0.246
Orbit A–Orbit B	1.324
Orbit B–Orbit C	1.324
Orbit C–De-orbit	0.124
Total	3.02

6.3.2 STDs

For the STDs, Table 6.7 has the required total Δv broken down by each maneuver.

Table 6.7: Total Δv for Kick Stage Maneuvers

Orbit	Δv [m/s]	
	Phasing	De-orbit
A	13.0	122
	33.7	
B	59.7*	123*
	13.7	
C	53.0	124
	53.7	
	7.00	
Maximum Total*	183	

Seen in Table 6.7, the maximum Δv any STD will need is 183 m/s. This was found by finding the largest phasing maneuver Δv and the largest de-orbit Δv and summing them. These maximums are indicated with a * in Table 6.7. To maintain symmetry in the overall design, all STDs will be equipped with the same Δv potential since the difference between the lowest and highest Δv required is only 48 km/s. Mass symmetry is important in the overall design since it will not tax the control system as much. An alternative consideration is to fill them only to their required amount with a safety factor and balance the STDs by mass, getting as close as possible to mass symmetry in the final design. Nonetheless, the values from Table 6.6 will be critical in sizing the kick stage rocket appropriately.

6.4 Mission Verification using Simulation

To verify the orbital mechanics calculations and perform more advanced analysis of re-entry, the mission was simulated in MATLAB. The orbital mechanics simulations were made by numerically solving the two-body problem given by the second-order ordinary differential equation (ODE)

$$\frac{d^2\vec{r}}{dt^2} = -\frac{\mu}{|\vec{r}|^3}\vec{r} \quad (6.16)$$

where \vec{r} is the position vector of the spacecraft in an (x,y,z) Earth-Centered Inertial frame. Solvers such as MATLAB's *ode45* will solve systems of first-order ODEs of the form

$$\frac{d\vec{y}}{dt} = \vec{f}(\vec{y}, t) \quad (6.17)$$

given an initial condition and a start and end time. The second-order ODE given by Equation 6.16 can be transferred to a first-order ODE by creating a new vector \vec{y} and defining it as

$$\vec{y} = \begin{bmatrix} x \\ y \\ z \\ \dot{x} \\ \dot{y} \\ \dot{z} \end{bmatrix} \quad (6.18)$$

and then solving for $\dot{\vec{y}}$

$$\dot{\vec{y}} = \begin{bmatrix} \dot{x} \\ \dot{y} \\ \dot{z} \\ \ddot{x} \\ \ddot{y} \\ \ddot{z} \end{bmatrix} \quad (6.19)$$

where the dots indicate time derivatives. Noticing that the components (x,y,z) are, by definition, \vec{r} , Equation 6.18 can be rewritten as

$$\vec{y} = \begin{bmatrix} \vec{r} \\ \dot{\vec{r}} \end{bmatrix} \quad (6.20)$$

and Equation 6.19 as

$$\dot{\vec{y}} = \begin{bmatrix} \ddot{\vec{r}} \\ \ddot{\vec{r}} \end{bmatrix} \quad (6.21)$$

Rewriting Equation 6.21 in terms of \vec{y} and substituting Equation 6.16 gives

$$\dot{\vec{y}} = \begin{bmatrix} \vec{y}_{(4,5,6)} \\ -\frac{\mu}{|\vec{y}_{(1,2,3)}|^3} \vec{y}_{(1,2,3)} \end{bmatrix} \quad (6.22)$$

where the notation $(1,2,3)$ represents elements one, two, and three of \vec{y} and $(4,5,6)$ represents elements four, five, and six of \vec{y} . With that, the ODE solver can simulate spacecraft motion for the initial conditions

$$\vec{y}_0 = \begin{bmatrix} \vec{r}_0 \\ \vec{v}_0 \end{bmatrix} \quad (6.23)$$

for a given time interval.

6.4.1 Convergence Analysis

When running preliminary simulations, there were issues with orbital decay over large time periods. This was of particular significance during the phasing maneuvers where the phasing time was on the order of 10^5 seconds. While orbital decay is expected in reality, this is not to be expected given the simplicity of the two-body problem where no atmospheric effects

are present. Convergence analysis was done using MATLAB's explicit ODE solver *ode45* for a spacecraft in a circular orbit for 500,000 s. It is expected that the radial distance will not change after the 500,000 s. Using Equation 6.2 to find the velocity, the initial conditions for a spacecraft in a circular orbit at a distance of 10,000 km is

$$\vec{y}_0 = \begin{bmatrix} 10000 \\ 0 \\ 0 \\ 0 \\ 6.33 \\ 0 \end{bmatrix} \quad (6.24)$$

where the initial position of (10000,0,0) was chosen for simplicity. To address this orbital drift, convergence analysis was conducted using MATLAB's ODE solvers. At the end of the time interval, the final orbital radius was compared to the expected value of 10,000 km in the form of a percent error.

The analysis was conducted for various tolerance sizes ranging from 10^{-4} to 10^{-12} for two types of tolerances: absolute and relative. Figure 6.10 shows the percent error for varying absolute tolerances for *ode45*.

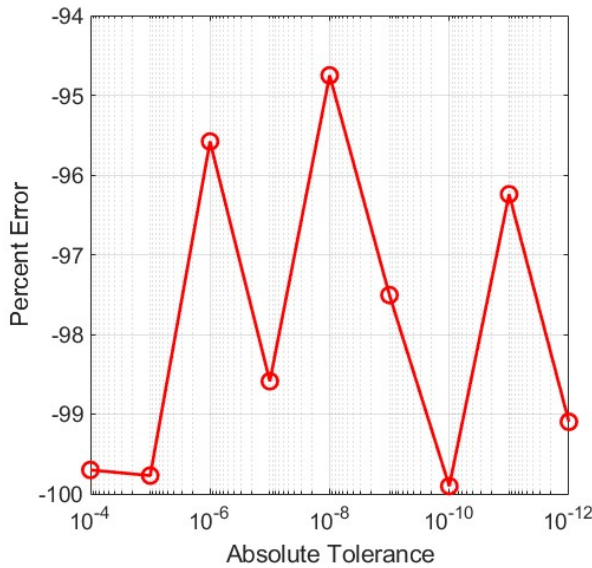


Figure 6.10: Convergence analysis for *ode45* using various absolute tolerances.

Figure 6.10 shows undesired results when performing convergence analysis. First, the percent errors are near 100% in magnitude, and second there is no convergence to a single solution as the tolerance increases. Switching from *ode45* to a higher-order solver *ode113* reduced error while increasing computational efficiency—a worthwhile upgrade. With the same initial

conditions, the same convergence analysis was done. Figure 6.11 shows the results.

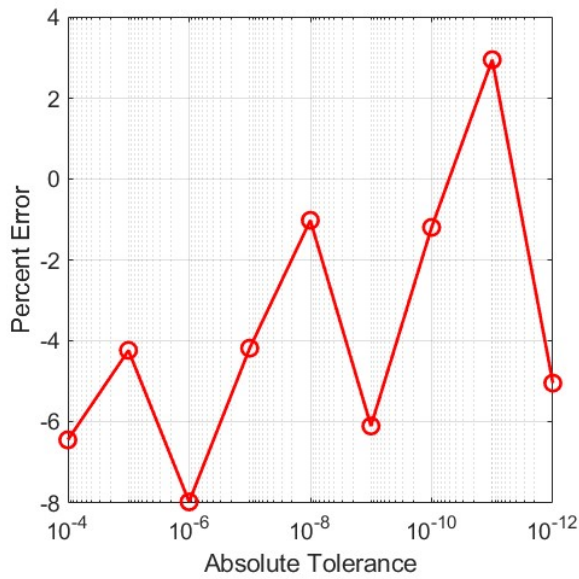


Figure 6.11: Convergence analysis for *ode113* using various absolute tolerances.

Although the magnitude of the error is lower using *ode113*, seen in Figure 6.11, there is no convergence in the solution. To achieve convergence, the tolerance was changed from absolute to relative. The results are shown in Figure 6.12.

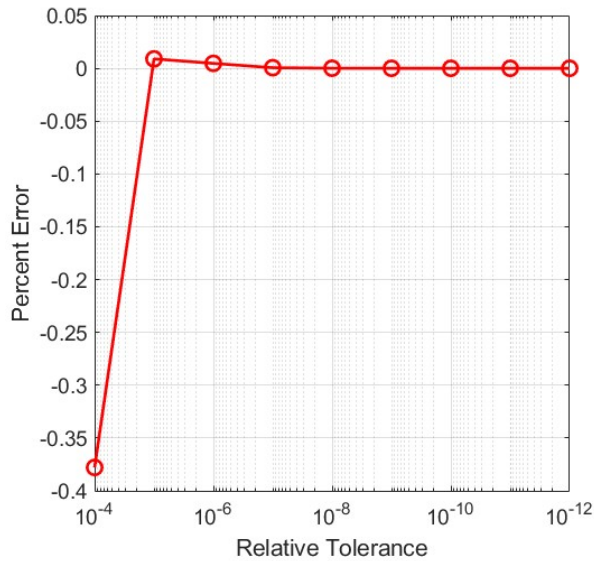


Figure 6.12: Convergence analysis for *ode113* using various relative tolerances.

Seen in Figure 6.12, the switch from absolute to relative tolerance yielded proper convergence in the solution. With this, the simulations were created using *ode113* using a relative tolerance of 10^{-10} and it can be trusted that the solutions are correct.

7 Design Concepts

7.1 Overall Design

To come up with the overall vehicle design for this project, a number of design concepts were quickly brainstormed, however, there was one overall design that made the most sense for this vehicle. Two guiding philosophies became clear. First, in order to de-orbit multiple satellites, it takes significantly more fuel to have a single vehicle de-orbit one satellite at a time and return to orbit after each satellite, so this type of drag-and-return vehicle is not feasible. Second, since multiple de-orbiters are necessary to de-orbit multiple satellites, it is similarly inefficient for each de-orbiter to carry the fuel and associated mass required to raise orbit to target altitude and de-orbit the satellite.

Both of these inefficiencies and guidelines are a result of the Tsiolkovsky rocket equation

$$\Delta v = v_e \ln \frac{m_0}{m_f} \quad (7.1)$$

where Δv is the change in velocity, v_e is the effective exhaust velocity (analogous to efficiency of propulsion system), m_0 is the initial mass, and m_f is the final mass [29]. Note that since Δv increases logarithmically, the larger the mass of your vehicle (requiring more capable propulsion system, structures, etc.), the mass of fuel required grows exponentially large. Therefore, it is in your best interest to optimize your vehicle through multiple stages.

The general design concept in Figure 7.1 consists of two sections. The first section, labeled "1", is called the "kick stage". This part of the vehicle contains a powerful engine and sufficient propellant to take the entire craft from low-Earth Orbit (LEO)—where it is placed by the launch vehicle—to the destination orbit and inclination where the target debris is.

Once brought to the destination orbit and inclination, one of the 7 Space Trash De-orbiters (STDs), labeled "2" in Figure 7.1 (top-down view in Figure 7.2) will separate from the kick stage, where it can perform a small maneuver to rendezvous with the target debris and the two will de-orbit together. The kick stage will then propel the remaining STDs to the next orbit altitude and inclination to repeat the process until there are no more STDs remaining. At this point, the kick stage will perform a de-orbit burn, and burn up upon re-entry into Earth's atmosphere.

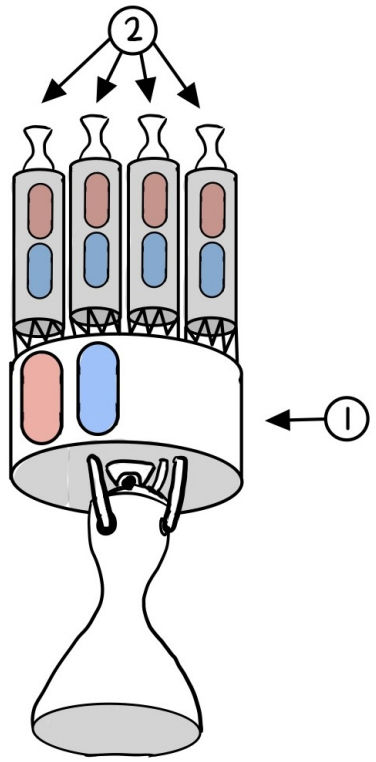


Figure 7.1: Overall design concept including 1: kick stage and 2: STDs.

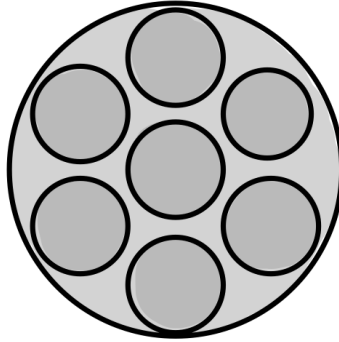


Figure 7.2: Top-down view of kick stage loaded with 7 STDs.

Ultimately, this design serves as a low-cost, single-use vehicle that can quickly and affordably remove specific debris that would otherwise take years to de-orbit naturally [30].

7.2 Propulsion System

Since the kick stage is responsible for significant maneuvering and effectively shuttling the STDs to their destinations, it requires a substantial propulsion system capable of the necessary thrust and total impulse.

Figure 7.3 shows the kick stage propulsion system concept, including the required ability to gimbal by angle θ about its mounting point on the kick stage. This is needed due to the fact that, as it deploys STDs, it may no longer have a symmetrical mass distribution about the connection point, and the thrust will generate a moment that must be counteracted to accelerate in a controlled manner.

There are a number of different propulsion systems that could be used, but three systems are most commonly used for this type of application: ion, cryogenic chemical, and hypergolic chemical. Ion thrusters use electricity and an electric field to ionize and accelerate a propellant such as xenon, generating very small thrust but extremely high efficiency. Cryogenic chemical engines use propellants like liquid hydrogen (LH₂) and liquid oxygen (LOX), and offer both high thrust and performance but at the cost of complicated insulated cryogenic tanks and standalone ignition systems. Hypergolic chemical engines use propellants that ignite on contact, such as monomethylhydrazine (MMH) and nitrogen tetroxide (NTO), to achieve high thrust and good efficiency, and reduced complexity due to auto-ignition [31].

The following design matrix in Table 7.1 was used to determine which propulsion system was to be used on the kick stage and each STD.

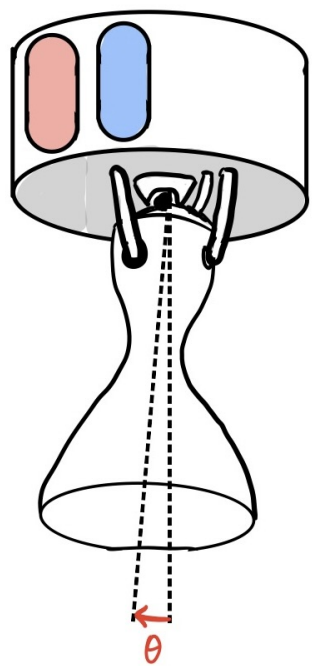


Figure 7.3: Kick stage propulsion system concept with engine thrust vector control.

Table 7.1: Propulsion System Design Matrix

Criteria	Weight	Propulsion Type		
		Ion thruster	Chemical: hypergolic	Chemical: cryogenic
Performance (time to de-orbit)	4	1 (years)	5 (minutes)	5 (minutes)
Efficiency (Isp)	3	5 (>1000s [32])	3 (320s [31])	4 (450s [33])
Ease of use	2	4	5	2
Total score	-	27	39	36

The following strategies were used to determine the scores in the table: Time to de-orbit (weighted highest for most important) was calculated roughly using orders of magnitude of each propulsion type's thrust and the required Δv . Efficiency (weighted second highest) was rated by specific impulse (Isp) available from public data on similar engines. Lastly, ease of use (weighted lowest since it can be mitigated) was determined by considering overall complexity and auxiliary components needed to operate the engine.

Based on the scores in Table 7.1, a hypergolic chemical propulsion system was chosen for both the kick stage and STD propulsion systems. Note that the kick stage propulsion system requires high thrust performance, so the only viable options are cryogenic and hypergolic chemical propulsion. Hypergolic systems are very commonly used for orbital maneuvering, like the Orbital Maneuvering System (OMS) pods on the space shuttle [34], and the AJ-10 [35] due to the balance of performance and efficiency. These systems do come with drawbacks however, one of them being the extremely caustic nature of the propellants. This risk is easily mitigated however when accounted for in launch and de-orbit procedures, since this spacecraft will not be near humans, unlike other systems.

7.3 Gripping Mechanism

Bringing two objects together in space and making sure they remain together, particularly during impulsive maneuvers, is a complex task that is still seeing development into the modern age. The gripping mechanism to attach each STD to the debris (effectively, its payload) is of vital importance to the mission's success, with multiple concepts already in circulation.

7.3.1 Armature Grip

Some proposals for a space debris retrieval system involve robotic "arms" that wrap around debris to capture it. The usage of an armature like this, one that relies on fully surrounding a piece of debris, could limit the potential use cases of the craft as the armature would be constrained to encapsulating objects below a certain size.

Alternatively, an armature could instead use clamps and pre-installed hardpoints to capture satellites with dimensions larger than what it can encapsulate, though this would limit debris capture to satellites that already have the specified hardpoints installed.

7.3.2 Puncture Drill

Offering a more rigid attachment, a mechanism following this design would use a drill to puncture the debris' structure and remain attached. This would allow for connections to satellites and debris with unconventional geometries, and would offer a far more rigorous connection depending on the sizing of the drill.

However, one concern with this method would be the possibility of generating further debris during the drilling process. A system would need to be implemented in order to ensure that no chips or swarf is ejected before the de-orbit burn is completed, as well as avoiding any fuel lines or sensitive equipment which may lead to potential rapid unscheduled disassemblies (RUD's) of both the debris and STD.

7.3.3 Snare/Lasso Capture

A flexible and adaptable method, snare or lasso capture involves deploying a tether or cable loop to ensnare debris. This technique can be effective for capturing objects of various sizes and shapes, particularly those with protrusions or structural features that allow for effective entanglement.

One major advantage of a snare system is its ability to work at a safe standoff distance, reducing the risk of collision during capture. Additionally, this method does not require precise alignment with the target, making it useful for capturing tumbling debris. However, snare capture may struggle with very smooth or compact objects that provide minimal grip points. Effective deployment and retraction mechanisms will need to be designed to prevent entanglement with the capturing spacecraft itself.

7.3.4 Hard-Soft Electroadhesive Capture

Hard-soft electroadhesion offers a promising approach for space debris capture by utilizing electrostatic forces to create a controlled and adaptable grip. This method combines rigid conductive electrodes (hard) with compliant dielectric materials (soft), enabling the system to conform to various surface geometries while maintaining a strong electrostatic attraction [36].

One key advantage of hard-soft electroadhesion is its ability to securely grip both regular and irregular surfaces without causing damage. Unlike traditional mechanical methods, it requires minimal physical contact force, reducing the risk of generating additional debris. Additionally, it can function effectively across a range of surface materials, provided there is sufficient charge interaction. However, limitations exist in highly conductive environments, where charge dissipation could weaken adhesion.

7.3.5 Dry Adhesives & Microspines

Inspired by the microstructures found in gecko feet, dry adhesives use van der Waals forces to adhere to surfaces without requiring additional energy input. These adhesives could provide a reliable means of gripping debris without causing surface damage. However, maintaining

adhesive effectiveness in the harsh environment of space—where contamination and temperature variations could degrade performance—remains an ongoing challenge.

Similar to dry adhesives, but on a larger, more macroscopic scale, are microspines. Microspines use small, hooked elements that latch onto surface irregularities, making them particularly well-suited for gripping rough or porous surfaces. This could be useful for capturing debris with complex, rough geometries. However, smooth or polished surfaces may not provide sufficient grip points for microspines to function effectively, which would prevent the mechanism from capturing most satellites. As such, microspines are not considered a viable gripping mechanism.

7.3.6 Gripping Mechanism Decision

To decide on an appropriate gripping mechanism, each option was weighed across three scales: compatibility, or the ability for the specified mechanism to attach to a wide variety of debris types; effectiveness, essentially the strength and reliability of said mechanism; and cost, considering both construction and research costs. The design matrix is presented in Table 7.2.

Table 7.2: Gripping Mechanism Design Matrix

Criteria	Weight	Grip Type				
		Armature	Drill	Snare	Electroadhesive	Dry Adhesive
Cost	8	5	3	4	3	4
Compatibility	6	3	4	3	5	4
Effectiveness	4	5	3	2	3	3
Total score	-	78	60	58	66	68

Based on these scores, an armature system was chosen for the grip mechanism. Although somewhat limited compared to other options, a pre-installed hardpoint would allow for a low-cost option for attachment. Furthermore, they will allow for a more thorough analysis of the capture and re-entry to ensure the debris safely and completely burns up in the atmosphere.

Within the selection of an armature for the gripping mechanism, still many methods of doing so still exist. A primary trait is from the orientation and number of grippers and mounting points. Four potential configurations shown in Figure 7.4 will be considered.

First, the simplest option, a single bar with a grabber centered on the STD, shown in Figure 7.4 (a). This design minimizes the mass required for SpaceX to mount to the Starlink. However, with a single clamp, there is no redundancy to the mechanism. Furthermore, the single grabber would likely experience very high bending and torsional loads during reorientation.

As for the second and third configurations shown in Figure 7.4 (b) and (c), they will differ from the single bar by adding more redundancy in the case of a gripper failure. Each will distribute the load of the de-orbit maneuver across multiple grabbers. The drawback is that more mass will be required on both the Starlink and STD.

Finally, the last configuration includes multiple grippers on the STD side and a circular ring for mounting on the Starlink. This will allow a rotational degree of freedom for the STD on approach due to most any roll angle being compatible with the grabber bar. This configuration suffers the most from the mass added to the Starlink because it will result in much more bar mass that is not used for gripping.

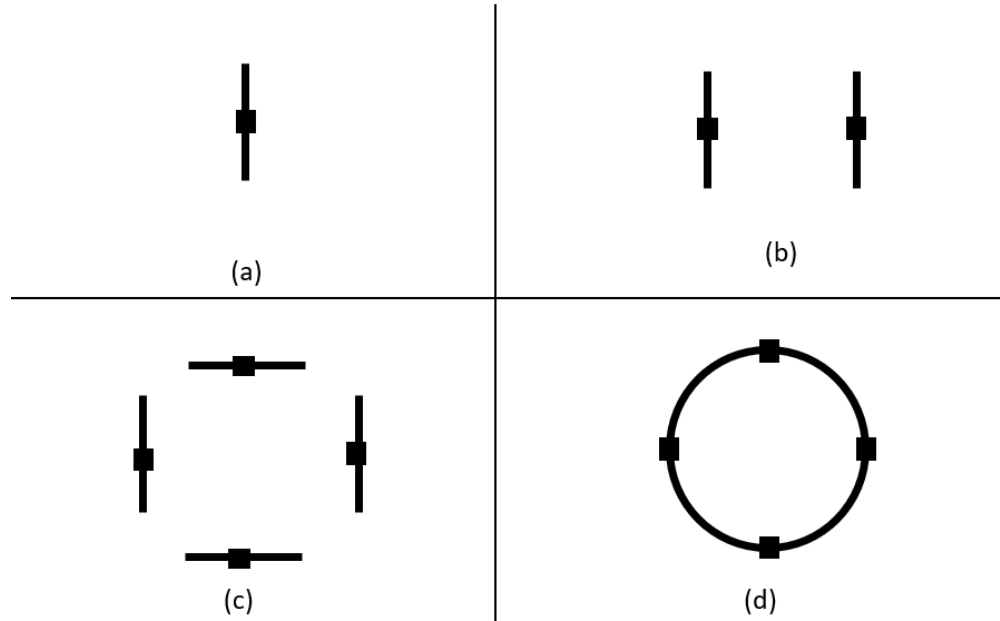


Figure 7.4: Potential Mounting Configurations

Each configuration will be evaluated based on its mass, redundancy, load distribution, and ease of docking. These criteria are critical to ensuring both mission success and safety, particularly under the dynamic conditions of capture, reorientation, and atmospheric re-entry. The final selection will prioritize a balance between minimizing additional mass on both the STD and Starlink, while maximizing mechanical reliability and alignment tolerance during docking. A scoring matrix will be used to objectively compare the four options and identify the configuration that offers the best overall performance.

The decision matrix in Table 7.3 summarizes these criteria and weightings to determine the best fit for the mission.

Table 7.3: Gripping Mechanism Design Matrix

Criteria	Weight	Configuration			
		a	b	c	d
Mass	3	5	4	3	2
Redundancy	1	1	2	4	4
Load Distribution	3	1	2	4	4
Ease of Docking	2	2	2	2	4
Total score	-	23	24	29	30

Table 7.3, shows that either configuration (c) or (d) is desirable. To determine between the two, an analysis of the reliability of the docking control will be required. If the control system is reliable without the roll degree of freedom that was presented for configuration (d), then configuration (c) will be a better solution.

Now, to take a closer look at the grabbing mechanism, the options are numerous. Therefore, the design process takes the path of choosing design aspects based on subjective reasoning. This is considered to be the best path forward because decision matrices may receive inaccurate weightings before a more rigorous analysis.

The following will be characteristics that a grabbing mechanism should [have](#):

1. The mechanism should have an active control to allow release and reattachment in the case of misalignment.
2. The mechanism should not have an auto lock upon closing from mechanisms to avoid failures such as a [misfire](#).
3. The mechanism should have two clamps that move [such that there is](#) clearance on both sides of each attachment point during approach.
4. The mechanism will provide force to the clamps through gears, which allows for gear reductions if needed.
5. The mechanism will provide torque to the gears through a stepper motor or pneumatic piston, depending [on](#) force requirements.
6. The mechanism will include actuators to provide axial extension and rotation for minor misalignment.

These guidelines will be followed for the initial design. If at any point in the sizing and analysis, it is clear there [is](#) a more desirable option, these guidelines will be reevaluated.

8 Equipment

To operate the satellite, various onboard hardware components and subsystems must be integrated into the vehicle. This section presents the major equipment categories, providing key specifications for each. A summary table at the end of this section compiles the mass and power data for system-level design tracking.

8.1 Propulsion System

Each Space Trash De-orbiter (STD) uses a monopropellant hydrazine engine, producing 3100 N of thrust with a specific impulse of 220 s. Hydrazine propellant mass is 215 kg, stored in a cylindrical tank. For attitude control, 25 N hydrazine thrusters are used, with a total RCS fuel reserve of 5 kg.

8.2 Docking Mechanism

The docking system uses an active, dual-clamp armature gripper, actuated by 1.5 Nm stepper motors and supported by a gear train providing a total reduction of 47.4:1. Each clamp must exert 1550 N of force to secure the connection, and the structure is designed for a maximum de-orbit burn load of 3100 N.

8.3 Attitude Control System

The attitude control subsystem includes four Honeywell HR14-25 reaction wheels (25 Nms capacity, 7.5 kg each)[37]. In addition, off-the-shelf hydrazine RCS thrusters from IHI AeroSpace producing 5 N of thrust[38] will be installed. Combined, they enable rapid reorientation for docking and despinning of a docked Starlink satellite rotating up to 10°/s.

8.4 Inertial Measurement Unit

A VectorNav VN-100 IMU is used, weighing 57 g and consuming 1.8 W. It provides real-time acceleration and angular rate data at high frequency for control and navigation [39].

8.5 Flight Computer

The onboard computer is the LEON3FT processor integrated with CubeComputer hardware, weighing 80 g and consuming 3 W. It coordinates control tasks, propulsion commands, and telemetry management [40].

8.6 GNSS Receiver

A NovAtel OEM719 GNSS receiver provides dual-frequency global positioning with 0.03 m horizontal accuracy. It weighs 13.5 g and consumes 50 mW on average [41].

8.7 Star Tracker

The ST200 star tracker with 0.005° pointing accuracy and a 0.047 kg mass provides high-precision attitude determination, consuming 165 mW [42].

8.8 S-band Communications

An EnduroSat S-band transceiver module is used, weighing 180 g and consuming 2.5 W. It supports data rates up to 1 Mbps and links to ground stations for telemetry and command [43].

8.9 Radar Tracking

A short-range Frequency Modulated CW radar system, like one from SSBV Aerospace & Technology Group, enables relative navigation within 100 m. The radar unit weighs 100 g and consumes 1 W [44].

8.10 LiDAR

A CE30-D solid-state LiDAR from Benewake provides 3D mapping within a 30 m range. It weighs 100 g and consumes 5 W, enabling precision docking maneuvers [45].

Table 8.1: Subsystem Mass and Power Summary

Subsystem	Mass (kg)	Power (W)
Main Engine	25	-
RCS Thrusters (32x)	2	-
Fuel Tank	25	-
Reaction Wheels (4x)	30	120
IMU	0.057	1.8
Flight Computer	0.08	3
GNSS Receiver	0.0135	0.05
Star Tracker	0.047	0.165
S-Band Comm.	0.18	2.5
Radar Sensor	0.1	1
LiDAR	0.1	5
Docking System	15	3
Total (approx.)	198.6	136.5

9 STD Sizing

In order to complete its mission, each individual STD must be built to meet several requirements. The most strict requirement is the one of impulsive capability, essentially the craft's ability to change the velocity of both itself and the mass it has attached to by a specified amount. Secondly, the STD must be capable of maneuvering in orbital environments to a degree that allows for safe, consistent attachment to debris that may be spinning.

9.1 Fuel tank

Table 9.1: Used properties of Monopropellant Hydrazine [46]

Monopropellant Hydrazine	
Chemical Formula	N_2H_4
Density ρ [kg/m^3]	1,004.5
Specific Impulse I_{sp} [s]	220

The fuel tank of the STD is a vital component that carries the fuel the STD needs during its mission. List components of the STD that use fuel. Explain that each STD will have one fuel tank that carries the total amount of required fuel during the STD mission.

The selected propellant for the STD is monopropellant hydrazine (N_2H_4), which is the industry standard for satellite propulsion. Hydrazine is widely used due to its high reliability, stability, and efficiency, making it an optimal choice for de-orbiting maneuvers.

Unlike bipropellant systems, which require precise fuel-oxidizer mixing, monopropellant systems rely on a single propellant and a catalyst to induce chemical decomposition. This process, rather than combustion, generates high-temperature gases for thrust, eliminating the need for complex ignition mechanisms, additional plumbing, and oxidizer storage. Consequently, hydrazine propulsion systems are lighter, more compact, and simpler, making them advantageous for small satellite applications. Additionally, the decomposition reaction allows for precise throttle control, providing greater maneuverability during de-orbiting [46].

Hydrazine is a hypergolic fuel with similar properties to water. It has a high density of about $1,004.5\text{ kg/m}^3$, allowing for a more compact fuel tank design compared to lower-density alternatives, and a specific impulse (I_{sp}) of approximately 220 s, which provides an efficient balance between thrust performance and fuel economy [46].

These factors make hydrazine an optimal choice for the STD propulsion system, providing the necessary thrust, fuel efficiency, and compact storage capabilities required for effective de-orbiting operations.

The downside of using hydrazine propellant is that it is highly toxic. Exposure to high levels of hydrazine can cause a host of health problems, including damage to the liver, kidneys and central nervous system. While the fuel itself is relatively inexpensive ($\sim 100\text{ \$ per pound}$), the need for protective measures significantly increases operational costs [47].

9.1.1 Fuel tank volume

The sizing of the fuel tanks of the STDs is determined based on the required Δv needed to de-orbit a Starlink satellite. Using the rocket equation (Equation 9.1, with u_{eq} the equivalent exhaust velocity and \mathcal{R} the mass ratio parameter) alongside reasonable predictions of the mass distribution of the STD, the necessary fuel mass can be estimated. Using the density of the selected propellant, an approximate sizing of the fuel tanks can be determined.

$$\Delta v = u_{eq} \cdot \ln \mathcal{R} \quad (9.1)$$

The dry mass of the STD is currently unknown and will be precisely determined upon finalizing the design. However, preliminary mass approximations are necessary for initial calculations.

- Main engine: estimated at 25 kg, based on typical hydrazine thrusters [48].
- Fuel tank: estimated at 25 kg, based on typical hydrazine tanks [49].
- Propulsion system (excluding main engine and tank): estimated at 35 kg, incorporating a margin to accommodate potential mass variations.
- Capturing mechanism: estimated at 15 kg, accounting for the structural integrity required to securely grasp a Starlink satellite.
- Reaction Control System (RCS): estimated at 30 kg, with further justification provided in Section 9.3 on attitude control sizing.
- Additional structural components: estimated at 50 kg, covering frame, support structures, and other mechanical elements.

The total structural mass of the spacecraft is

$$m_s = m_{engine} + m_{tank} + m_{propsys} + m_{capture} + m_{RCS} + m_{structural} = 180 \text{ kg} \quad (9.2)$$

At this stage, the propellant mass is determined. Assuming a total propellant mass of 215 kg with a safety factor of 1.15, the effective propellant mass is

$$m_p = \frac{m_{fuel}}{SF} = \frac{215 \text{ kg}}{1.15} = 186.96 \text{ kg} \quad (9.3)$$

The total initial mass of the STD is

$$m_0 = m_l + m_s + m_p = 2,266.96 \text{ kg} \quad (9.4)$$

The structural coefficient ϵ is defined as

$$\epsilon = \frac{m_s}{m_p + m_s} = 0.491 \quad (9.5)$$

Typical satellites have a structural coefficient of $0.15 - 0.25$ [50]. In the case of an STD, the structural coefficient is relatively high since complex orbital transfers are performed by the kick stage, resulting in a lower propellant requirement.

The payload ratio λ is given by

$$\lambda = \frac{m_l}{m_0 - m_l} = 5.178 \quad (9.6)$$

The mass ratio parameter (\mathcal{R}) is then computed as

$$\mathcal{R} = \frac{1 + \lambda}{\epsilon + \lambda} = 1.090 \quad (9.7)$$

Using the specific impulse of hydrazine ($I_{sp} = 220$ s) and the gravitational acceleration at Earth ($g_e = 9.81$ m/s²), the equivalent exhaust velocity is

$$u_{eq} = I_{sp} \cdot g_e = 2,158.20 \text{ m/s} \quad (9.8)$$

The resulting Δv for the system is then

$$\Delta v = u_{eq} \ln(\mathcal{R}) = 185.76 \text{ m/s} \quad (9.9)$$

This value exceeds the required 183 m/s outlined in Section 6.3.2, confirming that a total fuel mass of 215 kg is adequate for the de-orbiting operations.

The volume of required hydrazine fuel is determined based on its mass and density ($\rho = 1,004.5$ kg/m³) in Equation 9.10.

$$V_{fuel} = \frac{m_{fuel}}{\rho_{hydrazine}} = 0.214 \text{ m}^3 = 214 \text{ L} \quad (9.10)$$

The fuel tank is modeled as a cylindrical body with hemispherical end caps. Its total volume is determined using Equation 9.11.

$$V_{tank} = \frac{\pi}{4} D^2 h + \frac{4}{3} \pi \frac{D^3}{8}. \quad (9.11)$$

Assuming a height-to-diameter ratio of 2.8, the diameter D , height h , and cylindrical section length l of the tank are given by:

$$\begin{aligned} D &= 0.480 \text{ m} \\ h &= 1.344 \text{ m} \\ l &= 0.864 \text{ m} \end{aligned} \quad (9.12)$$

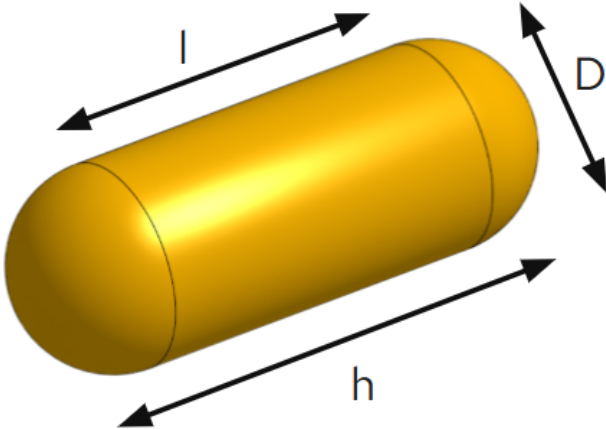


Figure 9.1: Illustration of D, h, and l of the fuel tank.

These dimensions are indicated in Figure 9.1. These values provide a reasonable estimate of the final fuel tank dimensions and serve as a good approximation for further design considerations.

9.1.2 Fuel tank thickness

The design of the fuel tank's thickness is crucial for ensuring the structural integrity of the tank under the operating pressures. For a pressurized, thin-walled cylindrical tank, the stresses acting on the tank are divided into hoop, axial, and radial components. The hoop stress is typically the most critical and is the limiting factor in the design of the tank thickness.

For the cylindrical part of the tank, the hoop stress, axial stress, and radial stress are given by:

$$\begin{aligned}\sigma_{hoop} &= \frac{pD}{2t} \\ \sigma_{axial} &= \frac{pD}{4t} \\ \sigma_{radial} &\approx \text{negligible}\end{aligned}\tag{9.13}$$

With p the internal pressure (gauge pressure inside vessel), D the diameter, t the thickness of the tank wall.

For the spherical end caps of the tank, the stress components are:

$$\begin{aligned}\sigma_{hoop} &= \frac{pD}{4t} \\ \sigma_{axial} &= \frac{pD}{4t} \\ \sigma_{radial} &\approx \text{negligible}\end{aligned}\tag{9.14}$$

The hoop stress is the most critical and dictates the required thickness for the tank. A factor of safety of 1.5 is applied to ensure that the tank operates within safe limits. The thickness of the cylindrical tank wall is determined using the yield stress of Ti-6Al-4V and an internal pressure of 10 bar, which is currently an estimate. The tank thickness is calculated as:

$$t = \frac{pD}{2 \left(\frac{\sigma_y}{SF_t} \right)} = 0.409 \text{ mm} \quad (9.15)$$

9.1.3 Additional considerations

In the case of a fuel tank, additional factors like fuel slosh (lateral motion of liquid propellant in a partially empty tank) and fuel venting must be considered. Fuel slosh can induce inertial forces that resonate with the flight motions, potentially affecting the stability of the tank. This issue is typically mitigated by baffling within the tank to reduce slosh effects. Additionally, thermal stresses due to temperature variations during flight must be accounted for in the design.

9.2 Propulsion

With the fuel for the STD set, an analysis on its engine must be performed in order to optimize the system for hydrazine.

With decomposition-based monopropellant engines, the main design factor comes into play with the choice of catalyst. With early development in the 1960's, the Shell Development Company introduced an alumina-based iridium catalyst that saw widespread use throughout the late 20th century [51], Shell 405. However, modern catalyst engines instead use a variant of Shell 405, S-405. S-405 is another iridium catalyst that matches the performance characteristics of Shell 405 closely [52], and is widely available.

In terms of the geometry of the engine, the nozzle is analyzed first based on experimental data and design of historical S405-based hydrazine engines [53]. Typical hydrazine engines have an expansion ratio (the ratio between the nozzle exit area and the throat area) in the range of 44:1 [46] in order to perform at specific impulses of 220 seconds.

Though this gives a ratio, it does not give an overall size. Thus, other examples of hydrazine decomposition engines are utilized to size the STD's. NASA's Skycrane system, a powered lander for Mars, utilizes six monopropellant hydrazine engines to bring payloads safely to the surface. Each engine can be throttled, and can provide a thrust of up to 3,100 N [54]. This thrust is used as a metric for determining the final size of the engine.

The nozzle is approximated as a Rao parabolic nozzle, a commonly used approximation of an ideal rocket nozzle shown in Figure 9.2.

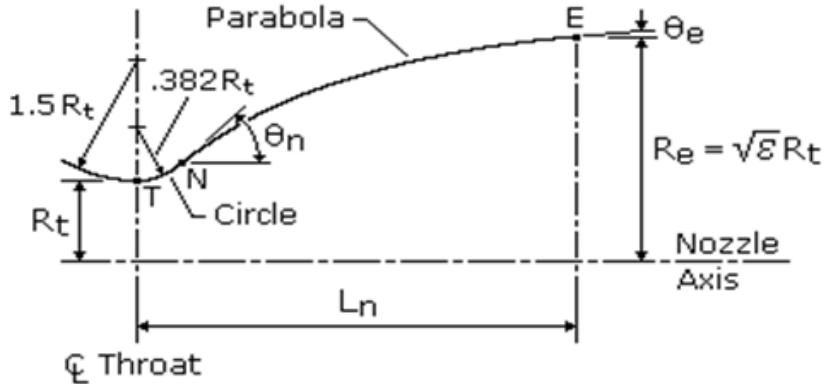


Figure 9.2: The cross section of a Rao parabolic nozzle [55].

The exit radius is directly related to the previously defined expansion ratio of 44:1 by

$$R_e = \sqrt{\varepsilon} R_t \quad (9.16)$$

given in Figure 9.2. A rough upper bound of the exit radius is constrained by the 7-STD cluster outlined in Section 7.2. The total diameter of the cluster is approximated as

$$D_{tot} \approx 3.5 D_{STD} \quad (9.17)$$

where D_{tot} is the total diameter of the cluster and D_{STD} is the diameter of a single STD.

Overall, the system will need to fit within the payload safety envelope bounds of the Falcon 9 with a height of 11.4 m and ceiling diameter of 1.3 m [20]). Thus, based on these constraints and the specified geometry of the nozzle in Figure 9.2, an exit radius of 0.186 m is used to size the total length of the nozzle to 0.35 m.

Assuming a vacuum-optimized engine (an engine that perfectly expands to a vacuum or near-vacuum pressure), the thrust is found as

$$\mathcal{T} = \dot{m} I_{sp} g_e \quad (9.18)$$

where \dot{m} is the mass flow rate through the engine, I_{sp} is the specific impulse of the engine, and g_e is standard gravity at the Earth's surface [21]. Knowing a desired thrust of 3100 N, Equation 9.18 can be used to solve for a mass flow rate of 1.436 kg/s. This measure specifies the capabilities of the pumping system.

9.3 Attitude Control

To understand the necessary specification for the attitude control system, it is important to specify the most demanding maneuvers required by the system. A qualitative overview of the main maneuvers will be defined.

The first maneuver will be the orienting the STD after the kick stage drops off the STD in the desired orbit. The STD must be able to sense its orientation and to ensure adequate control the fuel requirements will be to reorient the satellite up to 180° about the major axis for the phasing maneuver.

Once the satellite is nearing the Starlink satellite, the STD will need to make precise maneuvers in order to dock with the Starlink satellite. Due to the potential of a dysfunctional attitude control system on the Starlink satellite, the STD must create no relative linear or angular velocity between the two bodies. Control simulations must be conducted to determine the maximum allowable rate of stable rotation from the Starlink satellite. For the purpose of getting sizing estimates, a maximum angular velocity allowed for docking will be 10 degrees per second about a stable axis.

The mission intends on having the capabilities to be able to dock with the target satellite with an initial angular velocity. This initial angular velocity would be a valid case if the Starlink satellite has a dysfunctional attitude control system. If this were the case, after docking, the STD must lower the target satellite to zero angular velocity relative to the Earth. In all docking scenarios the STD must also reorient both satellites for the de-orbit burn. These two actions will likely occur simultaneously, but will be treated as two separate maneuvers for sizing. This maneuver will set the requirements for the necessary torque of the RCS system due to the high mass moments of inertia of the Starlink satellite.

9.3.1 Mass Moments of Inertia

The sizing of the attitude control system for the STD will stem from the moment of inertia of the STD and the combined mass moment of inertia of the Starlink and STD docked. The exact moments of inertia for the Starlink are undisclosed by SpaceX. However, a telecommunications partner of Starlink, T-Mobile, released an ad for Starlink direct-to-cell capabilities with the configuration of a deployed Starlink 2-mini shown in Figure 9.3 [56].



Figure 9.3: Starlink 2-mini configuration from T-Mobile advertisement [56].

Additionally, the mass and dimensions of the Starlink V3 satellite are provided in an FCC document from SpaceX [57]. The dimensions of the starlink are shown in Figure 9.4 and the corresponding numeric values from the filing are shown in Table 9.2.

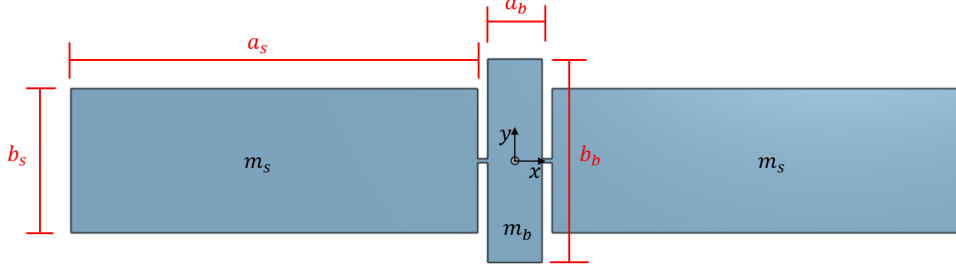


Figure 9.4: Dimension nomenclature for Starlink V3.

The density of the solar arrays will be approximated by quotes from solar space panel manufacturer, Spectrolab, with a mass at 2 kg/m^2 [58]. The remaining mass of the satellite from the total mass of 2000 kg provided FCC filing must distributed across the bus[57]. Numeric values for the masses are presented in Table 9.2.

Table 9.2: Satellite component dimensions and masses.

Component	a (m)	b (m)	ρ (kg/m ²)	m (kg)
Solar array	20.2	6.36	2	257
Bus	2.7	10.1	54	1486

The mass moments of inertia will be calculated by assuming the bodies of the solar arrays and bus are flat plates. Therefore, the mass moments of inertia about the centroid of a uniform flat plate is given by,

$$\begin{aligned} I_{xx} &= \frac{1}{12}m(b^2) \\ I_{yy} &= \frac{1}{12}m(a^2) \\ I_{zz} &= \frac{1}{12}m(a^2 + b^2) \\ I_{xy} &= I_{yz} = I_{zx} = 0 \end{aligned}$$

The resulting inertia tensor for the Starlink bus is,

$$\begin{bmatrix} 12632 & 0 & 0 \\ 0 & 903 & 0 \\ 0 & 0 & 13535 \end{bmatrix}$$

in $\text{kg} \cdot \text{m}^2$. The resulting inertia tensor for each of the solar arrays is,

$$\begin{bmatrix} 866 & 0 & 0 \\ 0 & 8739 & 0 \\ 0 & 0 & 9605 \end{bmatrix}$$

in $kg \cdot m^2$. The mass moment of inertia of the STD is also required for the de-spin maneuver. The shape of the STD will be approximated by a cylinder with uniformly distributed mass, shown in Figure 9.5.

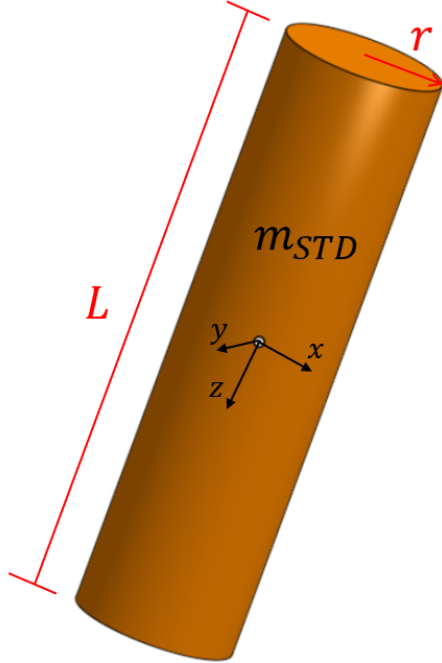


Figure 9.5: Dimension nomenclature for the composite shape for the STD.

The mass moment of inertia about the STD's centroid will be,

$$I_x = I_y = \frac{1}{12} m(3r + L^2)$$

$$I_z = \frac{1}{2} mr^2$$

$$I_{xy} = I_{yz} = I_{zx} = 0$$

where m is the mass, r is the radius, and L is the length [59]. The resulting inertia tensor for each of the solar arrays is,

$$\begin{bmatrix} 182 & 0 & 0 \\ 0 & 182 & 0 \\ 0 & 0 & 13 \end{bmatrix}$$

All of the defined mass moment of inertia tensors are with respect to each composite shape's centroid. The parallel axis theorem must be used to obtain a single moment of inertia for the total Starlink with the STD docked. Parallel axis theorem is defined by,

$$[\mathbf{I}_B] = [\mathbf{I}_G] + m \begin{bmatrix} y_B^2 + z_B^2 & -x_B y_B & -x_B z_B \\ -x_B y_B & x_B^2 + z_B^2 & -y_B z_B \\ -x_B z_B & -y_B z_B & x_B^2 + y_B^2 \end{bmatrix} \quad (9.19)$$

where, $[\mathbf{I}_B]$ is the mass moment of inertia tensor about the desired axis, $[\mathbf{I}_G]$ is the mass moment of inertia tensor about center of mass, m is the total mass of the body, and x_B , y_B , and z_B are distances from the mass center to the desired origin.

For just the Starlink satellite, the moments of inertia of the solar arrays will be described about the origin shown in Figure 9.4. Using Figure 9.4, it can be seen that the variables for the parallel axis theorem are,

$$\begin{aligned} x_B &= \frac{a_s}{2} + \frac{a_b}{2} \\ y_B &= 0 \\ z_B &= 0 \end{aligned}$$

Computing the moment of inertia about the origin using Equation 9.19,

$$\begin{bmatrix} 866 & 0 & 0 \\ 0 & 42432 & 0 \\ 0 & 0 & 43298 \end{bmatrix}$$

The total mass moment of inertia of the Starlink can be determined by adding the bus and two solar arrays about the origin from Figure 9.4. The resulting mass moment of inertia tensor is given by,

$$[\mathbf{I}_{sat}] = [\mathbf{I}_b] + 2[\mathbf{I}_s] \quad (9.20)$$

where $[\mathbf{I}_{sat}]$ is the moment of inertia tensor of the Starlink satellite, $[\mathbf{I}_b]$ is the moment of inertia tensor of the bus, and $[\mathbf{I}_s]$ is the moment of inertia tensor of a solar array. All of these tensors are expressed about the origin from Figure 9.4. The numeric result of the total inertia tensor of the Starlink Satellite is,

$$\begin{bmatrix} 14364 & 0 & 0 \\ 0 & 85767 & 0 \\ 0 & 0 & 100131 \end{bmatrix}$$

$kg \cdot m^2$. Once the STD is docked, the center of mass will shift up the z-axis shown in Figure

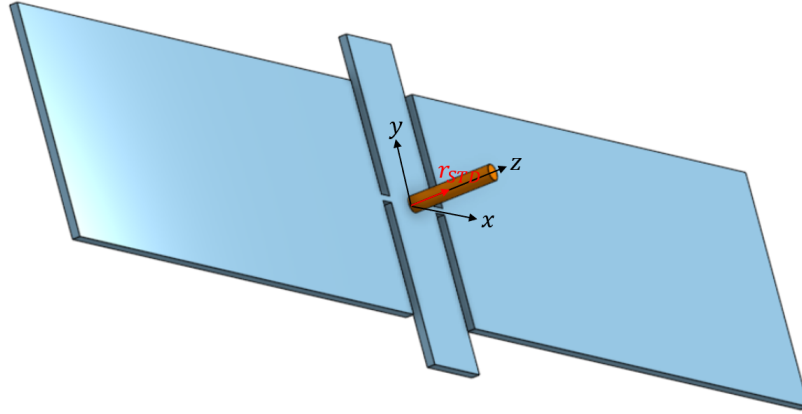


Figure 9.6: Docked STD with composite shapes

The distance the center of mass exists from the origin of the Starlink can be found by taking a weighted average of the masses of the STD and Starlink,

$$d_z = \frac{m_{STD}}{m_{STD} + m_{SL}} \cdot r_{STD}$$

where d_z is the distance the center of mass moved in the z-direction after docking, m_{STD} is the mass of the STD, m_{SL} is the mass of the Starlink, and r_{STD} is distance from the center of mass of the Starlink to the center of mass of the STD. d_z is found to be 0.225 m. Using this value of d_z in place of z_B in Equation 9.19, parallel axis theorem can be employed again to move the mass moment of inertia tensor of the Starlink to the mass center of the two docked satellites. The STD moment of inertia tensor will be moved to the center of mass with a z_B value of $(r_{STD} - d_z)$, which equals 2.475 m. Adding the two inertia tensors results in the final inertia tensor of the docked satellites about the combined mass center,

$$\begin{bmatrix} 17097 & 0 & 0 \\ 0 & 88500 & 0 \\ 0 & 0 & 100144 \end{bmatrix}$$

$\text{kg} \cdot \text{m}^2$. This inertia tensor will be used to calculate the impulse requirements in sections to follow.

9.4 Angular Momentum

The initial angular momentum will provide the necessary impulse the STD attitude control system will need to provide in order to slow the Starlink after docking. Previously stated, 10

degrees per second will be the maximum allowable spin rate prior to docking. The angular momentum of an object about it's center of mass is defined by,

$$\vec{H}_G = [I]\vec{\omega} \quad (9.21)$$

where \vec{H}_G is the angular momentum of the object about the mass center, $[I]$ is the mass moment of inertia tensor, and $\vec{\omega}$ is the body-fixed angular velocity vector. The coordinate system of this calculation is defined in Figure 9.6. The sizing calculations in following sections will reference angular momenta in pure x, y, or z direction for simplicity.

The angular velocity vectors, $\vec{\omega}$, for each of these cases are defined by,

$$\begin{aligned}\vec{\omega}_x &= [0.175, 0, 0]^T \\ \vec{\omega}_y &= [0, 0.175, 0]^T \\ \vec{\omega}_z &= [0, 0, 0.175]^T\end{aligned}$$

in radians per second. Calculating each case for angular momentum from Equation 9.21 results in,

$$\begin{aligned}\vec{H}_{G,x} &= 2992 \hat{i} \\ \vec{H}_{G,y} &= 15488 \hat{j} \\ \vec{H}_{G,z} &= 17525 \hat{k}\end{aligned}$$

9.4.1 Methodology Selection

There are many different methods of controlling attitude on board a satellite. The methods in consideration for the STD include magnetorquers, reaction wheels, cold gas thrusters, and mono-propellant thrusters. In the following calculations, the feasibility for each method will be analyzed.

Magnetorquers offer a lightweight method of torque for LEO maneuverability by interacting with the Earth's magnetic field by passing current through a coil [to create a local magnetic field](#). [Another draw towards magnetorquers is that they can continue to provide torque as long as power is supplied to the magnetorquer](#). This suggests that it could be a viable method of dumping momentum after docking with the Starlink Satellite and slowing its rotational speed. [To analyze this feasibility, the magnetorquer must provide the impulse required to de-spin the satellite from the maximum angular momentum defined in the previous section, \$H_{G,z}\$](#) .

The MT400-2-1 magnetorquer by ZARM Technik AG, Figure 9.7, has a large dipole moment at 400 Am^2 [60].



Figure 9.7: MT400-2-l magnetorquer by ZARM Technik AG [60].

The torque generated by the magnetorquer can be determined by

$$T = M \times B$$

where T is the torque generated, M is the magnetic dipole moment of the magnetorquer, and B is the magnetic field in LEO [61]. This estimate resulted in a moment of 10 mN m.

Applying a 10 mN m torque to the Starlink would provide a constant angular acceleration. The constant angular acceleration is calculated by,

$$H_i = \tau t$$

where H_i is the angular impulse, τ is the torque applied, and t is the time the torque is applied. This would decelerate the satellite at a rate that would slow the satellite in approximately 14 days. This is far above the specified mission profile, therefore, magnetorquers will not be a sufficient method of attitude control.

Reaction wheels are another common attitude control mechanism. Reaction wheels operate by applying torque to a flywheel and giving it angular momentum. This results in an equal torque on the satellite in the opposite direction since momentum is conserved. This concept is shown in Figure 9.8[62].

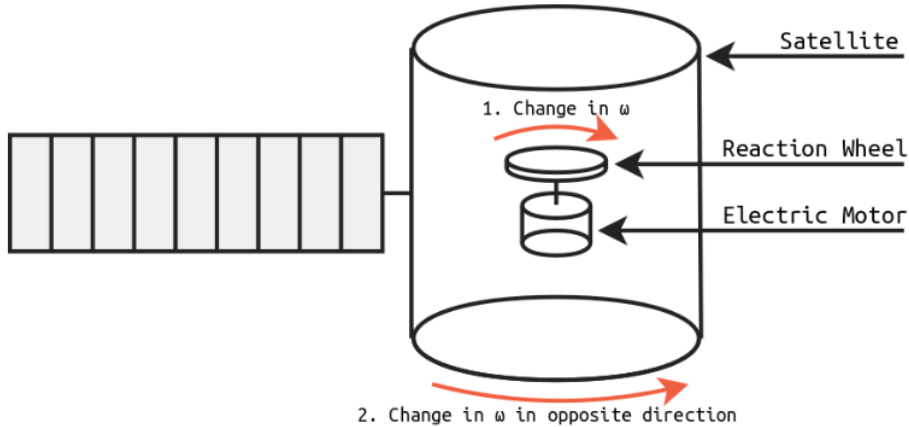


Figure 9.8: Dynamics of a reaction wheel [62].

However, reaction wheels have a momentum limit where the reaction wheel reaches a maximum speed due to bearing limitations. To determine if this method is feasible, the size of the wheel required to store the maximum angular momentum defined,

$$H_w = H_{G,max} = 17525$$

where H_w is the angular momentum of the wheel. Using a max speed of 6000 rpm from an off-the-shelf reaction wheel by Honeywell, shown in Figure 9.16 [37].



Figure 9.9: HR14-25, reaction wheel, by Honeywell [37].

From Equation 9.21, where ω is the maximum speed of the wheel and H_G is $H_{G,max}$, the mass moment of inertia required to store the de-spin momentum is $28 \text{ kg} \cdot \text{m}^2$. If the wheel were idealized to a disk with all of its mass at the circumference, then the mass moment of inertia would be given by,

$$I = \frac{1}{2}mr^2 \quad (9.22)$$

where I is the mass moment of inertia, m is the mass, and r is the radius. Using a generous value of 0.5 m for the radius, it would require a wheel of mass 112 kg. Considering the STD will require four reaction wheels of this size to cover all three axes and one for redundancy. This configuration would result in a total increase in mass by at least 448 kg, which is unreasonable considering the whole STD is expected to have a mass of 400 kg. However, reaction wheels serve as a potential method of precision for orienting satellites which will make it the favorable option in fine adjustments of the STD during the docking phase.

To obtain the impulse necessary to slow the Starlink satellite, the focus must shift to thrusters. Two common categories of reaction control thrusters exist: cold gas and monopropellant. Cold gas thrusters minimize complexity by purely using tank pressure to accelerate the gas through a nozzle, while monopropellants require a decomposition chamber and a catalyst before the nozzle. However, cold gas thrusters suffer from having a fraction of the specific impulse of the monopropellant thrusters. The following calculations will determine the legitimacy of both options by looking at the propellant mass required to perform critical attitude maneuvers.

To get rough estimates for the required fuel, the most torque-intensive maneuver of decelerating of the Starlink satellite will be analyzed. The sizing analysis for cold gas thrusters will utilize N_2 as its propellant. High-pressure gaseous nitrogen is selected because it is inert, non-contaminating, and will already be used as pressurant for main engine tanks. The specific impulse will be estimated at 60 seconds for an N_2 cold gas thruster [63]. The impulse required by the thruster may be calculated by

$$L_{N_2} = \frac{H}{r} \quad (9.23)$$

where H is the angular momentum of the Starlink and STD satellites and r is the approximate moment arm for the force couple by two opposing thrusters [59]. Each maximum angular momentum defined in Section 9.3.1 will be considered. The corresponding moment arms will be,

$$r_x = 0.5$$

$$r_y = 2.7$$

$$r_z = 2.7$$

The required linear impulses result in,

$$L_x = 5984$$

$$L_y = 5736$$

$$L_z = 6490$$

The mass used to create this impulse will be approximated by,

$$m = \frac{L_{max}}{I_{sp}g_0}$$

where L_{max} is the maximum impulse calculated, I_{sp} is the specific impulse, and g_0 is the gravitational constant [64]. This results in a mass of 11 kg of N_2 gas. Furthermore, as the N_2 tanks get lower pressure, the efficiency of the thruster is also lost.

As previously presented, monopropellant thrusters offer an increase in performance compared to cold gas thrusters. Hydrazine is the most prevalent monopropellant in RCS thrusters. Hydrazine decomposition offers a specific impulse of 220, which is almost four times that of N_2 cold gas thrust.[48] Additionally, hydrazine is stored as a liquid at room temperature, so the tank volume required can be greatly lowered. These improved characteristics result in less than 3 kg of hydrazine needed for the two maneuvers and a volume of 0.003 cubic meters [48]. Therefore, hydrazine monopropellant thrusters have been chosen as the method of attitude control for large impulse maneuvers.

9.4.2 Hydrazine Thruster Sizing

The hydrazine thruster will be placed such that pairs of thrusters will generate the most torque on the STD with the least amount of fuel consumed. The placement of the hydrazine thrusters will be equivalent on all six sides of the STD structure shown in Figure 9.10.

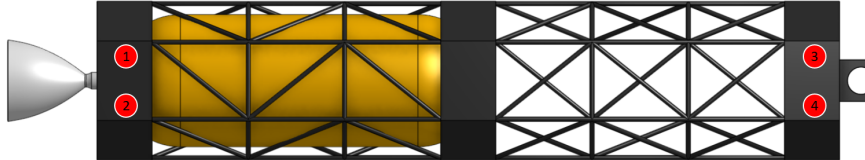


Figure 9.10: Placement of hydrazine thrusters on each side of the STD.

An additional four hydrazine thrusters will be placed to provide thrust normal to the top and bottom surfaces shown in Figure 9.11. This results in a total of 32 hydrazine thrusters on the STD.

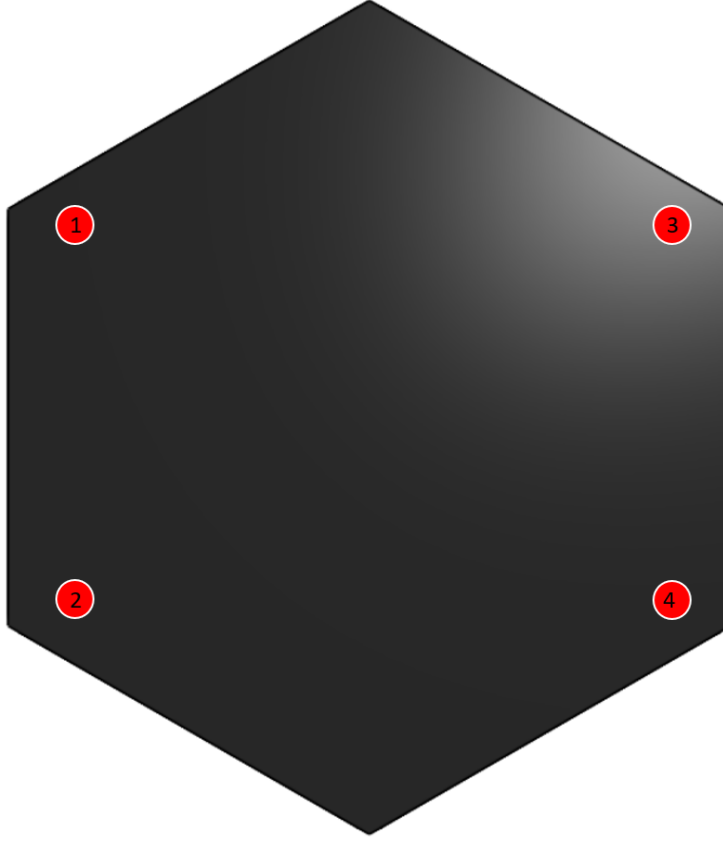


Figure 9.11: Placement of hydrazine thrusters on the top and bottom of the STD.

To define the required thrust of the hydrazine thrusters, the largest instantaneous torque will be from the approach of the STD to the Starlink satellite. This is because the de-spin maneuver can be slowed over a long time period. However, during docking, the STD will need to match the angular velocity of the spinning Starlink satellite to ensure the grabber is aligned with the docking point on the Starlink. The orientation of the Starlink can be described by Euler's equations of motion for an arbitrary body in torque-free motion.

$$\begin{aligned}\dot{\omega}_x &= \frac{I_y - I_z}{I_x} \omega_y \omega_z, \\ \dot{\omega}_y &= \frac{I_z - I_x}{I_y} \omega_z \omega_x, \\ \dot{\omega}_z &= \frac{I_x - I_y}{I_z} \omega_x \omega_y.\end{aligned}\tag{9.24}$$

where $\dot{\omega}$ are body-fixed angular accelerations, ω are body-fixed angular velocities, and I are principal mass moments of inertia of the Starlink [59]. For the STD to match the orientation, the STD must accelerate its angular velocity in the same manner as the Starlink. Therefore, the input torque on the STD is defined by,

$$\begin{aligned}\tau_x &= I_x \dot{\omega}_x + (I_z - I_y) \omega_y \omega_z, \\ \tau_y &= I_y \dot{\omega}_y + (I_x - I_z) \omega_z \omega_x, \\ \tau_z &= I_z \dot{\omega}_z + (I_y - I_x) \omega_x \omega_y.\end{aligned}\quad (9.25)$$

where τ are the input torques, $\dot{\omega}$ and ω the body-fixed angular accelerations and velocities, respectively, of the Starlink, and I are the principal mass moments of inertia of the STD [59]. To find the maximum torque, it is necessary to integrate 9.24 given an initial condition to find the ensuing motion of the Starlink. The integration will provide angular accelerations and velocities across time to calculate instantaneous torque requirements for the STD using Equation 9.25. This was through ODE45 in MATLAB using the script and functions in Appendix J. The ensuing motion of the Starlink is dependent on the initial conditions of the integration. The constraint that has been set previously on the docking is a maximum angular velocity of 10 degrees per second, however, the direction of angular momentum that will require the most demanding input torque is unknown. Various initial angular momentum directions will be defined by setting the initial angular velocity, ω_0 , to an inertia Z axis,

$$\vec{\omega}_0 = [0, 0, \omega_0]^T$$

in radians per second. The various directions will be defined through a 3-1-3 rotation sequence, where ψ is the precession angle, θ is the nutation angle, and ϕ is the spin angle. The rotation sequence from inertial frame to body-fixed is defined by,

$$R_z(\phi) = \begin{bmatrix} \cos \phi & -\sin \phi & 0 \\ \sin \phi & \cos \phi & 0 \\ 0 & 0 & 1 \end{bmatrix}, \quad R_x(\theta) = \begin{bmatrix} 1 & 0 & 0 \\ 0 & \cos \theta & -\sin \theta \\ 0 & \sin \theta & \cos \theta \end{bmatrix}, \quad R_z(\psi) = \begin{bmatrix} \cos \psi & -\sin \psi & 0 \\ \sin \psi & \cos \psi & 0 \\ 0 & 0 & 1 \end{bmatrix}.$$

$$\begin{pmatrix} x \\ y \\ z \end{pmatrix} = R_z(\phi) R_x(\theta) R_z(\psi) \begin{pmatrix} X \\ Y \\ Z \end{pmatrix}.$$

Rotating $\vec{\omega}_0$ into the body-fixed frame results in,

$$\begin{aligned}\tilde{\omega}_B &= R_3(\phi) R_1(\theta) R_3(\psi) \begin{pmatrix} 0 \\ 0 \\ \omega_0 \end{pmatrix} \\ &= \omega_0 \begin{pmatrix} \sin \theta \sin \phi \\ -\sin \theta \cos \phi \\ \cos \theta \end{pmatrix}\end{aligned}$$

Linearly spaced values for $\theta \in [0, \pi]$ and $\phi \in [0, 2\pi]$ were chosen and integrated; the magnitude of the instantaneous torques were recorded at each time step. The maximum of

these torques across each integration and each initial condition was found to be approximately $8 \text{ N}\cdot\text{m}$. The initial condition that required this was the body-fixed angular velocity, $[0, 0.1744, -0.0070]$, in radians per second. This result could have been predicted as it is the initial condition of the angular momentum about the intermediate axis, with a small perturbation in the z-axis to ensue more chaotic motion. The motion of the Starlink with this initial condition is shown in Figure 9.12

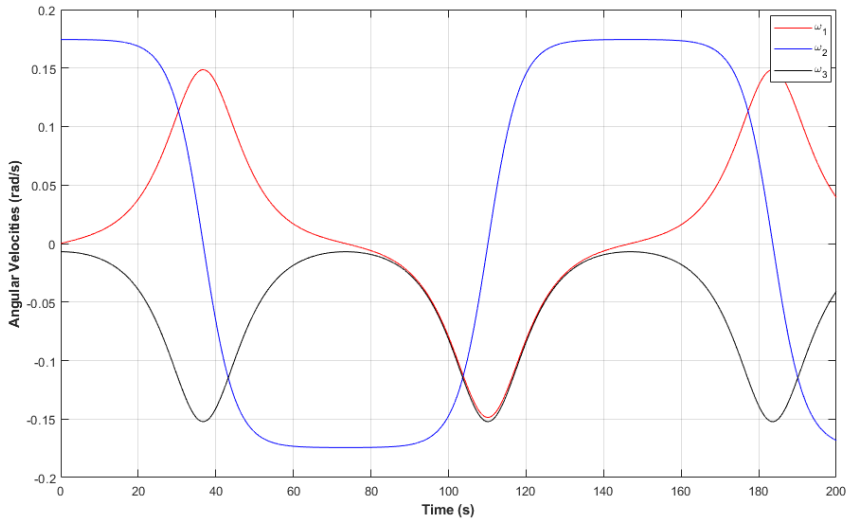


Figure 9.12: Body-fixed angular velocities of the most demanding condition for STD attitude alignment. Initial condition of $[0, 0.1744, -0.0070]$ radians per second.

The corresponding input torques required by the STD are shown in Figure 9.13

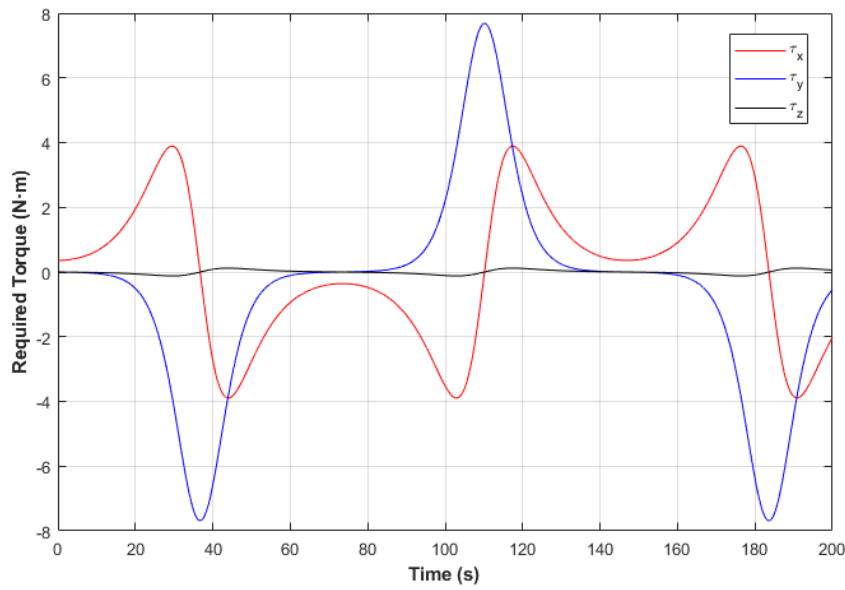


Figure 9.13: Input torques required for the most demanding condition for STD attitude alignment. Initial condition of $[0, 0.1744, -0.0070]$ radians per second.

An additional torque that should be considered that the STD may have to counteract during this maneuver is due to gravity gradients. This some of the mass of the STD is closer to the earth than other. This concept is shown in Figure 9.14 [65].

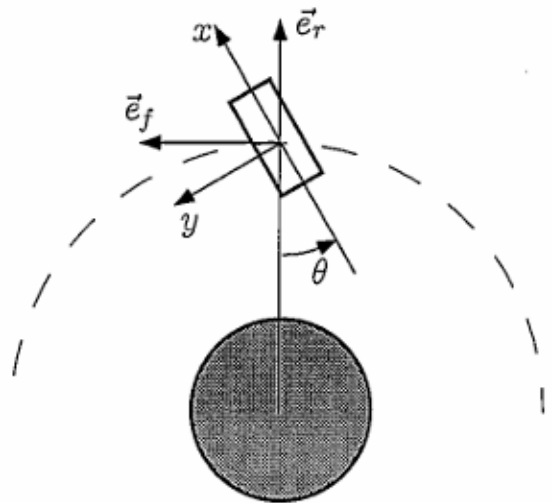


Figure 9.14: 2D gravity gradient diagram [65].

This difference in distance to the Earth results in a shift in the center of gravity, which

will then impart a moment about the center of mass. Gravity gradient torques in 2D are governed by,

$$M = -3 \frac{\mu}{r_c^2} (I_{yy} - I_{xx}) \sin \theta \cos \theta \quad (9.26)$$

where M is the moment from the gravity gradient, μ is the gravitational constant multiplied by the mass of Earth, r_c is the radial distance from Earth, I_{xx} and I_{yy} are mass moment of inertia, and θ is the angle shown in Figure 9.14 [65]. A 2-dimensional analysis of this is acceptable because this calculation only looks to find the maximum torque generated by gravity gradients. Using the largest and smallest mass moments of inertia of the STD along with maximizing $(\sin \theta \cos \theta)$ at $\theta = 45^\circ$, will yield the largest torque the STD may experience. Using the previously calculated moments of inertia and the lowest target orbit for STD docking at 525 km, in Equation 9.26, the largest torque imparted on the STD from gravity gradients is 0.7 N · m. Adding this to the previous required torque equates to a maximum instantaneous torque requirement of 8.7 N · m.

To meet the required torque, the required thrust of the hydrazine thruster can be determined by,

$$F = \frac{\tau}{r} \quad (9.27)$$

where F is the required thrust, τ is the required torque, and r is the distance between the force couple. Since the max torque required in Figure 9.13 is about the y-axis, the moment arm is the full length of the STD. The required force by the thruster to meet the required torque is 3.2N. A suitable off-the-shelf thruster that can provide this thrust is the MT-8A by IHI AeroSpace, shown in Figure 9.15. This thruster can provide between 1.47 and 5.50 N of thrust and can provide 850,000 pulses [38].

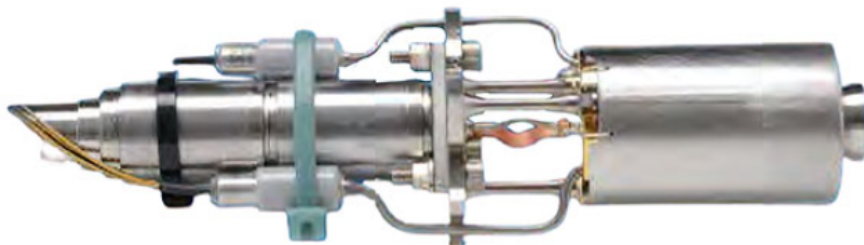


Figure 9.15: 4 N hydrazine thruster by IHI AeroSpace [38].

As previously mentioned, a combination of reaction wheels and RCS thrusters will be required

for the precision of docking to the Starlink satellite. To provide a rough specification for the size and mass of the reaction wheels, the limits will require the reaction wheels to turn the STD around in 1 minute using half of its potential momentum as it is believed by the team that to maintain maneuverability, 1 minute must be achieved and this benchmark can be moved in later control simulations if needed. This specification will give good control over the STD while being reasonable to achieve without a large reaction wheel. This momentum can be found using

$$H_{Wheel} = \frac{2\theta I}{t_{min}}$$

where H_{Wheel} is the required max angular momentum of the wheel, θ is the turn angle, I is the moment of inertia of the STD, and t_{min} is the minimum time allowed for the rotation. This equation assumes that the torque to half the wheel momentum is instantaneous, but for the purpose of initial sizing, it will suffice. The required angular momentum for the provided parameters results in a minimum specification of 28 N m s. Honeywell supplies a reaction wheel shown in Figure 9.16 that can store 25 N m s of momentum. Each of these wheels have a mass of 7.5 kg [37].



Figure 9.16: HR14-25, reaction wheel, by Honeywell [37].

Due to the short mission time-span, the STD will rely on batteries to provide power throughout the mission. The peak power required by these reaction wheels is listed to be 105 W and less than 22 W at steady state. Since the reaction wheels should only operate at peak power for short bursts. The average power draw will be estimated to 30 W from each of the four reaction wheels.

9.5 Power Requirements

Power requirements will come from various components stated in Section 8, such as the reaction wheels, onboard computer, sensors, etc. Table 9.3 outlines the equipment with power requirements.

Table 9.3: Electronic Sensors for Satellite Docking and Deorbiting

Sensor Name	Mass (kg)	Power Consumption (W)
Reaction Wheel (4) [66]	7.5	30
Flight Computer [66]	0.08	3
S-Band Communications [67]	0.18	2.5
LiDAR	0.1	5
Star Tracker [68]	0.047	0.165
IMU [69]	0.057	1.8
GNSS [70]	0.0135	0.05
Radar Sensor	0.1	1

The total power required by Table 9.3, along with the power required by the four reaction wheels specified in section ?? about 135 W. To support this total power for a two-day mission, the batteries must have a capacity of 6.4 kWh. Lithium-ion batteries have an energy density of approximately 0.330 kWh/kg [71]. Therefore, to meet the required capacity of X kWh, the battery will have a mass of 20 kg.

9.6 Gripping Mechanism Sizing

The largest factor of size regarding the gripping system will be how much force it can handle. Based on predicted propulsion metrics outlined in Section 9.2, the structure will need to endure forces of up to 3100 N during final deorbit burns. It is assumed that this will be the max-load case, as opposed to stabilization burns which can be drawn out over longer periods of time without impeding impulsive maneuver based assumptions.

The structure, referred to as the grip bar, is simplified for preliminary analysis and sizing as a simply supported, circular beam with a centered 3100 N force. This simplified structure is shown in figure 9.17.

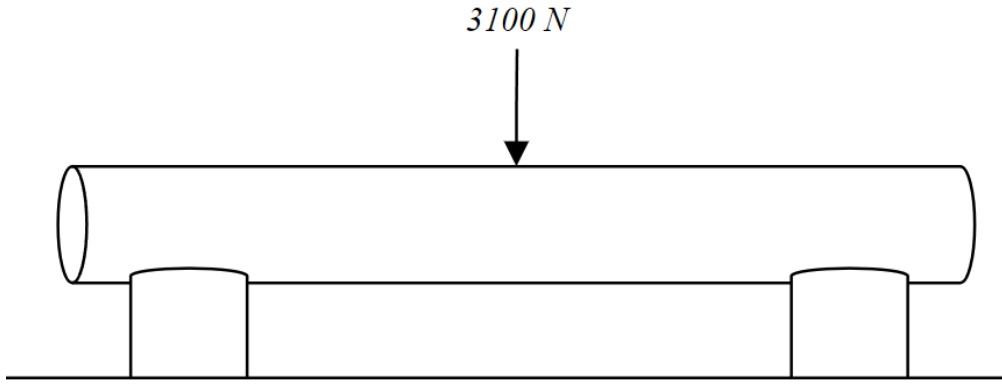


Figure 9.17: A free body diagram of the simplified grip bar.

Assuming the grip bar is made of solid 2024-T3 Aluminum, a commonly used alloy for aerospace applications [72], the material has a yield strength of 345 MPa [73]. For a cylindrical bar, the maximum stress is given by

$$\sigma_{max} = \frac{M_{max}R}{I} \quad (9.28)$$

where M_{max} is the maximum moment given by

$$M_{max} = \frac{3100 \cdot L}{4} \quad (9.29)$$

and I is the bar's polar moment of inertia, given by

$$J = \frac{\pi}{4} R^4 \quad (9.30)$$

where R is the cross-sectional radius of the bar and L is the length of the bar [74]. Depending on the size and shape of the debris, the length may need to be altered to prevent impeding systems and functions of the satellite during regular operation. In regards to Starlink v3 and for purposes of preliminary analysis, a somewhat arbitrary length of 300 mm is chosen.

Using this length, along with a safety factor of 2 based on potential ductile failures, Equation 9.29 is used to obtain a required cross-sectional radius for the grip bar at 1.197 cm. The gripping vice must be sized to adequately conform around this radius while maintaining proper force transfer, though the exact dimensions will depend on the finalized mechanism and further structural analysis.

10 Gripping Mechanism Sizing

The general concept of the gripping mechanisms at each of the 4 locations designated in the Design Concept section. Each of these four grabbers will have 2 rotary jaws that will provide the clamping force required to dock and stay docked with the Starlink satellite. The gripping mechanism will also be able to actuate linearly and rotationally at the base to make minor adjustments during the final approach. The current system design is shown in Figure 10.1. Where the blue section is a gearbox to translate input torques to clamping forces at the jaws.

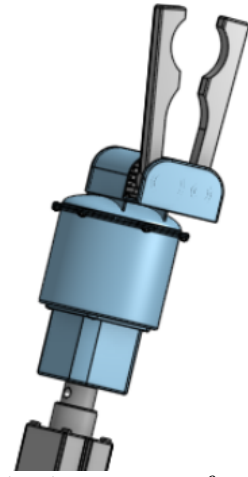


Figure 10.1: Gripping system for sizing reference.

After docking, the gripper will have closed onto a circular bar on the Starlink side. To determine the clamping force that the claws will need to exert on this bar, a closer inspection of the clamp is shown in Figure 10.2.

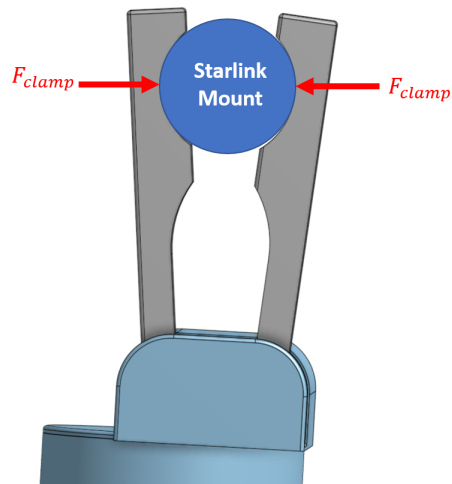


Figure 10.2: Grabbing force configuration at each of the mounting points

Using the RCS configuration described in Section 9.4.2, the maximum separation forces during and after docking can be defined by when the STD generates a torque that is perpendicular to the clamping force, shown in Figure 10.3, where each red arrow denotes a force vector from an RCS thruster and the blue arrow denotes the force from the clamp to resist separation. The force due to the RCS torque could be experienced by a single grabber in the case where it is the first to attach to the Starlink, therefore, each grabber will be required to maintain clamping force through this severe case.

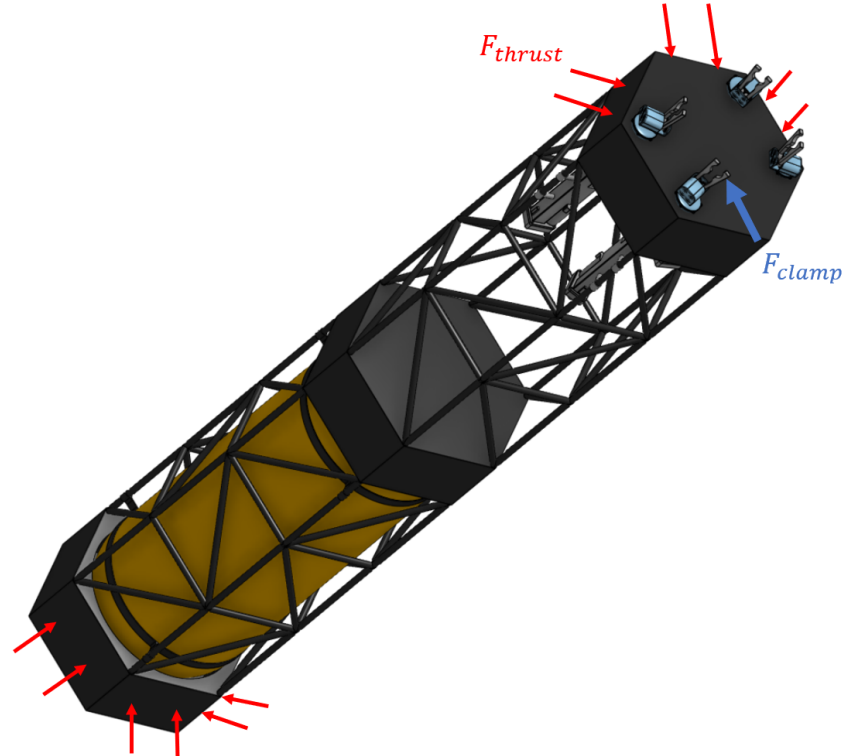


Figure 10.3: Worst case loading on gripper with torque perpendicular to the clamping force.

The maximum torque will be generated by firing all RCS thrusters that have a component in the direction of a side of the hexagon at the forward of the STD, along with the opposite-facing RCS thrusters on the aft of the STD.

The force of the couple can be defined by,

$$F_c = 2F_{RCS} + 4F_{RCS} \cos(\theta) \quad (10.1)$$

where F_c is the force couple, F_{RCS} is the force from one RCS thruster, and θ is the angle between faces of the STD structure.

This results in a coupling force of 20 N. To find the torque from this couple,

$$\tau = r_{couple} F_c \quad (10.2)$$

where τ is torque on the STD, r_{couple} is the distance between the forward and aft thrusters, and F_c is the maximum force couple. The resulting torque is $54 N \cdot m$. If one of the clamps is attached to the Starlink satellite during this torque, it would experience a separation force of:

$$F_{clamp} = \frac{\tau}{(l_{STD}/2)} \quad (10.3)$$

where τ is the calculated torque and l_{STD} is the length of the STD. This gives a max separation force of 40 N.

Another significant force on the clamp is during re-entry. The STD main engine will provide 3100N of thrust to accelerate the Starlink towards the Earth. This force will be distributed between four grabbers. Shown in Figure 10.4, the Starlink mount will contact the lower end of the arc to transmit the thrust to the Starlink. The Starlink mount will exert an equal and opposite force on the clamp, and since this reaction will have a component in the x-direction, it will create a separation force on the clamp.

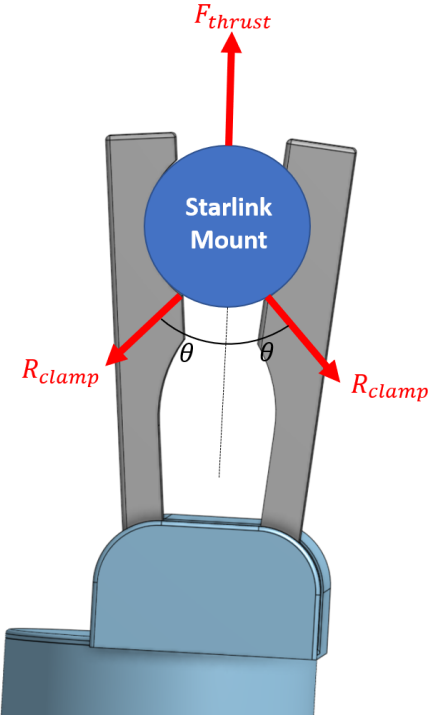


Figure 10.4: Re-entry case for separation force on the STD grabber clamp.

Summing the forces in the y direction,

$$\Sigma F_y = 0 = F_{thrust} - 2R_{clamp} \sin \theta \quad (10.4)$$

Solving for the reaction that the Starlink mount exerts on the clamp, results in $R_{clamp} = 2192N$. The x-component of this reaction force is 1550N. This is far greater than the initial attitude control case, so this will govern the required clamping force of the system.

From [Section 7.3.1](#), it was stated that a pneumatic piston or stepper motor should be used based on the required force. A force of 1550 N is achievable by a stepper motor with gear reductions and will likely have more precision than a pneumatic piston. Therefore, a stepper motor of $1.5 \text{ N} \cdot \text{m}$ will be used. A space-rated stepper motor of this torque can be found off-the-shelf from American Motion Systems, seen in Figure 10.5, with a mass of 1 kg and requiring 1.4 A current during operation [75].



Figure 10.5: NEMA 23 Hybrid Stepper Motor by American Motion Systems [75]

11 Kick Stage Sizing

Initial mass predictions are needed to begin design and analysis for the kick stage, since many systems such as propulsion will require thrust (which will depend on mass) as a design parameter. These predictions will most likely differ from the final masses, and are intended to be slightly overestimated in order to allow room for rough initial designs that can be optimized later on. Before calculating mass predictions, the propellants themselves must be determined.

11.1 Propellant Selection

Since hypergolic chemical propellants were determined to be the best fit for the kick stage in Table 7.1, the options are narrowed down to a short list. The propellants that are most commonly used in this type of single-use orbital maneuvering system are monomethylhydrazine (MMH) and dinitrogen tetroxide (NTO) [31]. Other fuel options include hydrazine, unsymmetrical dymethylhydrazine (UDMH), and Aerozine 50 (50/50 hydrazine and UDMH). Some of these offer benefits in lower freezing point or stability, but trade performance, where MMH excels. Specifically, MMH offers higher specific impulse and better density impulse compared to hydrazine and Aerozine 50, improving both efficiency and propellant mass fraction for spacecraft maneuvers [76]. For oxidizers, other options include Red Fuming Nitric Acid (RFNA) and White Fuming Nitric Acid (WFNA), both of which offer limited advantages over NTO in terms of performance and storability [76]. Therefore, monomethylhydrazine (MMH) and dinitrogen tetroxide (NTO) were selected as the propellant combination for the kick stage, balancing performance, storability, and extensive industry use.

11.2 Mass Predictions

Since the mass of fuel required to achieve the desired Δv depends on the mass of the tanks, and the mass of the tanks depends on the mass of the fuel stored, it is necessary to iteratively predict the masses simultaneously. This was done in Python, and the full code can be found in Appendix B.

Estimates of the individual masses of the kick stage components are as follows:

- Each fueled STD carried (up to 7): $m_{STD} = 400 \text{ kg}$
- Propellant tanks: $m_{tanks} = 350 \text{ kg}$ [77]
- Pressurant tank and mass: $m_{press} = 150 \text{ kg}$ [78]
- Propulsion system: $m_{prop} = 100 \text{ kg}$ [35]
- Reaction Control System (RCS): $m_{RCS} = 25 \text{ kg}$ [38]
- Other structural mass: $m_{structural} = 400 \text{ kg}$ [34]

Since the mass of the stage changes as STDs are dropped off at their respective destination orbits, the fuel mass must be calculated for each maneuver outlined in Table 6.6. The ideal

rocket equation (in a slightly different form than Equation 9.1) was used to obtain these values [76],

$$\Delta v = u_{eq} \ln \left(\frac{m_0}{m_f} \right) \quad (11.1)$$

where Δv is the required velocity to perform all of the kick stage maneuvers, u_{eq} is the exhaust velocity of the engine (a measure of efficiency), m_0 is the total mass of the stage including propellant, and m_f is the propellant mass of the kick stage. For each maneuver, the Δv required, number of STDs, spacecraft mass, and calculated fuel mass required are outlined in Table 11.1. Maneuver 1

Table 11.1: Kick Stage Mass Calculations.

Maneuver #	Description	Δv Required [m/s]	# of STDs Carried	Spacecraft Mass [kg]	Fuel Mass Required [kg]
1	Injection to orbit A	246	7	3825	339
2	Orbit A to orbit B	1324	5	3025	1750
3	Orbit B to orbit C	1324	3	2225	1287
4	Orbit C to de-orbit	124	0	1025	44.8
Total fuel mass required					4276

Once the fuel mass is obtained, the required volume of the tank was calculated using the density. A weighted average of the two propellant densities of $1,255 \text{ kg/m}^3$ was obtained, using the density of MMH around 880 kg/m^3 and of NTO around $1,442 \text{ kg/m}^3$, with an ideal stoichiometric mixture ratio of around 2 [76]. The relation between mass, volume and density

$$V_{req} = \frac{m_f}{\rho_{avg}} \quad (11.2)$$

was used to calculate required volume. Since these mass predictions are very rough estimates and likely overestimates, a cylindrical approximation was used instead of additional calculations for hemispherical end caps, which would be used in reality.

$$V_{req} = \pi \left(\frac{D}{2} \right)^2 H \quad (11.3)$$

with D and H being the diameter and height of the cylindrical tank. The diameter of the tank, and similarly the kick stage was set by first getting a minimum diameter of $3.5 \times D_{STD}$ and checking the corresponding diameter based on Equation 11.3. Some iteration was needed

to converge to a visually pleasing and acceptable ratio of diameter to height (≥ 1 , too large of a diameter results in reduced effectiveness of engine gimbaling and RCS thruster) and the diameter was narrowed down to a range of 2–2.5 m, with the corresponding height range of 1–1.6 m. Diameter and height dimensions are somewhat flexible and can be finalized later in the design process to allow for optimization. Tank mass can then be calculated by finding the surface area of the cylinder

$$A_{surf} = 2\pi r^2 + 2\pi rH \quad (11.4)$$

and multiplying it by the thickness, which can be estimated by calculating the minimum thickness to hold required pressure following a thin pressure vessel hoop stress equation

$$\sigma = \frac{pr}{t} \quad (11.5)$$

with a pressure guess value based on similar engines of 500 psi, and 75% of the yield stress of a commonly used Ti-6Al-4V alloy of 128 ksi [79][80]. Multiplying this estimated thickness 0.0052 m by the surface area 16.3 m^2 and density,

$$m_{tank} = \rho A_{surf} t \quad (11.6)$$

the final tank mass estimate was found by replacing the tank mass estimate in the fuel calculations in Table 11.1 and iterating until the mass converged on 342 kg.

This results in the following final estimate of mass distribution:

- Each fueled STD carried (up to 7): $m_{STD} = 400 \text{ kg}$
- Propellant tanks: $m_{tanks} = 342 \text{ kg}$
- Pressurant tank and mass: $m_{press} = 150 \text{ kg}$
- Propulsion system: $m_{prop} = 100 \text{ kg}$
- Reaction Control System (RCS): $m_{RCS} = 25 \text{ kg}$
- Other structural mass: $m_{structural} = 400 \text{ kg}$

Includes estimates for:

- Structural elements ($\sim 375 \text{ kg}$)
- Electronics, power and communication ($\sim 25 \text{ kg}$)
- Propellant mass: $m_{fuel} = 4,276 \text{ kg}$
- **Total spacecraft mass:** $m_{total} = 8,101 \text{ kg}$

With the following rough dimensions:

- Kick stage diameter: $D_{kick} = 2 \text{ m}$

- Kick stage length: $L_{kick} = 1.5$ m
- Overall spacecraft length: $L_{craft} = 3.5$ m

12 Analysis Introduction

This chapter provides a comprehensive overview of the analysis work conducted to validate the design integrity, safety, and performance of the STD and the Kick Stage. The following sections will cover a diverse range of analytical approaches, including but not limited to: propulsion system thermal and structural evaluation, injector and combustion chamber modeling, launch load verification, gripping mechanism stress evaluation, and re-entry trajectory and thermal degradation assessment.

The analyses presented utilize a consistent set of governing parameters to ensure that all evaluations are coherent and adhere to spaceflight standards. These parameters include material yield and ultimate stresses, NASA-defined safety factors, environmental and launch loads, and thermal and dynamic profiles experienced throughout the mission.

12.1 Material Properties and Yield Stresses

All structural and mechanical components were selected based on industry-standard aerospace materials, such as 6061-T6 aluminum, Inconel 718, and titanium alloys. The yield and ultimate strengths of each material were obtained from NASA-STD-6016 or reliable material handbooks.[17] Table 12.1 summarizes the mechanical properties employed throughout the analyses.

Table 12.1: Mechanical Properties of Selected Structural Materials [17]

Material	Yield Strength [MPa]	Ultimate Strength [MPa]
Aluminum 6061-T6	276	310
Titanium Ti-6Al-4V	880	950
Inconel 718	1030	1240

12.2 Safety Factors

Structural design and verification follow NASA-STD-5001B, which establishes minimum acceptable design and test safety factors to ensure the structural adequacy of spaceflight hardware. [19] The STD and kick stage, which utilize metallic structures and are evaluated under a prototypical test regime, use the following safety factors:

- Ultimate Design Factor: 1.4
- Yield Design Factor: 1.25
- Proof Test Factor: 1.05

These factors are applied to the calculated limit stresses to establish design allowables, ensuring that no detrimental yielding or failure occurs under expected mission conditions.

12.3 Launch and Global Load Conditions

All structural components are designed to withstand the most critical loading event—launch aboard a Falcon 9 vehicle. According to the Falcon 9 User Guide, vertical acceleration can reach up to 6 g, and lateral acceleration up to 2 g. Figure 12.1 illustrates the load factors expected during launch.[20]

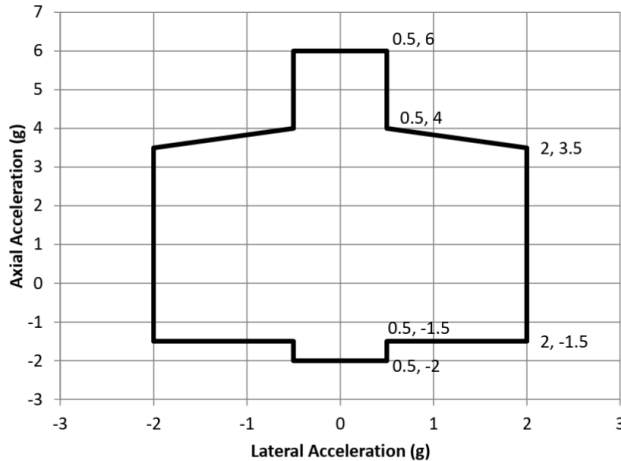


Figure 12.1: Expected load factors during launch for Falcon 9.[20]

Additional loading cases evaluated throughout this chapter include:

- Heating and pressure due to combustion
- Control and gravity gradient torques in orbit
- Propellant tank pressures and sloshing
- Aerodynamic heating and pressure during atmospheric descent

By integrating material properties, spaceflight safety factors, and representative loading conditions, the following analyses ensure that all hardware configurations maintain structural integrity and operational capability throughout their mission lifetimes.

13 Kick Stage Propulsion Analysis

In this section, the various components that make up the kick stage propulsion system will be discussed and analyzed. Some understanding of the layout of a rocket engine is necessary for some of the analysis, and a schematic of an example engine can be found in Figure 13.1.

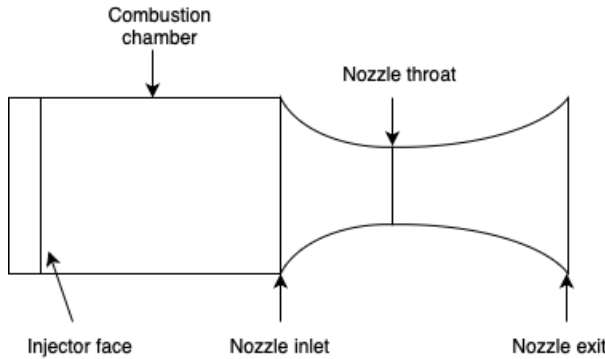


Figure 13.1: Simplified schematic of rocket engine pointing out areas referenced later in section.

This propulsions system is a hypergolic (autoignition from propellant contact) liquid bipropellant system optimized for vacuum operation. At a high level, the kick stage propulsion components serve the following functions, in order of inlet to outlet:

- Manifold/injector: Flow the propellants into the combustion chamber with the desired pressure drop and flow rates, promoting sufficient mixing between the propellants for stable combustion.
- Combustion chamber: Contain the combustion of propellants without melting, and have sufficient length to allow complete combustion.
- Nozzle: Accelerate the combustion products through the converging section up to sonic at the throat, then supersonically accelerate the combustion products through the diverging section, targeting ideal expansion at the exit.

These components will be analyzed in order to characterize performance and improve design based on results. Beyond the individual components, a thermal analysis of the entire system will be analyzed as well.

13.1 Material Selection

Three of the most common materials used in space applications are stainless steel, copper alloys, and Inconel alloys [17], with the following properties:

- Stainless Steel: Corrosion-resistant, easy to machine, and cost-effective but weaker at high temperatures [81].
- Inconel Alloys: High strength and oxidation resistance for extreme heat but difficult to machine [82].

- Copper Alloys: Excellent thermal conductivity for cooling but lower strength and oxidation-prone [83].

-

Notable omissions from this list include non-metals such as composite materials (including carbon-carbon composites), ceramics, and manufactured thermal protection materials like Beta cloth [17]. Despite their advantages in certain scenarios, these materials were not selected for initial consideration due to their anisotropic properties, difficulty in attachment, and lack of easily accessible material properties.

For high temperature and heat flux applications, the decision between stainless steel and Inconel can be made by plotting and comparing the tensile strength versus temperature for each material.

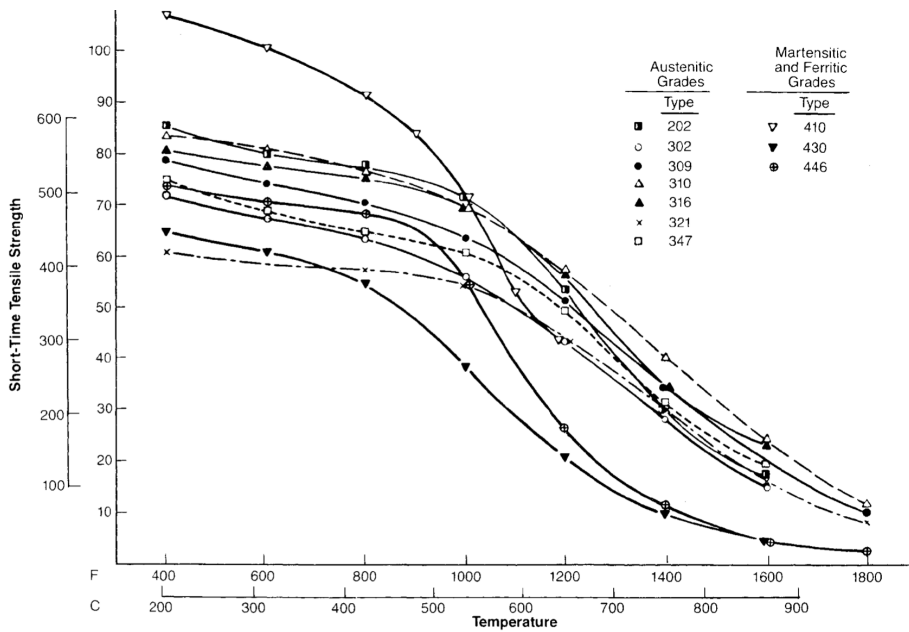


Figure 13.2: Typical short-time tensile strengths of various stainless steels at elevated temperatures.

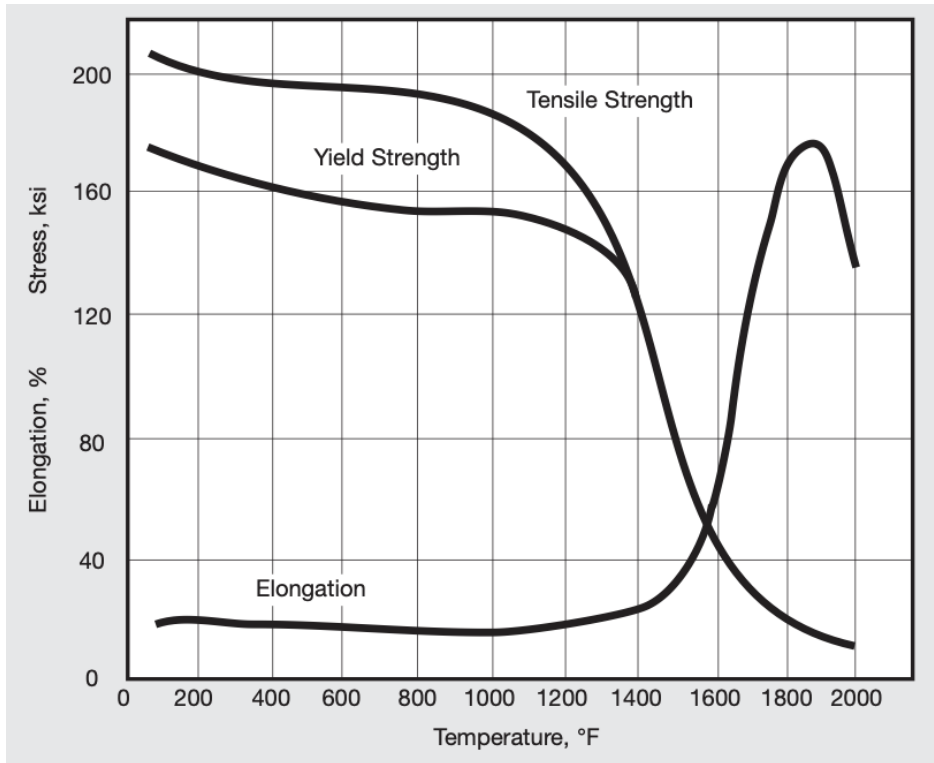


Figure 13.3: Properties of hot-rolled, annealed and aged Inconel 718 bar at elevated temperatures.

From Figure 13.2 and Figure 13.3, it is clear that Inconel has a higher tensile strength and maintains that tensile strength more steadily as it encounters higher temperatures, dropping below 60 ksi at 1,500 °F instead of 1,200 °F for 316 stainless steel.

For the manifold and injector, temperatures will be held low by the flow of propellants through them, so high temperature strength is not necessary. Additionally, machinability is especially important for the complex injector geometry. For these reasons, stainless steel is the best option. For chemical compatibility, the 316 alloy will be used.

For the combustion chamber, even though high conductivity is desirable, high temperature strength is the most important, and as such an Inconel alloy is the best option. The common 718 Inconel alloy will be used.

Lastly, the nozzle will require high temperature strength for the converging and throat sections. While the diverging section does not see as high of temperatures, to avoid thermal expansion stresses the material will be 718 Inconel throughout.

Summary of selected materials and alloys:

- Manifold/injector: Stainless steel (316)
- Combustion chamber: Inconel (718)
- Nozzle: Inconel (718)

13.2 Propulsion Parameters

To characterize a rocket engine, the following major parameters must be determined [76]:

- Propellants
- Mixture Ratio
- Engine Cycle Type
- Thrust
- Chamber Pressure
- Cooling Method(s)

The propellants (MMH and NTO) and engine cycle type (pressure-fed) were determined in Section 11. The remaining parameters include mixture ratio (determines relative flow rates of propellants and chamber temperature), thrust and chamber pressure (depend on each other, set by the required Δv and burn time limit) and cooling methods (determines how sophisticated the cooling system needs to be, depends on chamber temperature).

It is useful to note that many of these parameters depend on one another, and need to be determined iteratively and simultaneously. Because of this, some calculations may reference values that are determined in later calculations.

13.2.1 Mixture Ratio

When determining a mixture ratio, one of the limiting factors is the combustion temperature, and by extension, the cooling methods available. It is also important to keep in mind that most engines run fuel-rich, since fuel-rich mixture ratios result in lower combustion temperatures compared to oxidizer-rich mixture ratios of the same efficiency (Isp) [76]. This can also be seen in the plots further in this section, and this is why the low side of mixture ratios is the range of interest (left of stoichiometric on the plots).

Thus, to determine a desired mixture ratio, plotting temperature at the critical combustion temperature location (at the nozzle throat due to the highest heat flux) versus mixture ratio can indicate a general limit for your chosen material.

To generate plots with combustion properties, the combustion properties first need to be determined using chemical equilibrium calculations. This process becomes cumbersome for more than a handful species however, and NASA's Chemical Equilibrium Application (CEA) can solve systems with hundreds of species [84]. This CEA solver can be used to calculate gas properties after combustion at various locations in the idealized rocket engine. It's important to note that these values are purely a result of chemical kinetics with a handful of assumptions, so CEA results should be taken as a guideline for combustion properties and not the true behavior [85]. While CEA's website will output tables of values, a Python wrapper such as RocketCEA offers an easier way to calculate many data points at once [86], and a Python script utilizing RocketCEA was used to generate the following plots, the full code for which can be found in Appendix F.

Figure 13.4 shows the combustion temperature at the nozzle throat plotted against mixture ratio for MMH and NTO, with a line for the melting point of Inconel 718 ($\sim 1,609$ K [87]).

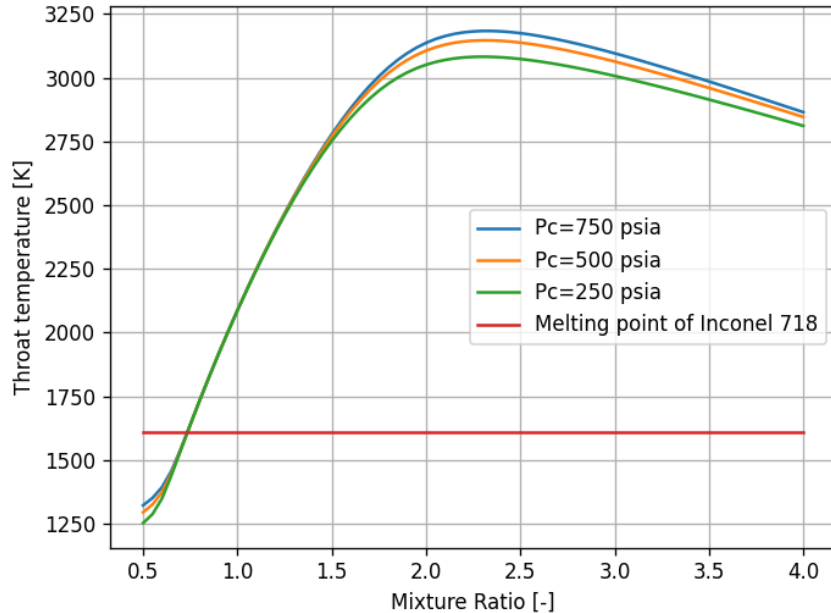


Figure 13.4: Plot of throat temperature versus mixture ratio for MMH and NTO, with a red line for melting point of Inconel 718, plotted with various chamber pressures.

The melting point is not necessarily a hard limit when finding a design value for mixture ratio, since the actual mechanism by which the heat is transferred to the rocket engine is not instantaneous, and the temperature provided by CEA is a conservative (high) estimate. This limit is especially soft if you are employing active cooling methods (as will be discussed in Section 13.2.4), which is why rocket engines used in industry can operate at stoichiometric temperatures of over 3,000 K [88].

Since combustion temperature isn't a hard limit and performance is a design objective, one also must consider the efficiency (Isp) versus mixture ratio. Figure 13.5 plots this in a similar fashion to Figure 13.4.

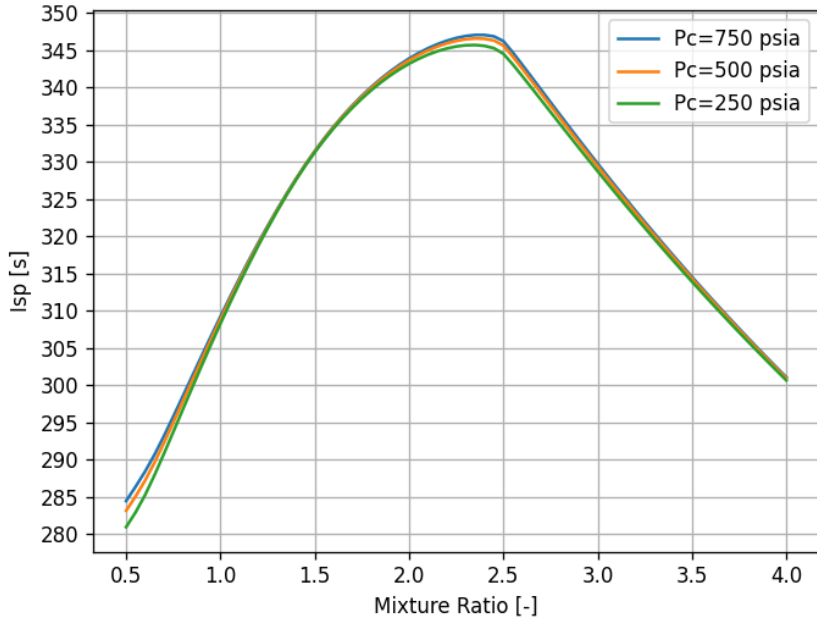


Figure 13.5: Plot of efficiency (Isp) vs mixture ratio for MMH and NTO with various chamber pressures.

Looking back and forth between these figures, the design of the engine is constrained by the desires to have lower combustion temperature (favors lower mixture ratio) and higher performance (favors higher mixture ratio). It's necessary to weigh the efficacy of the cooling methods available to decide on a mixture ratio, and considering the limited effect of film cooling (the cooling method determined in Section 13.2.4) unable to sufficiently cool stoichiometric conditions, $\sim 2,700$ K is a reasonable limit, so a mixture ratio of 1.5 was selected. Iteration was expected to be necessary after calculating the ratio of fuel used for film cooling, but it did not end up being necessary in this case.

13.2.2 Thrust

The thrust is one of the most important input parameters, and will decide the scale of the engine. Since the required Δv can be met with either a large thrust and a short burn time or a small thrust over a long burn time, it is necessary to find a lower limit for required thrust. A good value can be found by setting the burn time less than 180 s [22], thereby keeping the maneuver short enough for a valid impulsive maneuver assumption used in Section 6. Using the definition of constant acceleration (while engines have notable startup and shutdown transients, they each range between ~ 0.1 s–5 s depending on complexity, and thrust is approximately constant for over long maneuvers) and Newton's second law

$$F = ma = m \frac{\Delta v}{\Delta t} \quad (13.1)$$

and plugging in the largest Δv of 1,324 m/s, spacecraft mass of 3,825 kg, and Δt of 180 s, a minimum thrust (F) of 28,135 N is obtained, which for simplicity has been modified to 28 kN as the thrust design value. This is a lower bound for required thrust, but smaller burn times help the efficiency of maneuvers, so any further improvements to the design resulting in higher thrust are desirable.

13.2.3 Chamber Pressure

The chamber pressure of the engine is also a defining parameter of a rocket engine. To relate thrust to chamber pressure, the equation for the thrust coefficient [85] can be used

$$C_T = \frac{\mathcal{T}}{p_0 A^*} \quad (13.2)$$

where the thrust coefficient, C_T , is a representation of the acceleration of the flow in the diverging section versus a purely convergent nozzle [76], and can be obtained using NASA CEA. \mathcal{T} represents thrust (F in Equation 13.1), p_0 is the chamber pressure, and A^* is the throat area.

This is iterated using the exit diameter and expansion ratio, with the limiting constraint being the exit diameter of the nozzle not exceeding 1.5 m.

$$\epsilon = \frac{A_e}{A_t} \quad (13.3)$$

Since a higher tank pressure requires a thicker, and by extension heavier tank, it is necessary to find a compromise between tank pressure (which determines chamber pressure) and throat area (which determines nozzle size). In order to find this, the limit for tank pressure was set around 275 psi (this is compatible with commercial tank pressure ratings of ~ 400 psi).

This results in a chamber pressure limit of around 200 psi after an injector pressure loss of 20 % of chamber pressure (see Section 13.3.1 for details) and an approximate fluid loss from valves, fittings, and feed lines of 10 % [89] (see Section 20 for further details).

The Python code used to iterate and obtain values can be found in Appendix F.

13.2.4 Cooling Methods

To cool this engine, the primary method of cooling selected is film cooling. This simple method flows one of the propellants (very commonly fuel) along the walls of the combustion chamber, creating a boundary layer that reduces heat transfer and absorbs energy, reducing the temperature of the walls. To deliver the propellant for film cooling, passage holes will be drilled through the combustion chamber near the injector and mid-way along the combustion chamber in order to effectively cool the entire length of the chamber. Hole locations and specifics of the flow rates and thermal properties are determined in Section 13.6.

Additionally, this engine will utilize radiative cooling. This method is commonly used in similar orbital engines like Merlin Vacuum [90].

13.3 Injector Design

The injector is a critical component in a liquid rocket engine, responsible for atomizing and mixing the fuel with the oxidizer to enable combustion. Its design directly affects combustion efficiency, stability, and overall engine performance. When designing an injector plate, several factors must be considered, including injection type, flow dynamics, and fuel selection. A multitude of injector designs exist, each with unique characteristics tailored to specific performance needs. The most common general types of injectors include impinging, pintle, and swirl injectors. An example of an impinging injector plate is shown in Figure 13.6.

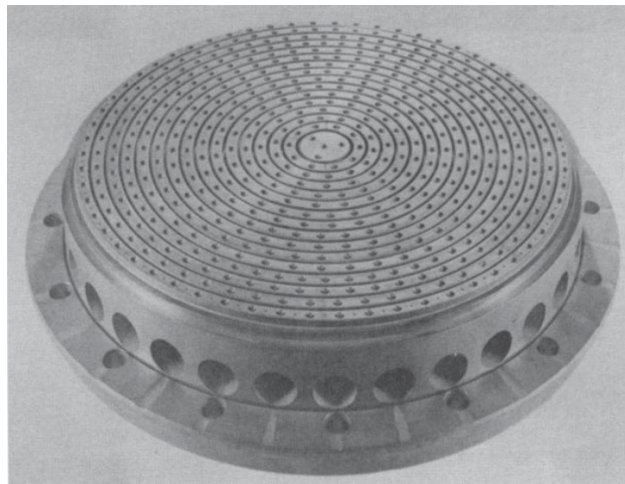


Figure 13.6: 10 in self-impinging injector plate [76].

The pintle injector method is relatively simple and has proven dependable through applications like the Apollo Lunar Module Descent Engine [91] and SpaceX's Merlin Engine [90]. This injection method consists of a central pintle, where one propellant is ejected from the center, while the other flows through an annular gap around it. The interaction between the two streams results in efficient mixing, partially due to the resultant recirculation zone created by the radial flow [90]. Pintle injectors are also highly advantageous for engines requiring throttling, as they allow for precise flow control and deep throttling with minimal performance impact. They can also be used for face-shutoff, eliminating separate valves. A visual representation of this design can be seen in Figure 13.7.

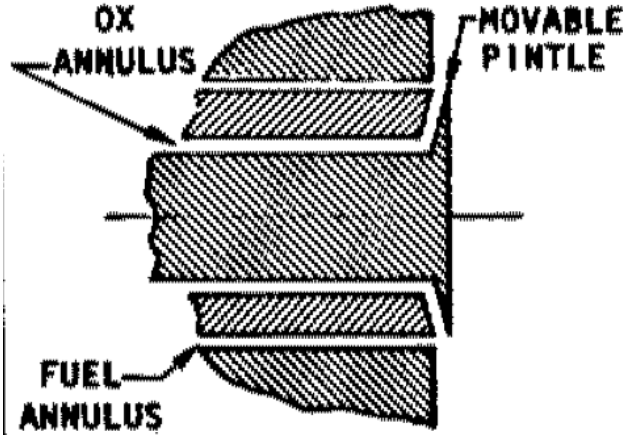


Figure 13.7: Example of pinte injector design [92].

Another injector type is the swirl injector. The swirl injector is designed to introduce a rotational motion to the propellants before they exit the injector, creating a fine, atomized spray. This is typically achieved using tangential or helical inlets that force the fluid to spin within a chamber, forming a hollow cone spray as it exits. Both fuel and oxidizer can be swirled independently or together, depending on the injector configuration. This method enhances atomization and combustion efficiency, however is more complex and can be difficult to manufacture than other injector types [92]. This method is depicted in Figure 13.8.

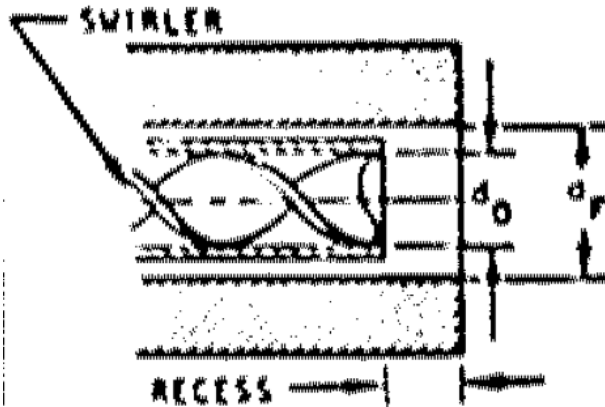


Figure 13.8: Example of swirl injector design [92].

Lastly, the impingement method involves directing two or more propellant streams to collide at a specific angle, breaking the fluids into fine droplets and promoting rapid mixing. This type of injector is widely used in hypergolic and liquid rocket engines due to its simplicity and effectiveness. While they offer reliable performance, maintaining proper alignment of the streams is critical to avoid combustion instability [92]. A representation of this method can be seen in Figure 13.9

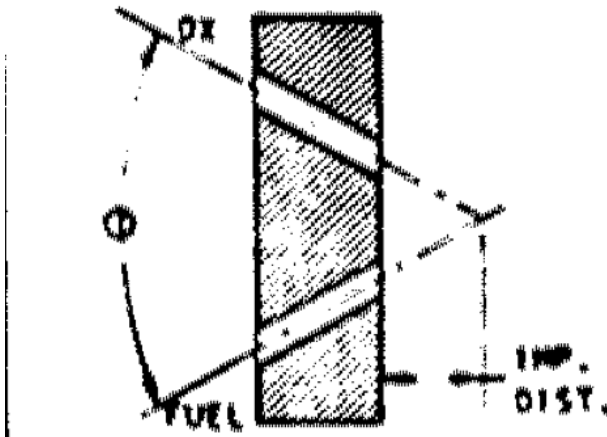


Figure 13.9: Example of impinging injector design [92].

Impinging injectors can be designed as doublet, triplet, or more complex configurations, depending on the number of propellant streams used and likeness of each stream. The two possible configurations are used: like-impinging and unlike-impinging elements [92].

Like-impinging elements involve identical streams, both fuel or oxidizer, meeting at the impingement point. After collision, the streams break apart and mix downstream with the other propellant. This configuration is particularly effective for ensuring uniform mixing and is highly reliable for hypergolic propellants. Additionally, it minimizes the risk of reactive stream separation, a phenomenon where the fuel and oxidizer streams separate due to rapid chemical reactions, potentially causing combustion instability.

Unlike-impinging elements involve fuel and oxidizer streams meeting directly at the impingement point. Mixing occurs through a dissipative exchange of momentum. While this configuration results in immediate ignition and chemical reaction near the injector face, it also leads to significantly higher heat flux at the injector face. This can cause thermal damage to the injector, especially with hypergolic propellants, which are prone to reactive stream separations.

To determine which injector type is best for the kick stage rocket engine, a design matrix was constructed. The typical criteria for selecting injectors include mixing performance (generally correlates to combustion stability), manufacturability, and throttleability. While the first two criteria are important for this engine, throttleability is not needed since all of the required engine burns will be at full throttle.

Table 13.1: Injector Design Matrix

Criteria	Injector Type			
	Weight	Pintle	Swirl	Impinging
Mixing Performance	5	4	5	4
Manufacturability	4	3	2	4
Throttleability	1	5	2	2
Total score	-	37	35	38

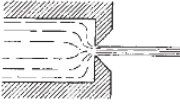
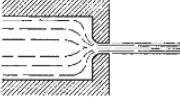
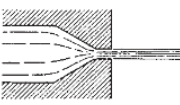
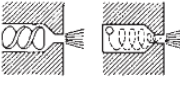
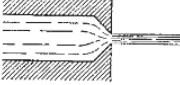
Orifice Type	Diagram	Diameter (mm)	Discharge Coefficient
Sharp-edged orifice		Above 2.5 Below 2.5	0.61 0.65 approx.
Short tube with rounded entrance $L/D > 3.0$		1.00	0.88
		1.57	0.90
		1.00 (with $L/D \sim 1.0$)	0.70
Short tube with conical entrance		0.50	0.7
		1.00	0.82
		1.57	0.76
		2.54	0.84–0.80
		3.18	0.84–0.78
Short tube with spiral effect		1.0–6.4	0.2–0.55
Sharp-edged cone		1.00	0.70–0.69
		1.57	0.72

Figure 13.10: Injector orifice discharge coefficients for various geometries [76].

For the kick stage engine, Dumpster Dynamics has chosen to design a like-impingement injector, with impinging doublets placed on alternating concentric rings of fuel and oxidizer as it offers a straightforward yet highly effective solution for hypergolic fuels. Its simplicity ensures reliable performance, while the efficient mixing provided by the impingement method supports stable and complete combustion. This choice aligns well with the engine's design goals, balancing ease of manufacturing with robust functionality.

13.3.1 Orifice Size and Number

Orifice size plays a crucial role in atomization, which directly impacts the combustion efficiency and performance of the rocket engine. Proper sizing ensures efficient mixing of the fuel and oxidizer, optimizing combustion and reducing the likelihood of instability. To determine the required number of orifices and their diameters, we need to calculate the total orifice area for both the oxidizer and fuel. The flow rate through each orifice is given by [76]

$$Q = C_d A \sqrt{2\Delta P / \rho} \quad (13.4)$$

where Q represents the flow rate, C_d is the discharge coefficient, A is the cross-sectional area of the orifice, ΔP is the pressure drop across the orifice, and ρ is the fluid density. The discharge coefficient that is dependent on the geometry of the orifice, as shown in Figure 13.10.

The estimates in Figure 13.10 offer a good starting point for initial design, and will require

iteration since the discharge coefficient estimate will change based on hole diameter. Generally discharge coefficients are calculated experimentally once manufactured in order to better characterize the engine's pressures and flow rates [76].

The mass flow rate can be calculated by multiplying the flow rate by the density of the propellant, giving the expression:

$$\dot{m} = Q\rho = C_d A \sqrt{2\rho\Delta P}. \quad (13.5)$$

To determine the mass flow rates of both the fuel and oxidizer, the general equation can be split into two parts: one for the fuel and one for the oxidizer. The mass flow rate for the fuel is given by:

$$\dot{m}_{fuel} = C_{d,fuel} A_{fuel} \sqrt{2\rho_{fuel}\Delta P_{fuel}} \quad (13.6)$$

And similarly, for the oxidizer:

$$\dot{m}_{ox} = C_{d,ox} A_{ox} \sqrt{2\rho_{ox}\Delta P_{ox}} \quad (13.7)$$

For this design, the mixture ratio is 1.5, which means that the oxidizer mass flow rate is 1.5 times the fuel mass flow rate. This relationship can be written as:

$$MR = \frac{\dot{m}_{ox}}{\dot{m}_{fuel}} \quad (13.8)$$

The rule of thumb for injector pressure drop ΔP is around 15 to 20% of the chamber pressure [64].

Using Equation 13.4 through Equation 13.8 as a system of equations, the total orifice area for the fuel was determined to be 244.4 mm^2 and the total orifice area for the oxidizer to be 286.4 mm^2 . The number of orifices and their individual diameters were calculated using the following equation:

$$d = \sqrt{4 \cdot A / (\pi \cdot N)} \quad (13.9)$$

Where d is the orifice diameter, A is the total orifice area (fuel or oxidizer), and N is the number of orifices. The orifice sizes came out to 1.47 mm for the fuel orifices and 1.59 mm for the oxidizer orifices.

Since orifice size is a function of the number of orifices, a plot generated with a Python script helps illustrate the relationship between orifice size and number of orifices in Figure 13.11.

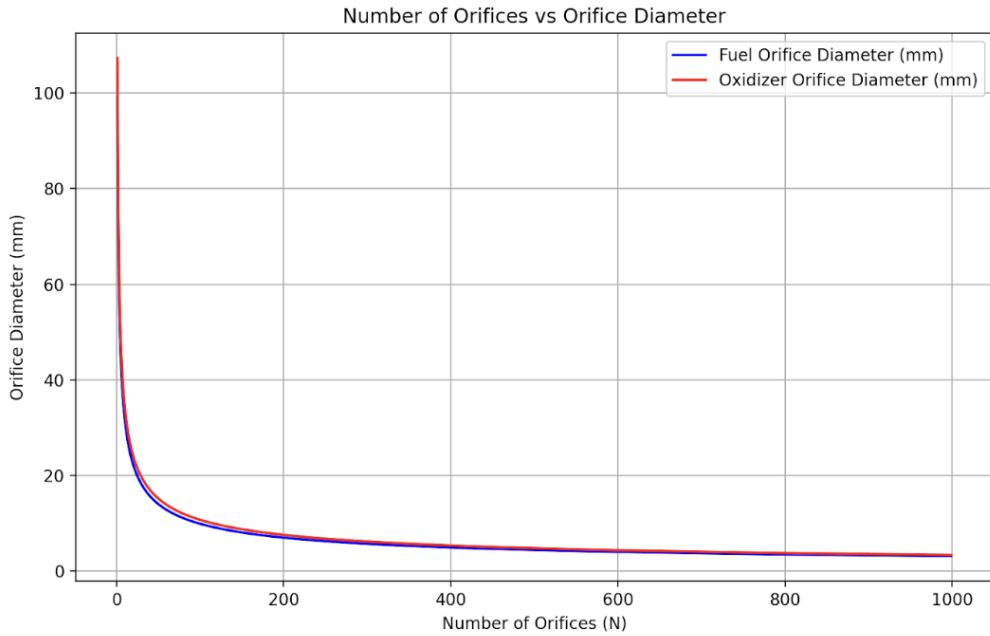


Figure 13.11: Size of orifice vs total number of orifices.

From the plot, it is interesting to note that after a certain number of orifices, the diameter tends to an asymptote. Some optimization could be attempted including calculations involving various stream conditions and maximizing atomization. Ideally, CFD and experimental data dictate optimal injector geometry, however they are out of the scope of this design. Thus, the practical decision is to determine the final number of orifices and their respective sizes as the injector plate and manifolds are designed, incorporating manufacturing considerations such as available drill bit sizes and machining capabilities.

As the injector geometry was modeled, a value of 36 radial orifices per concentric ring, and four rings of injection elements per propellant was selected. This results in 144 injection elements per propellant, as seen in Figure 13.12, showing a forward view of the injector, with fuel orifices highlighted in red and oxidizer orifices highlighted in blue.

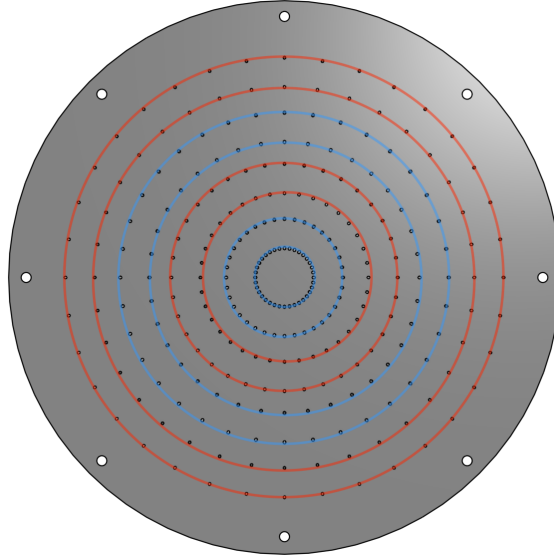


Figure 13.12: Forward view of the injector plate showing the injection orifices.

13.3.2 Impingement Angle

While impingement angle plays an important role in controlling spray momentum and mixing dynamics, it is typically treated as a second-order design parameter once injector type and flow rates are defined. Standard practice uses impingement angles near 30° from axial, and are slightly modified using fluid properties to determine the required angles for a net axial momentum, for ideal momentum conservation. For a film-cooled combustion chamber, if net momentum is not axial, any deviations from axial momentum should have a net negative angle (slightly radially inward) in order to prevent interference with film cooling flow on the wall.

Since this engine uses like-impinging elements, using the same impingement angle results in net axial momentum. Thus all orifices are set to the same 30° angle, simplifying the manufacturing process. Figure 13.13 shows a quarter cross section of the injector plate (the left edge is the axis of rotation, right side is the outside edge), displaying the angles of the injection orifices.

Many of the thicknesses shown in Figure 13.13 were determined based off of required thickness to contain the o-rings in between each manifold keeping the fuel and oxidizer separate. Discussion of these o-rings can be found in Section 13.3.5.

13.3.3 Impingement Distance

The impingement distance, defined as the length from the orifice exit to the point of jet impingement along the centerline, is a relevant parameter but not a major design consideration. Instead of focusing on a precise value, it should be chosen to be as close to the injector face as heat transfer and mixing efficiency permit [76]. The key is ensuring sufficient mixing and combustion stability without excessive distances that could result in mis-impingement.

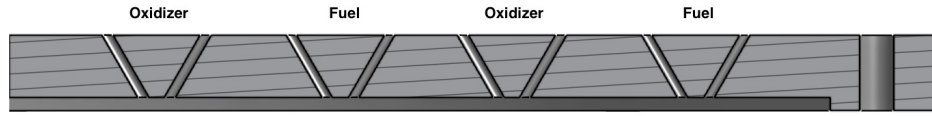


Figure 13.13: Quarter cross section of the injector plate showing the injection orifices, displayed with forward face on top and aft face on bottom.

Misalignment may cause poor mixing, incomplete combustion, and potential chamber wall erosion. Thus, the impingement distance should be optimized for heat transfer and not overemphasized as a design constraint.

13.3.4 Injector Geometry

Taking the previous design parameters into consideration, the major dimensions of the injector are:

- Diameter: 300 mm
- Thickness: 12.2 mm
- Gasket recess: 2.2 mm
- Number of radial orifice elements: 36
- Number of manifolds per propellant: 2
- Total number of orifices holes per propellant: 144

[Figure 13.14](#) and [Figure 13.15](#) help illustrate the injector design with aft and isometric views.

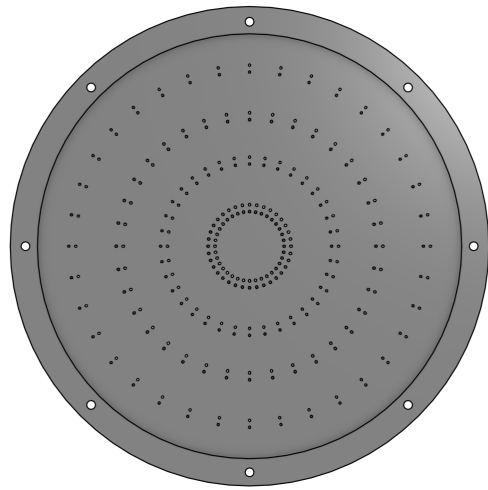


Figure 13.14: Aft view of the injector plate.

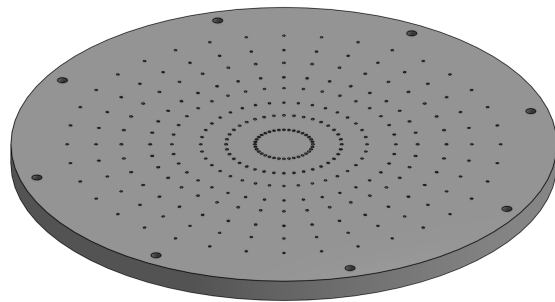


Figure 13.15: Isometric view of the injector plate.

13.3.5 Manifold Design

The purpose of the manifold is to distribute the propellants from the fluid system into the injection orifices. In order to do so for an injector with multiple concentric rings of fuel and oxidizer, a two manifold plates are employed: an aft manifold plate to create manifolds over the injection orifices, and a forward manifold plate to flow propellants into the manifolds on the first plate.

Figures 13.16, 13.17, and 13.18 display the geometry of the manifold plates and how they distribute flow to the injection orifices.

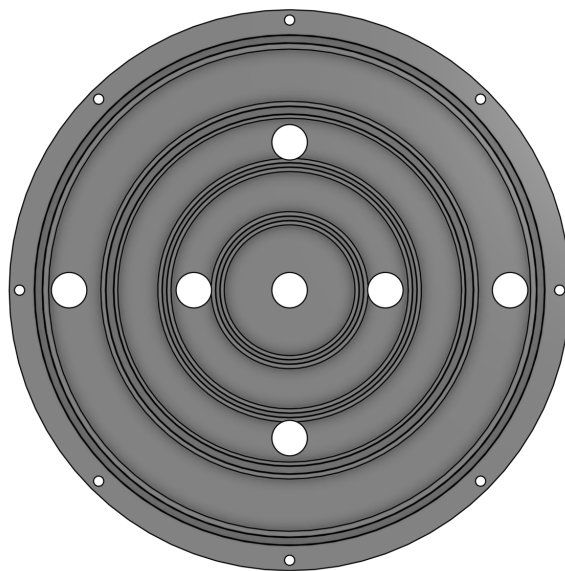


Figure 13.17: Aft view of the aft manifold plate.

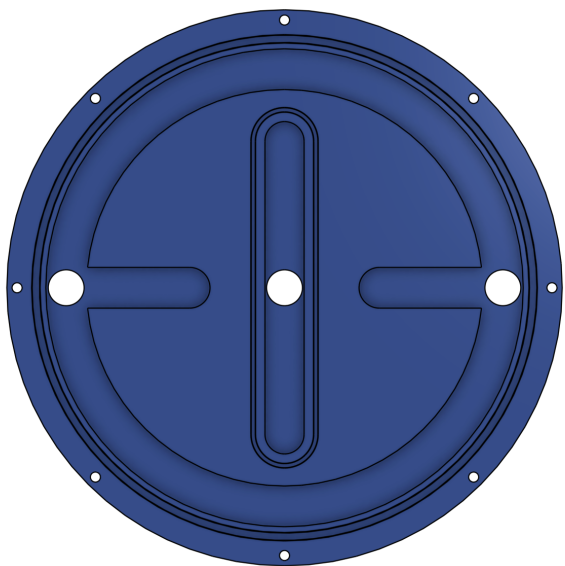


Figure 13.16: Aft view of the forward manifold plate.

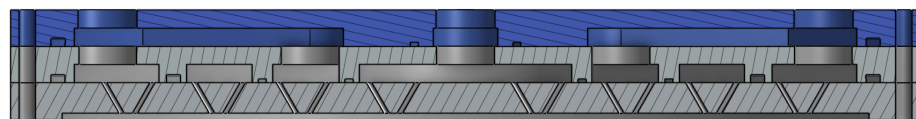


Figure 13.18: Cross section view of the manifold and injector assembly.

The seals between the injector and manifold plate will not see high temperatures, and can use a simple sealing method like o-rings. However, since FKM (rubber) elastomer o-rings are not chemically compatible with MMH and NTO, PTFE (teflon) o-rings must be used for their superb chemical resistance [93]. The o-rings require precise compression to ensure proper sealing, and the dimensions of the grooves can be sized with the Parker o-ring selector [94].

Using Parker o-ring selector and browsing the sizes of PTFE o-rings available, the following sizes were selected for the aft manifold plate, fitting in between the different orifices: 041, 050, 264, and 275. The forward manifold uses a the same 275 o-ring for the outer diameter, and a custom o-ring with the same cross section as a 0XX series o-ring. The grooves for these o-rings can be found in Figure 13.18

The thicknesses for most of the manifold geometry is based off of the required groove dimensions for the o-rings. Beyond that, the manifold volumes were selected at a middle value to compromise between low volumes (which promote low manifold fill times) and high volumes (which reduce manifold flow velocity).

13.4 Combustion Chamber Design

The combustion chamber size is best characterized by the parameter *characteristic chamber length* L^* . Defined as the ratio of chamber volume to nozzle throat area, L^* specifies the propellant stay time in the combustion chamber. While L^* increases the characteristic performance of a combustion chamber up to a certain point (as the propellant has more time to react completely), beyond this, larger values lead to higher chamber volume and weight, increased cooling surface area, and greater friction losses [85, 64]. In industry, optimization analysis is required to determine the minimum L^* for efficient combustion, with experimental firings used to validate this under specific conditions. An estimate from existing experimental data can be a good approximate value however, and can be obtained from Figure 13.19.

Propellant combination	Combustion chamber characteristic length (L^*), in.
Chlorine trifluoride/hydrazine-base fuel ..	30-35
Liquid fluorine/hydrazine	24-28
Liquid fluorine/liquid hydrogen (GH_2 injection).....	22-26
Liquid fluorine/liquid hydrogen (LH_2 injection).....	25-30
Hydrogen peroxide/RP-1 (including catalyst bed)	60-70
Nitric acid/hydrazine-base fuel	30-35
Nitrogen tetroxide/hydrazine-base fuel	30-35
Liquid oxygen/ammonia	30-40
Liquid oxygen/liquid hydrogen (GH_2 injection).....	22-28
Liquid oxygen/liquid hydrogen (LH_2 injection).....	30-40
Liquid oxygen/RP-1	40-50

Figure 13.19: Recommended combustion chamber characteristic length (L^*) for various propellant combinations [64].

From the table in Figure 13.19, a combination of MMH and NTO gives an estimate of 30 – 35 in. Once L^* is determined, the combustion chamber can be sized based on the throat area, which is defined when designing the nozzle as in Section 13.5.

A reasonable thickness for the combustion chamber can be calculated by using the thin-walled pressure vessel hoop stress equation

$$\sigma = \frac{pr}{t} \quad (13.10)$$

Solving for the required thickness t

$$t = \frac{pr}{\sigma_{\text{allowable}}} \quad (13.11)$$

Using an inner radius of 125 mm, and the yield strength of Inconel 718 approximately 758 MPa (110,000 psi) at (760 °C) [95], and the yield safety factor in Section 12.2, the allowable stress is

$$\sigma_{\text{allowable}} = \frac{\sigma_{\text{yield}}}{\text{FoS}} = \frac{758 \text{ MPa}}{1.25} = 606.4 \text{ MPa} \quad (13.12)$$

Substituting into Equation 13.11 with a chamber pressure of 200 psi (1.379 MPa),

$$t = \frac{(1.379 \times 10^6) \cdot 125}{606.4 \times 10^6} = 0.284 \text{ mm} \quad (13.13)$$

The thin-walled pressure vessel assumption requires $t/r < 0.1$, which is satisfied in this case; however, while the resulting theoretical minimum wall thickness of 0.284 mm meets this criterion, it does not account for several critical design considerations. In practical combustion chamber design, additional thickness is required to accommodate:

- **Thermal stresses** from steep gradients and cyclic heating, which can induce significant additional stress beyond hoop pressure loads.
- **Axial and bending loads**, including those from flanges, mounting hardware, and thrust transmission through the chamber wall.
- **Manufacturing tolerances and weld quality**, especially for thin walls, where imperfections can significantly reduce strength.
- **Buckling resistance** in regions not supported externally.
- **Minimum manufacturable thickness** for welding, machining, and joining processes, typically no less than 1.5 mm for metal chambers.

Based on these considerations, a practical baseline thickness of 3 mm to 5 mm is commonly used for small pressure-fed engines, consistent with historical design data and experimental systems [96]. Additional manufacturing constraints and analysis should be used to refine this value.

To calculate the number and thickness of bolts to secure the manifold/injector to the combustion chamber, the force due to injector pressure drop (pushing the injector face and combustion chamber apart) can be calculated from the definition of pressure

$$F = P \cdot A \quad (13.14)$$

where P is the injector pressure drop (20% of the chamber pressure), and A is the injector area ($r = 0.125$ m)

$$A_{\text{inj}} = \pi(0.125)^2 = 0.0491 \text{ m}^2 \quad (13.15)$$

and the resulting force due to the pressure drop is

$$F_{\text{inj}} = \Delta P \cdot A_{\text{inj}} = 13,541.76 \text{ N} \quad (13.16)$$

Distributing this load among 8 bolts, the force per bolt is

$$F_{\text{per bolt}} = \frac{F_{\text{inj}}}{8} = 1,692.72 \text{ N} \quad (13.17)$$

To select an appropriate bolt from standard bolt grades [97], we use the listed tensile strength of a grade 8.8 bolt, 800 MPa. Applying a factor of safety from Section 12.2 (FoS = 1.4), the allowable stress is

$$\sigma_{\text{allowable}} = \frac{\sigma_{\text{tensile}}}{\text{FoS}} = \frac{800 \text{ MPa}}{1.4} = 571.43 \text{ MPa} \quad (13.18)$$

The required tensile stress area for each bolt is

$$A_t = \frac{F_{\text{per bolt}}}{\sigma_{\text{allowable}}} = \frac{1692.72}{571.43 \times 10^6} = 2.96 \times 10^{-6} \text{ m}^2 = 2.96 \text{ mm}^2 \quad (13.19)$$

From standard metric bolt tables [98], the tensile stress area (A_t) for M3 bolts (fine thread, $A_t \approx 5 \text{ mm}^2$) is more than sufficient to handle the load.

To properly preload the bolts, the required tightening torque can be estimated using the general relation from [99]:

$$T = K \times F_i \times d \quad (13.20)$$

where T is the required torque applied to fastener, K is a constant depending on bolt material and size, F_i is the preload (1,556.63 N in this case), and d is the nominal bolt diameter (3 mm for an M5 bolt). An estimate for the value of K of 0.18 may be used for lubricated stainless steel bolts, however this value should be experimentally determined to obtain a final value [99]. Using the estimated value, the required torque is estimated to be 0.84 N – m.

The seal between the combustion chamber and injector face necessitates a high-temperature high-pressure seal since it will be in direct contact with high temperature combustion gases. For this reason, graphite pipe gaskets are commonly used in industry [100].

To accomplish the film cooling, a fraction of the fuel will be injected through angled radial holes in the combustion chamber as seen in Figures 13.20 and 13.21.

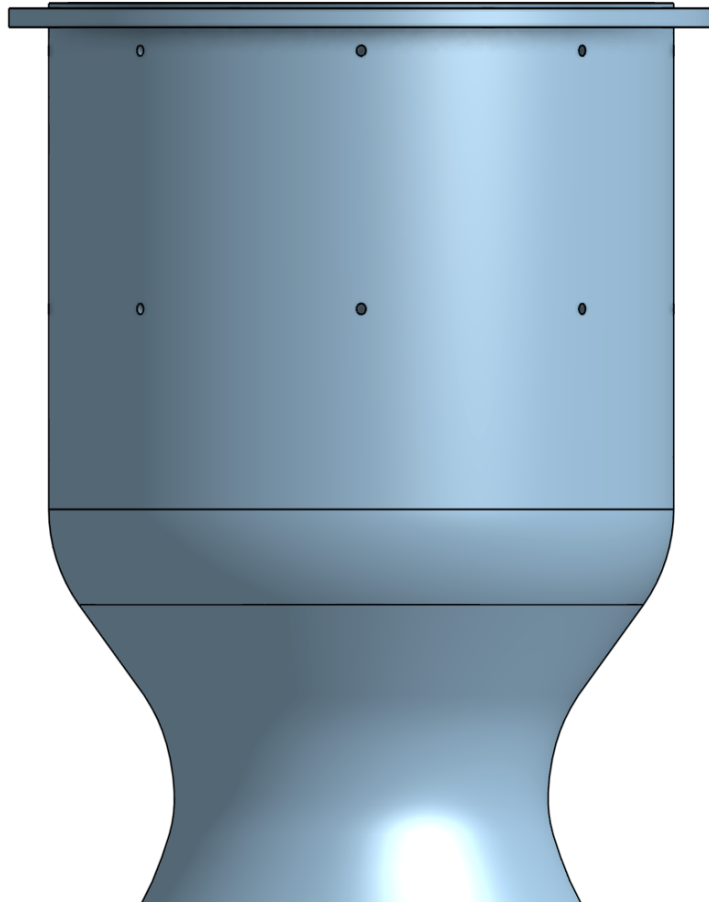


Figure 13.20: Side view of the combustion chamber showing the film cooling orifices covered by external manifold.

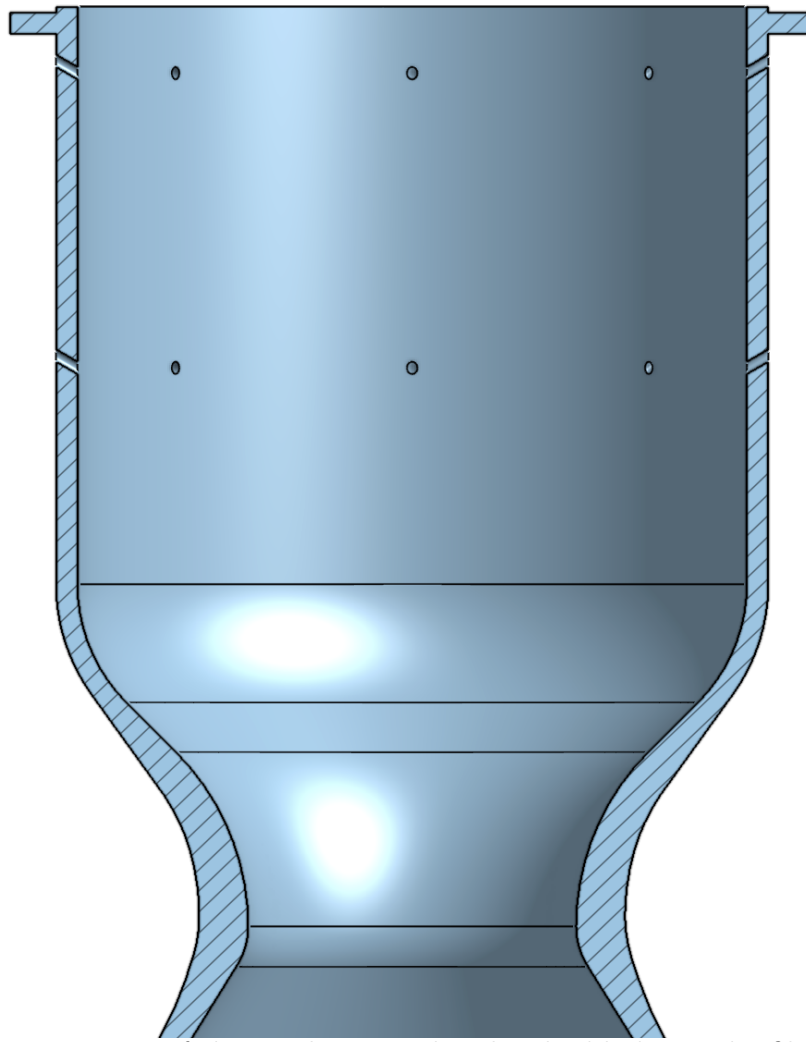


Figure 13.21: Cross section of the combustion chamber highlighting the film cooling orifices without external film cooling manifold.

As seen in Figure 13.21, the holes come in at an angle of 30° and are 1.246 mm in diameter, calculated using Equation 13.5 to obtain the flow rate determined in Section 13.6.2.

There is an additional manifold that distributes fuel to the film cooling orifices along the combustion chamber. This can be accomplished with a "cover" that goes over the film cooling orifices and holds pressure. This can be seen in Figure 13.22.

The film cooling manifold pictures in Figure 13.22 will be brazed onto the combustion chamber, and has an inlet on the side for fluid routing.

13.5 Nozzle Design

The expansion ratio (described earlier in Equation 13.3) is an important parameter in engine design as it determines the exit pressure of the nozzle, which in turn dictates the performance

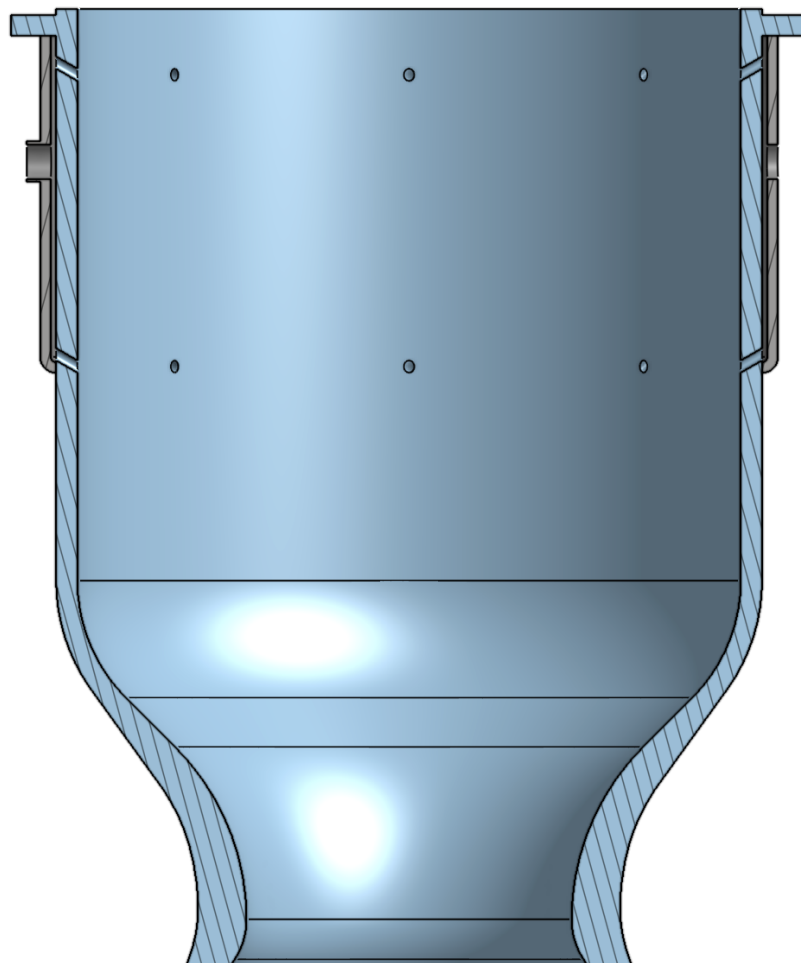


Figure 13.22: Cross section view of the combustion chamber with film cooling manifold attached.

of the engine. This is because the divergent supersonic nozzle serves to convert pressure and temperature energy into kinetic energy, and the lower the exit pressure of the nozzle, the higher the exit velocity of the combustion products. Ideally expanded nozzles aim to match ambient pressure, and for a vacuum-optimized engine, this means obtaining as high of an expansion ratio as is feasible [85], since a perfectly-expanded nozzle would be effectively infinitely large.

The expansion ratio was obtained by iterating over various chamber pressure values as described in Section 13.2.3.

The final expansion ratio is determined to be 150, which is in the range of similar engines like Raptor Vacuum (~ 200) [88] and Merlin Vacuum (~ 165) [101].

The nozzle geometry was constructed using a Rao parabolic approximation [55], which approximates an ideal nozzle shape. The length of this nozzle is based off of the percent length of a full bell nozzle, and the efficiency can be visualized in Figure 13.23.

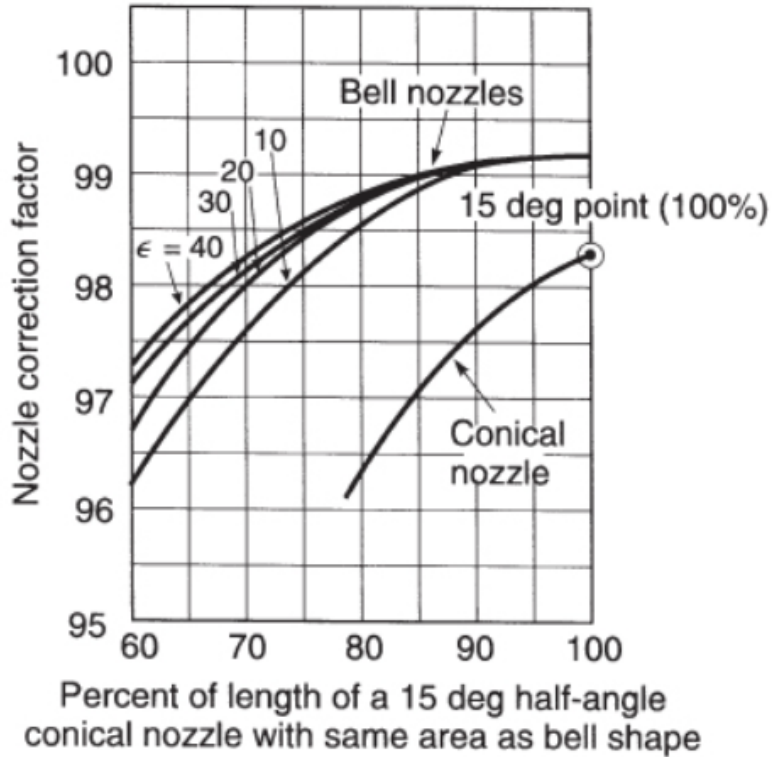


Figure 13.23: Plot of nozzle correction factor (efficiency) varies with percent length of bell nozzles [76].

From Figure 13.23, an 85% length was selected since higher percent lengths come at the cost of increased weight. The other important parameters of the nozzle design are the initial and final angle of the nozzle, which can be determined using Figure 13.24.

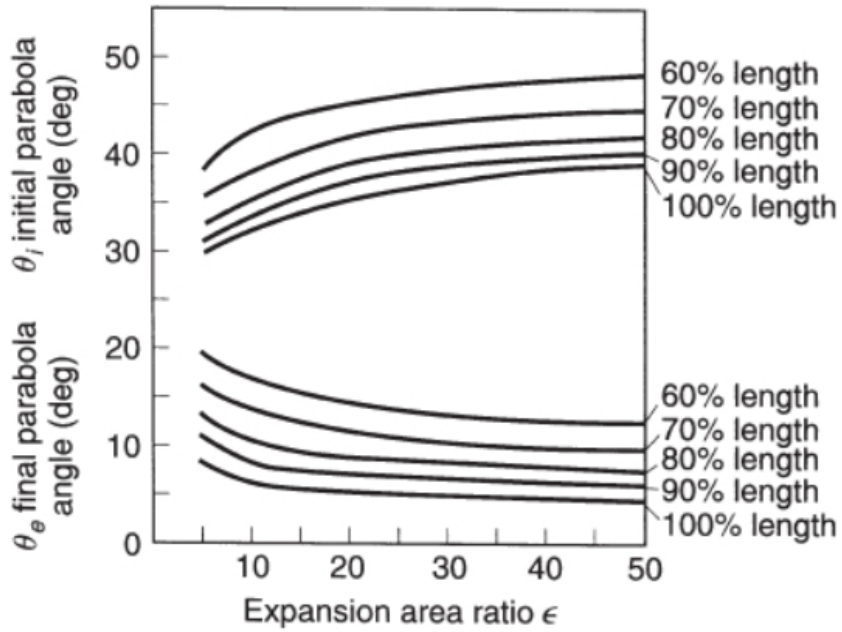


Figure 13.24: Initial and final angles of a Rao nozzle based on expansion ratio and percent length [76].

These parameters can then be applied to the geometric method of a Rao parabolic nozzle shown in Figure 13.25, where lines NQ and EQ are at the initial and final angles respectively.

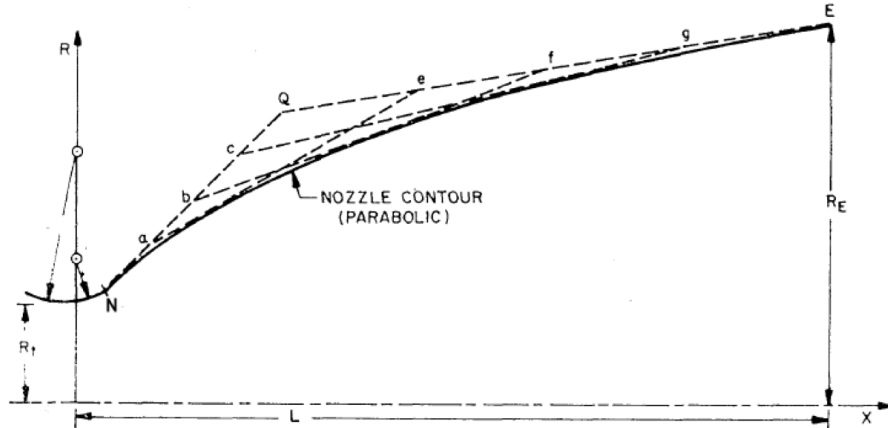


Figure 13.25: Geometric method of modeling a Rao parabolic nozzle [102].

The geometry obtained is shown in Figure 13.26.

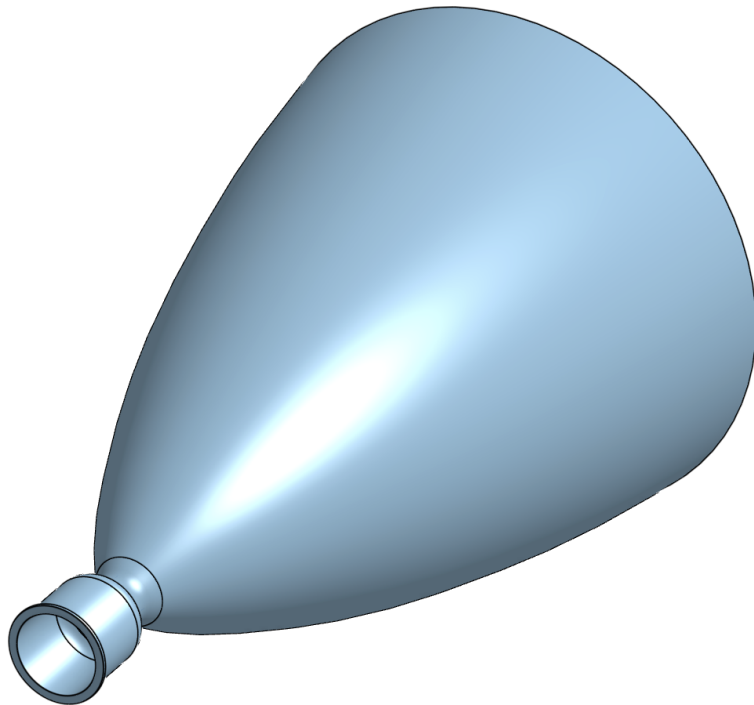


Figure 13.26: CAD of the nozzle modeled using the geometric Rao method.

Key dimensions include the previously mentioned exit diameter of 1.5 m, and a length of 2.184 m.

13.6 Thermal Analysis

The objective of this thermal analysis is to characterize the thermal stresses in the rocket engine during transient operation over the extended burns that occur during the maneuvers.

The principal failure mode of the engine that needs to be investigated is melting and/or temperature-induced yielding of the combustion chamber and nozzle due to the high thermal load. The critical location for this failure mode is the throat since it has the largest heat flux [85].

13.6.1 1D Steady-State Approximation

To determine initial estimates of thermal conditions in the engine with film cooling, a simple 1-D steady-state thermal model can be constructed, using the adiabatic flame temperature from CEA, convection through the film cooling with an estimated convection coefficient, conduction through the wall of the combustion chamber, and radiation to space. This model is illustrated in 13.27.

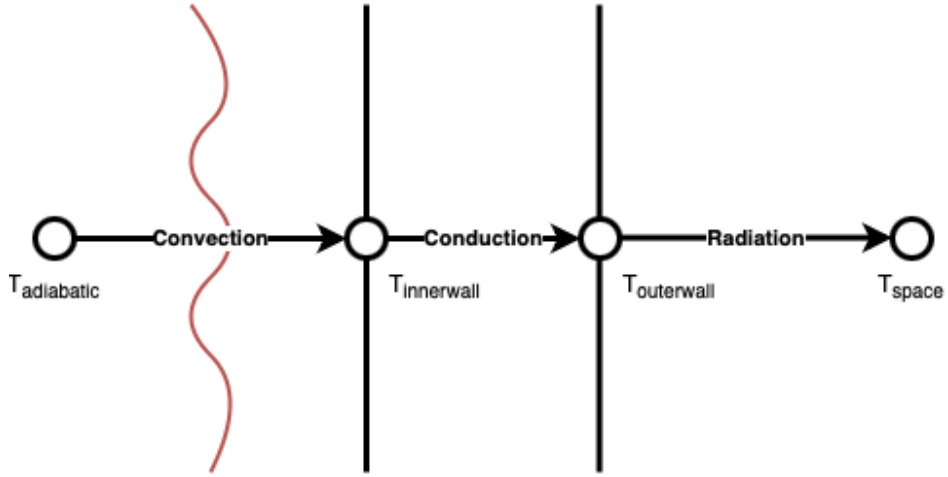


Figure 13.27: Diagram of simplified 1-D thermal model.

The governing steady-state heat transfer equations used in the model are as follows, incorporating the three primary modes of heat transfer, conduction, convection, and radiation [103].

$$q''_{\text{conv}} = h(T_{\text{adiabatic}} - T_{\text{innerwall}}) \quad (13.21)$$

$$q''_{\text{cond}} = \frac{k}{t_w}(T_{\text{innerwall}} - T_{\text{outerwall}}) \quad (13.22)$$

$$q''_{\text{rad}} = \varepsilon\sigma(T_{\text{outerwall}}^4 - T_{\text{space}}^4) \quad (13.23)$$

At steady-state, with no heat generation or storage in the wall, heat flux is conserved through each mode:

$$q''_{\text{conv}} = q''_{\text{cond}} \quad (13.24)$$

$$q''_{\text{cond}} = q''_{\text{rad}} \quad (13.25)$$

Here, T_{flame} is the adiabatic flame temperature (idealized, theoretical temperature from chemical equilibrium) from CEA [84] (e.g., 2972.3 K), and T_{∞} is the space ambient temperature (assumed to be 2.7 K [104]). The film-cooled side of the chamber wall is at temperature T_{wall} , while the outer surface radiating to space is at temperature T_{outer} . k is the wall material thermal conductivity (e.g., 16.3 W/m-K for 316 stainless steel), and t_w is the wall thickness (e.g., 10 mm). The surface emissivity ε (e.g., 0.5) and the Stefan-Boltzmann constant σ account for radiative losses [103].

To find the convection coefficient h , an EES analysis was carried out using the Bartz correlation. The equation is presented in Rocket Propulsion Elements [76] as:

$$h_g = \frac{0.026}{D^{0.2}} \left(\frac{c_p \mu^{0.2}}{\text{Pr}^{0.6}} \right) (\rho v)^{0.8} \left(\frac{\rho_{am}}{\rho'} \right) \left(\frac{\mu_{am}}{\mu_0} \right)^{0.2} \quad (13.26)$$

This equation is a simplified version of the full correlation, which can be found in Section 16 as Equation 16.12. Evaluating this equation using gas properties obtained from CEA finds a value for h_g of 2,713 W/m²–K. This value does not model any effects of film cooling however. Incorporating film cooling effectiveness η_c , for which a reasonable estimate is 0.5 [64], the corrected value is 1,899 W/m²–K.

This approximate analysis calculates an inner wall temperature of 2,554 K. This value should be used to validate the steady-state finite element model. The full EES code for the 1D approximation can be found in Appendix G. 2,554 K is well above the melting point of Inconel 718 ($\sim 1,500$ K)[87] and even further above the point at which tensile strength drops significantly ($\sim 1,000$ K) [82].

13.6.2 Advanced Film Cooling Model

In order to determine the required mass flow of fuel used for film cooling, a different model will need to be analyzed. This more advanced film cooling model includes the heat absorbed by the fluid as well as incorporating the vaporization energy of the fluid as it transitions from liquid to gas.

The required mass flow rate of film coolant for cooling a rocket engine combustion chamber is determined using the film cooling equation from Huzel & Huang [64] (Eq. 4-33), given as:

$$\frac{G_c}{G_g} = \frac{1}{\eta_c} \cdot \frac{H}{a \left(1 + b \frac{C_{pvc}}{C_{pg}} \right)} \quad (13.27)$$

where:

- G_c is the film coolant weight flow rate per unit area of the cooled chamber wall,
- G_g is the combustion gas weight flow rate per unit area perpendicular to the flow,
- η_c is the film cooling efficiency, typically ranging from 0.3 to 0.7 due to losses,
- H is the film coolant enthalpy, given by:

$$H = \frac{C_{pvc}(T_{aw} - T_{wg})}{C_{plc}(T_{wg} - T_{co}) + \Delta H_{vc}} \quad (13.28)$$

where C_{plc} and C_{pvc} are the average specific heats of the coolant in liquid and vapor phases, respectively, T_{aw} is the adiabatic wall temperature of the gas, and T_{wg} is the maximum allowable gas-side wall temperature.

The constants a and b are given by:

$$a = \frac{2V_d}{V_m f_{tp}}, \quad b = \left(\frac{V_g}{V_d} \right) - 1 \quad (13.29)$$

where V_g , V_d , V_m are the axial stream velocities of combustion gases at the centerline, boundary layer, and average velocity, respectively, and f_{tp} is the friction coefficient for two-phase flow.

The mass flow ratio of the film coolant is then determined by:

$$\frac{\dot{m}_{\text{film}}}{\dot{m}_{\text{total}}} = \frac{G_c}{G_g} \quad (13.30)$$

where \dot{m}_{film} is the required mass flow rate of the coolant, and \dot{m}_{total} is the total mass flow rate of the engine.

This calculation incorporates thermodynamic properties from NASA CEA, fluid velocity parameters, and empirical corrections from friction and heat transfer models. The final percent mass flow rate calculated was 0.3714 %. This is a suspiciously low value, but at this point in time the discrepancy between the calculated value and expected value (5%) could not be identified, and will be determined as a part of future work.

13.7 Finite Element Model

The objective of this Finite Element Model is to gain insight into transient effects of the finite burn time and see how much the thermal results differ. It will also reveal if the steady-state assumption made in the initial approximation model was valid.

The Finite Element Analysis will be conducted using two solutions: Steady-state to validate the model using the hand-calculated value, and transient to evaluate transient effects.

The transient model will need a range of time to use, so the burn times can be calculated from the fuel mass required presented in Table 6.6, using the mass flow rate of 8.4 kg/s in a simple calculation.

Table 13.2: Kick Stage Burn Time Calculations.

Maneuver #	Δv Required [m/s]	Fuel Mass Required [kg]	Burn Time [s]
1	246	339.0	40.36
2	1324	1750.0	208.33
3	1324	1287.0	153.21
4	124	44.8	5.33
Total		3420.8	407.24

This Finite Element Model will improve on the initial approximate model by:

1. Using the Bartz correlation to compute the convective heat transfer coefficient (h_g).

2. Applying convection to a thermal FEA model.

13.7.1 Geometry

While at first this model seemed like it would be a good fit for shell elements, the varied thicknesses in the combustion chamber, throat, and nozzle would have to be manually inputted. As such, a 2D axisymmetric analysis was chosen.

The geometry was imported into ANSYS, and bonded contacts were made between the manifold plate, injector plate, and combustion chamber, since these will be strongly bolted together and never expected to separate. Figures 13.28 and 13.29 illustrate the geometry and contacts used in the model.

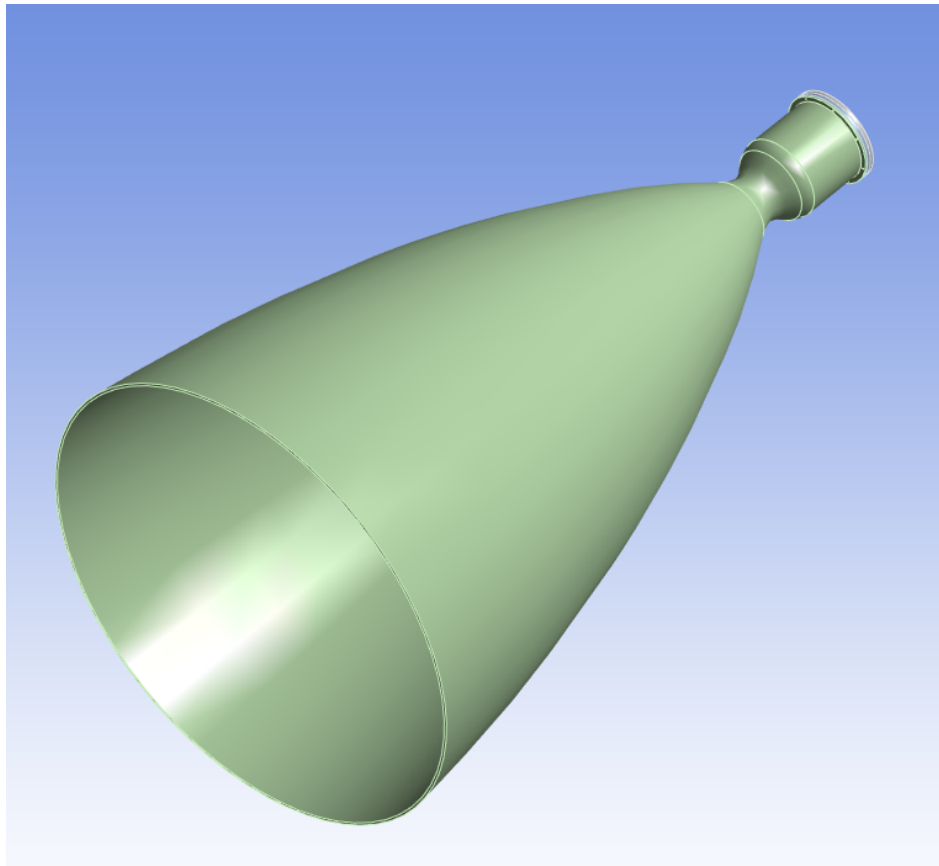


Figure 13.28: Geometry imported into ANSYS.

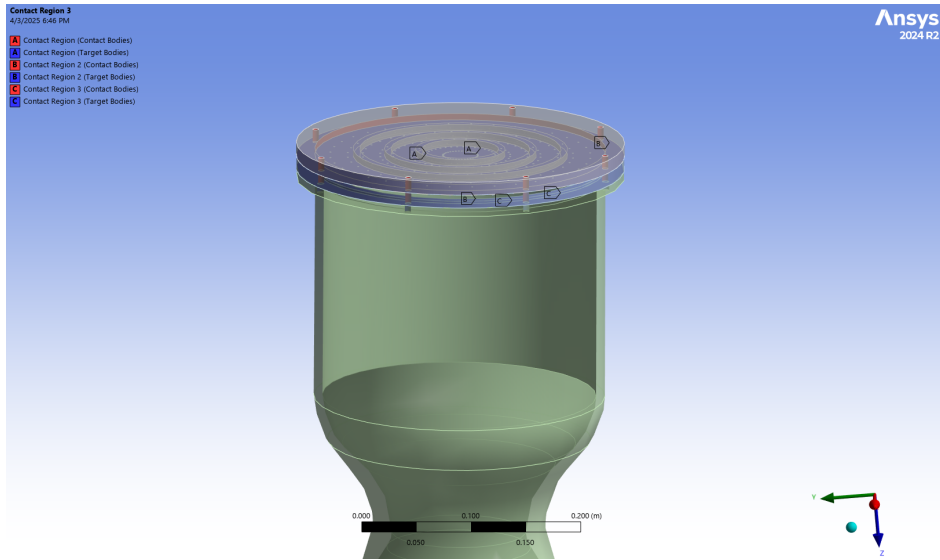


Figure 13.29: Contacts used in ANSYS.

13.7.2 Mesh

The mesh was refined using edge sizing on the nozzle, and face meshing to generate a mapped mesh along the combustion chamber and nozzle. Figures 13.30 and 13.31 illustrate the mesh refinements and final mesh used.

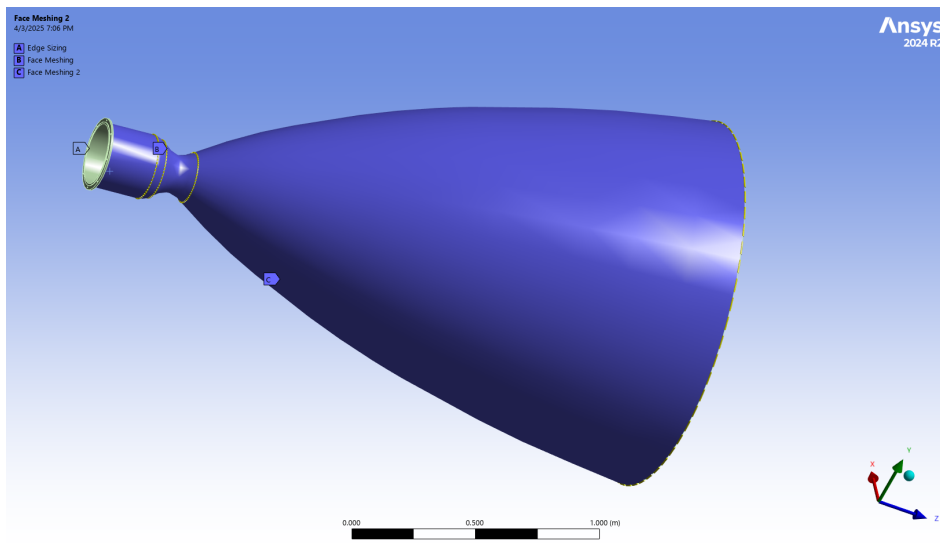


Figure 13.30: Mesh refinement locations in ANSYS.

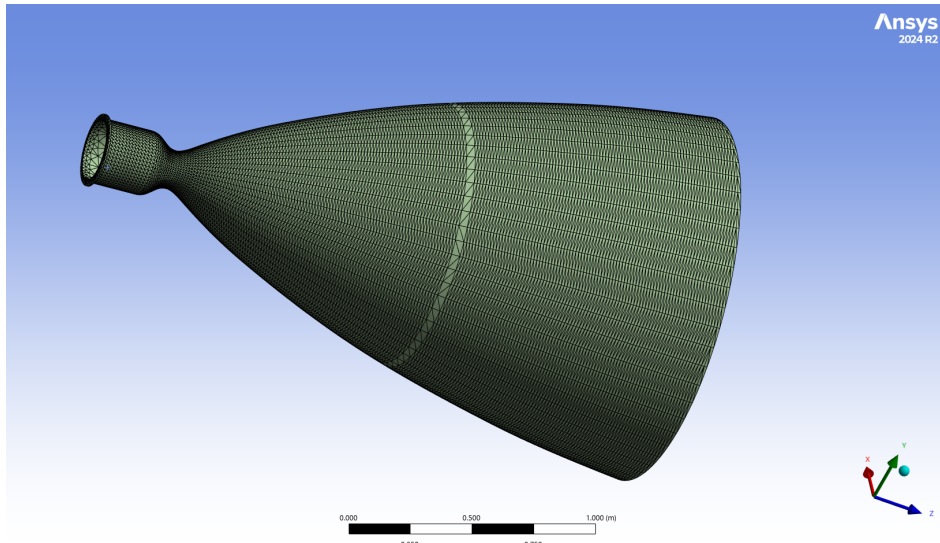


Figure 13.31: Final mesh used in ANSYS.

13.7.3 Boundary Conditions and Loads

The applied boundary conditions are summarized in Table 13.3.

Boundary Condition	Description	Where Applied
Convection	From combustion gases within chamber and nozzle using convection coefficient from EES analysis	Inside walls of combustion chamber and nozzle
Radiation	From outer walls radiating heat to space	Outside walls of combustion chamber and nozzle

Table 13.3: Boundary conditions applied to finite element model.

Figures 13.32 and 13.33 illustrate the convection and radiation boundary conditions applied to the model.

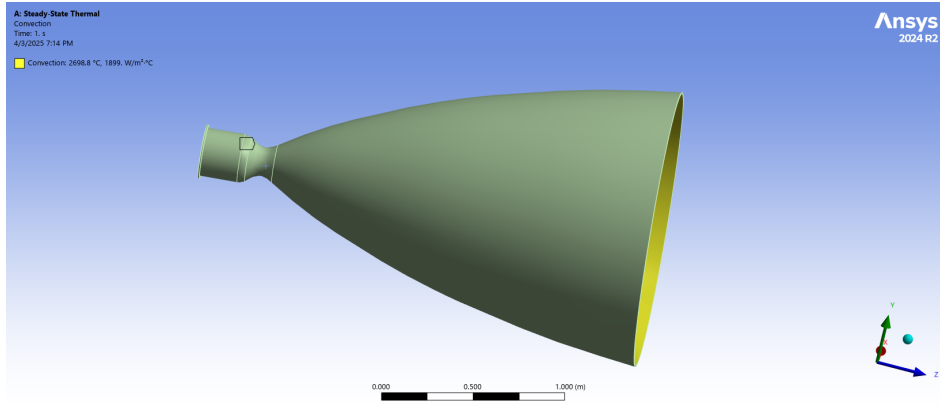


Figure 13.32: Convection boundary condition applied to inside walls.

The convection BC was applied with a convection coefficient calculated from Bartz ($h = 1,899 \text{ W/m}^2\text{-K}$).

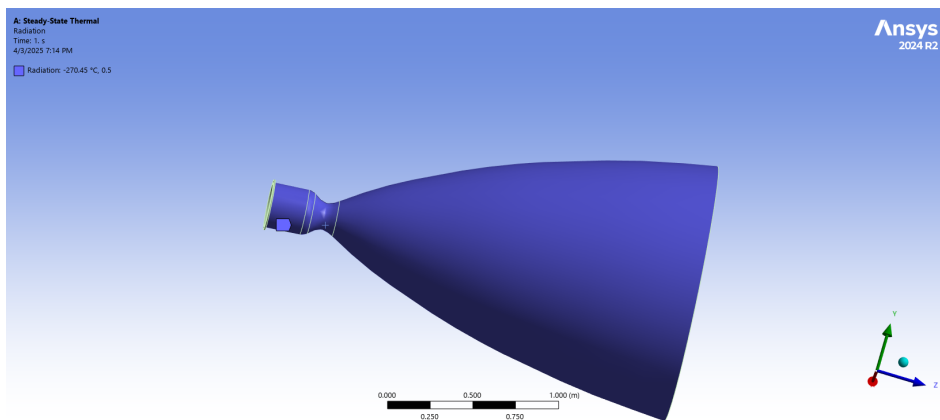


Figure 13.33: Radiation boundary condition applied to the outside walls.

The radiation BC was applied with the ambient temperature of empty space, 2.7 K, with an estimate of emissivity of machined Inconel being 0.5.

13.7.4 Steady-State Results

The purpose of the steady-state analysis is

To display the results of this steady-state analysis, the temperature and heat flux are of interest to determine which areas need more cooling.

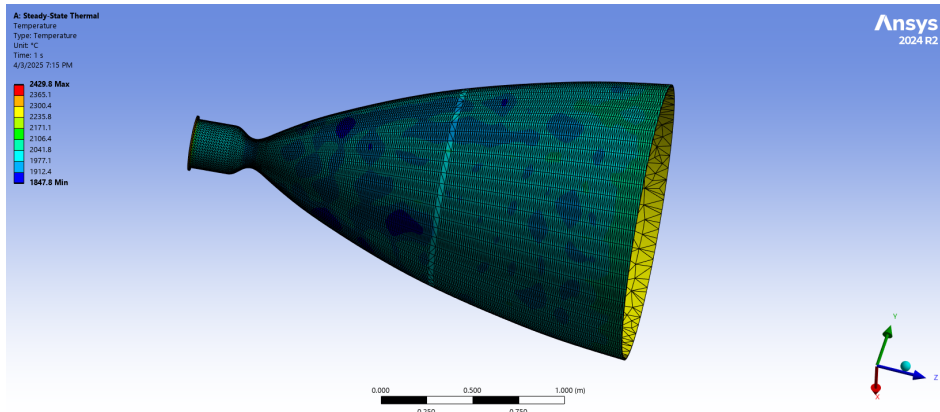


Figure 13.34: Temperature distribution on the outside of the engine.

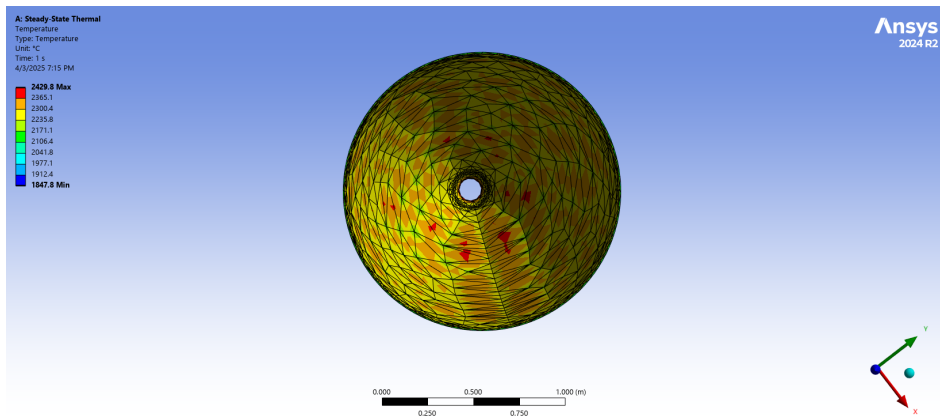


Figure 13.35: Temperature distribution on the inside of the engine.

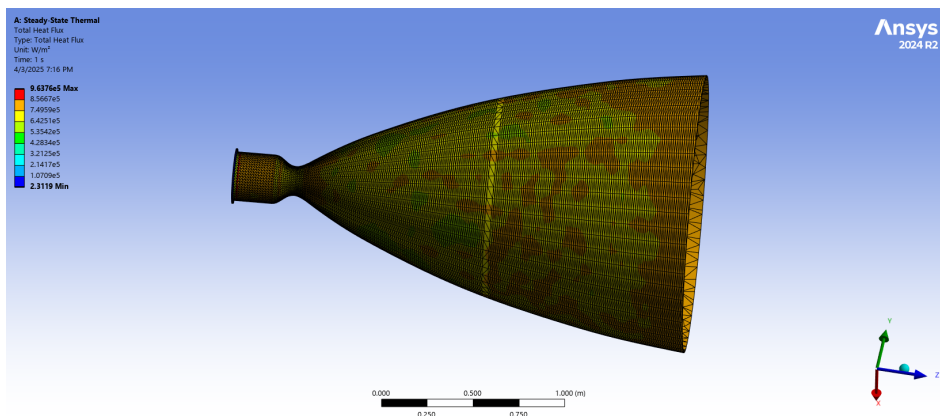


Figure 13.36: Heat flux distribution on the outside of the engine.

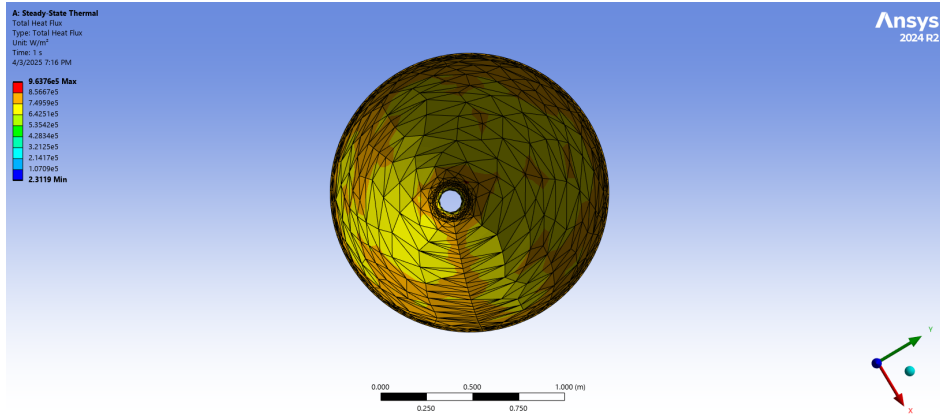


Figure 13.37: Heat flux distribution on the inside of the engine.

As shown in Figures 13.34-13.37, the maximum temperature reaches $2,429.8^{\circ}\text{C}$, indicating significant hot spots inside the engine. This is validated by the value calculated in the initial approximation, and confirms that further adjustments to the cooling of the engine must be made to prevent melting the chamber.

The goal for this thermal analysis was to:

- Obtain a 1D steady state thermal result using the basic EES calculation
- Improve that EES calculation using the film cooling model to get film cooling flow rates and use a corrected heat transfer coefficient
- Run a steady-state FEA analysis and validate the FEA model with the 1D calculation
- Run a transient FEA analysis to obtain transient thermal data and challenge the steady-state assumption and compare

Unfortunately due to timing, workload, and technical issues on one of the author's part, this was not completed. This author is extremely disappointed and takes responsibility for the lack of results.

14 Kick Stage Structural Analysis

The structure of the kick stage must be able handle to forces exerted due to the masses of the seven STDs that are mounted on top of the kick stage. The structure will experience the highest stresses at launch. From the Falcon 9 User Guide, the maximum vertical and lateral accelerations seen during accent are seen in Figure 12.1. The maximum vertical acceleration of 6g will be analyzed first.

When analyzing the STD mount frame, the mounted STDs on top will be situated as seen in Figure 14.1. There are 6 STDs spaced evenly on the outer ring of the frame and a singular STD in the middle of the frame.

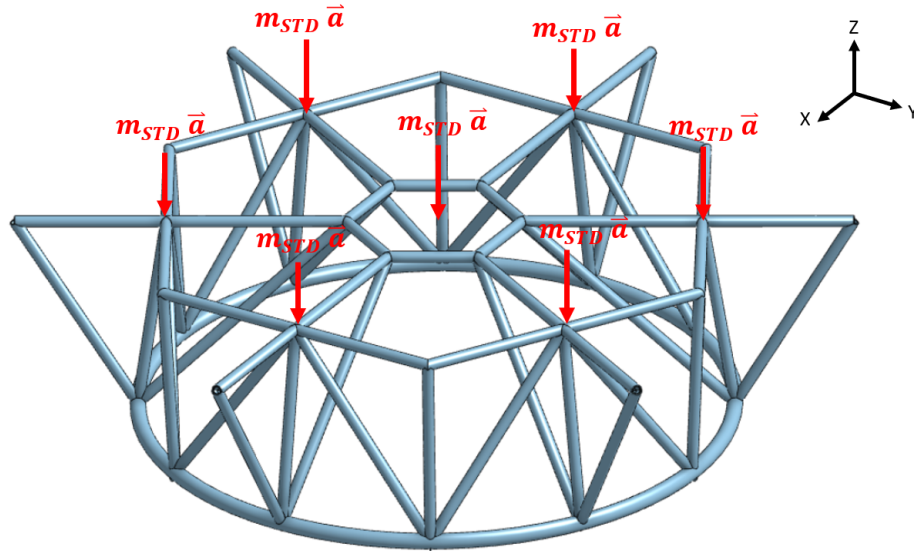


Figure 14.1: Loading locations viewed from above the kick stage mounting frame

14.1 Analytic Calculation

For the analysis going forward, various views will be used to set up free-body diagrams in order to estimate the reaction forces at the base of the frame. Figure 14.2 shows where each view is located throughout the analysis.

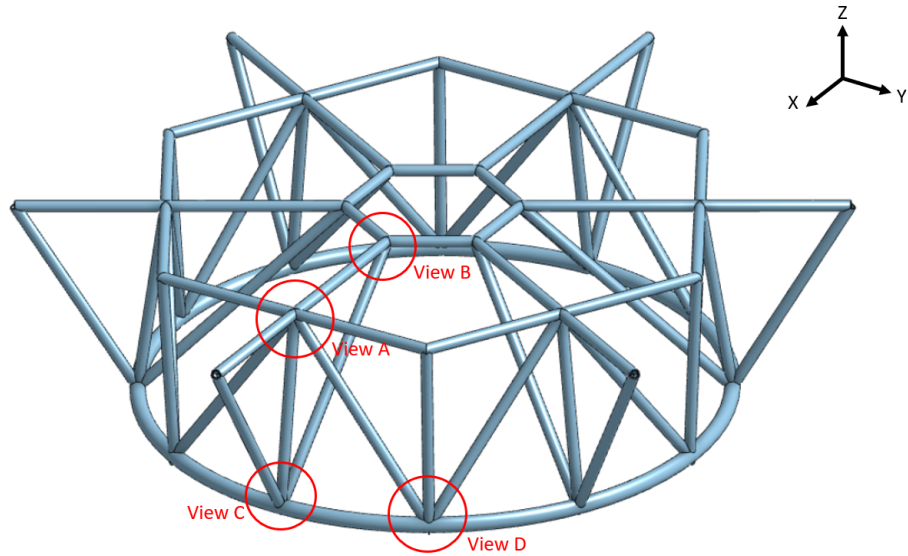


Figure 14.2: Detail view reference for individual joints of the kick stage frame.

Due to the symmetry of the problem, all reaction contributions due to the outer six STDs will be equivalent. By looking at View A in Figure 14.3, the vertical load must be transmitted through Forces F_1 , F_2 , and F_3 . F_1 and F_3 have a projection angle onto the z-axis of θ_1 .

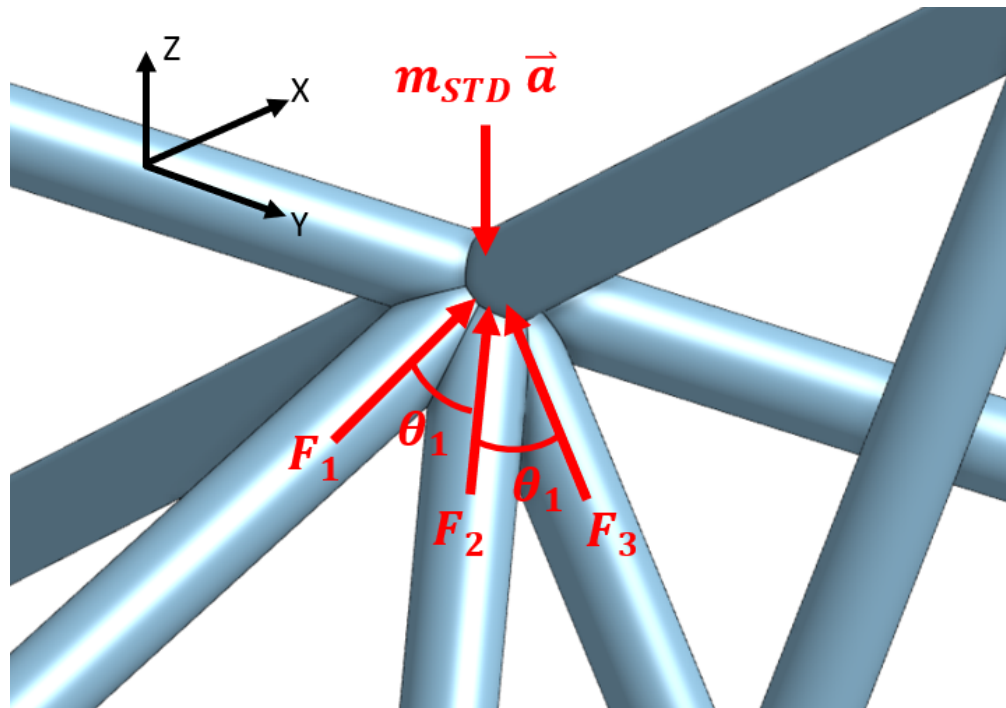


Figure 14.3: Free body diagram of View A

When the perspective of view A is shifted to the XZ plane, it can be seen that F_2 has a projection angle onto the z-axis of θ_2 , which is approximately 9 degrees. This angle is shown

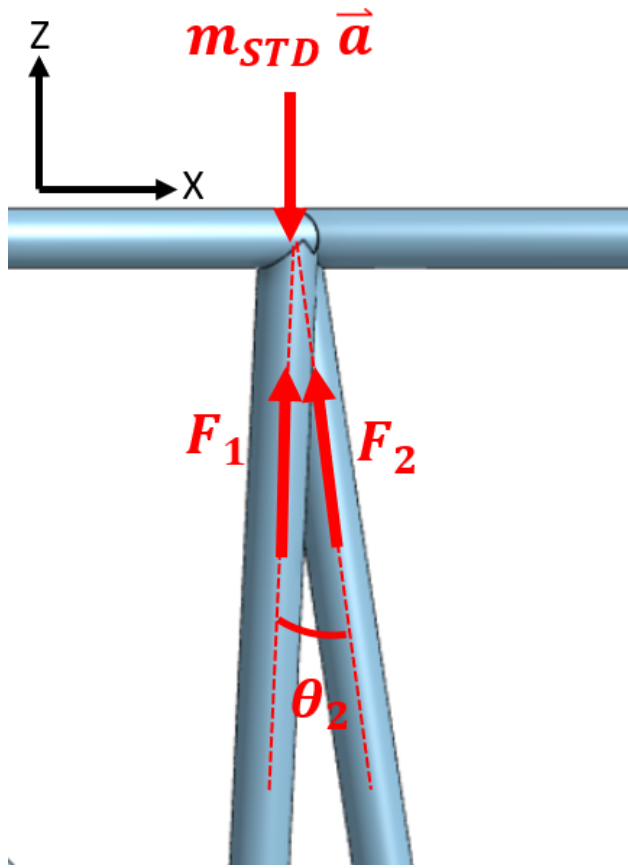


Figure 14.4: View A shown on the XZ plane.

in Figure 14.4.

The loads associated with the STDs can be determined by,

$$F_{STD} = m_{STD} \vec{a} \quad (14.1)$$

where m_{STD} is the mass of one STD and \vec{a} is the acceleration of payload. In this case, the acceleration is all in the vertical, z, direction.

With vertical force components at each member joint and the input load at the center of gravity defined, static equilibrium analysis can be applied. The sum of forces in the z-direction is,

$$\Sigma F_z = 0 = -F_{STD} + F_{1,z} + F_{2,z} + F_{3,z} \quad (14.2)$$

This leads to a statically indeterminate situation where there are 3 unknown vertical loads and only one equilibrium to describe them. Deformations will be considered to determine the vertical loads through each member.

To express the axial deformation in member 2, each force direction must be determined

relative to F_2 . From Figure 14.4, it can easily be observed that the angle between F_{STD} and F_2 is θ_2 . As for F_1 and F_3 , the unit vectors must be expressed,

$$\begin{aligned}\hat{F}_1 &= [0, \sin \theta_1, \cos \theta_1] \\ \hat{F}_2 &= [-\sin \theta_2, 0, \cos \theta_2]\end{aligned}$$

By definition, the cosine of the angle between two unit vectors can be obtained from the dot product of the vectors,

$$\hat{F}_1 \cdot \hat{F}_2 = \cos \theta_3 \quad (14.3)$$

Evaluating this equation results in,

$$\cos \theta_3 = \cos \theta_1 \cos \theta_2$$

The deformations can now be described by,

$$\delta = \frac{FL}{EA} \quad (14.4)$$

where F is the sum of forces acting axially on the member, L is the length, E is the Young's Modulus, and A is the cross-sectional area [**deformation**].

The deformation of member 2 is described by,

$$\delta_2 = (-F_1 \cos \theta_3 - F_3 \cos \theta_3 + F_{STD} \cos \theta_2) \frac{L_2}{EA} \quad (14.5)$$

Similarly, the deformation of member 1 is described by,

$$\delta_1 = (F_{STD} \cos(\theta_1) - F_3 \cos(2\theta_1) - F_2 \cos(\theta_3)) \frac{L_1}{EA} \quad (14.6)$$

By a simple observation, members 1 and 3 are symmetric across the loading of the joint; therefore,

$$\delta_1 = \delta_3 \quad (14.7)$$

Projecting these deformations onto the z-axis, the deformation of member 2 in the z-direction is,

$$\delta_{2,z} = \delta_2 \cos \theta_2 \quad (14.8)$$

and deformations of members 1 and 3 in the z-direction,

$$\delta_{1,z} = \delta_{3,z} = \delta_1 \cos(\theta_1) \quad (14.9)$$

Substituting Equations 14.5 and 14.6 into Equations 14.8 and 14.9, respectively,

$$\delta_{2,z} = (-F_1 \cos \theta_3 - F_3 \cos \theta_3 + F_{STD} \cos \theta_2) \frac{L_2 \cos \theta_2}{EA} \quad (14.10)$$

$$\delta_{1,z} = (F_{STD} \cos(\theta_1) - F_3 \cos(2\theta_1) - F_2 \cos(\theta_3)) \frac{L_1 \cos \theta_1}{EA} \quad (14.11)$$

With the vertical displacements determined, the system can be resolved by equating the deformations in the z-direction,

$$\delta_{1,z} = \delta_{2,z} = \delta_{3,z} \quad (14.12)$$

From this conclusion, Equation 14.10 can be set equal to Equation 14.11,

$$(-F_1 \cos \theta_3 - F_3 \cos \theta_3 + F_{STD} \cos \theta_2) \frac{L_2 \cos \theta_2}{EA} = (F_{STD} \cos(\theta_1) - F_3 \cos(2\theta_1) - F_2 \cos(\theta_3)) \frac{L_1 \cos \theta_1}{EA} \quad (14.13)$$

Since members 1 and 3 experience the same deformation and are identical members mirrored across the joint, the forces must be equal.

$$F_1 = F_3 \quad (14.14)$$

Lastly, each member's total force can be related to the force in the z-direction by assuming the force is primarily axial in each member.

$$F_{2,z} = F_2 \cos \theta_2 \quad (14.15)$$

$$F_{1,z} = F_1 \cos \theta_1 \quad (14.16)$$

Equations 14.2, 14.13, 14.14, 14.15, and 14.16 can be solved simultaneously for the force in each member.

$$F_{1,z} \approx 7290N$$

$$F_{2,z} \approx 8965N$$

$$F_{3,z} \approx 7290N$$

These forces will be used to estimate the z-direction reactions at View D, seen in Figure 14.5.

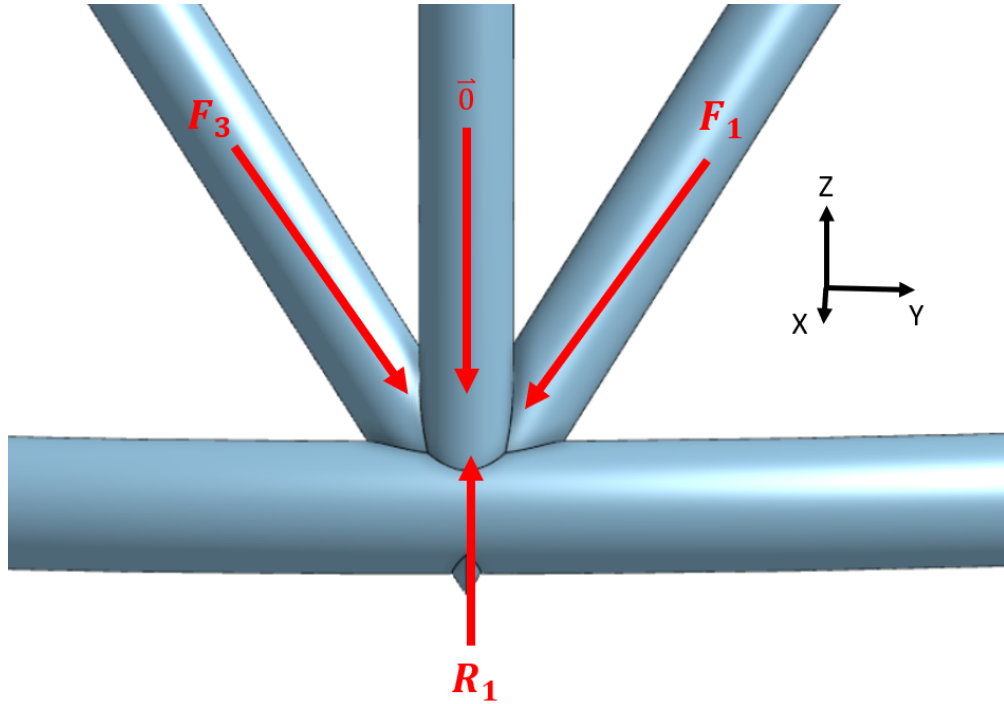


Figure 14.5: Free body diagram at View D.

The member that acts as a zero force member has no force because of the approximation made that the load due to the STD acts as a point load. From Figure 15.5, it is clear that no vertical force acts through the joint above this zero force member.

From Figure 14.5, forces in the z-direction are summed,

$$\Sigma F_z = 0 = R_{1,z} - F_{1,z} - F_{3,z} - 0 \quad (14.17)$$

The resulting vertical reaction is

$$R_{1,z} = 14579N \quad (14.18)$$

The load from the center STD must be transmitted through each member equivalent members seen in View B, Figure 14.6. This is with the assumption that the angle of the horizontal member at the top of the frame stays sufficiently horizontal.

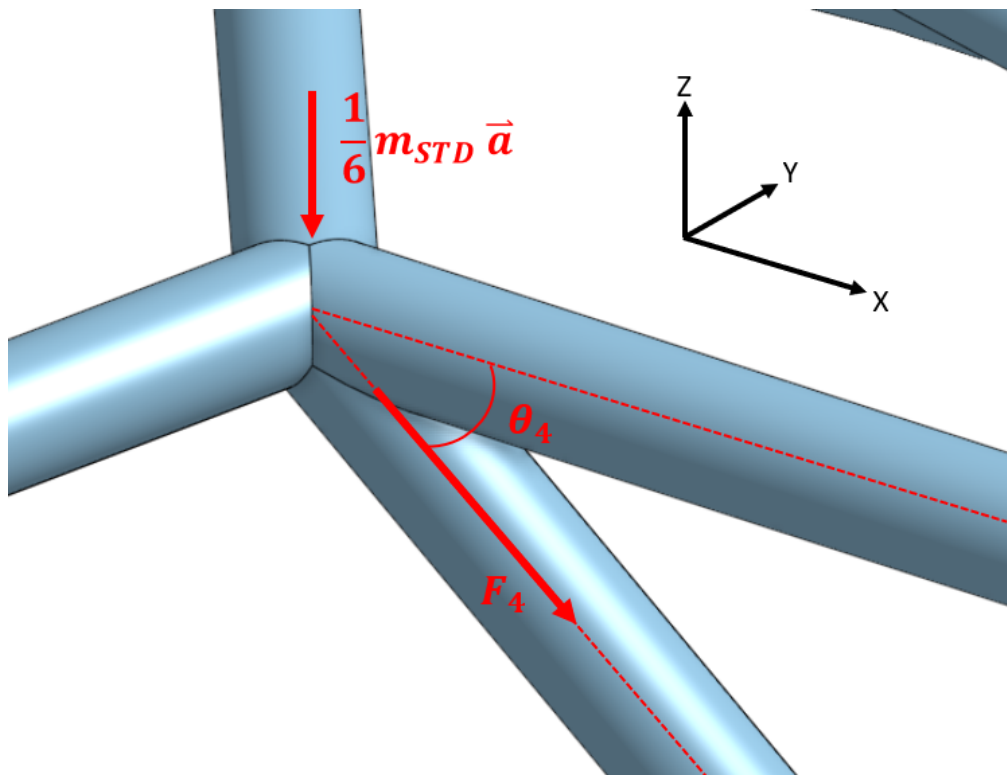


Figure 14.6: Free body diagram at View B.

Each diagonal member must bear the load of one-sixth of the mass of the center STD, since six members are equally spaced radially.

The force balance in the z-direction at view B results in,

$$\Sigma F_z = 0 = -\frac{1}{6}F_{STD} + F_4 \sin(\theta_4) \quad (14.19)$$

where $F_4 \sin \theta_4$ the projection of the force in member 4 projected onto the z-axis. Solving for this projection provides the vertical force due to member 4,

$$F_{4,z} = 3924N \quad (14.20)$$

This force component, along with the force in member 2, allows for the reaction at View C to be analyzed. The free body diagram is shown in Figure 14.7

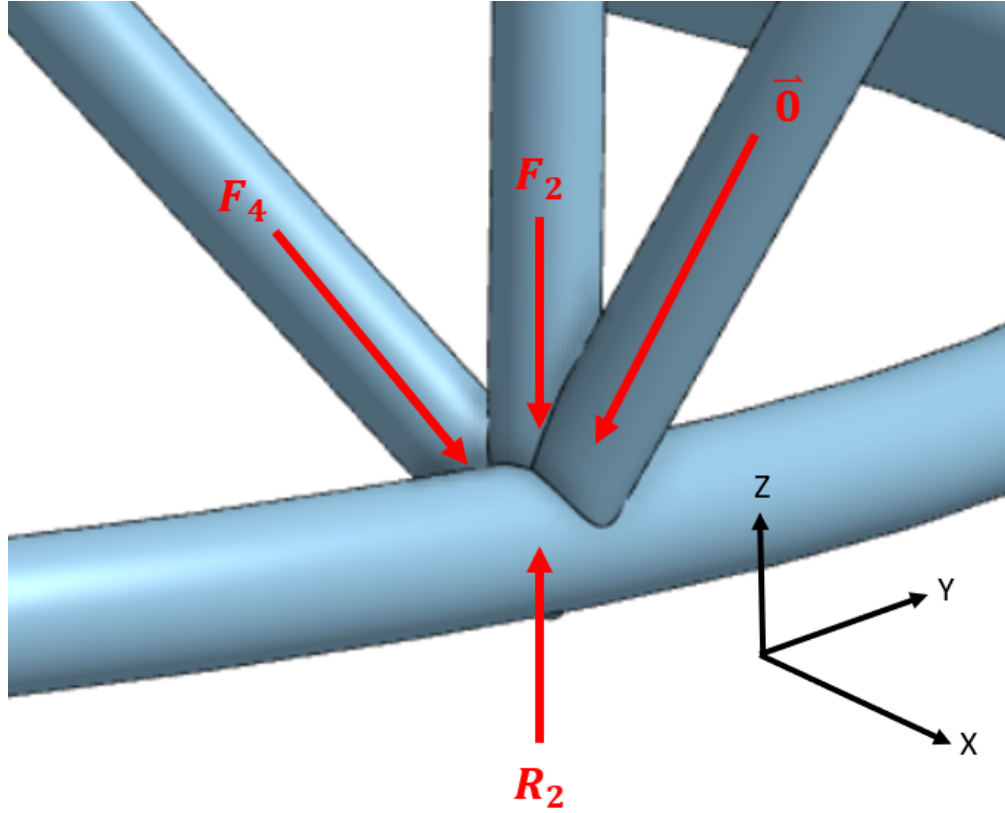


Figure 14.7: Free body diagram at View C.

Similar to the previous reaction, a zero force member is present due to no point load acting on the joint above the zero force member shown in Figure 14.7.

Summing the forces in the z-direction results in,

$$\Sigma F_z = 0 = R_{2,z} - F_{4,z} - F_{2,z} - 0 \quad (14.21)$$

The vertical reaction at View C can be solved,

$$R_{2,z} = 12889N \quad (14.22)$$

These reactions will be used to validate the FEA model to determine stresses and ensure yield does not occur. As a starting point, the necessary cross-section will be estimated. Since member 2 is primarily under axial loading, an adequate hollow circle cross-section will be analyzed and then applied to all other members as a starting point.

The axial load on member 2 was previously determined to be 9752 N. A safety factor of 1.25 against axial yield per NASA-STD-5001B [19]. From these values, a required cross-section can be determined by,

$$\sigma_y = FS \cdot \frac{F}{A} \quad (14.23)$$

where F is the axial force, σ_y is the yield stress of Aluminum 6061 T-6, FS is the factor of safety, and A is the cross-sectional area of the member. Solving for A results in a required cross section of 38.6 mm^2 . From standard circular tube sizing, this makes CHS 16 x 2 cross-section a sufficient choice to begin analyzing stresses.

This analytical calculation will make no further attempt to define stresses because of the lack of bending stress present in the calculation, which is likely to dominate the stresses in the mounting frame.

14.2 Finite Element Analysis

To better determine the stresses experienced by each member, ANSYS Mechanical will be utilized to conduct a static structural analysis to resolve maximum loading cases at launch on the mounting frame due to the mass of the seven STDs.

14.2.1 Model

In OnShape, the line structure from the frame model, shown in Figure 14.8 was imported into ANSYS and a hollow circular cross section of CHS 16 x 2 was assigned to all lines of the structure. The material used for the model was Aluminum 6061 T-6 because of its low density and high strength properties.

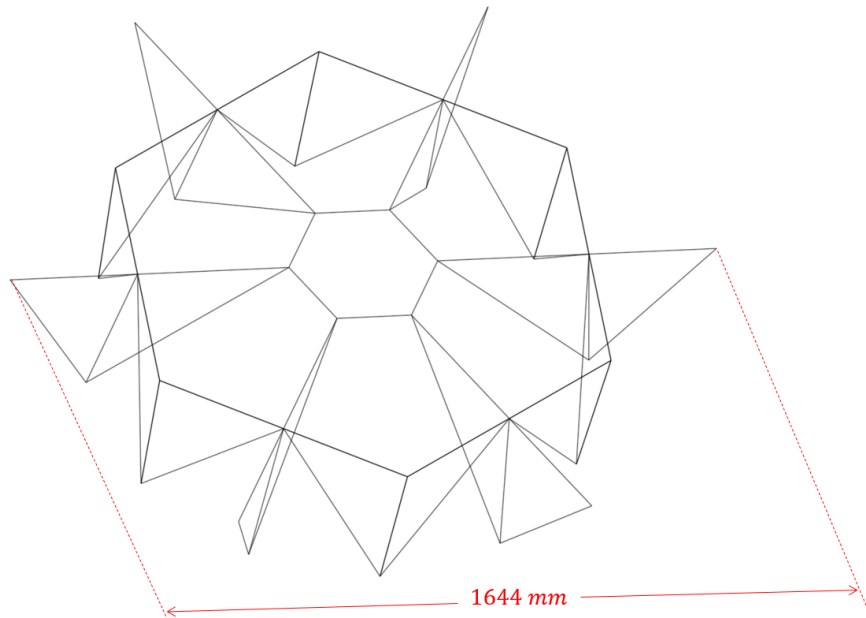


Figure 14.8: Line structure from OnShape to define model geometry.

14.2.2 Mesh

To create a mesh for the model, line elements were chosen due to the length of all members being much larger than the diameter of the cross-section. An element size of 4cm was used across all members of the frame to ensure accurate bending moment calculations across the length of high-stress members. No bias was used across any members. The generated mesh of the model with 1632 nodes and 840 elements is shown in Figure 14.9

14.2.3 Environment

To aid in determining if the model is accurate compared to that of the analytical solution. Point loads will be applied to the six outer vertices with magnitude of $m_{STD}(6g)$, 23544N, and a load of $\frac{1}{6}m_{STD}(6g)$, 3924N, to each of the vertices in the inner ring, shown in Figure 14.9. These loads will act purely in the vertical direction.

For supports, fixed supports were added to all 12 vertices at the base of the frame. Fixed supports were chosen because the frame will then be mounted to a ring structure that extends for the remainder of the kick stage structure. These reactions will hold the same nomenclature from the analytical calculation, R_1 and R_2 . Locations of the fixed supports are shown in Figure 14.10. The reaction forces in the z-direction will be probed from these points in order to validate the model.

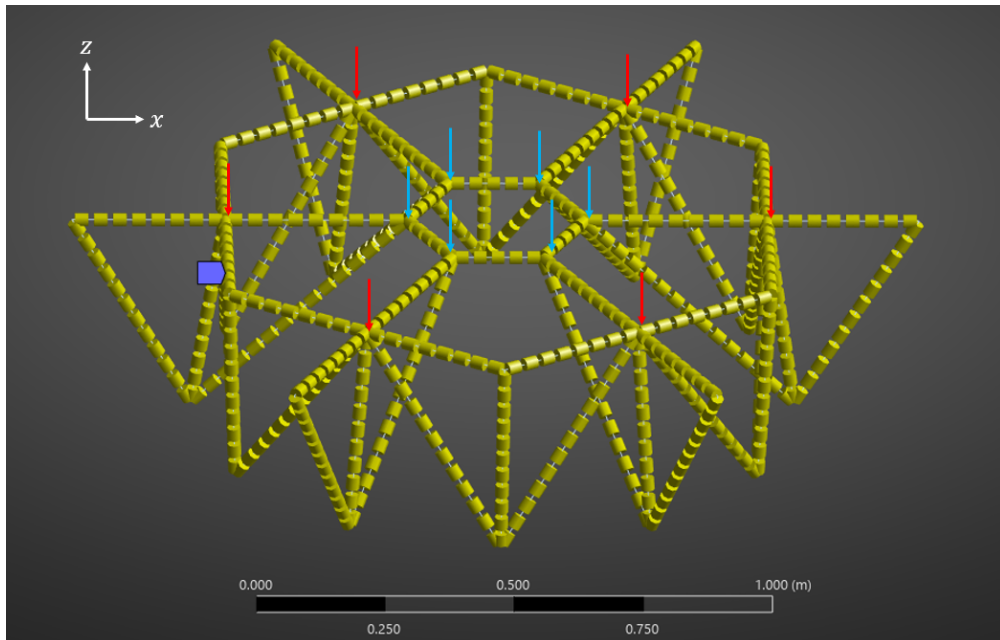


Figure 14.9: Mesh and applied loads on the kick stage frame. Red vectors denote load of 23544N. Blue vectors denote load of 3924N.

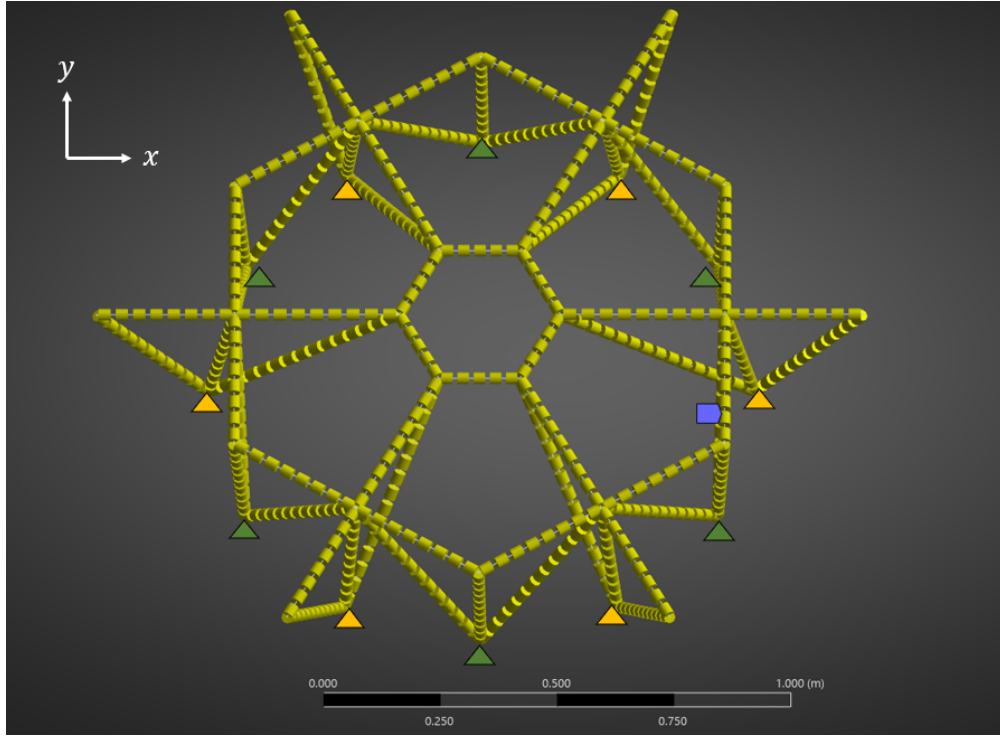


Figure 14.10: Fixed supports for ANSYS model. Green triangles denote locations of R_1 and orange triangles denote locations of R_2 .

14.2.4 Results

The static structure model was resolved, and as mentioned in the previous section, the reactions in the z-direction were probed to get the following results,

$$R_{1,z} = 14856N$$

$$R_{2,z} = 12612N$$

This closely aligns to those found at reactions $R_{1,z}$ (14579 N) and $R_{2,z}$ (12889 N) from the analytic calculation, suggesting that the system is modeled well.

Additional beam results were resolved from the model using the Beam Tool, which uses the calculated forces and bending moments in each line body and applies beam theory to resolve maximum and minimum normal stresses of each member. These stresses are visualized in Figures 14.11 and 14.12.

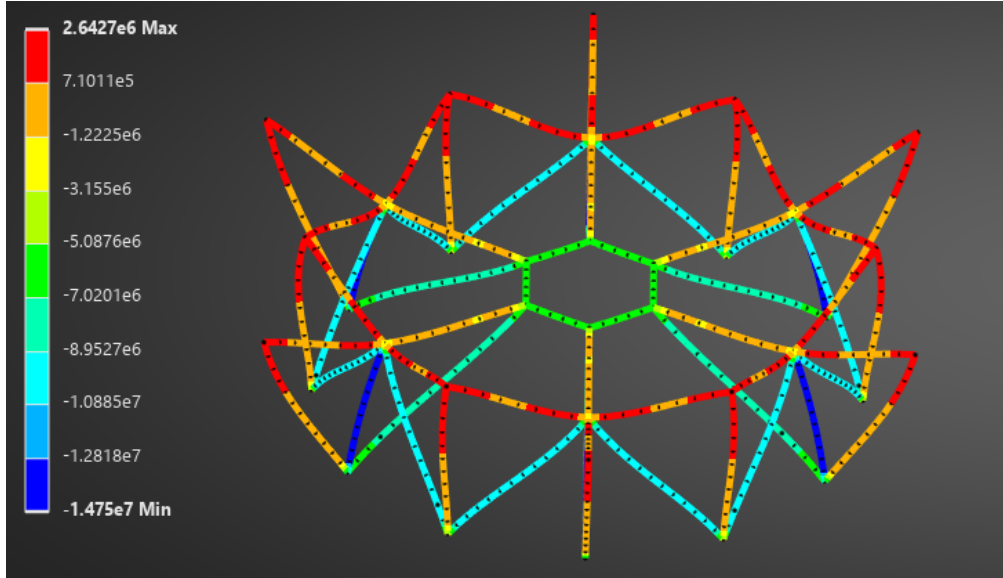


Figure 14.11: Maximum tensile stress from a vertical acceleration of 6g.

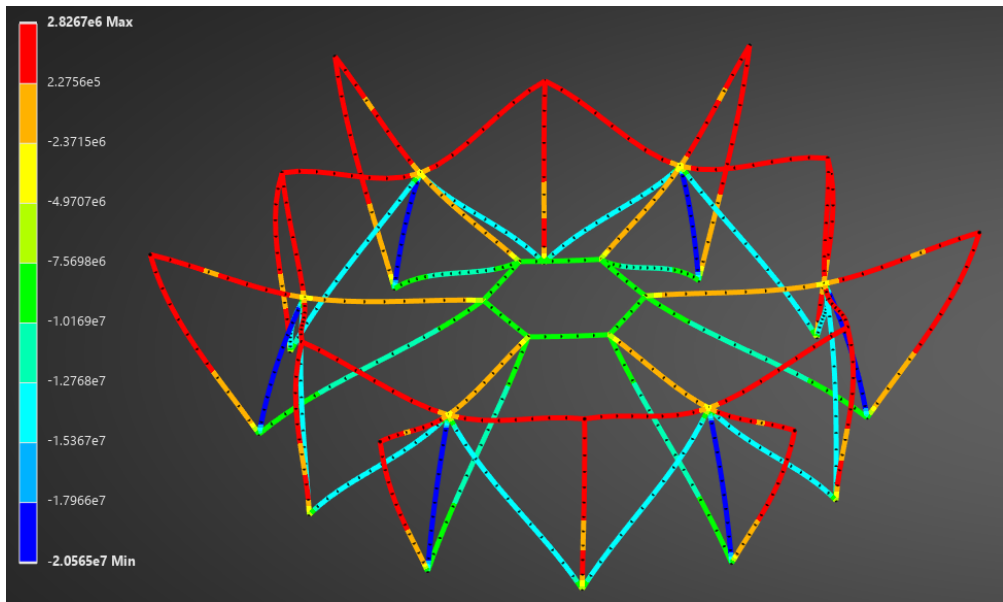


Figure 14.12: Maximum compressive stress from a vertical acceleration of 6g.

Next, the shearing force of the frame structure is shown in Figure 14.13. The magnitude of the shearing force is maximum at about 6N, and these shearing forces are present on members with lower normal stress magnitudes; therefore, they will be negated for this case. These forces will become non-negligible when lateral loading is incorporated.

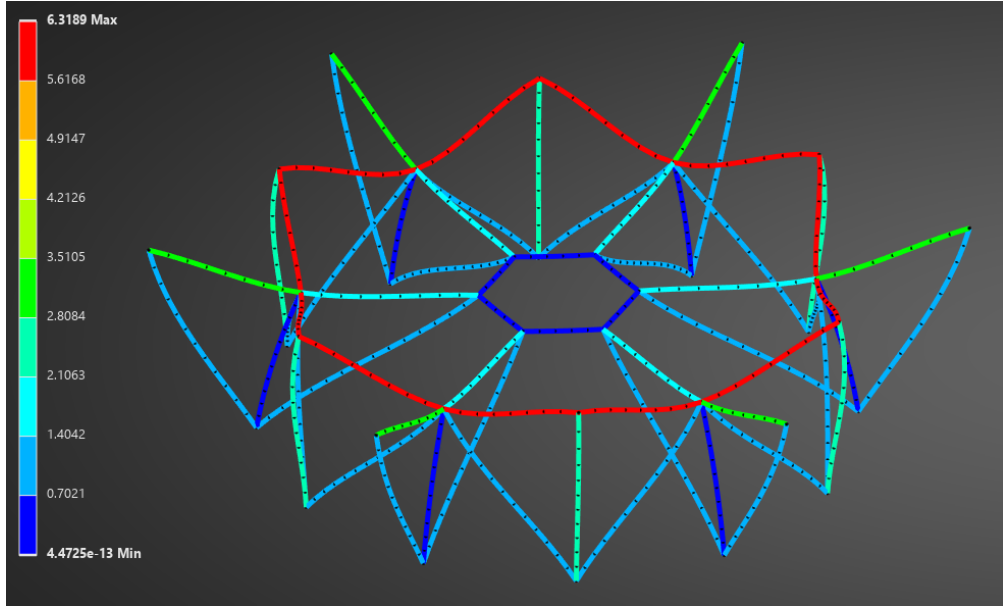


Figure 14.13: Shearing force in kick stage frame under 6g vertical loading.

From the vertical loading case, the members under compression experienced a maximum stress of 21 MPa. This is far below the yield stress of Aluminum 6061 T-6. However, before reducing the cross-section of the frame, lateral loads must be analyzed.

Another potential failure mode of the frame is buckling due to the slenderness of each member. Analyzing the axial forces through each member is shown in Figure 14.14, the two members colored blue are subject to a potential buckling failure. The maximum compressive stress can be calculated by,

$$P_{cr} = \frac{\pi^2 EI}{KL^2} \quad (14.24)$$

where P_{cr} is the critical buckling load, E is the Young's Modulus, I is the second moment of area, K is the effective length coefficient, and L is the length of the member. For the coefficient K , a value of 0.5 will be used since both ends are welded to resist rotation [105].

The second moment of area for a hollow circular cross section is given by,

$$I = \frac{\pi}{2}(r_o^4 - r_i^4) \quad (14.25)$$

where r_o and r_i are the outer and inner radii, respectively [105]. For cross section CHS 16 x 2, the second moment of area is $4.4 \times 10^{-9} m^4$. With the lengths 0.47 m and 0.38 m for members 1 and 2, respectively, the critical forces are calculated.

$$P_{cr,1} = 27089N \quad (14.26)$$

$$P_{cr,2} = 41441N \quad (14.27)$$

From Figure 14.14, the maximum compressive axial force is 1800N, so there is a significant margin against buckling.

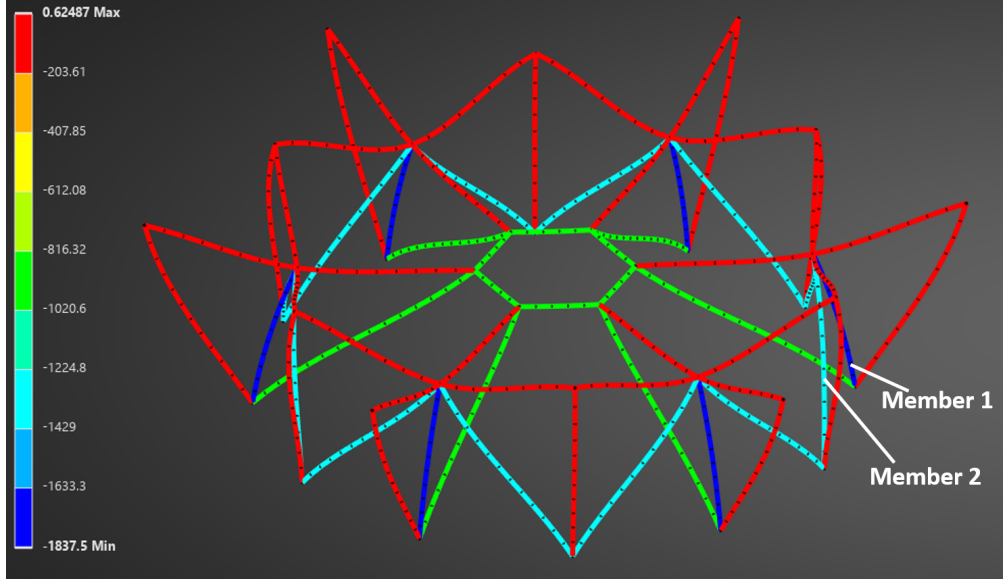


Figure 14.14: Axial forces in kick stage frame under 6g acceleration loads.

14.2.5 Lateral Loading

To ensure the design is structurally sound, the effects of lateral acceleration should be considered per the Falcon 9 User Guide [20].

The inertial load vector on the frame will have a lateral component and a vertical component. From Figure 12.1, a likely high stress case is that at 2g of vertical acceleration (z-direction) and 3.5g of lateral acceleration. The lateral acceleration will be considered across two cases, shown in Figure 14.15. These direction were chosen because it is expected to put peak stress on the members that are in the plane that is formed by the acceleration vector and the z-axis.

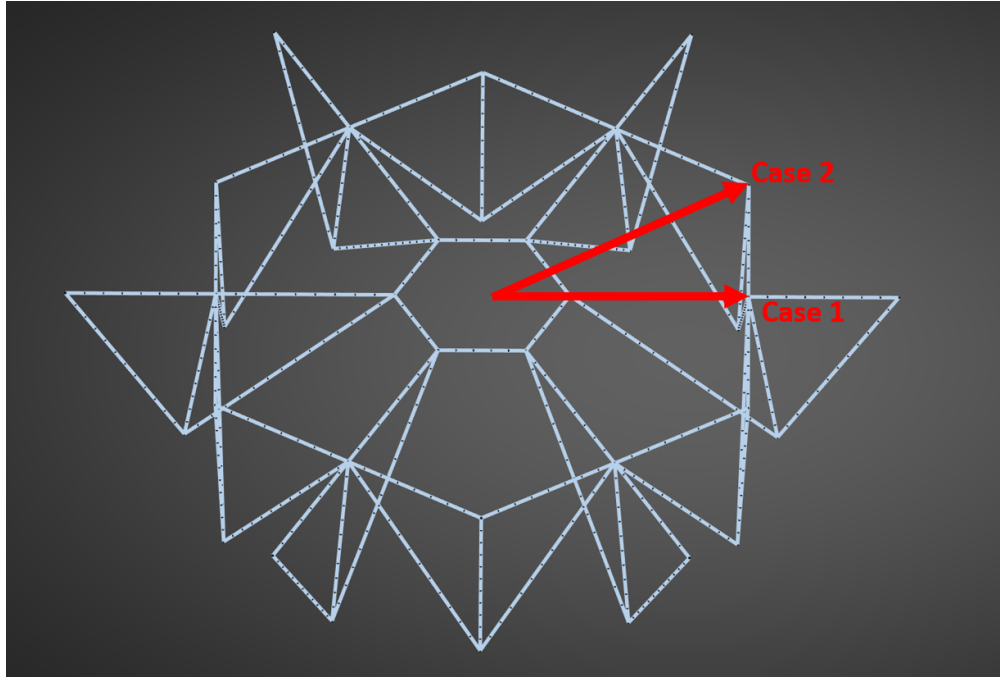


Figure 14.15: Lateral acceleration direction for Case 1 and Case 2 for launch acceleration of 2g vertical and 3.5g lateral.

Calculating the loads in each direction by,

$$\vec{F} = -m_{STD}\vec{a} \quad (14.28)$$

where m_{STD} is the mass of an STD and \vec{a} is defined by,

$$\vec{a} = 3.5\hat{i} + 2\hat{k} \quad (14.29)$$

where the direction \hat{i} is general to the lateral acceleration directions in Figure 14.15. The resulting inertial load due to a single STD is,

$$\vec{F} = (-13734\hat{i} - 7848\hat{k})N \quad (14.30)$$

The model methodology will remain the same as the vertical acceleration case for geometry, mesh, load application points, and fixed supports. It will only differ by the input loads.

14.2.6 Lateral Loading Results

For lateral loading Case 1, the maximum (tension) and minimum (compressive) combined stresses were tabulated for each member; the results are shown in Figure 14.16 for the maximum tensile stresses and in Figure 14.17 for the maximum compressive stresses.

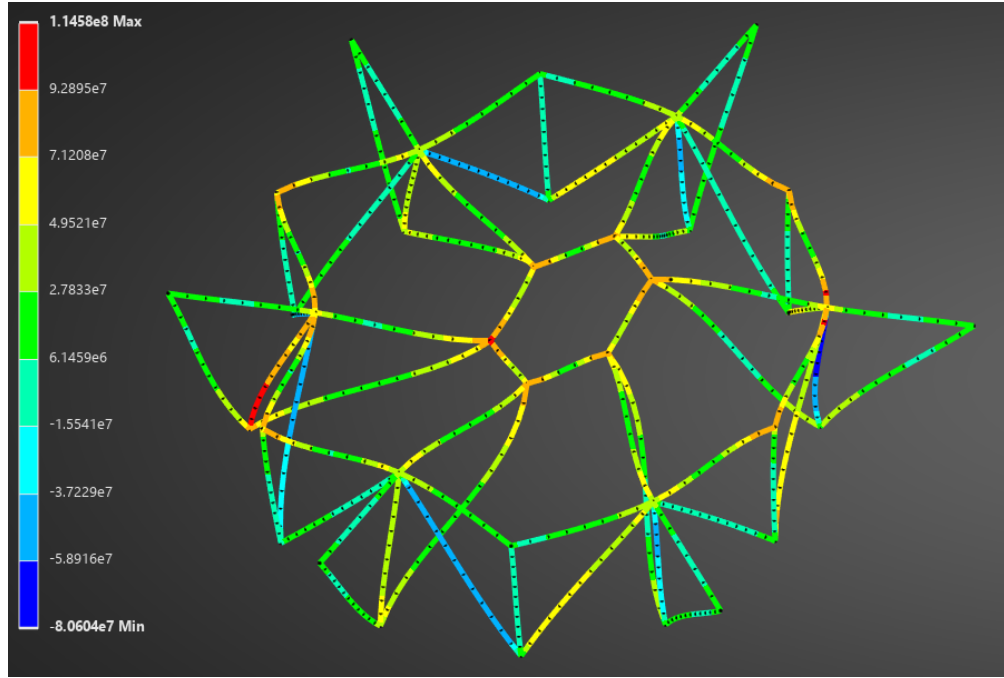


Figure 14.16: Maximum Tensile Stress from accelerations of 3.5g lateral and 2g vertical for Case 1.

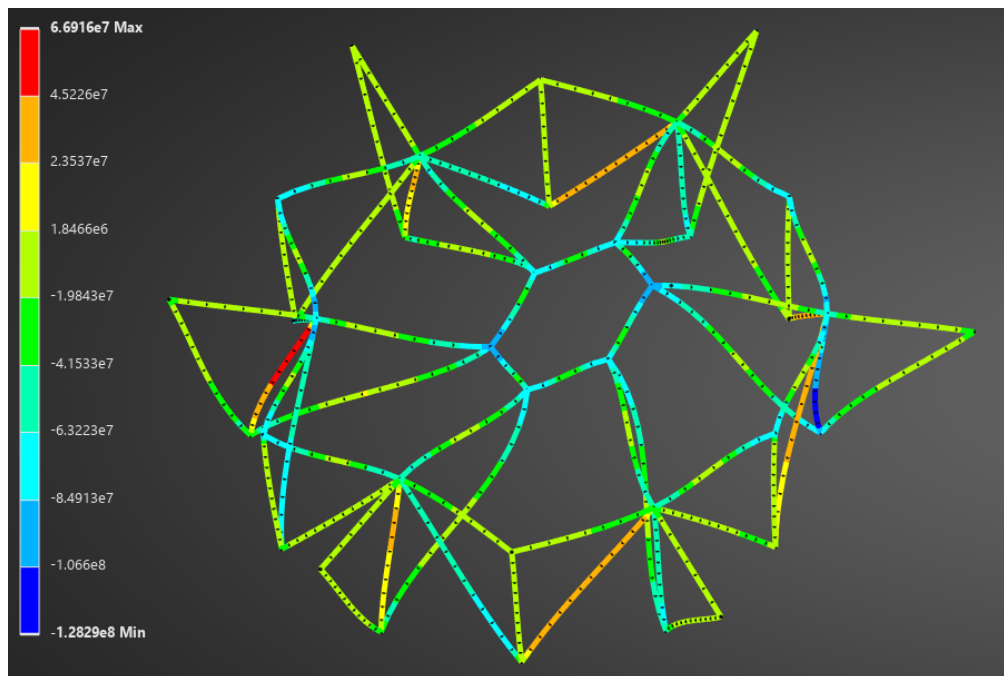


Figure 14.17: Maximum Compressive Stress from accelerations of 3.5g lateral and 2g vertical for Case 1.

Similarly, the results for Case 2 are shown in Figure 14.18 for the maximum tensile stresses

and in Figure 14.19 for the maximum compressive stresses.

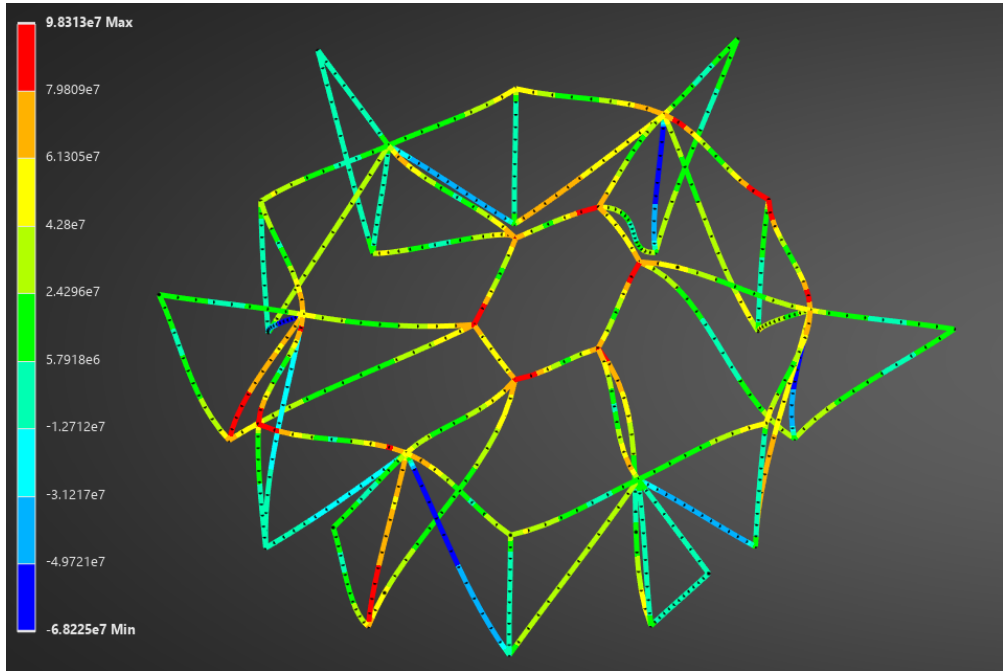


Figure 14.18: Maximum Tensile Stress from accelerations of 3.5g lateral and 2g vertical for Case 2.

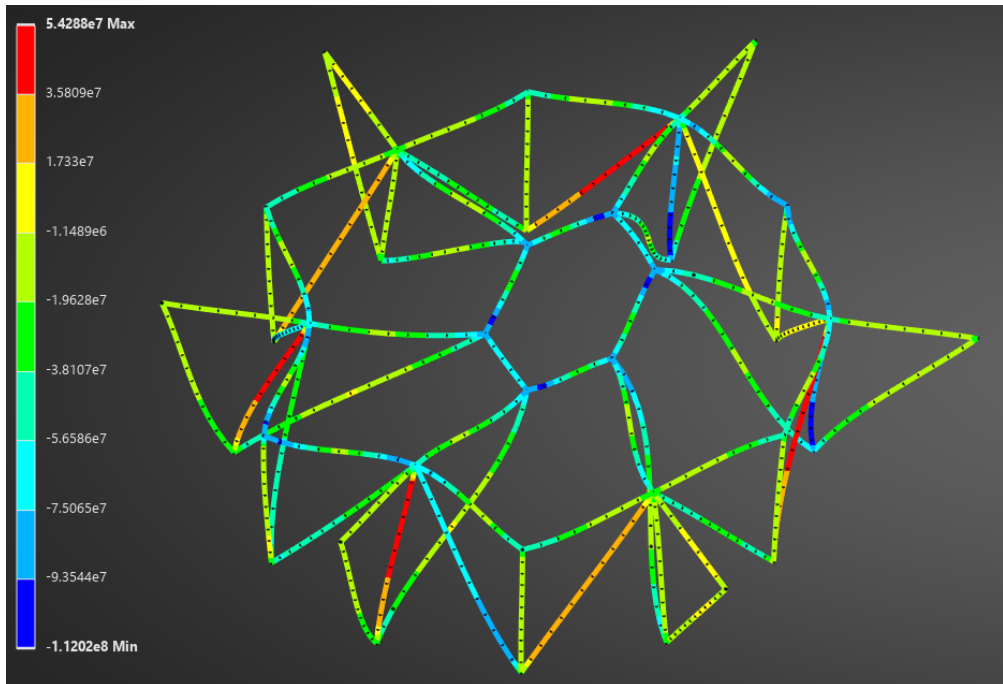


Figure 14.19: Maximum Compressive Stress from accelerations of 3.5g lateral and 2g vertical for Case 2.

As shown, the max stress was seen in Case 1 with a maximum tensile stress of 115 MPa and the maximum compressive stress of 128 MPa. As expected, the lateral loading cases result in higher shearing forces compared to the vertical loading. The shearing forces for Case 1 and Case 2 are shown in Figure 14.20 and 14.21, respectively.

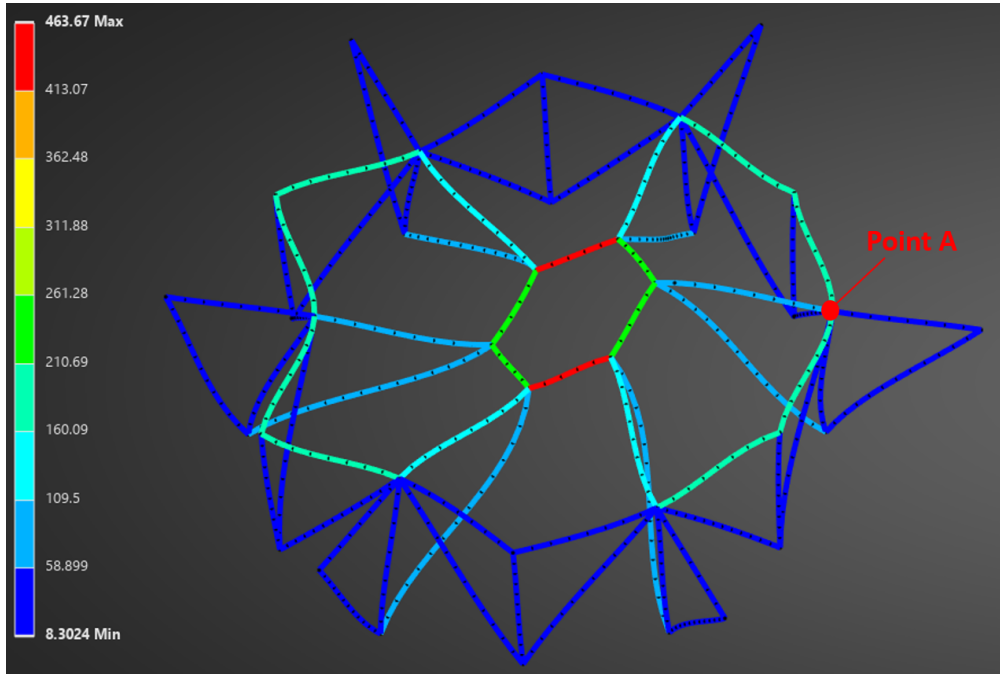


Figure 14.20: Shearing force in frame under lateral loading Case 1.

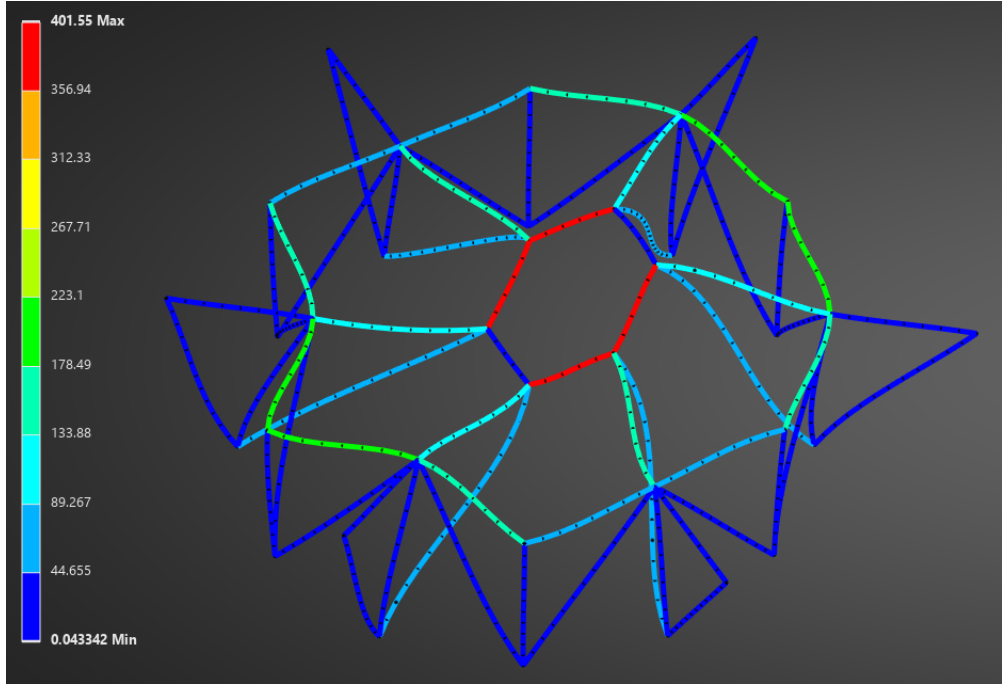


Figure 14.21: Shearing force in frame under lateral loading Case 2.

When comparing Cases 1 and 2, Case 1 has higher normal stresses and shear forces. Therefore, Case 1 will be considered for von Mises failure criterion,

$$\sigma_v = \sqrt{\frac{1}{2} [(\sigma_x - \sigma_y)^2 + (\sigma_y - \sigma_z)^2 + (\sigma_z - \sigma_x)^2 + 6(\tau_{xy}^2 + \tau_{yz}^2 + \tau_{zx}^2)]} \quad (14.31)$$

where σ_i are normal stresses and τ_{ij} are shear stresses. In this beam analysis, the only significant stresses are normal stress from bending moments, normal stress from axial loading, and shear stress from transverse loading. This simplifies Equation 14.31 to,

$$\sigma_v = \sqrt{\sigma^2 + 3\tau^2} \quad (14.32)$$

Where σ is the total normal stress and τ is the shear stress from transverse loading. The normal stresses have been determined directly from Figure 14.17. Shear stress can be evaluated by,

$$\tau = \frac{VQ}{Ib} \quad (14.33)$$

where V is the shear force, Q is the first moment of area, I is the second moment of area, and b is the width of the cross-section. The max shear stress from a transverse load exists at the neutral axis of the cross-section. Evaluating at this location, the first moment of area is given by,

$$Q_{max} = \frac{2}{3}(R_o^3 - R_i^3) \quad (14.34)$$

where R_o is the outer radius and R_i is the inner radius. The second moment of area is given by,

$$I = \frac{\pi}{2}(R_o^4 - R_i^4) \quad (14.35)$$

and b is twice the wall thickness of the circular tube.

Point A from Figure 14.20 will be evaluated for its failure criterion because it is a location of high normal stress and shear stress relative to the entire frame. Using the shear force at point A, 210N, Equation 14.33 evaluates to 2.4 MPa. Using this value and the normal stress of 107 MPa at this point in Equation 14.32, results in 107.1 MPa. This result is very close to the normal stress in the beam, therefore, the von Mises stress will be approximated by the normal combined stress.

The maximum stress magnitude for this loading case is 128 MPa, which has a large margin from the desired safety factor of 1.25 for yielding, therefore, a weight reduction can be investigated.

14.3 Reduced Cross Section

From Section 14.2.6 a safety factor of 2.15 against compressive yield, therefore, a reduction in the cross section may be investigated to achieve the desired safety factor of 1.25 against compressive yield and 1.4 against buckling, per NASA-STD-5001B [19].

To determine a desirable cross section, Case 1 of Section 14.2.6 will be reanalyzed in the same manner while decreasing the wall thickness. A cross-section of CHS 16 x 1 was used for this new calculation.

The results with this new cross-section in Figure 14.22 show that maximum compressive normal stresses in the frame increase to 224 MPa. This provides a good safety factor of 1.23 against compressive yield.

To check for buckling failure, the axial forces in each member with the reduced wall thickness are shown in Figure 14.23.

The maximum compressive force in Figure 14.23 in members 1 and 2 from 14.26 and 14.27, respectively, are 5300N and 6700N, respectively. With the reduced cross-section, the critical load must be reevaluated because the second moment of area has decreased to $2.66 \times 10^{-9} m^4$. The new critical buckling loads are,

$$P_{cr,2} = 16376N \quad (14.36)$$

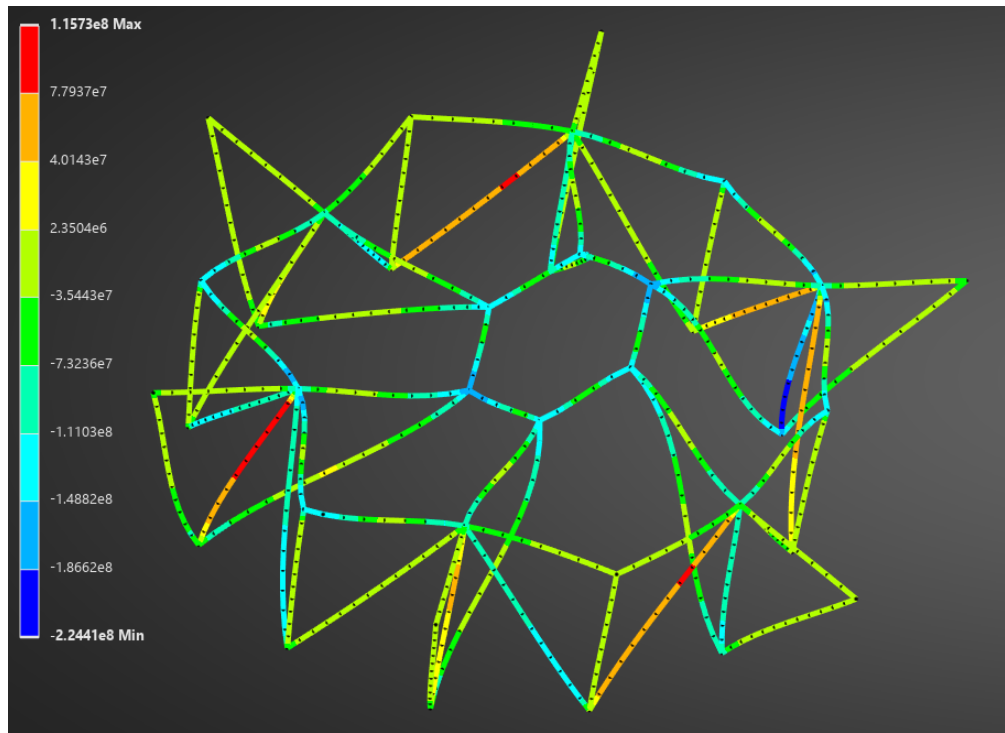


Figure 14.22: Maximum compressive stresses in Case 1 lateral loading with a cross section of CHS 16 x 1.

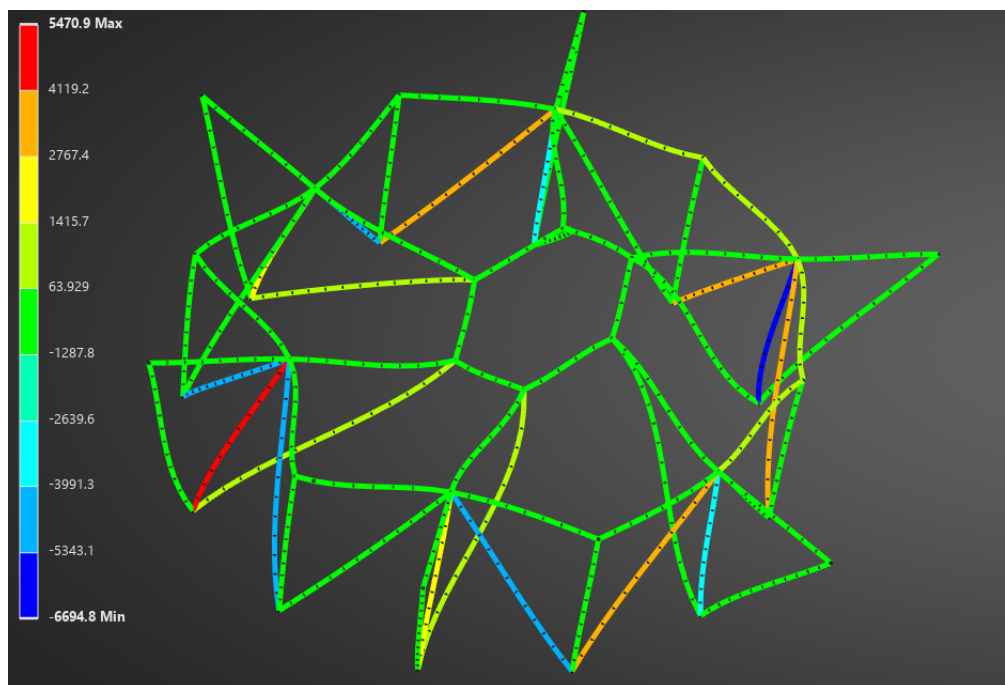


Figure 14.23: Axial forces in Case 1 lateral loading with a cross section of CHS 16 x 1.

$$P_{cr,2} = 25053N \quad (14.37)$$

The max loads are well below the critical loads, therefore, buckling will not be a concern for the structural integrity of the kick stage frame.

14.4 Summary

The results of the finite element analysis have shown that the frame is functional in bearing the weight of seven STDs mounted through launch with aluminum 6061 T-6 members with a consistent cross-section of CHS 16 x 1. The frame has a safety factor of 1.23 against axial yield with this cross-section, and critical buckling loads were confirmed to have a significant margin. This model was validated by the preceding analytical solution. Therefore, the design of the frame can be used going forward for higher assembly analyses to ensure a functional satellite de-orbiter system.

15 STD Structural analysis

The structure of the STD must provide rigid support for its internal components, including the RCS system, fuel tank, propulsion system, and engine. Beyond simply housing these systems, the structure must ensure rigidity and durability, preventing deformation or failure during mission operations. The most significant loads the STD will experience occur during launch, where it must withstand the extreme acceleration forces as outlined in Figure 12.1.

A key design challenge in space missions is balancing this robust design that is able to withstand mechanical loads during its operation with a lightweight construction. A frame structure is an effective solution, as it distributes loads efficiently while keeping overall weight low, making it well-suited for both launch resilience and orbital operations.

15.1 Preliminary Design of STD Structure

Preliminary design of the STD structure models it as three thin-walled hexagonal prisms, interconnected by a frame of CHS beams, as shown in Figure 15.1. This configuration was selected to facilitate stacking on the kick stage. The initial dimensions of the STD are displayed in Figures 15.2 and 15.3, and are based on prior sizing for the STD fuel tank size, nozzle geometry, kick stage size, as well as the payload fairing of the Falcon 9 launch vehicle [20]. The hexagonal prisms will include cutouts to accommodate internal components.

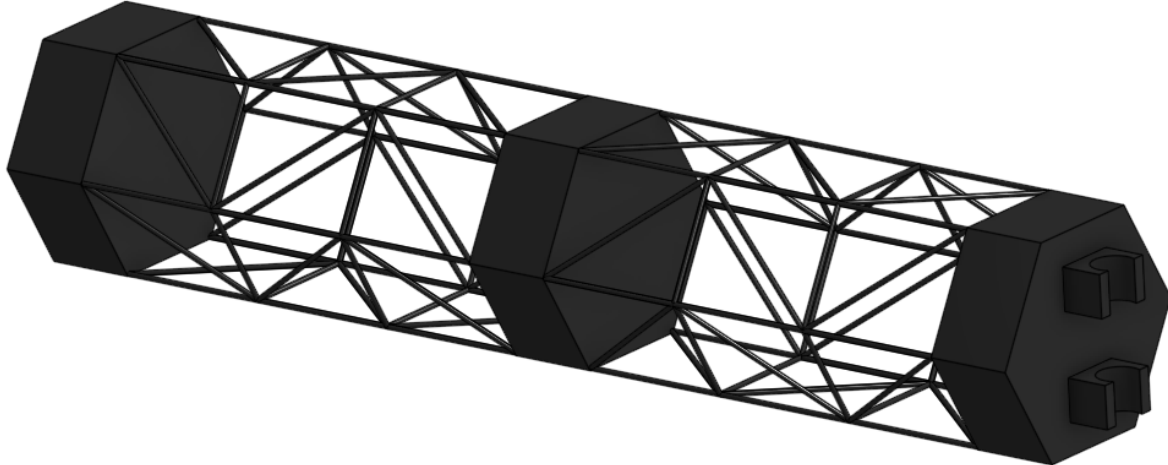


Figure 15.1: Preliminary CAD of the STD structure.

15.2 Launch Forces on STD

Figure 15.4 displays the preliminary configuration of the internal components within the STD structure. These internal components all have a mass that will exert an inertial force on the STD structure due to the extreme acceleration these masses experience during launch, given by

$$\vec{F} = -m \cdot \vec{a} \quad (15.1)$$

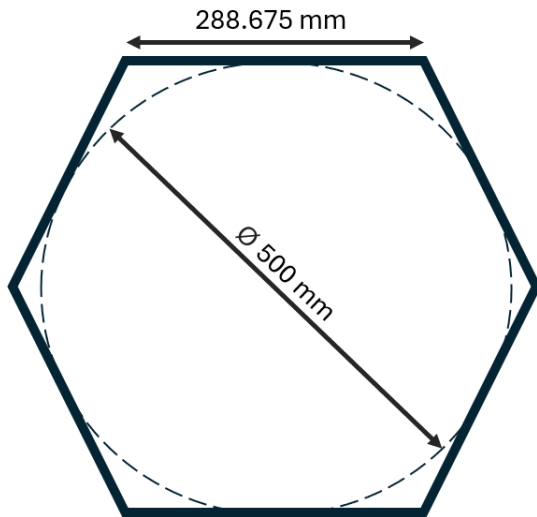


Figure 15.2: STD cross-sectional dimensions.

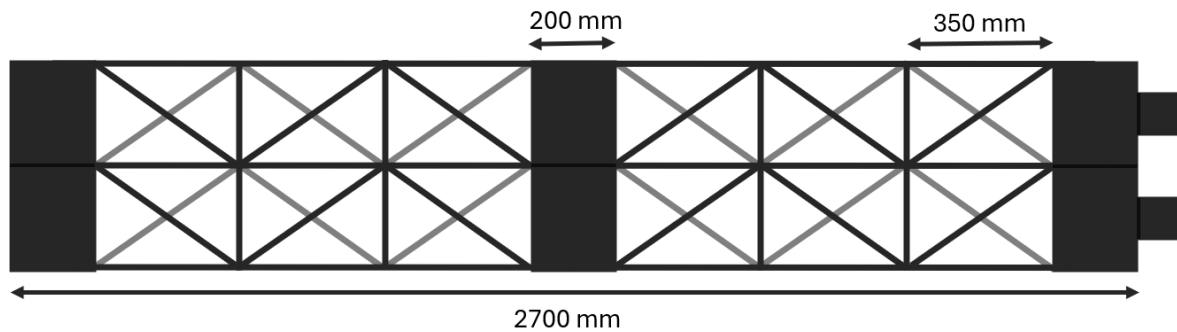


Figure 15.3: STD longitudinal dimensions.

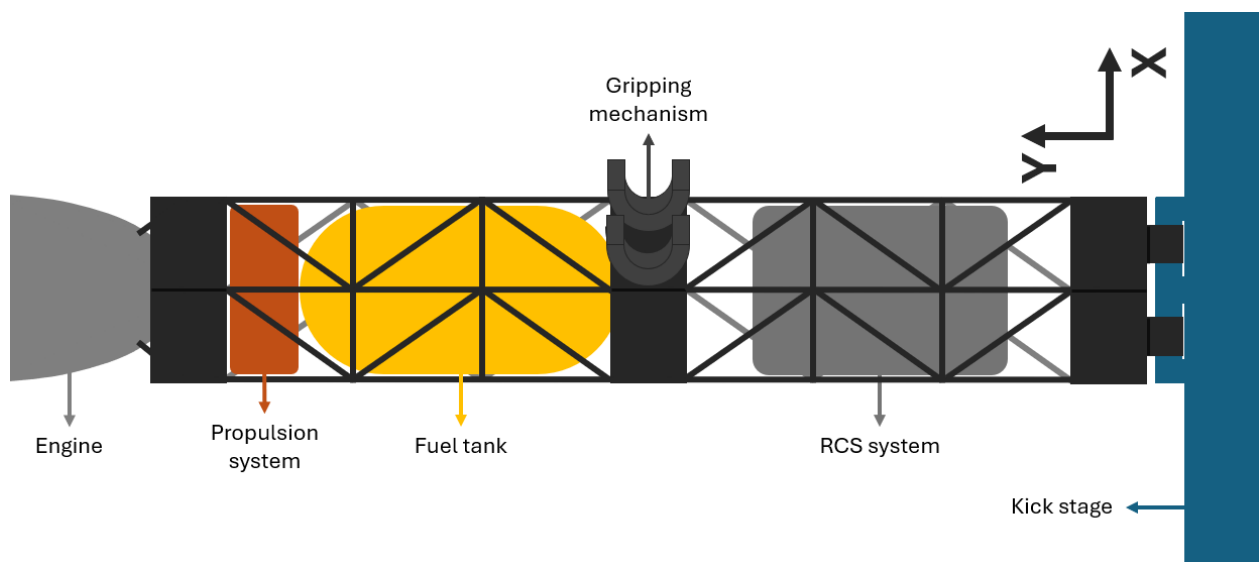


Figure 15.4: STD with its internal components.

Figure 12.1 indicates two critical combinations of lateral (in the xz-plane) and axial (in y-direction) accelerations that must be analyzed: $(0.5, 6)g$ and $(2, 3.5)g$. These launch accelerations are static equivalents, meaning that a static analysis of the STD can be performed using these accelerations. A free-body diagram of the STD is shown in Figure 15.5. The reaction force of the kick stage on the STD can be calculated using

$$\begin{aligned}\sum \vec{F} &= 0 \\ \vec{F}_{\text{kick}} + \vec{F}_{\text{engine}} + \vec{F}_{\text{tank}} + \vec{F}_{\text{propsys}} + \vec{F}_{\text{capture}} + \vec{F}_{\text{RCS}} + \vec{F}_{\text{structural}} + \vec{F}_{\text{fuel}} &= 0 \quad (15.2) \\ \vec{F}_{\text{kick}} - \vec{a} \cdot (m_{\text{engine}} + m_{\text{tank}} + m_{\text{propsys}} + m_{\text{capture}} + m_{\text{RCS}} + m_{\text{structural}} + m_{\text{fuel}}) &= 0\end{aligned}$$

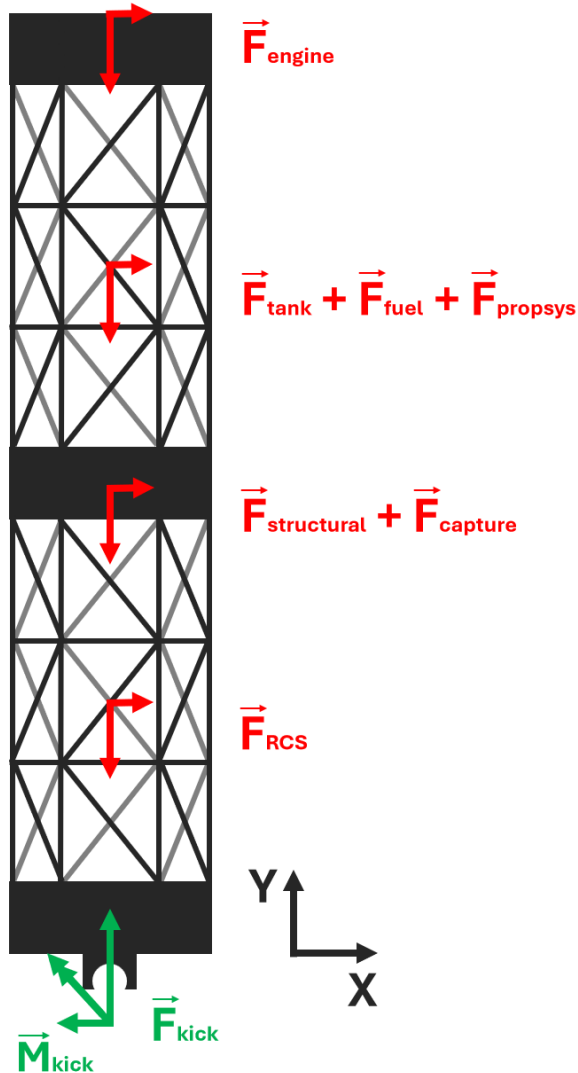


Figure 15.5: Free-body diagram of STD structure during launch.

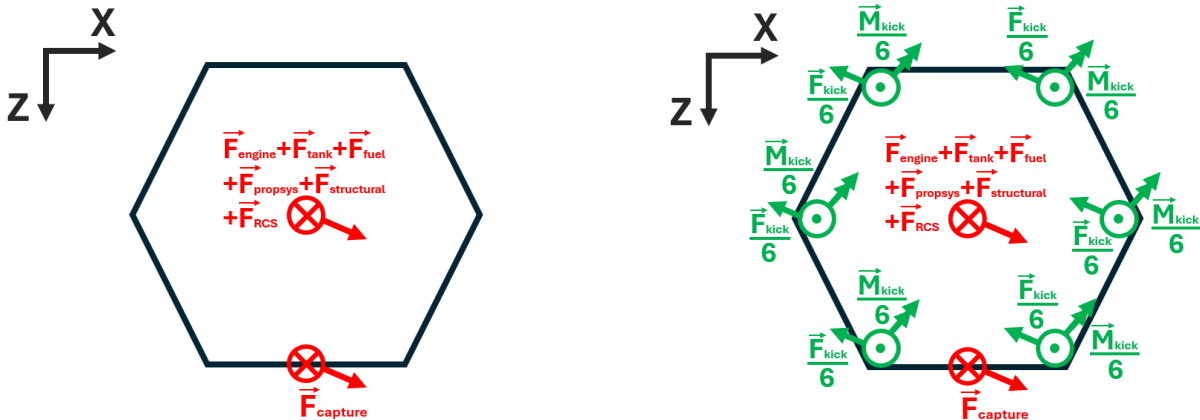
The forces acting on the STD are summarized in the Table 15.1.

Table 15.1: Forces acting on the STD structure during launch.

Component	mass [kg]	(0.5, 6)g		(2, 3.5)g	
		Lateral force [kN]	Axial force [kN]	Lateral force [kN]	Axial force [kN]
Engine	25	0.123	1.472	0.491	0.858
Fuel tank	25	0.123	1.472	0.491	0.858
Propulsion system	35	0.172	2.060	0.687	1.202
Capturing mechanism	15	0.074	0.883	0.294	0.515
RCS system	30	0.147	1.766	0.589	1.030
Structural	50	0.245	2.943	0.981	1.717
Fuel	215	1.055	12.655	4.218	7.382
Kick stage reaction		1.937	23.250	7.750	13.562

To determine the reaction moment exerted by the kick stage on the STD, the force application points must be more precisely defined. It is assumed that all internal components—except for the capturing mechanism—are centered along the central axis of the STD. The capturing mechanism, however, is mounted along the side of the middle hexagonal prism. The top-view locations of the resulting forces are illustrated in Figure 15.6a.

The bottom hexagonal prism of the STD, where the kick stage reaction force is applied, is connected to the rest of the structure by six CHS beams. It is assumed that the total reaction force from the kick stage is distributed equally among these six beams, meaning each beam carries $\frac{1}{6}$ of the total reaction force. Similarly, the reaction moment is assumed to be shared equally across the six beams as well. Although these assumptions introduce some inaccuracy—since the capturing mechanism causes a slight asymmetry—they provide reasonable approximation for preliminary analysis. The assumed reaction forces and moments are shown in Figure 15.6b.



(a) Top view of the STD showing internal force locations.

(b) Top view of the STD showing kick stage reaction forces and moments.

Figure 15.6: Force distribution and reaction forces on the STD structure.

The moment equation is taken about the center of the top face of the bottom prism. Table 15.2 summarizes the locations of the forces acting on the STD relative to this reference point.

Table 15.2: Locations of forces relative to reference point.

Component	Approximate Location		
	x [m]	y [m]	z [m]
Beam 1	0.2500	0	0
Beam 2	0.1250	0	0.2165
Beam 3	-0.1250	0	0.2165
Beam 4	-0.2500	0	0
Beam 5	-0.1250	0	-0.2165
Beam 6	0.1250	0	-0.2165
Engine	0	2.5000	0
Fuel tank	0	1.7750	0
Propulsion system	0	1.7750	0
Capturing mechanism	0	1.1500	-0.2500
RCS system	0	0.5250	0
Structural	0	1.1500	0
Fuel	0	1.7750	0

Since the lateral forces can act along any direction within the xz-plane, a parametric study was conducted to determine the worst-case lateral loading direction. The study showed that when the lateral acceleration acts along the positive z-axis, the resulting moment in the xz-plane is maximized. Conversely, when the lateral acceleration acts along the x-axis, the resulting torsional load due to the lateral force of the capturing mechanism on the STD is maximized. Based on these findings, the applied forces on the STD can be more precisely defined, as outlined in Tables 15.3 and 15.4.

Table 15.3: Forces leading to maximum bending moment on the STD structure.

Component	(0.5, 6)g			(2, 3.5)g		
	F_x [kN]	F_y [kN]	F_z [kN]	F_x [kN]	F_y [kN]	F_z [kN]
Engine	0	-1.472	-0.123	0	-0.858	-0.491
Fuel tank	0	-1.472	-0.123	0	-0.858	-0.491
Propulsion system	0	-2.060	-0.172	0	-1.202	-0.687
Capturing mechanism	0	-0.883	-0.074	0	-0.515	-0.294
RCS system	0	-1.766	-0.147	0	-1.030	-0.589
Structural	0	-2.943	-0.245	0	-1.717	-0.981
Fuel	0	-12.655	-1.055	0	-7.382	-4.218
Kick stage reaction	0	23.250	1.937	0	13.562	7.750

Table 15.4: Forces leading to maximum torsional moment on the STD structure.

Component	(0.5, 6)g			(2, 3.5)g		
	F_x [kN]	F_y [kN]	F_z [kN]	F_x [kN]	F_y [kN]	F_z [kN]
Engine	-0.123	-1.472	0	-0.491	-0.858	0
Fuel tank	-0.123	-1.472	0	-0.491	-0.858	0
Propulsion system	-0.172	-2.060	0	-0.687	-1.202	0
Capturing mechanism	-0.074	-0.883	0	-0.294	-0.515	0
RCS system	-0.147	-1.766	0	-0.589	-1.030	0
Structural	-0.245	-2.943	0	-0.981	-1.717	0
Fuel	-1.055	-12.655	0	-4.218	-7.382	0
Kick stage reaction	1.937	23.250	0	7.750	13.562	0

Finally, the total reaction moment at the base of the STD can be determined by summing the moments generated by each applied force about the center of the bottom prism, as given by

$$\vec{M}_{\text{total}} = \sum_i \vec{r}_i \times \vec{F}_i \quad (15.3)$$

where \vec{r}_i is the position vector from the reference point to the location of the i^{th} force \vec{F}_i . In this case, the total moment exerted on the STD by the kick stage and internal components becomes

$$\begin{aligned} \vec{M}_{\text{kick}} = & \vec{r}_1 \times \frac{\vec{F}_{\text{kick}}}{6} + \vec{r}_2 \times \frac{\vec{F}_{\text{kick}}}{6} + \vec{r}_3 \times \frac{\vec{F}_{\text{kick}}}{6} + \vec{r}_4 \times \frac{\vec{F}_{\text{kick}}}{6} + \vec{r}_5 \times \frac{\vec{F}_{\text{kick}}}{6} + \vec{r}_6 \times \frac{\vec{F}_{\text{kick}}}{6} \\ & + \vec{r}_{\text{engine}} \times \vec{F}_{\text{engine}} + \vec{r}_{\text{tank}} \times \vec{F}_{\text{tank}} + \vec{r}_{\text{propsys}} \times \vec{F}_{\text{propsys}} + \vec{r}_{\text{capture}} \times \vec{F}_{\text{capture}} \\ & + \vec{r}_{\text{RCS}} \times \vec{F}_{\text{RCS}} + \vec{r}_{\text{structural}} \times \vec{F}_{\text{structural}} + \vec{r}_{\text{fuel}} \times \vec{F}_{\text{fuel}} \end{aligned} \quad (15.4)$$

The resulting reaction moments for the two critical loading cases are summarized in Table 15.5.

Table 15.5: Calculated reaction moments at the STD base under critical load cases.

Loading Case		M_x [kNm]	M_y [kNm]	M_z [kNm]
(0.5, 6)g	Max Bending	-3.365	0	0
	Max Torsion	-0.221	0.018	3.145
(2, 3.5)g	Max Bending	-12.708	0	0
	Max Torsion	-0.129	0.074	12.579

Table 15.6 summarizes the total kick stage reaction forces and moments acting on the STD for both maximum bending and maximum torsional loading cases.

Table 15.6: Summary of kick stage reaction forces acting on STD.

Loading Case		Reaction Force [kN]			Reaction Moment [kNm]		
		F_x	F_y	F_z	M_x	M_y	M_z
(0.5, 6)g	Max Bending	0	23.250	1.937	-3.365	0	0
	Max Torsion	1.937	23.250	0	-0.221	0.018	3.145
(2, 3.5)g	Max Bending	0	13.562	7.750	-12.708	0	0
	Max Torsion	7.750	13.562	0	-0.129	0.074	12.579

15.3 Cross-Sectional Area of STD Frame Bars

Detailed analysis of the STD frame structure requires an initial estimate of the cross-sectional area of the frame bars to ensure they can withstand the loading experienced during launch. Assuming that all six bars connected to the bottom prism of the STD collectively support the kick stage reaction force and moment, the required cross-sectional area of the bars can be estimated. Three structural checks are required: the bars must withstand the axial stress, bending stress, and shear stress induced by the kick stage reaction force and moment. A safety factor SF of 2 is applied to all checks.

The frame bars are designed as circular hollow section (CHS) beams, with a chosen inner radius of 7.00 mm. Hollow tubes were selected over solid bars to improve the structure's resistance to vibration while maintaining a low mass. The STD structure is manufactured out of Ti-6Al-4V, with its material properties outlined in Table 12.1.

15.3.1 Axial stress

The axial loading configuration is illustrated in Figure 15.7

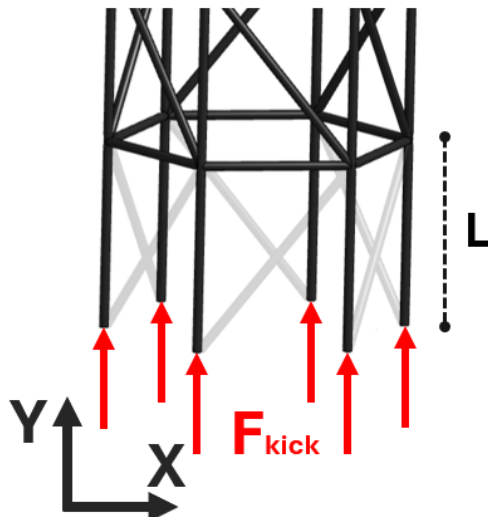


Figure 15.7: Axial loading configuration on STD.

The critical acceleration that results in the highest axial force is $6g$. Since this force is compressive, both a simple compressive strength check and a buckling analysis must be performed. Compressive loading can lead to buckling instability even when the material's yield strength is not exceeded, making it a potentially more critical design constraint.

For a purely compressive (non-buckling) scenario, the required cross-sectional area and corresponding outer radius can be calculated using

$$A = \frac{F_{\text{kick}}}{\frac{\sigma_y}{SF}} = 8.81 \text{ mm}^2 \quad (15.5)$$

$$r_o = 7.20 \text{ mm} \quad (15.6)$$

To assess the risk of buckling, the Euler buckling equation is given by [106]

$$\sigma_{cr} = \frac{\pi^2 \cdot E}{(K \cdot \frac{L}{r_g})^2} \quad (15.7)$$

where r_g is the radius of gyration, given by

$$r_g = \sqrt{\frac{I}{A}} = \sqrt{\frac{r_o^2 + r_i^2}{4} + \rho L r_{\text{STD}}^2} \quad (15.8)$$

The moment of inertia I includes both the geometric moment of inertia about the central axis and the Steiner term,

$$I = 6 \cdot (I_y + m \cdot r_{\text{STD}}^2) = 6 \cdot \left(\frac{\pi}{4} (r_o^4 - r_i^4) + m \cdot r_{\text{STD}}^2 \right) \quad (15.9)$$

The effective length factor K , which depends on the support and loading conditions, is determined to be 1.20 based on Figure 15.8. The bar length L is limited to 350 mm due to lateral support beams.

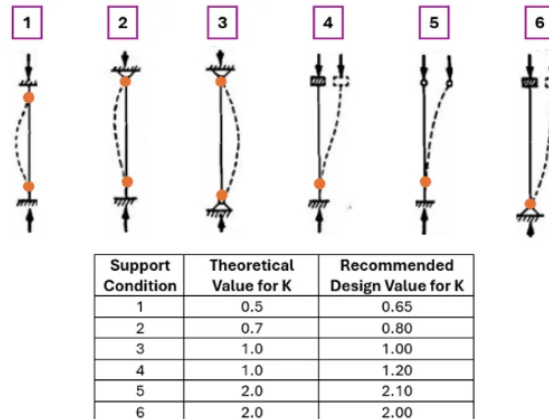


Figure 15.8: Effective length factor K for various support conditions [107].

The critical stress σ_{cr} is the stress the bar must be able to withstand to prevent buckling, and can be approximated using

$$\sigma_{cr} = \frac{F_{\text{kick}}}{A} = \frac{F_{\text{kick}}}{6\pi(r_o^2 - r_i^2)} \quad (15.10)$$

The outer radius of the bars in the frame can then be determined using

$$\frac{SF \cdot F_{\text{kick}}}{6\pi(r_o^2 - r_i^2)} = \frac{\pi^2 \cdot E \cdot (\frac{r_o^2 + r_i^2}{4} + \rho L r_{\text{STD}}^2)}{K^2 \cdot L^2} \quad (15.11)$$

$$r_o \approx 7.00 \text{ mm}$$

This corresponds to a required cross-sectional area of each bar of

$$A = \pi(r_o^2 - r_i^2) \approx 0.00 \text{ mm}^2 \quad (15.12)$$

The extremely small required area indicates that there is virtually no risk of buckling. This result is due to the significant contribution of the Steiner term to the effective moment of inertia, which greatly enhances the frame's resistance to buckling.

15.3.2 Bending stress

The bending loading configuration is illustrated in Figure 15.9.

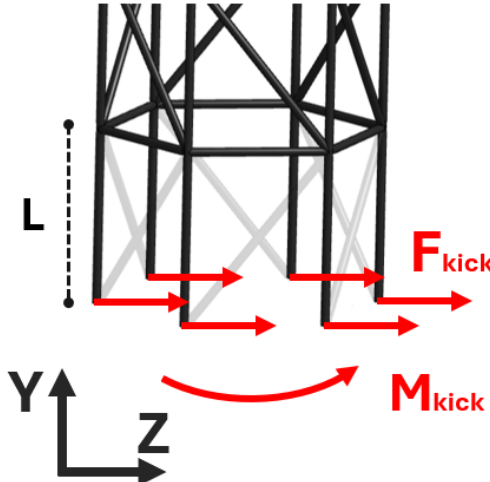


Figure 15.9: Bending stress loading configuration on STD.

The highest lateral loading occurs under a lateral acceleration of 2g, resulting in a kick stage reaction force of $F_{\text{kick}} = 7.750 \text{ kN}$ and a bending moment of $M_{\text{kick}} = -12.708 \text{ kNm}$. These loads combine to produce a net bending moment on the STD structure. The total moment is computed using

$$M = F_{\text{kick},xz} \cdot 350 \text{ mm} + M_{\text{kick},xz} = 15.421 \text{ kNm} \quad (15.13)$$

The bending stress is given by [108]

$$\sigma_b = \frac{M \cdot r_o}{I} \quad (15.14)$$

where I represents the second moment of inertia, again including both the geometric component and the contribution from the offset of each bar to the central axis, given by Equation 15.9.

Solving the equation for the required outer radius yields

$$r_o \approx 7.00 \text{ mm} \quad (15.15)$$

The corresponding cross-sectional area is

$$A \approx 0.00 \text{ mm}^2 \quad (15.16)$$

Similar to the buckling case, the Steiner term substantially increases the effective stiffness of the structure, leading to low stress levels and very small required cross-sectional dimensions. Therefore, bending does not govern the design of the STD frame bars.

15.3.3 Shear stress

The shear loading configuration is illustrated in Figure 15.10

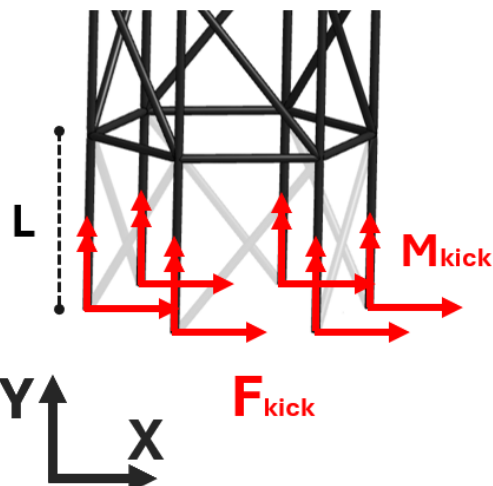


Figure 15.10: Shear stress loading configuration on STD.

Under the same lateral acceleration that drives bending, shear stress is also developed in

the bars. These arise from both the transverse shear force F_{kick} and the torsional moment $M_{\text{kick},y}$. The combined shear stress in a hollow circular section is given by [109, 110]

$$\begin{aligned}\tau &= \tau_{\text{force}} + \tau_{\text{torsion}} \\ \tau &= \frac{4 \cdot F_{\text{kick}}}{3 \cdot A} \left(1 + \frac{r_o \cdot r_i}{(r_o^2 + r_i^2)}\right) + \frac{r_o \cdot M_{\text{kick},y}}{J}\end{aligned}\quad (15.17)$$

The second term represents the torsional contribution, where J is the polar moment of inertia, including the Steiner term

$$J = 6 \cdot \left(\frac{\pi}{2}(r_o^4 - r_i^4) + m \cdot r_{\text{STD}}^2\right) \quad (15.18)$$

To evaluate whether shear stress is critical, the von Mises yield criterion is applied [111]. According to this criterion, the maximum allowable shear stress is

$$\tau = \frac{\sigma_y}{\sqrt{3}} = 508 \text{ MPa} \quad (15.19)$$

Solving the shear stress equation with this limiting value yields the required cross-sectional area and outer radius of the bars

$$A = 10.17 \text{ mm}^2 \quad (15.20)$$

$$r_o = 7.23 \text{ mm} \quad (15.21)$$

Compared to the axial and bending stress results, the shear stress case proves to be the most demanding. Among all structural checks, it imposes the strictest requirement on the frame's cross-sectional size and therefore governs the final sizing of the STD frame bars.

15.3.4 Conclusion

Since shear is the most critical constraint, it defines the minimum required cross-sectional area and outer radius of the frame bars as 10.17 mm^2 and 7.23 mm , respectively. To simplify manufacturing, ensure compatibility with standardized structural profiles, and incorporate additional safety margin, a circular hollow section (CHS) with an outer diameter of 16 mm and wall thickness of 1 mm is selected. The CHS 16×1 profile provides sufficient structural capacity in all loading cases, while offering excellent vibration resistance, and improved buckling stability due to its increased section stiffness.

15.4 Simple Finite Element Model

Before developing a complete finite element model (FEM) of the STD structure, which includes its full 3D geometry, a simplified model is first constructed to assess preliminary

design choices and identify necessary improvements. This simplified model consists solely of the frame structure, excluding the hexagonal prisms at the bottom, middle, and top. Additionally, only one face of the structure is analyzed, with all applied masses evenly distributed across the six faces, meaning each face carries one-sixth of each mass component. This model is a good initial approach, but does severely underestimate the out of plane bending stiffness of the frame structure. Therefore, this model will only be subjected to in-plane inertial forces.

The model is implemented in ANSYS APDL using BEAM188 elements for the frame, and MASS21 elements (indicated as 'M0' on Figure 15.11) to represent the concentrated masses. This analysis was conducted prior to performing analytical calculations to determine the required cross-sectional area of the frame structure's beams. In this preliminary analysis, the beam cross-sections were arbitrarily assumed to be solid cylinders with a radius of 11 mm. To ensure a well-posed system of equations, the bottom beam is fully constrained in all directions. As a result of this boundary condition, the reaction force of the kick stage does not need to be explicitly applied—ANSYS calculates it automatically. The frame is meshed using 89 nodes into 100 elements.

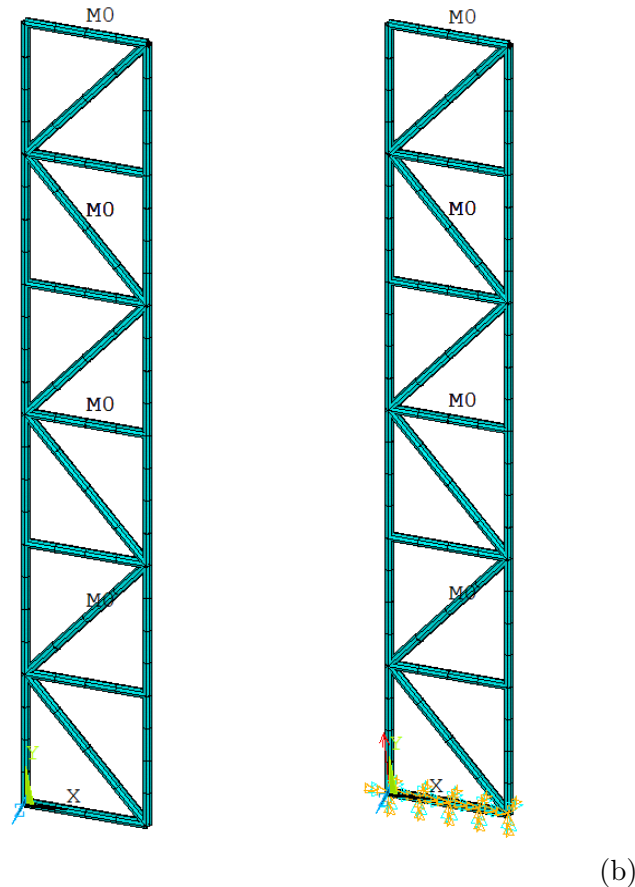


Figure 15.11: (a) Simple model of STD frame using BEAM188 and MASS21 elements. (b) Boundary conditions: blue and orange prevent translation and rotation, red is acceleration of frame.

To improve accuracy, further refinements can be made, such as assigning mass to the beams by incorporating the material density. Additionally, the elastic modulus and Poisson's ratio are considered in the analysis.

The acceleration is applied to the non-inertial frame of the model. As a result, inertial forces are generated from the mass elements. The simple FEM is statically analyzed under both extreme acceleration cases.

The APDL code used for this analysis can be found in Appendix H.

15.4.1 FEA of (0.5, 6)g

The combination of lateral and axial acceleration of (0.5, 6)g yields results that are presented in Figures 15.12, 15.13, and 15.14.

Figure 15.12 shows the displacement vector sum and the von Mises stress distribution in the frame structure. The largest displacements are observed at the top of the frame, which is expected given that the bottom of the frame is fixed. The von Mises stress reaches a maximum value of 53.2 MPa, well below the yield strength of Ti-6Al-4V (880 MPa).

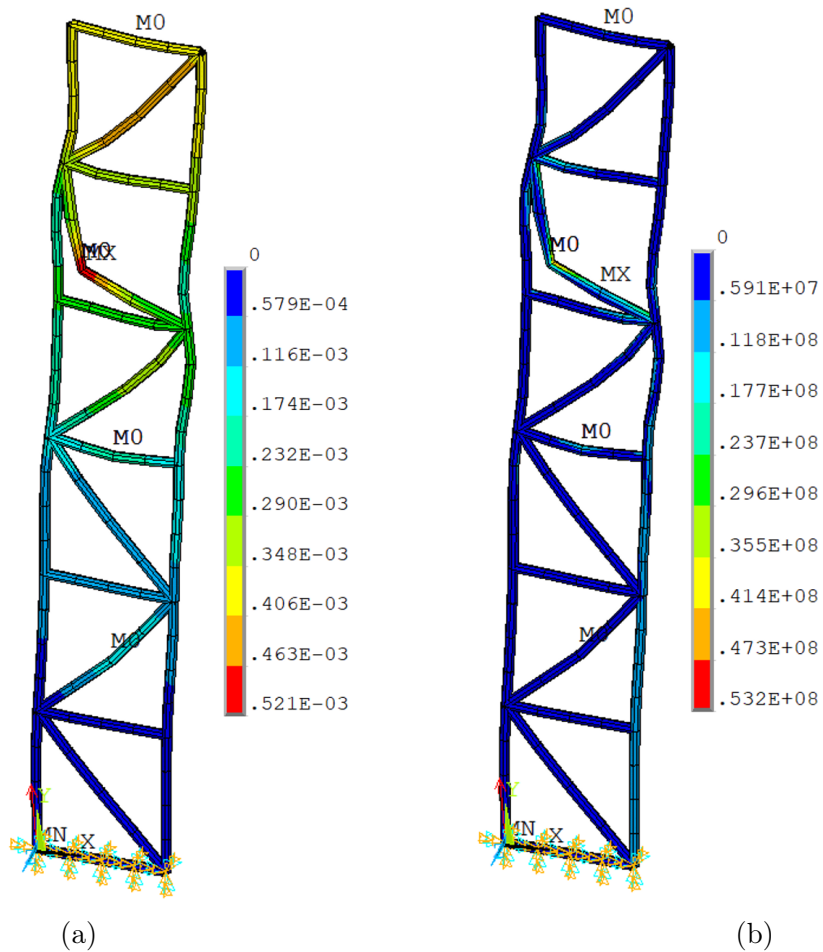


Figure 15.12: (a) Displacement vector sum [m]. (b) Von Mises stress distribution [Pa].

Figure 15.13 shows the distribution of axial force and axial stress. The axial force in the lower-right bar is approximately equal to the reaction force from the kick stage divided by 6, confirming the accuracy of the approximation made in the analytical calculation for the cross-sectional area. Most of the stresses in the frame structure are compressive, as anticipated given the loading conditions. Additionally, the axial stresses are well below the critical stress required for buckling to occur.

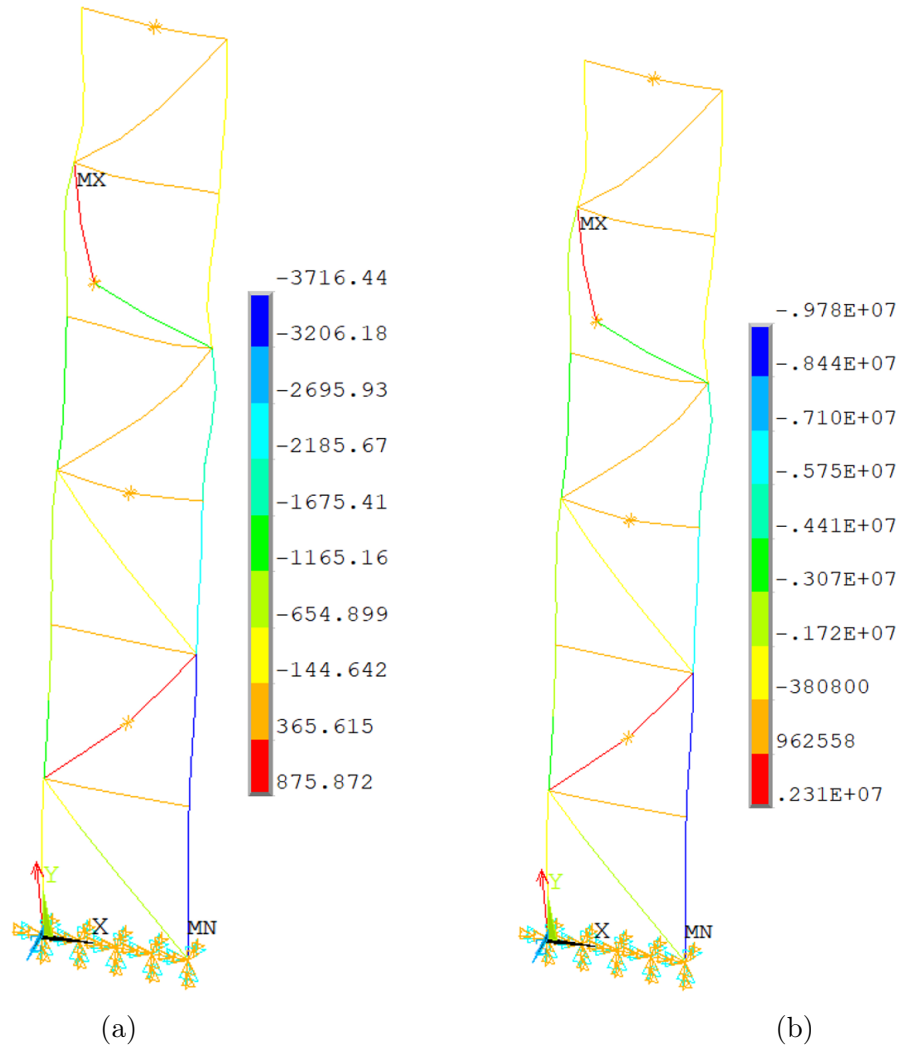


Figure 15.13: (a) Axial force distribution [N]. (b) Axial direct stress distribution [Pa].

Figure 15.14 illustrates the bending stress distribution on the upper and lower surfaces of the bars within the frame structure. The "top" (Figure 15.14a) and "bottom" (Figure 15.14b) refer to the outermost fibers of the beam cross-section relative to the neutral axis—where tension and compression are at their maximum during bending. As seen in the analytical calculations, these regions experience the highest and most critical bending stresses. Nevertheless, all values remain well below the material's yield stress, indicating a safe design under the evaluated loading conditions.

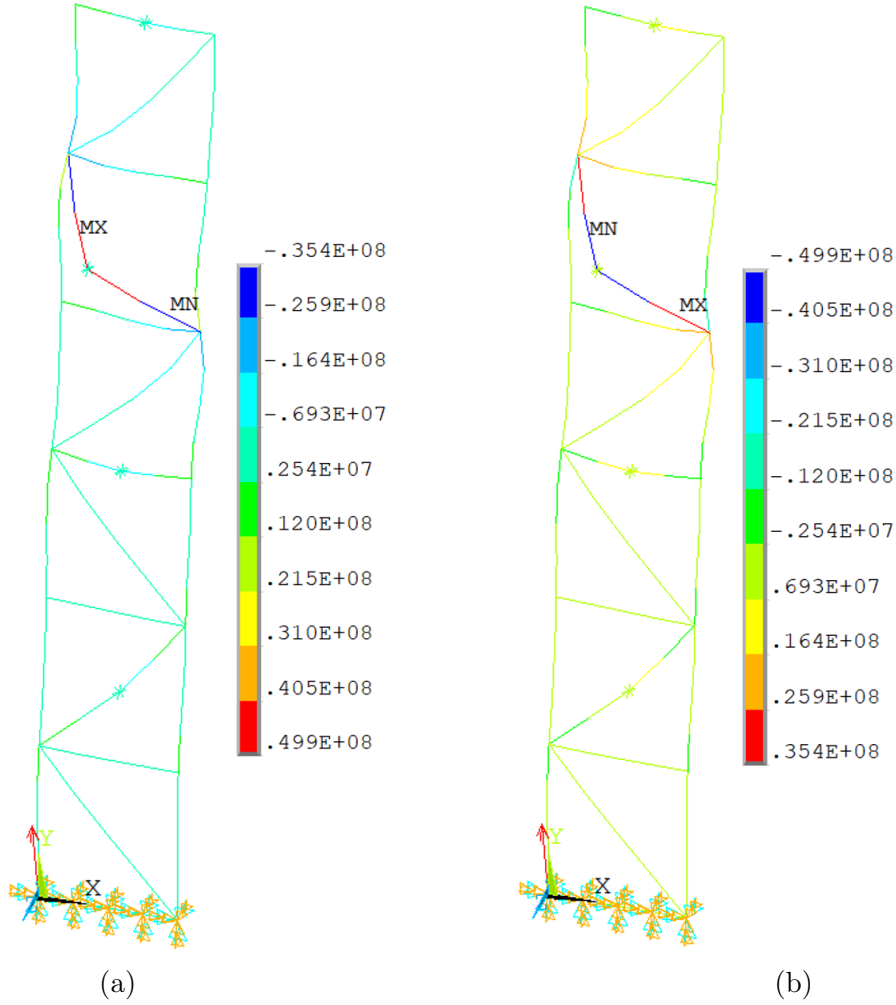


Figure 15.14: (a) Top bending stress [Pa]. (b) Bottom bending stress [Pa].

One way to verify the accuracy of the finite element model is by comparing the reaction force from the FEM with that predicted by the analytical model. The analytical model predicts a reaction force of $(-0.323 \text{ kN}, 3.875 \text{ kN})$. The finite element analysis yields a reaction force of $(-0.397 \text{ kN}, 4.761 \text{ kN})$. It is important to note that, since density is accounted for in the FEM, the reaction force is slightly higher than in the analytical model. Without considering density, the reaction force exactly matches the analytical solution. Given this, the reaction force obtained from the FEM is close enough to the analytical model, thereby confirming the accuracy of the finite element analysis.

15.4.2 FEA of (2, 3.5)g

For the $(2, 3.5)g$ acceleration case, the results of the finite element analysis are presented in Figures 15.15, 15.16, and 15.17. This loading scenario induces substantial bending, particularly out-of-plane bending, which is not accurately captured in this simplified model. As a result, the reported stresses are highly conservative and likely overestimate the actual structural response.

Figure 15.15 shows the displacement vector sum and the von Mises stress distribution in the frame structure. The largest displacements are once again observed at the top of the frame. The displacement vector sum is significantly higher than the (0.5, 6)g acceleration case, while the von Mises stress is much lower.

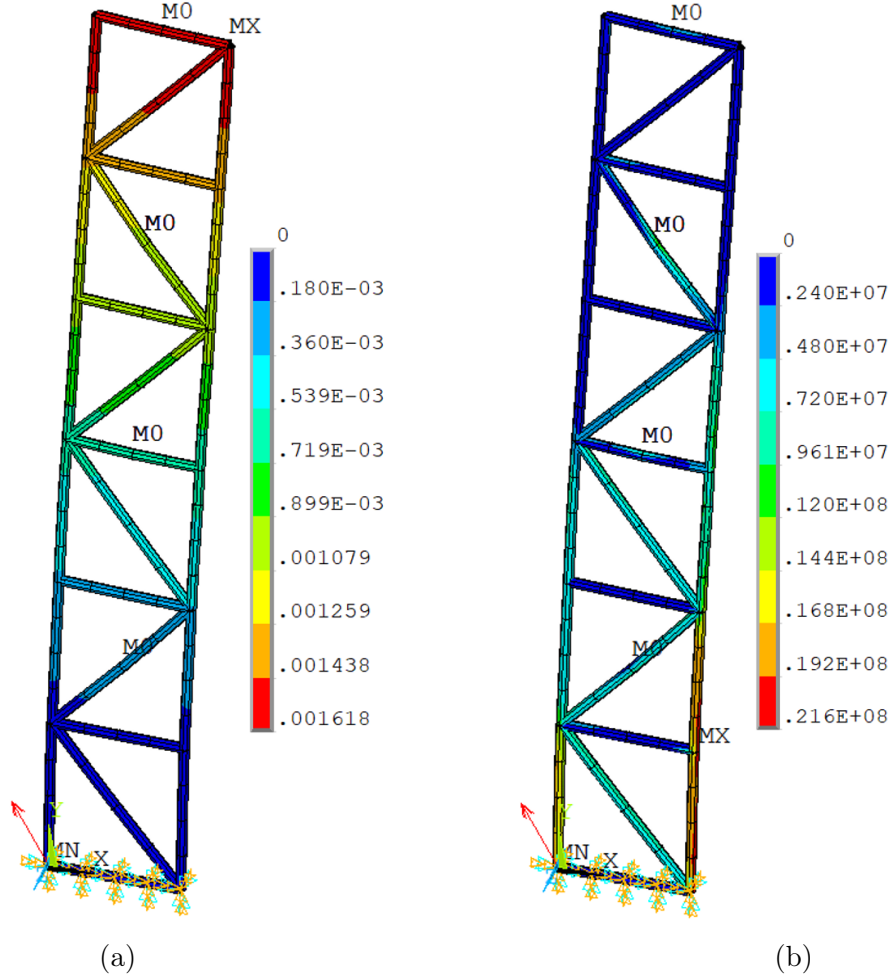


Figure 15.15: (a) Displacement vector sum [m]. (b) Von Mises stress distribution [Pa].

Figure 15.16 shows the distribution of axial force and axial stress. The axial forces for this acceleration configuration are higher than anticipated, however, the resulting axial stresses do not exceed any critical value.

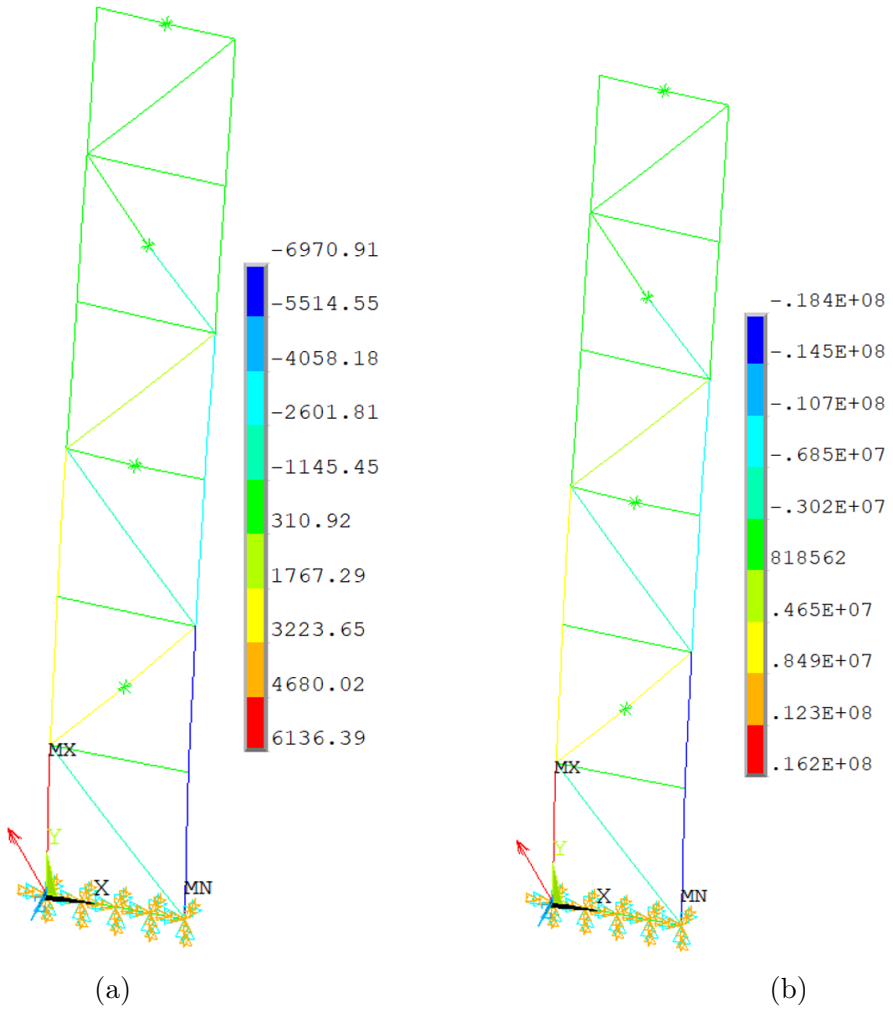


Figure 15.16: (a) Axial force distribution [N]. (b) Axial direct stress distribution [Pa].

Figure 15.17 shows the bending stress in the upper and lower halves of the bars. These bending stresses are an order of magnitude lower than the bending stresses from the (0.5, 6)g acceleration case, and therefore, do not pose any risk for failure of the frame structure.

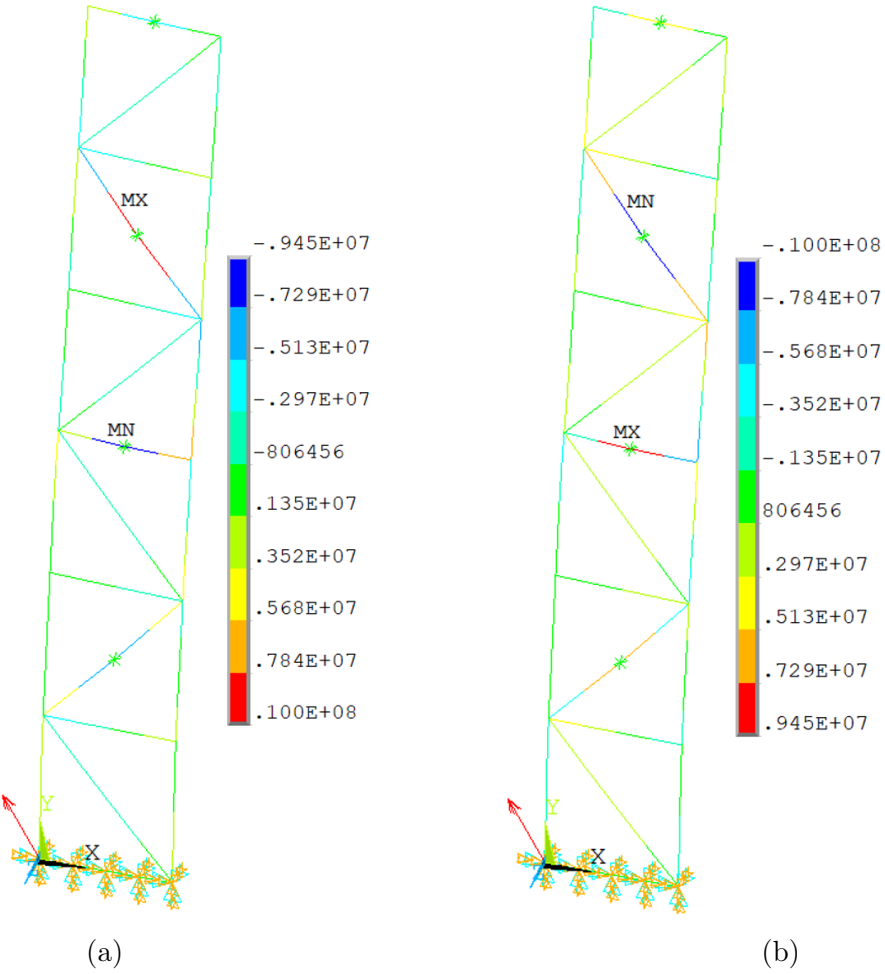


Figure 15.17: (a) Top bending stress [Pa]. (b) Bottom bending stress [Pa].

Also for this finite element model, the accuracy can be verified by comparing the reaction force from the FEM with that predicted by the analytical model. The analytical model predicts a reaction force of $(-1.292 \text{ kN}, 2.260 \text{ kN})$. The finite element analysis yields a reaction force of $(-1.587 \text{ kN}, 2.777 \text{ kN})$. The reaction force obtained from the FEM is close enough to the analytical model, thereby confirming the correct implementation of the finite element analysis.

15.4.3 Reflection

While the 2D finite element analysis provides useful insights into the behavior of the structure, it has limitations in terms of accuracy, especially for lateral stresses. The axial stresses are relatively well-predicted, but the analysis of the lateral stresses is less reliable due to the angled faces, which are not fully captured in 2D. To improve the accuracy of the results, a 3D finite element analysis in ANSYS Workbench is be performed. This will provide a more comprehensive and precise understanding of the stresses.

15.5 Complete Finite Element Model

The complete finite element model of the STD structure was developed in ANSYS Mechanical using a CAD geometry import. The original CAD file contained the full STD structure assembly, which was modified in the preprocessing to reduce computational complexity and align with the modeling assumptions. The frame structure was modeled using 1D beam elements with a CHS 16x1 cross-section, while the hexagonal prisms were represented as thin-walled 3D solids with a uniform wall thickness of 1 mm. The overall geometry used in the simulation is shown in Figure 15.18.

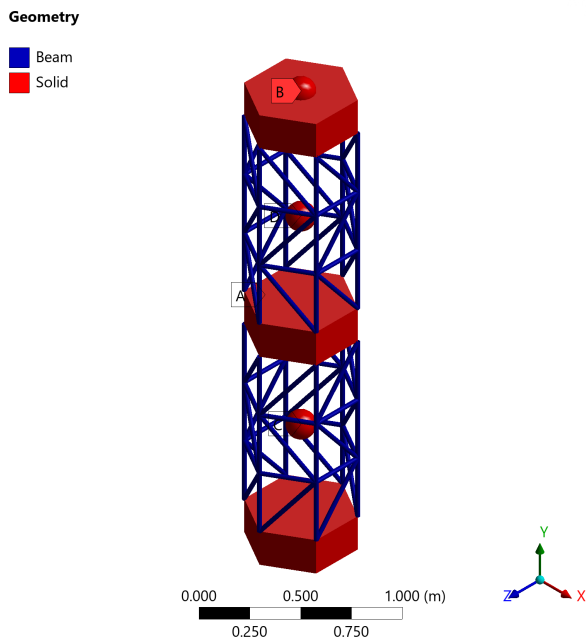


Figure 15.18: Geometry of STD used in FEA.

To simulate the mass of internal subsystems—such as the propulsion system, engine, and fuel tank—point masses were placed at their respective locations within the model. These point masses do not exert direct forces, but generate inertial loads when acceleration is applied to the non-inertial frame of the model, accurately replicating launch conditions.

All structural components were assigned the material properties of Ti-6Al-4V. The built-in ANSYS library values for density, Young's modulus, and Poisson's ratio were used.

The frame was discretized using 1D beam elements, allowing for efficient representation of axial and bending loads while minimizing computational cost. The thin-walled hexagonal shell was meshed using 3D tetrahedral solid elements. An adaptive mesh sizing approach was applied with a target resolution setting of 2, balancing detail and performance. The final mesh consisted of 8,138 nodes and 4,039 elements, with the majority of the elements associated with the hexagonal prism shells. Mesh continuity was ensured at key interfaces, including beam-to-beam junctions and beam-to-shell transitions, where nodes were merged to avoid discontinuities. The resulting mesh is shown in Figure 15.19.

Geometry

Figure 15.19: Meshing of STD.

Boundary conditions were applied by fixing the bottom face of the lowest hexagonal prism in all translational and rotational degrees of freedom. This represents a rigid connection to the kick stage, providing a realistic constraint scenario without over-constraining the model.

A static structural analysis was carried out for the four acceleration loading cases summarized in Table 15.6. These were applied as body accelerations, which act on the point masses and generate realistic inertial loads. An example load configuration is shown in Figure 15.20.

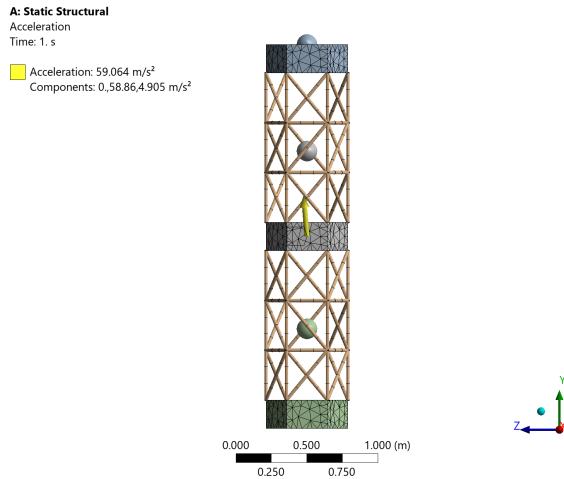


Figure 15.20: Example of applied loading to the STD.

15.5.1 (0.5, 6)g with max bending

Results for the lateral and axial acceleration case of (0.5, 6)g that leads to a maximum bending reaction moment are shown in Figures 15.21 and 15.22. The axial force distribution in the frame beams, shown in Figure 15.21a, reveals a pronounced anti-symmetric pattern. This is a direct consequence of the mass offset corresponding to the capturing mechanism. In the analytical model, the axial force was presumed to be equally distributed among the six vertical beams. This assumption is clearly invalidated by the FEM results. The corresponding axial stresses, presented in Figure 15.21b, indicate that the highest compressive stress reaches 182.14 MPa, a significant value but still well below the Ti-6Al-4V yield strength of 880 MPa, preserving a healthy margin of safety.

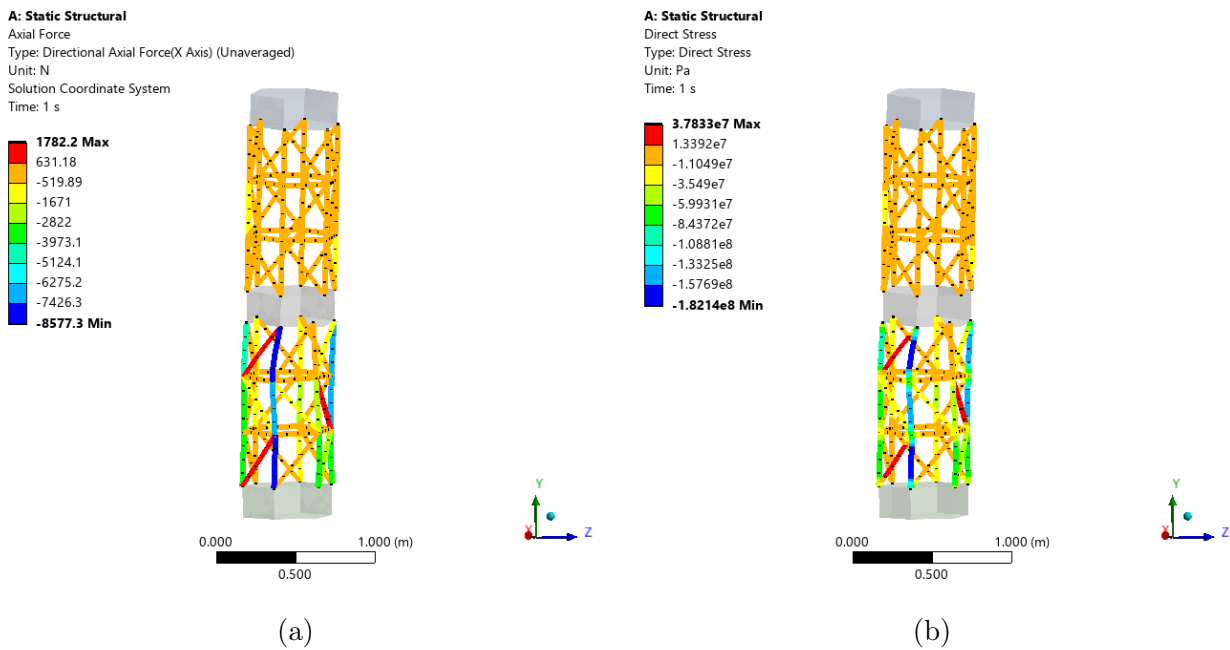


Figure 15.21: (a) Axial force in STD beams [N]. (b) Axial stress in STD beams [Pa].

The high compressive stress values raise concerns about potential buckling. However, as outlined in the analytical calculations, the beam configuration benefits from a substantial Steiner term, enhancing bending stiffness. Combined with the relatively short beam lengths and full lateral constraint at the bottom interface, the risk of buckling remains negligible under the simulated loads.

The total structural deformation, shown in Figure 15.22a, peaks at approximately 7.7 mm. Given the overall size of the STD, this level of deflection is acceptable and does not compromise structural integrity or operational functionality. The corresponding maximum von Mises stress distribution, depicted in Figure 15.22b, closely mirrors the axial stress pattern and remains comfortably below material limits.

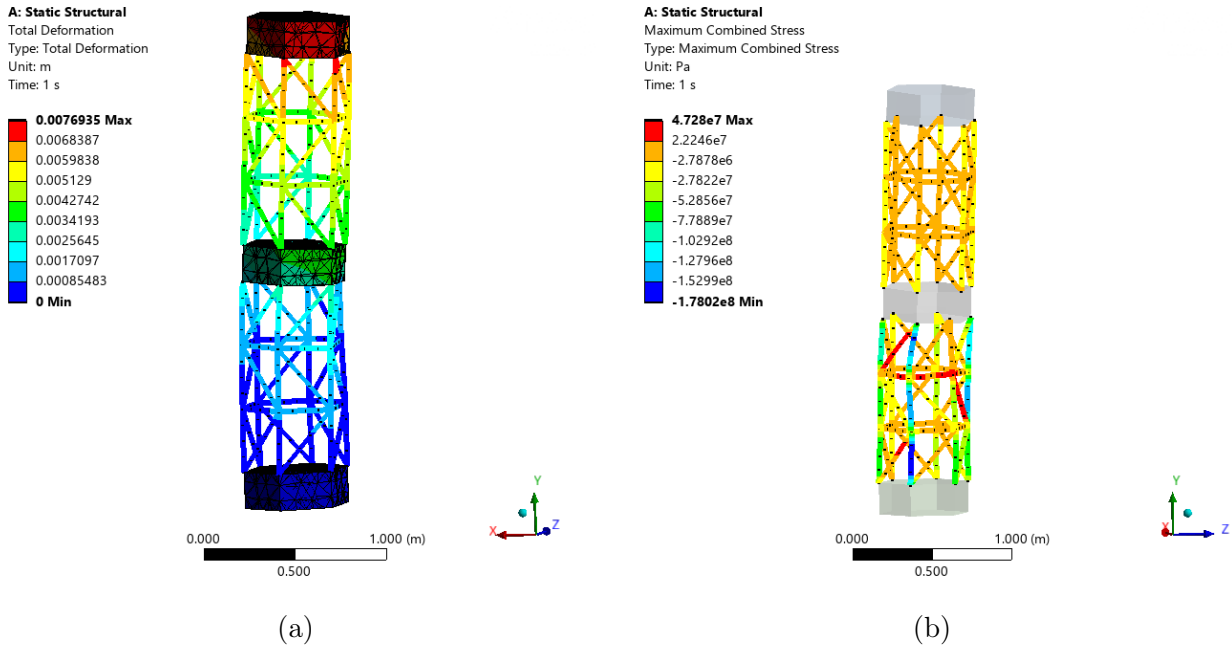


Figure 15.22: (a) Total deformation in STD [m]. (b) Maximum combined stress in STD beams [Pa].

To validate the fidelity of the finite element model, the reaction forces and moments obtained from the simulation were compared against those derived from the analytical approach. These values are summarized in Table 15.7. The close agreement—less than 2% relative error in all components—confirms that the applied loads, boundary conditions, and point mass distributions were implemented correctly in the model. This comparison serves as a key verification step, lending confidence to the reliability of the simulation results.

Table 15.7: Comparison of analytical and ANSYS predictions of reaction force and moment.

(0.5, 6)g	Reaction Force [kN]			Reaction Moment [kNm]		
	F_x	F_y	F_z	M_x	M_y	M_z
Analytical	0	23.250	1.937	-3.365	0	0
ANSYS	0	23.708	1.976	-3.306	0	0

15.5.2 (0.5, 6)g with max torsion

Results for the lateral and axial acceleration case of (0.5, 6)g that leads to a maximum torsion reaction moment are shown in Figures 15.23 and 15.24. These results are very similar to the results of the acceleration case of (0.5, 6)g that leads to a maximum bending reaction moment. The axial force distribution in the frame beams is anti-symmetric, and the corresponding axial stresses indicate that the highest compressive stress reaches a slightly higher value of 195.37 MPa, which is still within a healthy margin of safety.

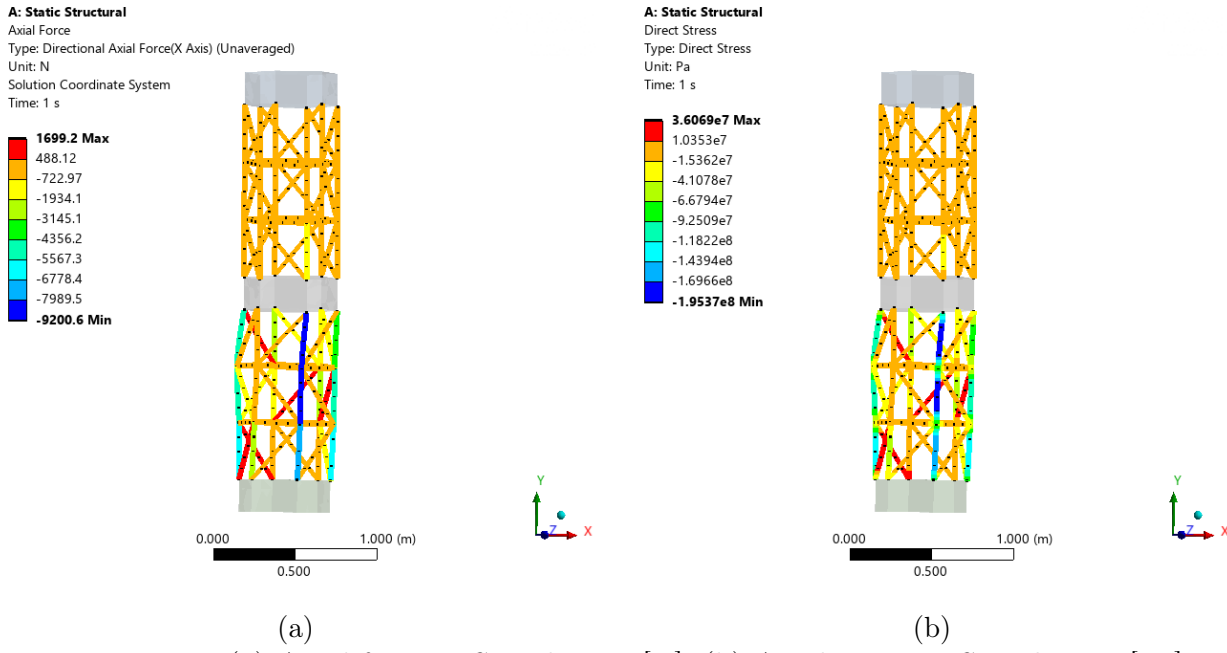


Figure 15.23: (a) Axial force in STD beams [N]. (b) Axial stress in STD beams [Pa].

The total structural deformation, shown in Figure 15.24a, peaks at approximately 9.6 mm. Given the overall size of the STD, this level of deflection is still acceptable and does not compromise structural integrity or operational functionality. The corresponding maximum von Mises stress distribution, depicted in Figure 15.24b, closely mirrors the axial stress pattern and remains comfortably below material limits.

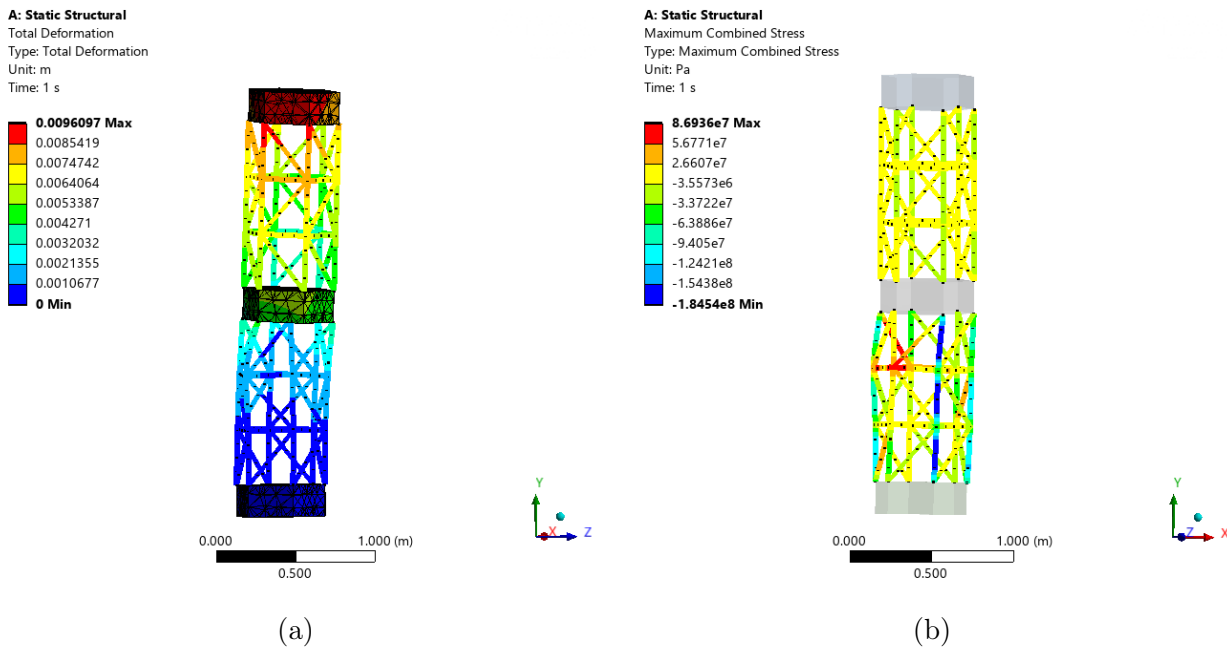


Figure 15.24: (a) Total deformation in STD [m]. (b) Maximum combined stress in STD beams [Pa].

Again, to validate the fidelity of the finite element model in this loading case, the reaction forces and moments obtained from the simulation were compared against those derived from the analytical approach. These values are summarized in Table 15.8. The close agreement confirms that the applied loads, boundary conditions, and point mass distributions were implemented correctly in the model.

Table 15.8: Comparison of analytical and ANSYS predictions of reaction force and moment.

(0.5, 6)g	Reaction Force [kN]			Reaction Moment [kNm]		
	F_x	F_y	F_z	M_x	M_y	M_z
Analytical	1.937	23.250	0	-0.221	0.018	3.145
ANSYS	1.976	23.708	0	-0.221	0.018	3.526

15.5.3 (2, 3.5)g with max bending

Results for the lateral and axial acceleration case of (2, 3.5)g that leads to a maximum bending reaction moment are shown in Figures 15.25 and 15.26. The axial force distribution in the frame beams, shown in Figure 15.25a, reveals forces that are two to four times higher than in the (0.5, 6)g acceleration cases. The corresponding axial stresses, presented in Figure 15.25b, are therefore also higher. However, the maximum compressive stress of 366.88 MPa still provides a safetyfactor of 2.4 for Ti-6Al-4V, which has a yield strength of 880 MPa.

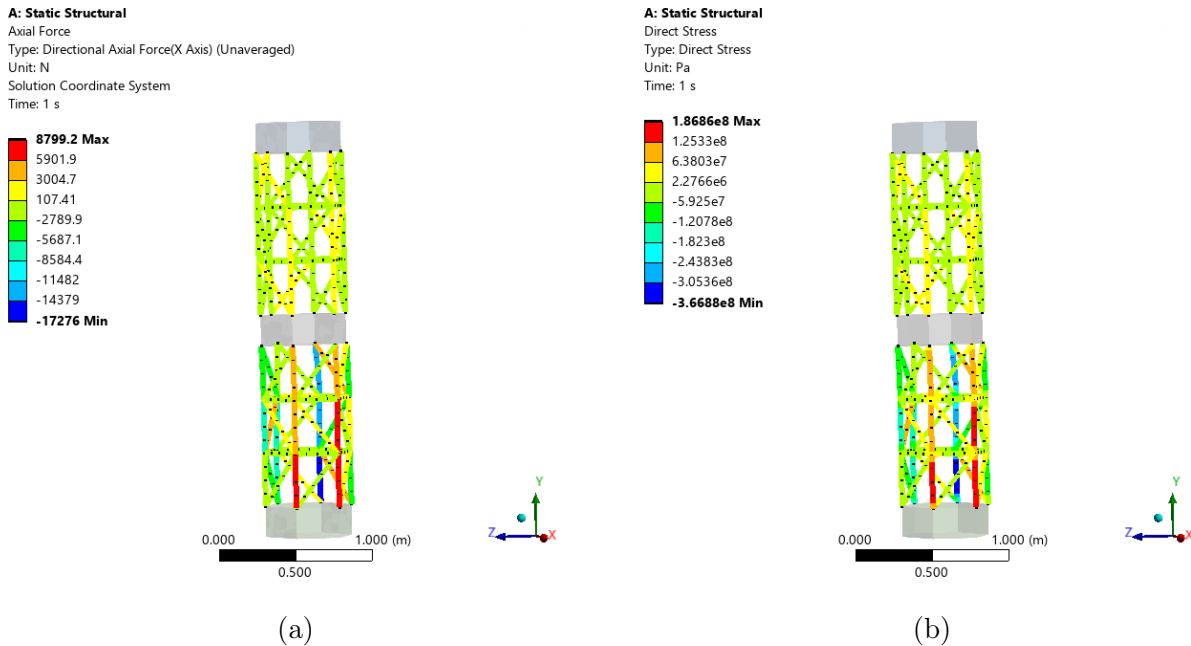


Figure 15.25: (a) Axial force in STD beams [N]. (b) Axial stress in STD beams [Pa].

Buckling is not a concern in this case, as previously discussed. The combination of a significant Steiner contribution, short beam lengths, and full lateral constraint at the base ensures sufficient resistance to compressive instability.

The total structural deformation, shown in Figure 15.26a, peaks at approximately 22.6 mm. This is a significant increase compared to the (0.5, 6)g acceleration cases, and might serve as a concern for plumbing. However, these large deformations decrease rapidly towards the rigid support, and given the overall size of the STD, this level of deflection is still acceptable. The corresponding maximum von Mises stress distribution, depicted in Figure 15.26b, closely mirrors the axial stress pattern and remains comfortably below material limits.

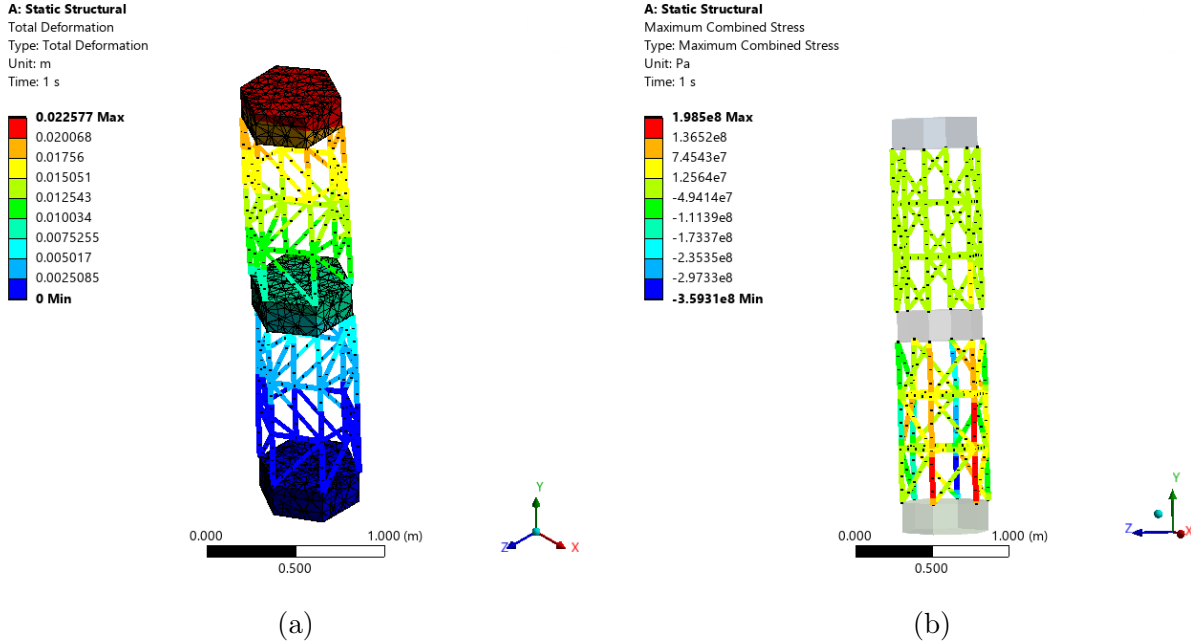


Figure 15.26: (a) Total deformation in STD [m]. (b) Maximum combined stress in STD beams [Pa].

Table 15.9 presents a comparison between the reaction forces and moments obtained from the finite element simulation and those predicted by the analytical model. As with the previous cases, the results show close agreement.

Table 15.9: Comparison of analytical and ANSYS predictions of reaction force and moment.

(2, 3.5)g	Reaction Force [kN]			Reaction Moment [kNm]		
	F_x	F_y	F_z	M_x	M_y	M_z
Analytical	0	13.562	7.750	-12.708	0	0
ANSYS	0	13.829	7.903	-13.978	0	0

15.5.4 (2, 3.5)g with max torsion

Results for the lateral and axial acceleration case of (2, 3.5)g that leads to a maximum torsion reaction moment are shown in Figures 15.27 and 15.28. Out of all the four cases discussed, this acceleration case leads to the highest axial forces and stresses, however, these values are still within a factor of safety of 2.33.

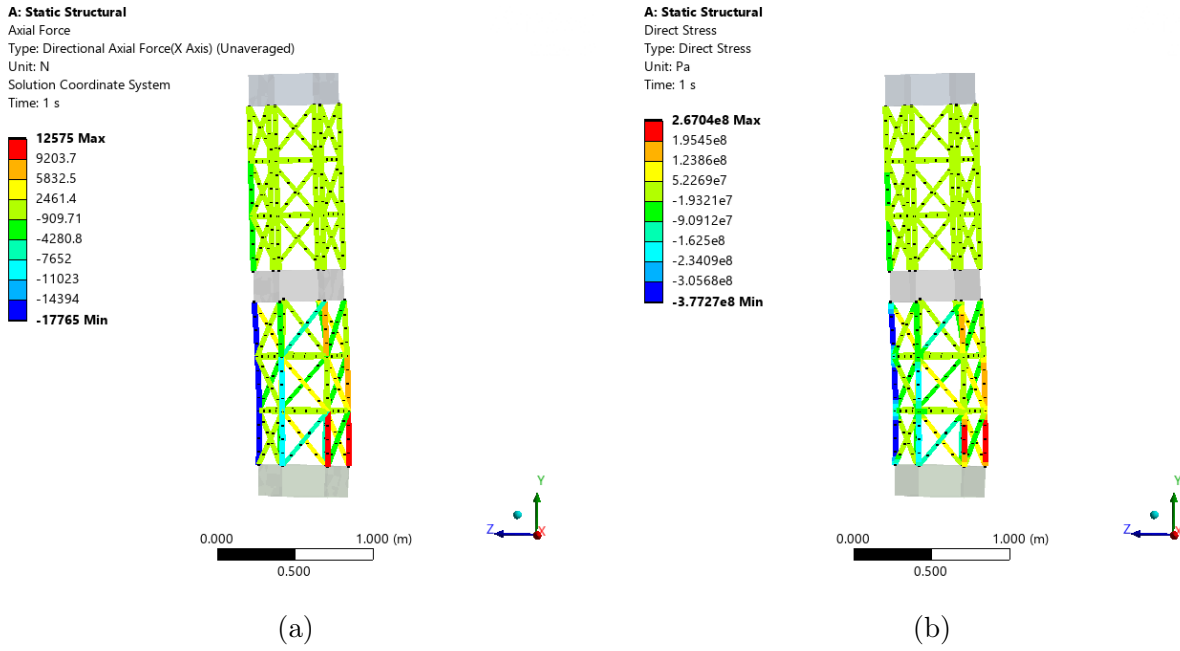


Figure 15.27: (a) Axial force in STD beams [N]. (b) Axial stress in STD beams [Pa].

The total structural deformation, shown in Figure 15.26a, peaks at approximately 29.0 mm. While this is a relatively large value, it is primarily due to in-plane bending from the lateral acceleration component, rather than compressive distortion along the beam axes. The deformation is mostly localized and occurs in non-critical regions of the structure. As such, it does not compromise the integrity of load-bearing elements. Any potential concerns related to internal components—such as rigid piping—can be mitigated through minor layout adjustments or the use of flexible couplings. Overall, the deformation remains acceptable for a preliminary design iteration. The corresponding maximum von Mises stress distribution, shown in Figure 15.26b, aligns with the axial stress pattern and remains well below the material yield strength, confirming structural adequacy.

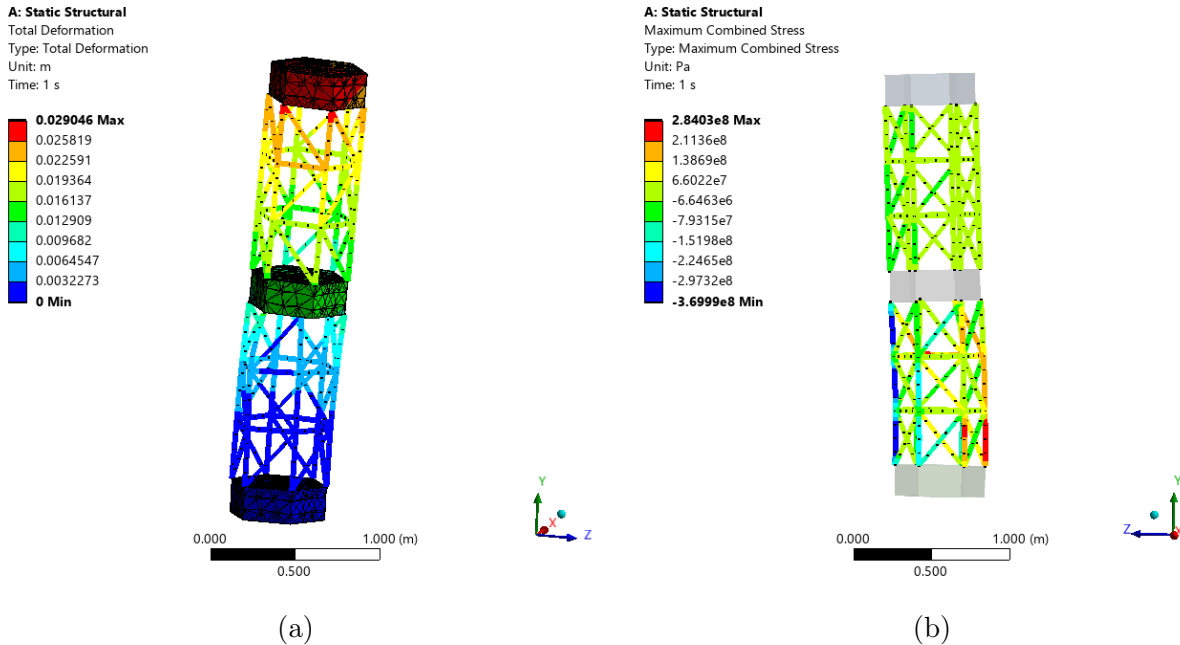


Figure 15.28: (a) Total deformation in STD [m]. (b) Maximum combined stress in STD beams [Pa].

Table 15.10 presents a comparison between the reaction forces and moments obtained from the finite element simulation and those predicted by the analytical model. As with the previous cases, the results show close agreement.

Table 15.10: Comparison of analytical and ANSYS predictions of reaction force and moment.

(2, 3.5)g	Reaction Force [kN]			Reaction Moment [kNm]		
	F_x	F_y	F_z	M_x	M_y	M_z
Analytical	7.750	13.562	0	-0.129	0.074	12.579
ANSYS	7.903	13.829	0	-0.129	0.074	14.107

15.5.5 Conclusion

The simulation results across all four loading scenarios demonstrate that the selected CHS 16x1 cross-section provides sufficient structural performance for the STD frame. Maximum stress values remain well below the yield limit of Ti-6Al-4V, and deformation levels, while varying with loading direction, do not pose critical risks to structural integrity. Buckling concerns are mitigated through favorable geometry and support conditions. Even under the most demanding torsional and bending loads, the CHS 16x1 configuration ensures a robust and reliable structural response, confirming its suitability for the current design stage.

16 STD Engine Analysis

In order to meet the specified propulsion targets, the STD engine must be analyzed to ensure safe and effective operation. Of particular interest is the given geometry of the nozzle, as the change in area will dictate the gas' local properties as it moves through the system [64]. Additionally, the decomposition bed plays a very large role in how the engine behaves, and shapes how the pressures and temperatures vary throughout the reaction chamber.

16.1 Decomposition Analysis and Gas Properties

The decomposition bed and how it affects the propellant during its residence time is mostly an issue of chemistry, as the hydrazine first decomposes exothermically into ammonia then endothermically into a mixture of hydrogen, nitrogen, along with unreacted ammonia. The final ammonia decomposition percentage influences the performance of the engine and is mainly a function of bed length [46]. NASA's testing in the late 1960's shows that this decomposition percentage levels out at about 14.5% after a bed length of approximately 0.25 ft, or 0.08 m [46]. This value is used as the gas properties are known and can thus be used in further analysis.

The decomposition chamber's geometry itself is sized to the STD fuel tank's [aft](#) diameter of 0.372 m for structural compatibility and to reduce edge-case complications with underpacked or non-optimal bed arrangements [causing a loss of efficiency or thrust](#) [64]. This [size](#) is further motivated by the engine's significant mass flow rate of 1.436 kg/s, calculated earlier in Section 9. [This is](#) significantly higher than engines used for attitude control or lower thrust maneuvers, [and is motivated by the requirement for a higher volumetric flow rate without significantly changing the density or flow velocity from literature values](#) [48].

The final decomposed gas' properties essentially act as the nozzle's stagnation state, and depend upon the mole fractions and properties of each individual gas comprising it. The mixture's specific heat ratio, γ_m is calculated using

$$\gamma_m = \frac{\sum \chi_i c_{pi}}{\sum \chi_i c_{vi}} \quad (16.1)$$

Where χ_i is each gas' mole fraction, c_{pi} its constant pressure specific heat, and c_{vi} its constant volume specific heat [85]. Based on final experimental mole fractions of 0.145, 0.31, and 0.545 for ammonia, nitrogen gas, and hydrogen gas respectively [46], a mixture gamma of 1.405 is calculated.

The mixture's gas constant, R_m , is also necessary for further analysis, and is calculated using

$$R_m = \frac{\bar{R}}{\bar{M}_m} \quad (16.2)$$

where \bar{R} is the universal gas constant, 8.3145 J/kg K, and \bar{M}_m is the mixture's molar mass, calculated by

$$\bar{M}_m = \sum \chi_i M_i \quad (16.3)$$

where M_i is each gas' individual molar mass: [nitrogen gas at 14.01 g/mol, hydrogen gas at 2.02 g/mol, and ammonia at 17.03 g/mol \[64\]](#). Equation 16.2 thus gives a gas constant of 678.7 J/kg K.

16.2 Pressure Analysis

The first pressure solved for must be the post-decomposition stagnation pressure, P_0 , as it will characterize the performance of the nozzle and necessary injector pressure. As both the propellant mass flow rate and throat area (sonic area, A^*) have been set, the sonic conditions are thus set by the 1-dimensional mass flow relation

$$\dot{m} = \rho^* a A^* \quad (16.4)$$

where ρ^* is the density at sonic conditions and a is the local speed of sound, given by

$$a = \sqrt{\gamma_m R_m T^*} \quad (16.5)$$

where T^* is the temperature at sonic conditions [85]. The post-decomposition mixture temperature, T_0 , is based on S405's properties and sits at about 1100 K [52]. The sonic temperature can then be found using [the isentropic relation](#)

$$T^* = T_0 \left(\frac{\gamma_m + 1}{2} \right)^{-1} \quad (16.6)$$

and is calculated [85] at 917 K, giving a local speed of sound of 933.3 m/s and thus a sonic density of 0.6260 kg/m³. This is then related to the stagnation density, ρ_0 , by another isentropic relation

$$\rho_0 = \rho^* \left(\frac{\gamma_m + 1}{2} \right)^{\frac{1}{\gamma_m - 1}} \quad (16.7)$$

which gives a stagnation density of 0.9875 kg/m³ [85]. Finally, the stagnation pressure of the decomposition products can be simply calculated using

$$P_0 = \rho_0 R_m T_0 \quad (16.8)$$

The final post-decomposition stagnation pressure is thus calculated at 730 kPa.

As the nozzle is assumed to expand the decomposition products isentropically, a simple analysis can be done to obtain the local Mach number, M , at each axial position x along the

nozzle according to the ratio between the local area $A(x)$ and throat area. This relationship is given by

$$\frac{A(x)}{A^*} = \frac{1}{M} \left[\frac{2}{\gamma + 1} \left(1 + \frac{\gamma - 1}{2} M^2 \right) \right]^{\frac{\gamma+1}{2(\gamma-1)}} \quad (16.9)$$

and must be backsolved for each local area ratio [85].

From a known Mach number, a ratio between the local pressure $P(x)$ and stagnation pressure P_0 can be obtained using

$$\frac{P(x)}{P_0} = \left(1 + \frac{\gamma - 1}{2} M^2 \right)^{\frac{\gamma}{1-\gamma}} \quad (16.10)$$

whose value can then be multiplied by the post-decomposition stagnation pressure to obtain a pressure distribution along the nozzle's inner walls. A plot of this distribution is shown in Figure 16.1, and begins at the throat.

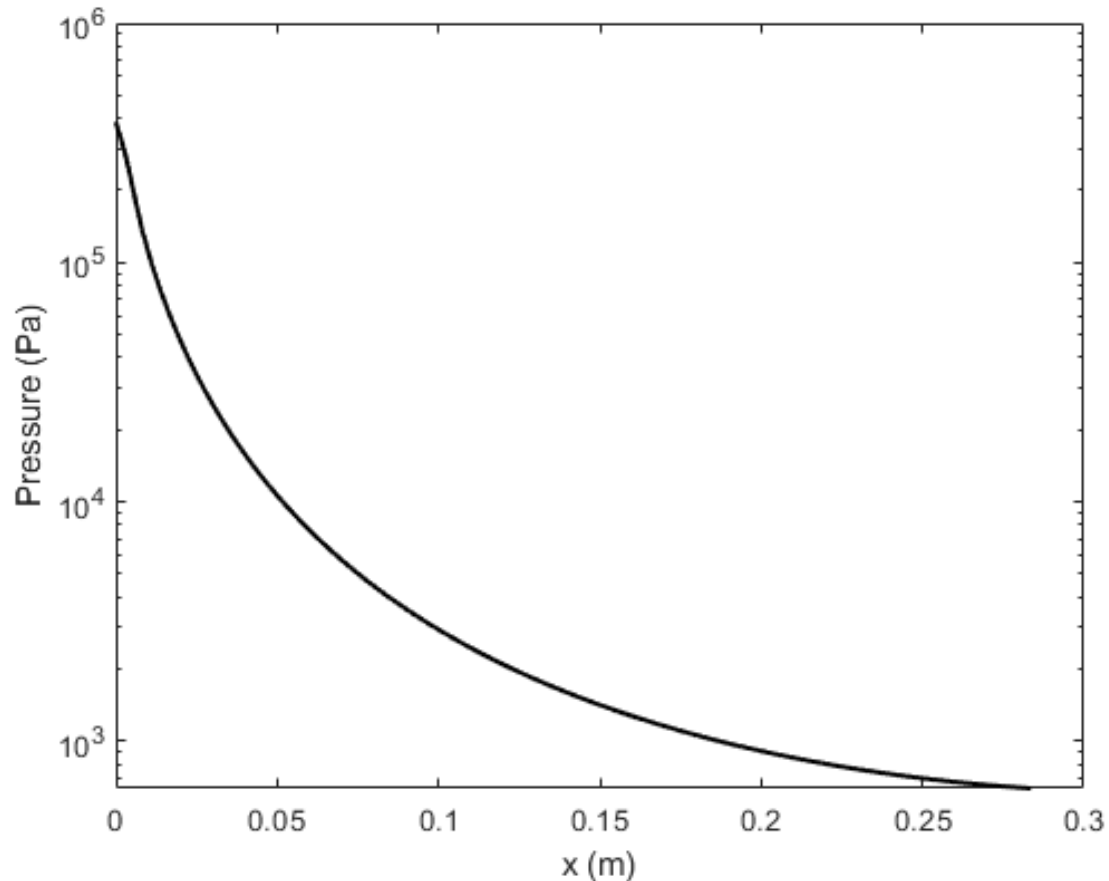


Figure 16.1: Inner pressure distribution on the nozzle walls, beginning at the throat

In regards to total pressure drop over the decomposition bed, a conservative estimate of a pressure rise of 5 bar from the previously found stagnation pressure of 730 kPa was chosen based on experimental data and testing of similar hydrazine decomposition engines [112], giving a pre-decomposition pressure of 1.23 MPa, or 12.3 bar.

The pressure drop along the decomposition bed is assumed to be linear. A weighted average is then taken and the decomposition chamber is approximated as a thin-walled pressure vessel. The nozzle as a whole is designed using a common nozzle alloy, Haynes 25 [113]. Using a factor of safety of 1.25, a common value used in rocketry and aerospace, a wall thickness is calculated using

$$th = \frac{P_{avg} d_c}{\sigma_{h25}/FS} \quad (16.11)$$

Where P_{avg} is the precalculated average pressure of 14.32 bar, σ_{h25} is the yield strength of Haynes 25 at an expected operating temperature of 700 C, 237 MPa, and FS is the aforementioned factor of safety of 1.25. Knowing these values, a necessary wall thickness of 2.81 mm is calculated.

16.3 Thermal Analysis

The primary method of heat transfer from a nozzle's propellant to the walls is through convection. Several methods exist for estimating this, though the Bartz correlation developed in 1965 is perhaps the most widely used [114]. Based on fully developed turbulent pipe flow, it is adapted for rocket nozzles and is used to find the local convective coefficient, h_g , which is given by [115]

$$h_g = \left[\frac{0.026}{(d^*)^{0.2}} \left(\frac{\mu^{0.2}}{Pr^{0.6}} C_p \right)_0 \left(\frac{P_0}{c^*} \right)^{0.8} \left(\frac{D^*}{r_c} \right)^{0.1} \right] \left(\frac{A^*}{A(x)} \right)^{0.9} \sigma_b \quad (16.12)$$

where d^* is the throat diameter, μ is the dynamic viscosity (approximated as air), r_c is the throat radius of curvature (equal to 1.5 times the throat radius for a Rao parabolic nozzle), Pr is the Prandtl number approximated by [115]

$$Pr = \frac{4\gamma_m}{9\gamma_m - 5} \quad (16.13)$$

c^* is the characteristic velocity, given by [85]

$$c^* = \frac{\sqrt{\gamma_m R_m T_0}}{\gamma_m \left(\frac{2}{\gamma_m + 1} \right)^{\frac{\gamma_m + 1}{2(\gamma_m - 1)}}} \quad (16.14)$$

and σ_b is a dimensionless factor accounting for the variation of density and viscosity along

the boundary layer of the flow, given by

$$\sigma = \frac{1}{\left[\frac{1}{2} \frac{T_{wg}}{T_0} \left(1 + \frac{\gamma-1}{2} M^2 \right) + \frac{1}{2} \right]^{0.8-0.2\omega} \left(1 + \frac{\gamma-1}{2} M^2 \right)^{0.2\omega}} \quad (16.15)$$

where T_{wg} is the temperature of the inner wall surface, and ω is a constant to describe the temperature exponent of the gas, assumed to be equal to 0.6.

As the convective heat transfer coefficient itself is dependent upon the temperature of the wall surface using this correlation, an initial guess is provided to be the average of the local gas temperature and the initial wall temperature.

The coefficient is then calculated, and a lumped capacitance model is used, an assumption valid for thin-walled vessels where the variation in temperature between both sides is minimal. In the case of internal convection and external radiation, the equation for the time derivative of temperature is given by [103]

$$\frac{dT_w}{dt} = \frac{\bar{h}_g(T_w - T^*) + \varepsilon \sigma_s (T_w^4 - T_\infty^4)}{\rho_{h25} c_{h25} \cdot th} \quad (16.16)$$

Where T_w is the local wall temperature, T^* is the gas temperature at the throat (maximum temperature and stress), ε is the emissivity of Haynes 25 at operating temperature and pressure (about 0.2 [116]), σ_s is the Stefan-Boltzmann constant, and c_{h25} is the specific heat of Haynes 25 at operating temperature and pressure [113].

The initial temperature before the burn is solved using a similar analysis with only radiation present and the nozzle launched into orbit at an initial temperature of 293 K. Equation 16.17 becomes

$$\frac{dT_w}{dt} = \frac{\varepsilon \sigma_s (T_w^4 - T_\infty^4)}{\rho_{h25} c_{h25} \cdot th} \quad (16.17)$$

which is solved from when the Falcon 9 vehicle hits 100 km, up to the final transfer for a total of seven days outlined in Section 6.2.5 for an initial pre-burn nozzle wall temperature of -162.76 °C.

With this, Equation 16.17 is solved forward as well over the expected 2 minute burn time. A plot of the wall temperature over the burn is shown in Figure 16.2.

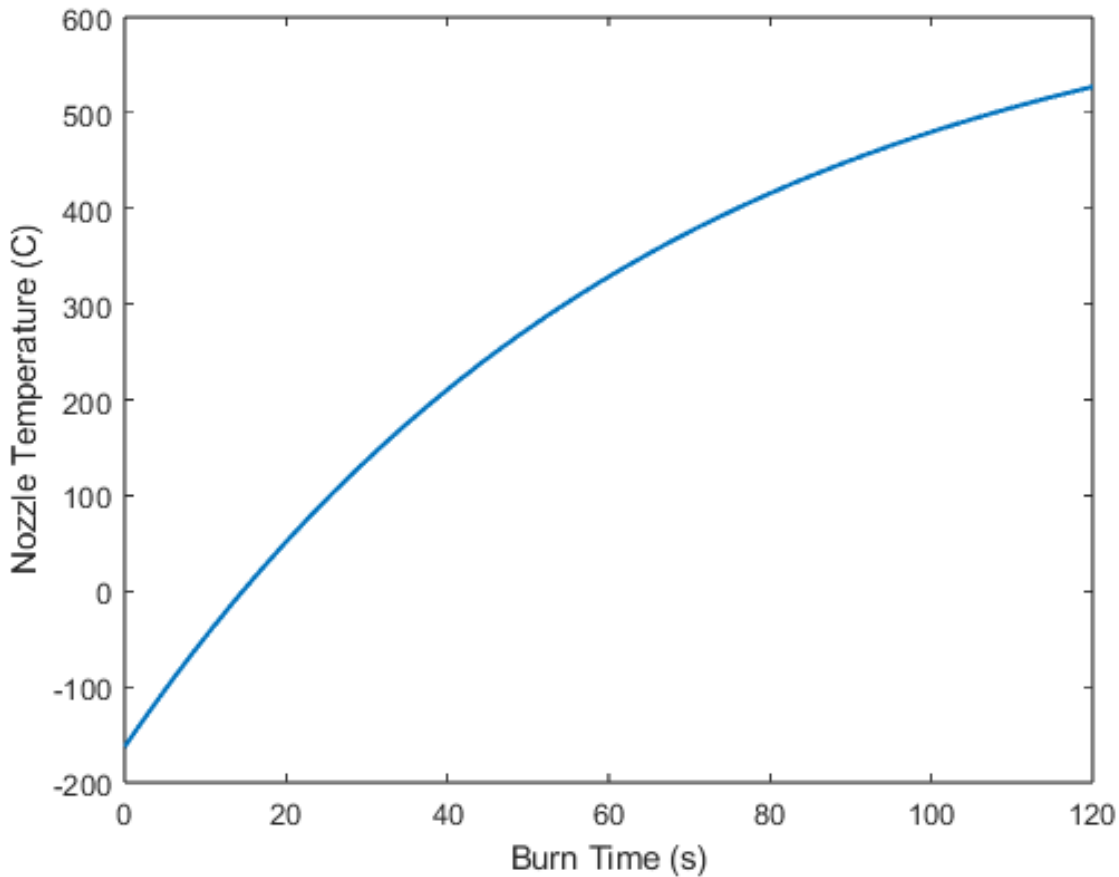


Figure 16.2: Nozzle wall temperature over burn time

A final, maximum temperature of the nozzle post-burn is thus calculated at 527.16 °C. This is lower than the conservative estimate of 700 °C used to calculate the material properties, and confirms that the engine is not at risk of strength loss due to thermal effects at any point in the burn process.

16.4 Injector Area Specifications

The injector used is a full cone nozzle, a type of nozzle able to evenly distribute particles over a full surface, often at angles ranging from 45 degrees to over 120 degrees. A visualization of an axial flow full cone nozzle, along with its droplet distribution, is shown in Figure 16.3.



Figure 16.3: An axial-flow full cone nozzle [117]

The necessary volumetric flow rate of the nozzle is calculated using

$$\dot{V} = \frac{\dot{m}}{\rho_{N_2H_4}} \quad (16.18)$$

where \dot{V} is the volumetric flow rate, \dot{m} is the previously calculated mass flow rate, and $\rho_{N_2H_4}$ is the density of hydrazine at the stored pressure. However, at the stored temperature, Hydrazine is a liquid and is treated as incompressible. Thus, it can be treated as equal to its room temperature density of 1021 kg/m^3 [85], giving a volumetric flow rate of $0.001406 \text{ m}^3/\text{s}$, or about 22.3 gal/min . There are several axial flow full cone nozzles capable of this while maintaining a high spray angle, such as the Lechler company's 405 or 459 series [117]. Often, these are constructed of either stainless steel or brass due to their ease of manufacturing and widespread availability.

The height required for the flow to fully distribute over the bed is simply calculated using

$$h_s = \frac{d_c}{2\tan(\alpha_s/2)} \quad (16.19)$$

where h_s is the spray height, d_c is the chamber diameter (0.372 m), and α_s is the spray angle, taken as 120 degrees (described as "large" [117]). This gives a necessary spray height of 0.1074 m for a total chamber length, pre nozzle convergence, of 0.1874 m. To reduce pressure vessel concentrations at the edge of the combustion chamber, the spray angle was used to create a hemispherical envelope later outlined in Section (ASSEMBLY SECTION).

As a general rule of thumb, the necessary storage pressure before an injector is estimated at about 10% higher than the pressure it is injecting into [64], which means the storage pressure sits at 14.1 bar. Though this does not impact the hydrazine's density, as stated, it is important to understand for the final sizing of the storage tanks.

16.5 Finite Element Work

The nozzle geometry was constructed in SOLIDWORKS and imported directly to ANSYS' DesignModeler program to perform a static structural analysis. As the analysis would be concerned with the geometry of the inner surface only, the model was converted into a surface, and the drill holes needed for mounting the end of the nozzle and combustion chamber to the thrust plate were covered over. However, the end condition present is approximated as being fixed around these holes only, and thus requires end geometry to be defined. These supports can be seen in Figure 16.4.

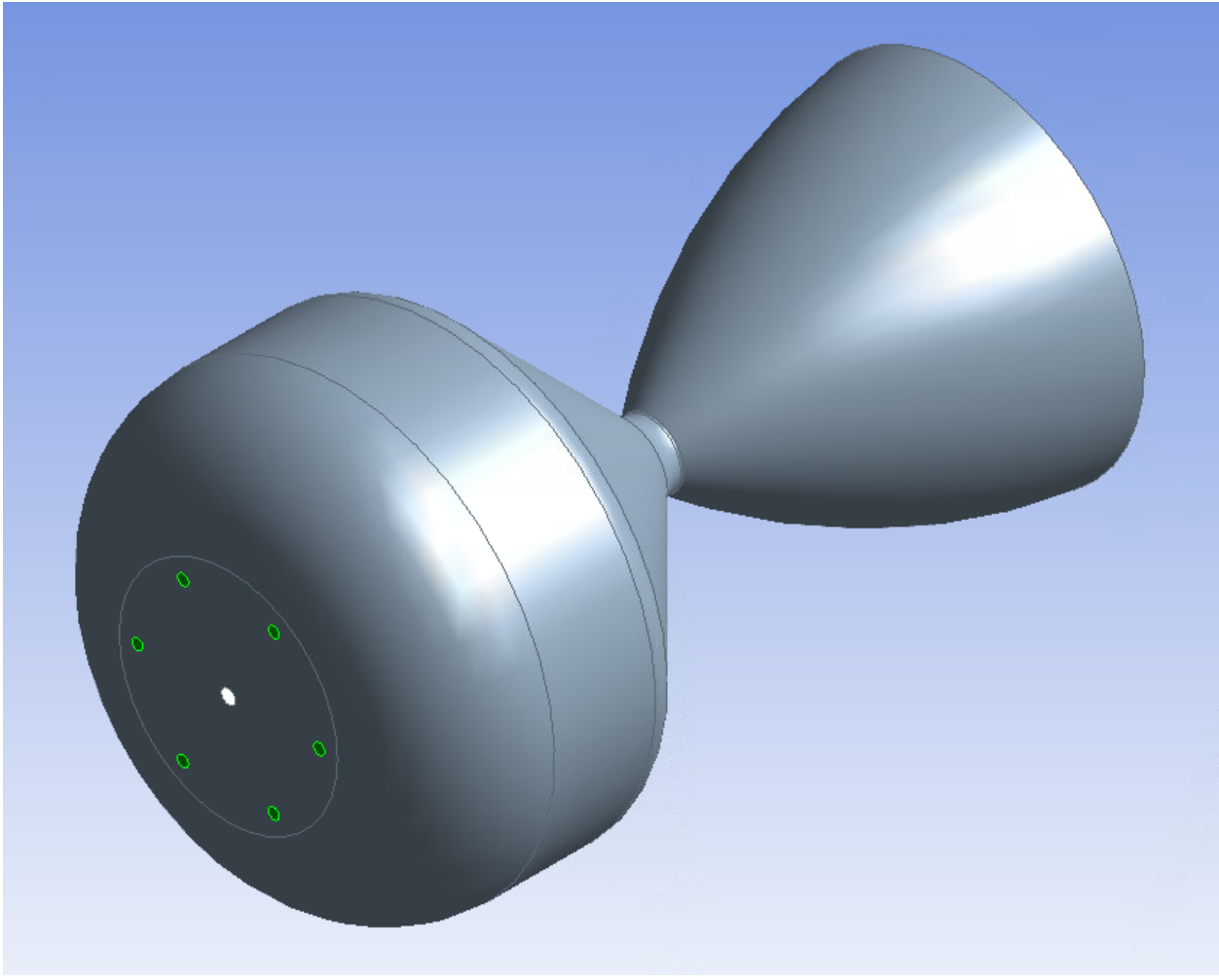


Figure 16.4: An isometric view of the nozzle surface, with fixed supports highlighted in green

Next, the Haynes 25 material was defined at a density of 9.07 g/cm^3 and its tabulated modulus of elasticity at a range of temperatures [113] (sitting around 188 GPa at the final burn temperature).

As the model is approximated as a surface, the default model type SHELL181 is used, a six degree of freedom quadrilateral element. The element size was set to 8 mm, mainly done so to ensure that any stress concentrations at the injector hole would not be overestimated due to overly coarse modeling. The meshed model can be seen in Figure 16.5.

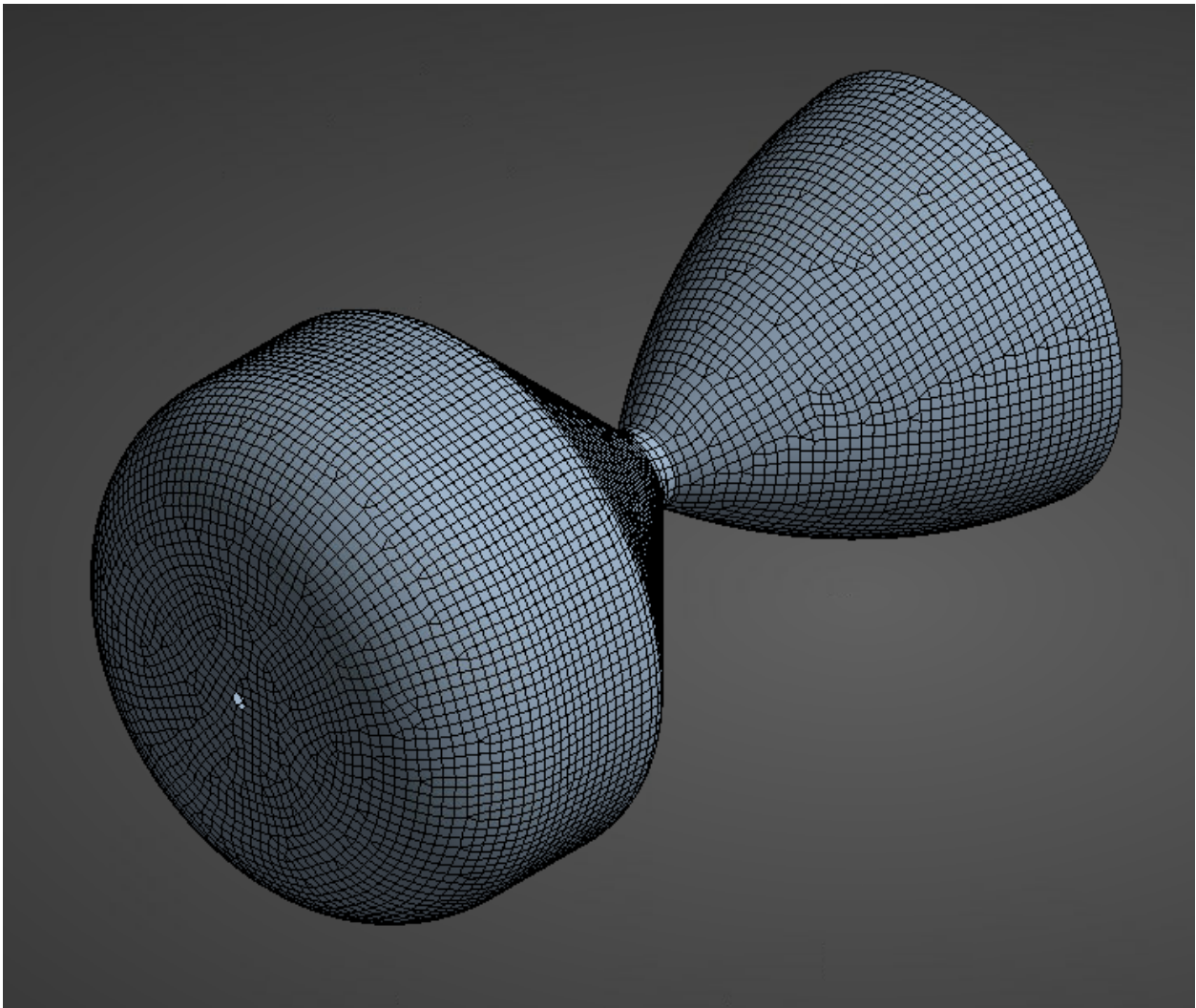


Figure 16.5: An isometric view of the meshed nozzle

The final element count for the mesh as a whole is 11007 elements, and 10888 nodes.

Apart with the fixed supports around the thrust plate connections, the primary force is the pressure previously outlined in Section 16.2. A plot of the full pressure distribution, beginning from the injector hole at $y=0$, is shown in Figure 16.6.

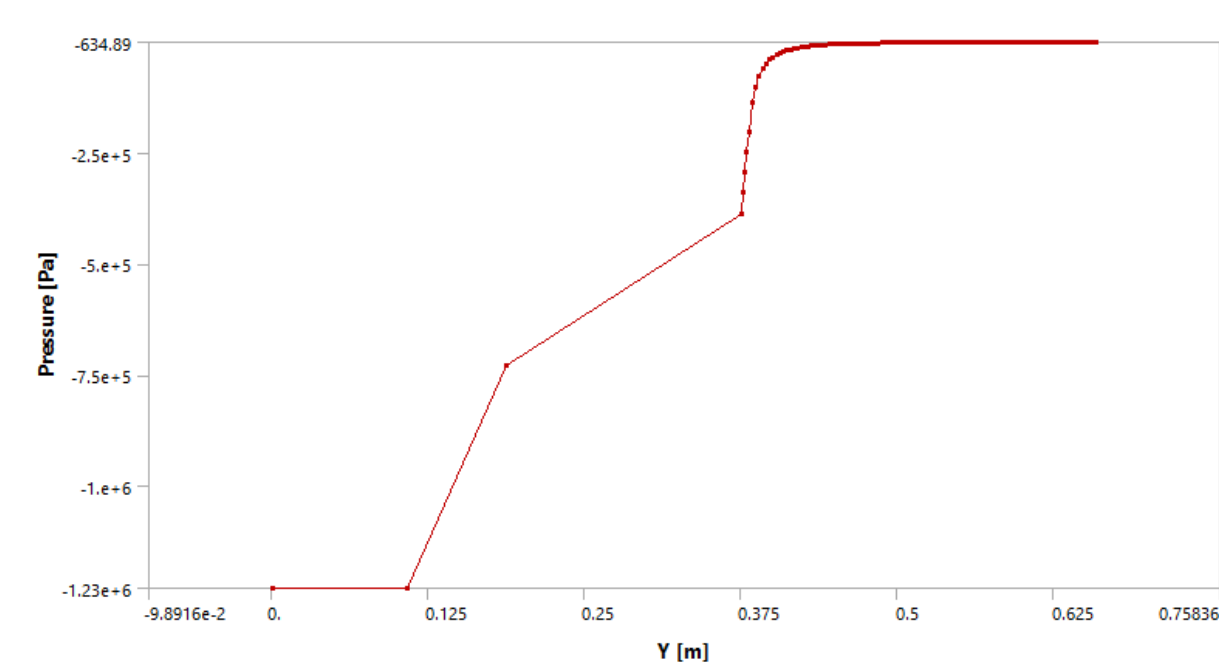


Figure 16.6: The full pressure distribution along the inner wall

Note that due to the pressure being internal, all values must be negative in ANSYS. The full pressure distribution is tabulated in Appendix I.

A solution was obtained and the equivalent stress is plotted in Figure 16.7.

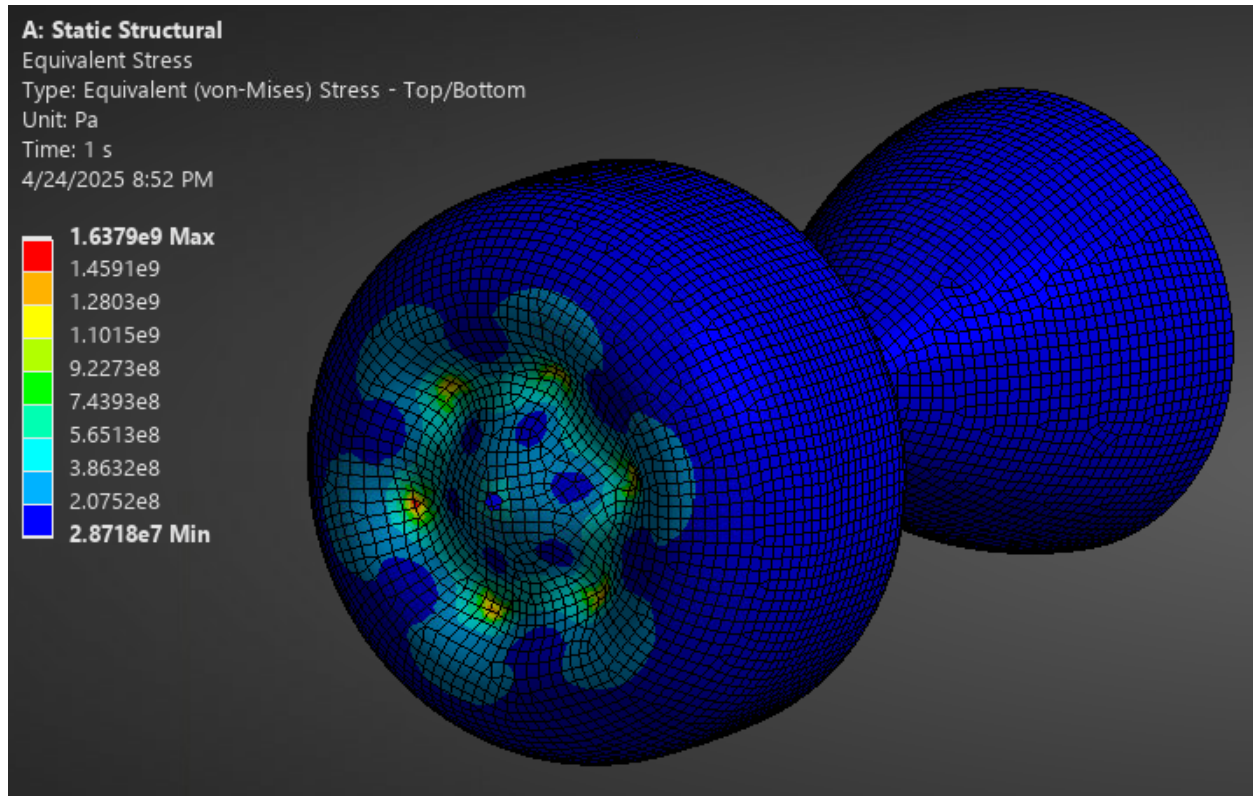


Figure 16.7: A contour plot of the von Mises stress

As seen, the maximum stress present significantly exceeds the yield strength of Haynes 25 at a wall temperature of 527 °C of about 265 MPa. Although the maximum stress present occurs at the fixed supports, there is also significant stress at the throat of the nozzle, shown in 16.8.

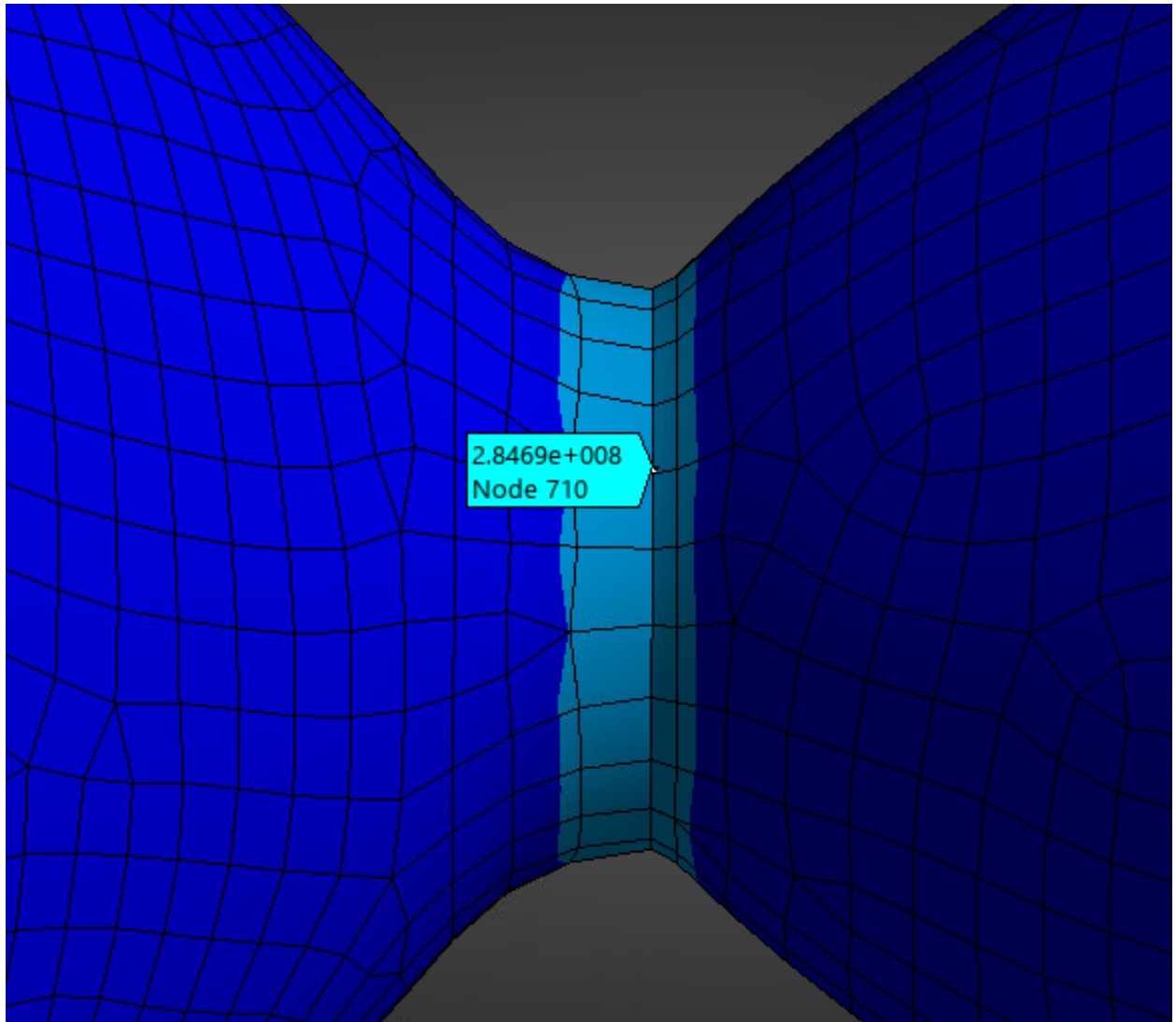


Figure 16.8: A contour plot of the von Mises stress around the nozzle throat

This high stress of 284 MPa is due to initial oversights in stress concentrations as well as a lack of weighting fidelity when performing the initial analysis. In order to combat these stress concentrations, the nozzle walls were thickened until this stress met the safety factor, and the endplate was given a separate thickness to do the same. Also to be considered is engagement length for bolts between the nozzle and thrust plate, assuming a #5-44 inch die thread (a commonly used bolt for engine-specific thrust mounting [16]).

As such, a final nozzle thickness of 5.62 mm and an endplate thickness of 11.87 mm were fine-tuned to yield, engagement length, and hole-based stress concentrations. A final von Mises diagram is shown in Figure 16.9.

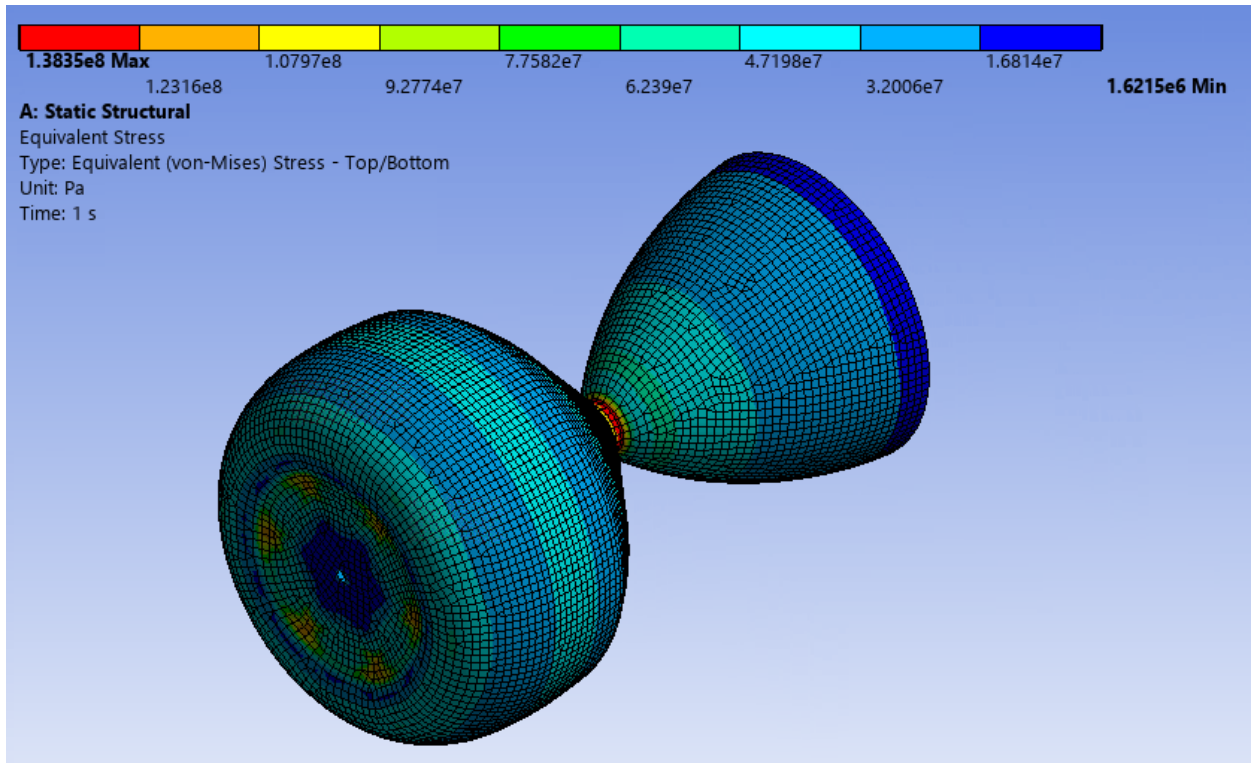


Figure 16.9: A contour plot of the von Mises stress around the updated nozzle throat

As seen, the maximum stress present is 138 MPa, and is newly centered at the throat of the nozzle.

16.6 Reflection and Future Work

Though the SHELL181 model performs well and yields consistent results under static loading at a specified burn-end temperature, more work is needed to further optimize the nozzle. Future work will include varying the thickness of the nozzle, as well as a more refined transient analysis for both structural and thermal effects. Furthermore, an injector analysis and more in-depth decomposition analysis will be performed to further optimize the size and shape of the engine.

17 Gripping Mechanism Analysis

The critical stress areas of the gripping mechanism are primarily in the torque responsible for generating the required clamping torque. This critical area will be analyzed in the section to follow to ensure teeth of the gear train remain unyielded.

17.1 Gear Reduction

From the sizing report for the gripping mechanism, the required clamping force was determined for the gripping mechanism. This requirement will drive the calculations the structural analysis of the gripping mechanism. To achieve this clamping force, gear reductions from the stepper motor will be required, therefore it is vital to ensure sufficient gear ratios are achieved and the teeth of each gear remains structurally sound. This should be done while also attempting to create a compact and efficient design. Figure 17.1 shows the inside of the planetary gearbox to achieve this reduction.

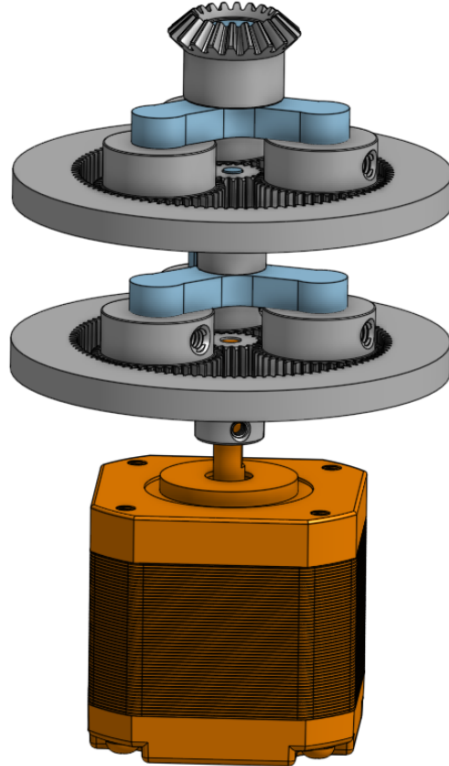


Figure 17.1: Inside view of planetary gearbox for gear reductions.

In Figure 17.1, there are two gear reductions present, both of which are equal in gear reduction, therefore the total gear reduction will be,

$$R_{total} = R^2 \quad (17.1)$$

where R is the gear reduction by one planetary gear set. The gear reduction by one planetary gear set is defined by,

$$R = \frac{N_i}{N_s} \quad (17.2)$$

where N_i is the number of teeth of the internal gear and N_s is the number of teeth on the sun gear.

The output of the second planetary gear set drives a bevel gear which drives the shaft connected to the clamps. It is known that the tip load on the final gear must be equal to F_{clamp} , 1550 N, from the sizing calculation. The required torque is,

$$\tau_o = F_{clamp}r_o \quad (17.3)$$

where τ_o is the output torque of the last shaft, F_{clamp} is the desired force, and r_o is the radial distance the force is applied from the center of the rotary clamp's gear. This results in a required output torque of 35 N·m. To achieve this torque from the stepper motor, the two gear reductions must provide the following increase in torque [118].

$$\tau_o = \tau_m R^2 \eta^i \quad (17.4)$$

Where τ_m is the stepper motor torque, R is a gear reduction, η is the efficiency of transmission between gears, and i is the number of gears meshed. For lubrication, Molybdenum Disulfide will be used which can achieve an efficiency of 97 percent for spur gears, conservatively. [118]

Solving the equation for (R^2), the required gear ratio is approximately 25. This gear ratio can be approximately achieved through a gear ratio of 5 for both planetary gear sets.

The teeth on the internal gear and the sun gear is constrained by Equation 17.2 to reach the desired gear reduction. The three planetary gears in the set must be sized such that,

$$D_{p,i} = 2D_{p,p} + D_{p,s} \quad (17.5)$$

where $D_{p,i}$ is the pitch diameter of the internal gear, $D_{p,p}$ is the pitch diameter of the planetary gears, and $D_{p,s}$ is the pitch diameter of the sun gear. Table 17.1 compiles the defining traits of the gears in each planetary gear set.

Table 17.1: Gear Specifications

Gear	Module	Pitch Diameter (mm)	Shaft Diameter (mm)	Number of Teeth
Internal	0.5	50	N/A	100
Planetary	0.5	20	6	40
Sun	0.5	10	8	20

It will be vital to ensure that the teeth of each gear will not yield due to the force it transmits. This stress will be dominated by bending stresses at the root of the tooth caused by tip loads during meshing. The bending stress due to a tip load on a tooth is

$$\sigma_t = \frac{W_t P_d}{F Y} \quad (17.6)$$

where σ_t is the stress in the tooth, W_t is the tangential force load, P_d is the diametral pitch (in in^{-1}), F is the face width (in in), and Y is the Lewis form factor [118]. The Lewis form factor, shown in Figure 17.2 is dependent on the number of teeth as well as the contact angle. A 20-degree full involute pressure angle is selected for the gear design as it provides an optimal balance between strength and efficiency, ensuring adequate load capacity while minimizing friction and excessive axial forces.

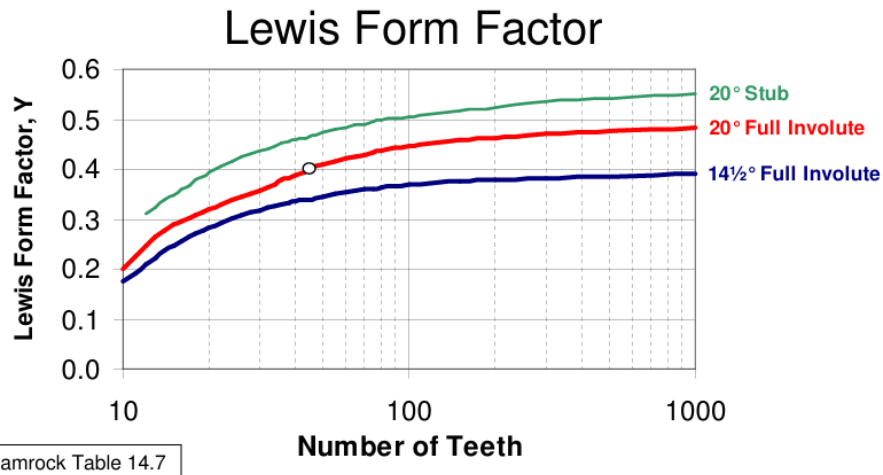


Figure 17.2: Lewis form factors for gears based on the contact angle.[118]

The total tip load outputted from the sun gear can be found using Equation 17.3 where τ_o is the torque of the shaft and r_o is half the sun gear's pitch diameter. The tip load is equally distributed between each mesh with the planetary gears.

$$W_{t,m} = \frac{F_{t,total}}{N} \quad (17.7)$$

where $F_{t,m}$ is the tip load at each mesh, $F_{t,total}$ is the total tip load from the sun gear, and N is the number of planetary gears [118]. Table 17.2, presents the numeric values for stress calculations for the second reduction since the gears are the same as the first set and the torque will be higher in the second set.

Table 17.2: Bending stresses in gears of the second planetary gearset

Gear	F (mm)	$W_{t,m}(N)$	σ_t (MPa)
Internal	5	467	415
Planetary	5	467	479
Sun	5	467	584

To not yield under this stress a martensitic stainless steel will be required. The gears will be made of stainless steel 410 for its strength and thermal properties. The yield stress of 410 stainless steel can reach 600 MPa [119]. To find the safety factor,

$$SF = \frac{\sigma_y}{\sigma_{max}} \quad (17.8)$$

where SF is the safety factor, σ_y is the yield stress, and σ_{max} is the max stress experienced by the gear. The safety factors are populated in Table 17.3.

Table 17.3: Gear Specifications

Gear	Safety Factor
Internal	1.45
Planetary	1.25
Sun	1.03

The safety factors of the internal and planetary gears are in line with those specified in NASA-STD-5001B [19]. The sun gear, being the highest stress gear, will be of concern moving forward. The sun gear is not expected to yield, however, the margin for production or usage error is minimal.

In addition to the bending stress already calculated, the gear teeth are subjected to shear stress due to the transmitted tangential force F_t . The nominal shear stress at the tooth root can be estimated by

$$\tau = \frac{F_t}{A_s}$$

where

$$A_s = b h_s$$

is the shear-plane area, with b the face width and h_s the shear-plane height (approximated by the dedendum, $h_s \approx 1.25$ m) [105]. The tangential force follows from the applied torque T and pitch diameter d :

$$F_t = \frac{2T}{d}.$$

Therefore, for each gear i (sun “s”, planet “p”, ring “r”), the shear stress becomes

$$\tau_i = \frac{2T_i}{d_i b h_{s,i}}, \quad i = s, p, r.$$

Substituting the dimensions and torques from Table 9.2:

$$\tau_s = \frac{2 T_s}{d_s b h_{s,s}},$$

$$\tau_p = \frac{2 T_p}{d_p b h_{s,p}},$$

$$\tau_r = \frac{2 T_r}{d_r b h_{s,r}}.$$

The resulting shear stress at the root for all gears in the second reduction is approximately 149 MPa, which is not a negligible stress as was previously expected [118]. This will surely cause the sun gear to yield in combination with the bending stress previously calculated. Future work will be required to increase the module of the gear to ensure structural integrity.

18 Re-entry Analysis

Another failure mode that must be considered is a failure to burn-up upon re-entry. A successful mission requires a burn-up of the STD, kick stage, and the target satellites as well as a safe burn-up away from populated areas. It will be assumed that upon re-entry, the Starlink satellites will burn-up on their own, as they have been designed to do so already [25]. The re-entry analysis will be broken into two parts. The first of which is trajectory analysis—will the satellite, if it fails to burn-up, land in a safe area? The second is if the STD and kick stage components will burn up at all.

18.1 Trajectory Analysis

It cannot be assumed that the kick stage and STD will automatically burn-up upon re-entry. For this analysis, it will be assumed that the kick stage and STDs do not burn-up and that their trajectory must put them in a safe landing zone away from populated areas. Section 6.4 used a model that just incorporated gravity. This section will use a 2-DOF (x,y) simulator with lift and drag effects. The equation of motion of the spacecraft Equation 6.16 must be updated.

The updated equation of motion will need to include lift and drag effects in terms of the inertial coordinate system (X,Y). Figure 18.1 shows the geometric relationship between the Earth-centered inertial (ECI) coordinates and the fixed-body coordinates (\hat{x}, \hat{y}) .

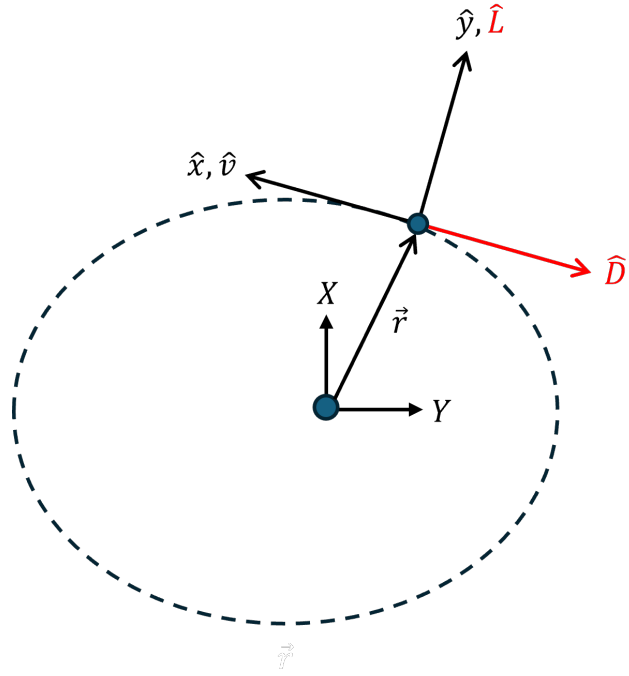


Figure 18.1: Lift and drag directions relative to ECI coordinate system.

From Figure 18.1, it is seen that the velocity vector \hat{v} is in the same direction as \hat{x} . This is a minor simplification, indicating that there would be a flight controller on-board the

spacecraft that maintains the attitude of the spacecraft to be in-line with the velocity. This allows for easier computation of the lift \vec{L} and drag \vec{D} without having to worry about angle of attack effects directly. The general equation of motion that includes lift and drag is

$$\frac{d^2\vec{r}}{dt^2} = -\frac{\mu}{|\vec{r}|^3}\vec{r} + \frac{\vec{D}}{m} + \frac{\vec{L}}{m} \quad (18.1)$$

where m is the mass of the spacecraft. The lift and drag vectors can be rewritten as

$$\vec{L} = L\hat{y} \quad (18.2)$$

and

$$\vec{D} = -D\hat{x} \quad (18.3)$$

where the scalar lift and drag values are

$$L = \frac{1}{2}\rho|\vec{v}|^2 A_s C_L \quad (18.4)$$

and

$$D = \frac{1}{2}\rho|\vec{v}|^2 A_s C_D \quad (18.5)$$

where ρ is the air density, A_s is the surface area of the spacecraft's lift and drag surfaces, C_D is the drag coefficient, and C_L is the lift coefficient. Substituting into Equation 18.1 yields

$$\frac{d^2\vec{r}}{dt^2} = -\frac{\mu}{|\vec{r}|^3}\vec{r} + \frac{1}{m} \left[\frac{1}{2}\rho|\vec{v}|^2 A_s C_L \hat{y} - \frac{1}{2}\rho|\vec{v}|^2 A_s C_D \hat{x} \right] \quad (18.6)$$

Using the fact that the velocity is in the same direction as \hat{x} , Equation 18.6 can be further rewritten as

$$\frac{d^2\vec{r}}{dt^2} = -\frac{\mu}{|\vec{r}|^3}\vec{r} + \frac{1}{m} \left[\frac{1}{2}\rho|\vec{v}|^2 A_s C_L \hat{y} - \frac{1}{2}\rho|\vec{v}|^2 A_s C_D \frac{\vec{v}}{|\vec{v}|} \right] \quad (18.7)$$

Since \hat{y} is 90° clock-wise from \hat{x} , a rotation matrix can be used to find the direction of \hat{y}

$$\hat{y} = \begin{bmatrix} 0 & -1 \\ 1 & 0 \end{bmatrix} \hat{x} \quad (18.8)$$

Since MATLAB's *ode113* solver calls the $\vec{f}(\vec{y}, t)$ for each time step, the direction of \hat{y} is calculated based on the current direction of the velocity which will be known.

Equation 18.7 has many variables that need to be addressed before simulating. The first of which is the air density ρ . A common model for air density is an exponential model [120] given by

$$\rho = \rho_0 \exp\left(\frac{h}{H_n}\right) \quad (18.9)$$

where ρ_0 is the density at sea level (1.225 kg/m^3), h is the altitude, and H_n is the scale height

(10.4 km). At each time step, the altitude is

$$h = |\vec{r}| - r_e \quad (18.10)$$

where r_e is the radius of Earth (6,378 km). The next variable to consider is A_s . Per [121], the lift and drag surface areas can be approximated as half of the total outside surface area. Without a final design for the kick stage or STD, 5 m^2 was used for the kick stage and 1 m^2 for the STD. From Section 11.2, the total mass of the kick stage will be around 5,000 kg when it de-orbits. From Section 9, the mass of the STD will be around 2,000 kg when it de-orbits. The last parameters to determine are the lift and drag coefficients. Since these values are highly dependent on the geometry of the satellite, they can only be approximated. Figure 18.2 shows the approximate drag and lift coefficients that can be expected upon re-entry. [These values come from \[122\] and assumed the body to be a particle of mass m, the same assumption used in the orbital mechanics calculations.](#)

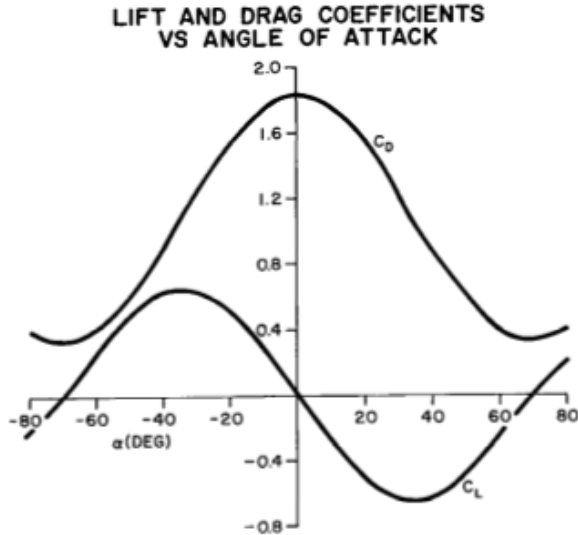


Figure 18.2: Drag and lift coefficients vs. angle of attack for re-entry vehicles [122].

Continuing the assumption that the flight controller will keep the spacecraft in alignment with the velocity, the angle of attack will be 0° . To account for some variability in this assumption, a perturbation of $\pm 10^\circ$ in the angle of attack will be accounted for by assuming worst-case scenarios. From Figure 18.2, the coefficient of drag ranges from 1.6–1.8 while the coefficient of lift varies from -0.4–0.4 in this $\pm 10^\circ$ band. When running the trajectory analysis, the lift and drag coefficients were fixed, giving a worst-case scenario and a potential landing zone.

The initial conditions of the re-entry trajectory are nearly identical for both the STD and kick stage. From their final orbits, they will go on a transfer ellipse with a perigee altitude of 100 km. Since the final orbits of the kick stage and STDs are all circular and have altitudes of $530 \pm 5\text{ km}$, the simulation only needs to be done from an altitude of 530 km. This is

because there is no practical difference in the $\pm 5\text{km}$ altitude of the orbits. The only thing that will vary for the STD and kick stage analyses is the mass and surface area.

MATLAB's *ode113* was used to solve the initial value problem. The kick stage de-orbit trajectory can be seen in Figure 18.3 for $C_D = 1.8$, $C_L = 0.4$.

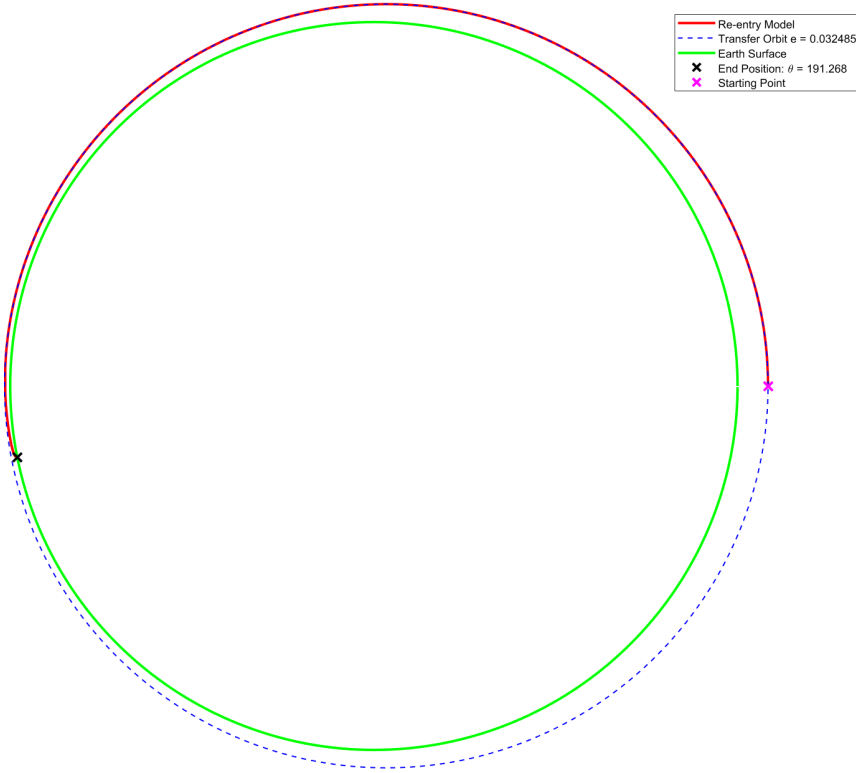


Figure 18.3: Re-entry trajectory of kick stage for $C_D = 1.8$, $C_L = 0.4$.

Figure 18.3 shows that the re-entry model predicts the kick stage, under the highest lift and drag conditions, to land 191.3° from where it is initially sent out on the de-orbit transfer ellipse. Under the same initial conditions and lift and drag coefficients, Figure 18.4 shows the re-entry trajectory for the STD.

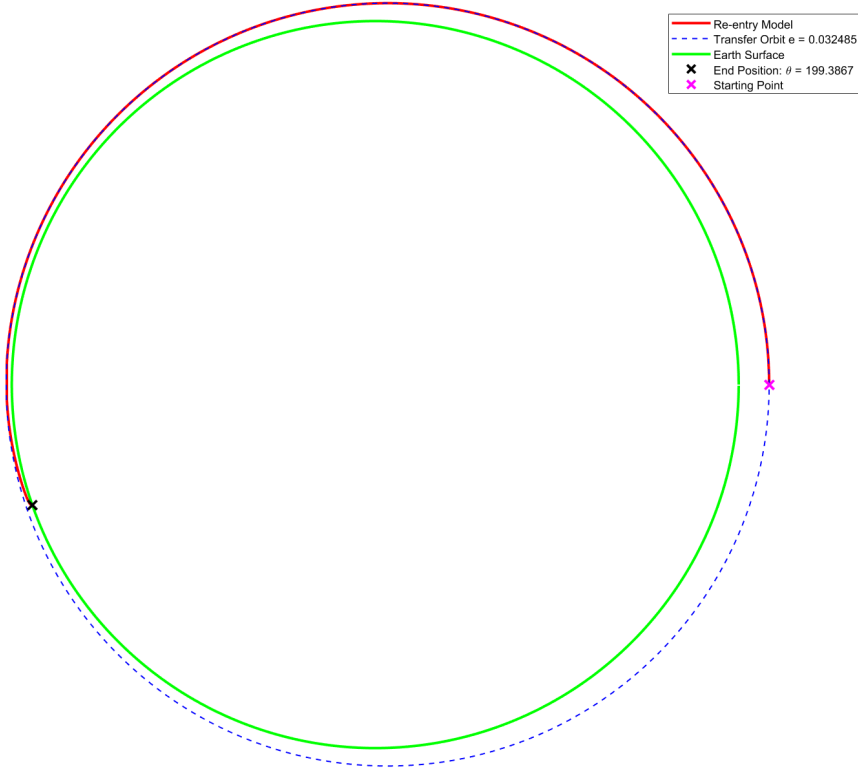


Figure 18.4: Re-entry trajectory of STD for $C_D = 1.8$, $C_L = 0.4$.

From Figure 18.4, the STD will land 199.4° from the initial transfer point. Compared the kick stage landing spot, this 8° difference equates to a 900 km difference in landing location assuming a perfectly spherical Earth. Figures 18.3 and 18.4 give only one case of constant C_D, C_L values. A parametric study was conducted to determine what the worst-case scenarios would be under the C_L and C_D ranges of $-0.4\text{--}0.4$ and $1.6\text{--}1.8$, respectively. The shortest trajectory, with the smallest θ -value, occurred when the drag was highest and the lift lowest at $C_D = 1.8$ and $C_L = -0.4$. The longest trajectory occurred when the drag was lowest and the lift was highest at $C_D = 1.6$ and $C_L = 0.4$. This result makes intuitive sense and is a good sanity check for surface-level model validity. Figures 18.5 and 18.6 shows the worst-case re-entry profiles for the kick stage and STD, respectively.

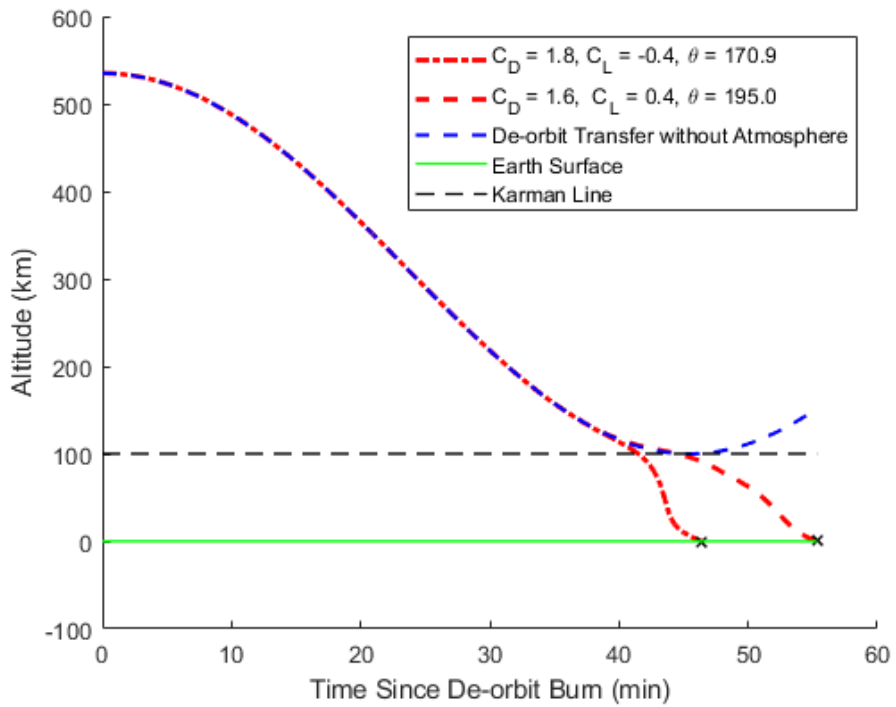


Figure 18.5: Re-entry profile of kick stage.

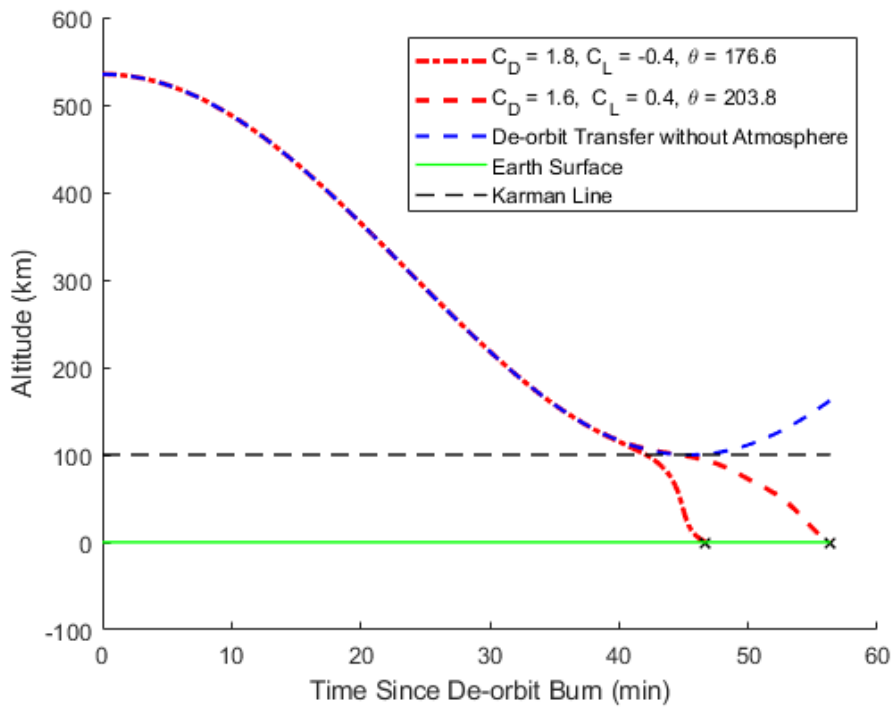


Figure 18.6: Re-entry profile of STDs.

From Figure 18.5, the kick stage, considering the worst-case conditions, will land at a θ -

value in the range of 170.9° – 195.0° occurring approximately 45 to 55 minutes after the initial de-orbit burn. This corresponds to a distance of 2,683 km. From Figure 18.6, the STDs, considering the worst-case conditions, will land at a θ -value in the range of 176.6° – 203.8° occurring approximately 46 to 56 minutes after the initial de-orbit burn. This corresponds to a distance of 3,028 km.

Additionally, it is important to note that the re-entry model suggests that both the kick stage and STDs will not ‘feel’ atmospheric effects until roughly 110–120 km, a result that matches common satellite de-orbits [123]. That is, the kick stage and STDs follow the transfer ellipse until atmospheric drag becomes high enough to lower the orbit, creating a positive feedback loop that results in the satellite crashing into Earth. This result validates the team’s choice to de-orbit the kick stage and STD by burning into an ellipse that takes it to the Karman line (100 km altitude).

18.1.1 Conclusion

Through the 2-DOF re-entry analysis, the landing zones for both the kick stage and STDs can be determined under worst-case scenarios of constant lift and drag coefficients. This now makes it possible to specify and target safe zones away from densely populated areas such as oceans. Currently, the model offers a very wide range (approximately 30° at most) in possible landing sites and is of no practical use if the site must be specified within a few kilometers. This wide range is due to the very conservative estimate in $\pm 10^\circ$ in angle of attack directly causing constant lift and drag. More robust control surfaces and a better flight controller could realistically make this $\pm 1^\circ$ giving more precision in the landing site. Nonetheless, if the de-orbit is done at the correct time, it could burn up over an ocean with great certainty as 70 percent of the Earth’s surface is covered in oceans. There should be no issues finding a 30° window of ocean. For example, Point Nemo is a common target location for satellite re-entry and is 2,688 km from the nearest coastline [124]. Assuming a spherical radius of 6,378 km, Point Nemo is approximately 24.15° from the nearest coast line. Centering the de-orbit burn to occur at Point Nemo will give approximately 9° ($24.15^\circ - \frac{30}{2}^\circ$) of clearance.

18.2 Thermal Analysis

In Section 18, to specify a landing zone, it was assumed that the kick stage and STDs will not burn-up upon re-entry. This section will explore the thermal effects present when performing atmospheric re-entry and ultimately decide whether the kick stage and STDs will burn-up upon re-entry. This will be done by doing a transient finite-difference analysis of the spherical tanks during re-entry.

18.2.1 Setup

After the trajectory analysis was completed, the entire flight profile is defined. That is, the velocity and altitude are known at each time step and can go into a model that calculates heat transfer effects. The foundational equation of this heat transfer analysis comes from

[125] as is given by

$$\dot{q}_{entry} = \frac{\alpha_T \rho V^3}{2} \quad (18.11)$$

where \dot{q}_{entry} is the stagnation point heat transfer rate, α_T is the thermal accommodation coefficient (assumed to be 0.7 [126]). V is the spacecraft's speed, and ρ is the air density. This heat transfer equation acts as an upper-bound for heat transfer rate and is widely used when engineering spacecraft that must safely return to Earth's surface rather than a spacecraft that must burn-up. Unfortunately, the exact heat transfer rates requires extensive finite-element analysis and cannot be obtained analytically in most regimes. Despite this, Equation 18.11 will be used to quantify re-entry heating effects.

One could imagine the extreme difficulty in solving this problem, especially given the complex geometry of the kick stage and STDs. Fortunately, it is widely assumed that upon re-entry, due to the immense forces, any structure or satellite will separate into its individual components (if not intentionally designed to) [127]. For this heat transfer analysis, not every sub-system on the kick stage and STD can be individually analyzed. This section will look at the Ti-6Al-4V (Ti64) fuel and pressurant tanks.

From Equation 18.11, V comes from the trajectory analysis completed in Section 18. Figure 18.7 shows the flight profile of the re-entry for the kick stage.

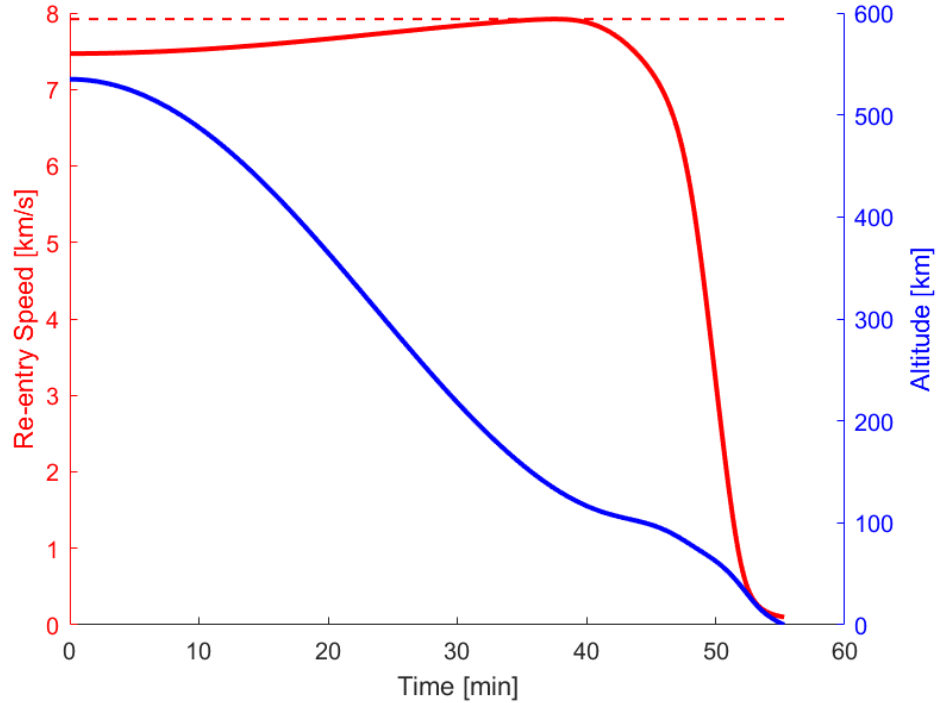


Figure 18.7: Re-entry profile of kick stage.

ρ is given by the exponential model for atmospheric density from Equation 18.9 and a function of the altitude values seen in Figure 18.7. Using Equation 18.11, the re-entry heating rate can be found at each time step and can be seen in Figure 18.8.

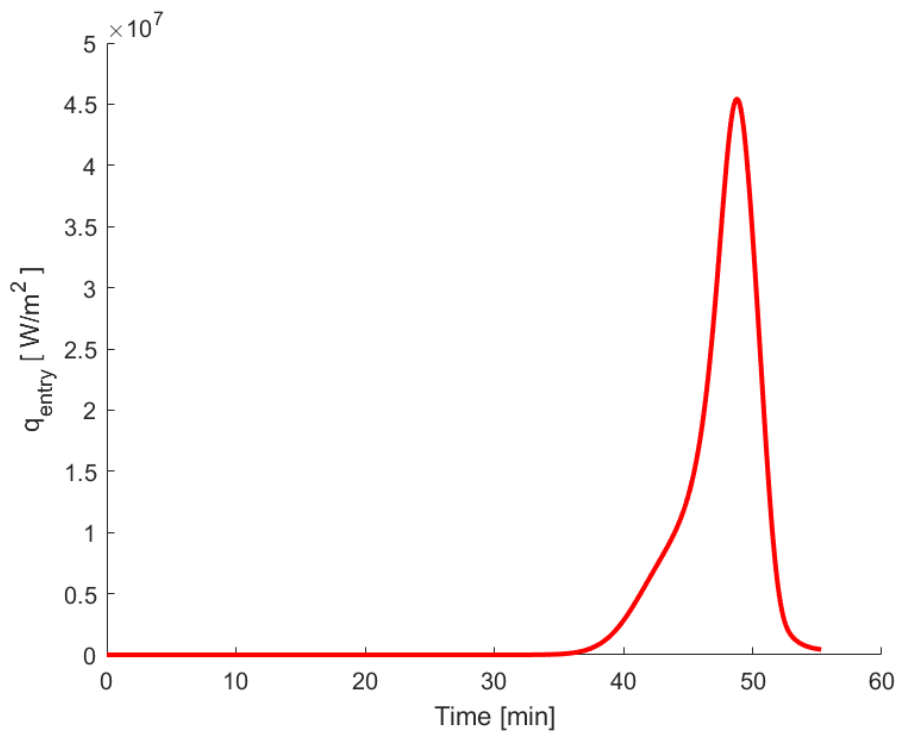


Figure 18.8: Re-entry \dot{q}_{entry} vs time for kick stage.

Seen in Figure 18.8, \dot{q}_{entry} can be seen reaching a maximum value of 4.5×10^7 W/m². To better visualize this heating, Figure 18.9 shows the kick stage altitude versus \dot{q}_{entry} .

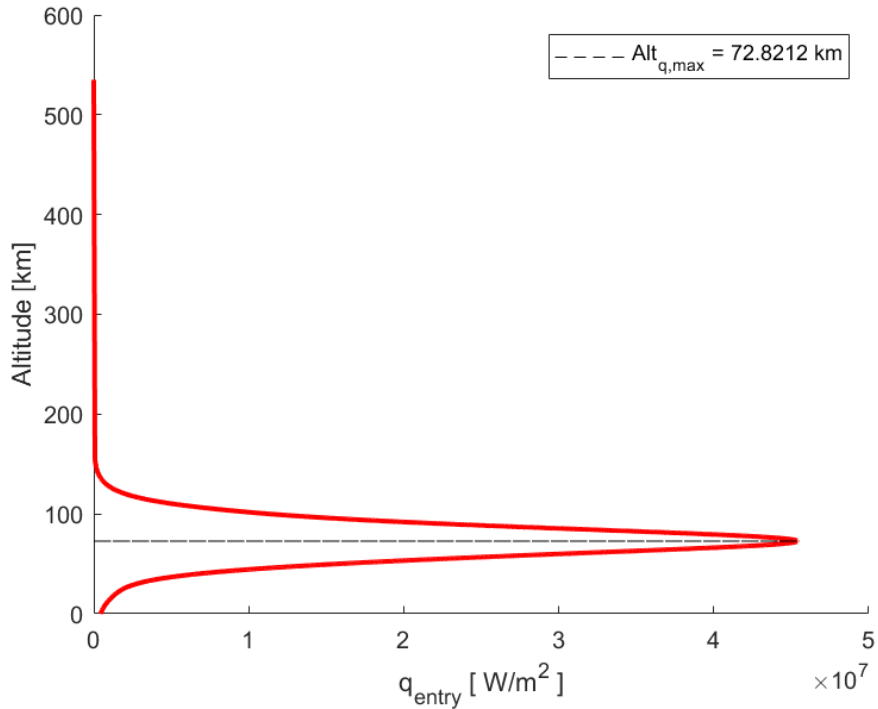


Figure 18.9: Re-entry altitude vs \dot{q}_{entry} for kick stage.

Visualized in Figure 18.9, the maximum heating rate occurs at an altitude of approximately 73 km. Additionally, in Figure 18.9, it can be seen that there is negligible heating before the atmospheric effects are present at an altitude of around 150 km.

18.2.2 Finite-Difference Method

The kick stage tank thermal analysis was completed assuming a spherical radius of 0.5 m with a thickness of 5 mm. The STD tank thermal analysis was completed assuming a spherical radius of 0.25 m with a thickness of 3 mm. Both the ambient (atmosphere) and hydrazine temperatures were held at constant extreme values. These would provide additional cooling to the tanks as they de-orbit. Whether or not this is a good assumption would need to be analyzed further. From [128], the temperature in LEO can reach -65°C (208.15 K). This was used as the constant ambient temperature as well as the hydrazine temperature. The hydrazine thermal properties were assumed constant and were found using EES [129].

The properties for Ti64 were also found using EES and imported into MATLAB for use. Density was assumed to be constant at $4,437 \text{ kg/m}^3$. However, the thermal conductivity and specific heat capacity will vary a lot in the operating temperature range of 200 K–1,943 K. Figures 18.10 and 18.11 show the thermal conductivity and specific heat capacity vs. temperature.

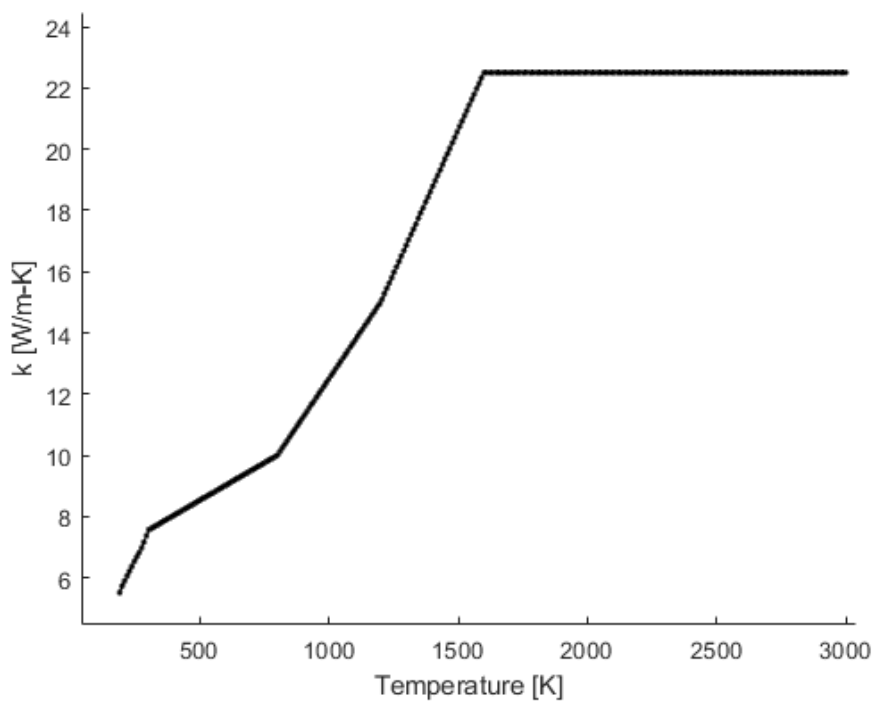


Figure 18.10: Thermal conductivity vs temperature for Ti64.

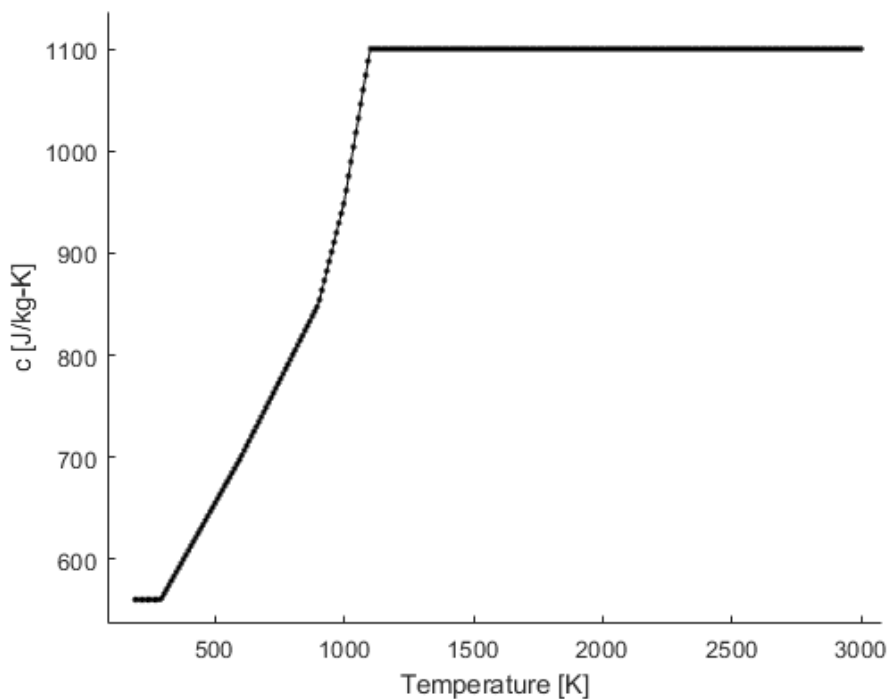


Figure 18.11: Specific heat capacity vs temperature for Ti64.

These correlations were used in the MATLAB script to calculate the thermal properties

at each time step. Similar to the assumption made when linearizing radiation, all of the properties at the current time step j were evaluated at the $j - 1$ time step at the control volume surface, ensuring energy conservation is met for each node. It is a valid approximation to evaluate properties using the $j - 1$ time step given that Δt is sufficiently small.

To measure the extent of ablation upon re-entry, a finite-difference method was used to analyze the temperature distribution within the wall thickness. Figure 18.12 shows the 1-D node setup for N spatial nodes.

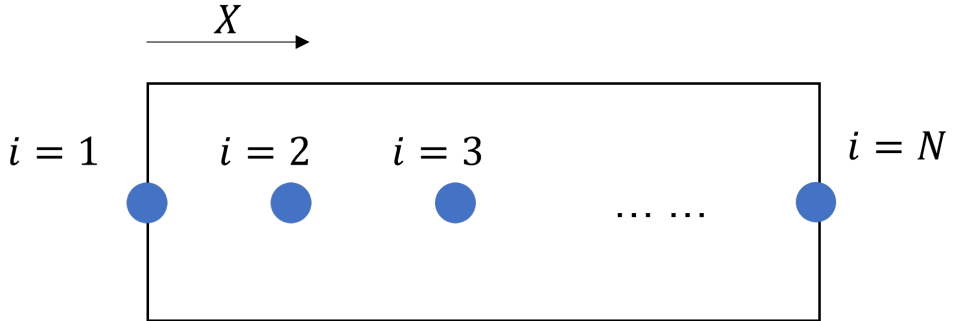


Figure 18.12: 1-D mesh setup for finite difference method.

From Figure 18.12, the nodal setup is represented by a 1-D line of nodes, representing a spatial location in the wall thickness cross section, seen by the black box. It can be seen that nodes 1 and N are on the inner and outer surface, respectively. The Crank-Nicolson method is an implicit method that gives second-order temporal and spatial accuracy. Its implicit property makes it not-so sensitive to temporal and spatial mesh sizing, unlike explicit methods that are highly sensitive to mesh sizes. The governing equation for the Crank Nicolson method came from [130] and is

$$T_{i,j} = T_{i,j-1} + \frac{\Delta t}{2} \left[\left. \frac{dT}{dt} \right|_{i,j} + \left. \frac{dT}{dt} \right|_{i,j-1} \right] \quad (18.12)$$

where T is the temperature, i is the spatial node, j is the time step, and Δt is the time step size. $\frac{dT}{dt}$ comes from an energy balance at node i generalized as

$$\sum \dot{q}_{in} = \sum \dot{q}_{out} + \dot{U} + \dot{g} \quad (18.13)$$

where \dot{q}_{in} is the heat rate into the node, \dot{q}_{out} is the heat rate out of the node, \dot{U} is the stored energy rate, and \dot{g} is generated heat. Equation 18.13 must be written for the the first node ($i=1$) at the inside surface of the spherical tank, the internal nodes ($2 \leq i \leq N - 1$), and the last node ($i=N$) at the outside surface of the spherical tank. For the first node ($i=1$), the energy balance is

$$\dot{q}_{2 \rightarrow 1,j} = \dot{q}_{1 \rightarrow H,j} + \dot{U}_{1,j} \quad (18.14)$$

where the terms can be expanded by

$$\dot{U}_{i,j} = \rho c \Delta x \left. \frac{dT}{dt} \right|_{i,j} \quad (18.15)$$

and Fourier's Law

$$\dot{q}_{m \rightarrow n,j} = \frac{k}{\Delta x} (T_{m,j} - T_{n,j}) \quad (18.16)$$

where ρ is the density, c is the specific heat capacity, and k is the thermal conductivity. Rewriting Equation 18.14 using Equations 18.15 and 18.16 gives

$$\frac{k_T}{\Delta x} (T_{2,j} - T_{1,j}) = \frac{k_H}{\Delta x} (T_{1,j} - T_H) + \rho_T c_T \Delta x \left. \frac{dT}{dt} \right|_{i,j} \quad (18.17)$$

where the subscripts T and H refer to the materials Ti64 and Hydrazine, respectively. Solving Equation 18.17 for $\left. \frac{dT}{dt} \right|_{i,j}$ and substituting into Equation 18.12 where $i = 1$ gives

$$T_{1,j} = T_{1,j-1} + \frac{\Delta t}{2} \left[\frac{\alpha_T}{\Delta x^2} (T_{2,j} - T_{1,j}) - \frac{k_H}{\rho_T c_T \Delta x^2} (T_{1,j} - T_H) \right] + \frac{\Delta t}{2} \left[\frac{\alpha_T}{\Delta x^2} (T_{2,j-1} - T_{1,j-1}) - \frac{k_H}{\rho_T c_T \Delta x^2} (T_{1,j-1} - T_H) \right] \quad (18.18)$$

Equation 18.18 must be simplified by grouping like-terms, putting all j terms on the left-hand side and $j - 1$ terms on the right-hand side giving

$$T_{1,j} \left[\frac{2}{\Delta t} + \frac{\alpha_T}{\Delta x^2} + \frac{k_H}{\rho_T c_T \Delta x^2} \right] + T_{2,j} \left[\frac{-\alpha_T}{\Delta x^2} \right] = T_{1,j-1} \left[\frac{2}{\Delta t} - \frac{\alpha_T}{\Delta x^2} - \frac{k_H}{\rho_T c_T \Delta x^2} \right] + T_{2,j-1} \left[\frac{\alpha_T}{\Delta x^2} \right] + T_H \left[\frac{2k_H}{\rho_T c_T \Delta x^2} \right] \quad (18.19)$$

For the internal nodes ($2 \leq i \leq N - 1$), the energy balance from Equation 18.13 gives

$$\dot{q}_{i+1 \rightarrow i,j} = \dot{q}_{i \rightarrow i-1,j} + \dot{U}_{i,j} \quad (18.20)$$

Following a similar process as the first node, Equation 18.20 can be put into the same form as Equation 18.19 giving

$$T_{i,j} \left[\frac{1}{\Delta t} + \frac{\alpha_T}{\Delta x^2} \right] + T_{i+1,j} \left[\frac{-\alpha_T}{2\Delta x^2} \right] + T_{i-1,j} \left[\frac{-\alpha_T}{2\Delta x^2} \right] = T_{i,j-1} \left[\frac{1}{\Delta t} - \frac{\alpha_T}{\Delta x^2} \right] + T_{i+1,j-1} \left[\frac{\alpha_T}{2\Delta x^2} \right] + T_{i-1,j-1} \left[\frac{\alpha_T}{2\Delta x^2} \right] \quad (18.21)$$

For the external node ($i = N$), the energy balance is

$$\dot{q}_{entry,j} = \dot{q}_{N \rightarrow N-1,j} + \bar{h}(T_{N,j} - T_{\infty,j}) + \dot{U}_{N,j} \quad (18.22)$$

Repeating the same procedure gives

$$\begin{aligned} T_{N-1,j} \left[\frac{-\alpha_T}{\Delta x^2} \right] + T_{N,j} \left[\frac{2}{\Delta t} + \frac{\alpha_T}{\Delta x^2} + \frac{\bar{h}}{\rho_T c_T \Delta x} \right] &= T_{N-1,j-1} \left[\frac{\alpha_T}{\Delta x^2} \right] \\ + T_{N,j} \left[\frac{2}{\Delta t} - \frac{\alpha_T}{\Delta x^2} - \frac{\bar{h}}{\rho_T c_T \Delta x} \right] + \left[\frac{\bar{h}}{\rho_T c_T \Delta x} \right] (T_{\infty,j} + T_{\infty,j-1}) + \left[\frac{1}{\rho_T c_T \Delta x} \right] (\dot{q}_{entry,j} + \dot{q}_{entry,j-1}) \end{aligned} \quad (18.23)$$

Equations 18.19, 18.21, and 18.23 can be put into matrix form

$$\mathbf{A} \vec{T}_{i,j} = \vec{b} \quad (18.24)$$

where \mathbf{A} is an $N \times N$ matrix of coefficients, $\vec{T}_{i,j-1}$ is a $N \times 1$ vector of current time step temperatures, and \vec{b} is the right-hand side terms. From Equation 18.19, \bar{h} is the heat transfer coefficient given by

$$\bar{h} = h_{conv} + h_{rad} \quad (18.25)$$

where h_{conv} is the convective heat transfer coefficient and h_{rad} is a linearized approximation of the radiation heat transfer coefficient. h_{conv} , from [130], is given by

$$h_{conv} = \frac{\text{Nu}_D k_{air}}{D} \quad (18.26)$$

where D is the diameter of the spherical tank and Nu is the Nusselt number given by the correlation

$$\text{Nu}_D = 2 + \left(0.4 \text{Re}_D^{0.5} + 0.06 \text{Re}_D^{\frac{2}{3}} \right) \text{Pr}^{0.4} \quad (18.27)$$

where Pr is the Prandtl number (assumed to be 0.7 for air [129]) and Re_D is the Reynolds number given by

$$\text{Re}_D = \frac{\rho V D}{\mu_{air}} \quad (18.28)$$

where μ_{air} is the kinematic viscosity of the air (50×10^{-3} W/K – m [130]). The linearized approximation of radiation heat transfer comes from [the non-linearized governing equation](#)

$$\dot{q}_{rad} = 4A_s \varepsilon \sigma (T_{N,j}^4 - T_{\infty,j}^4) \quad (18.29)$$

where A_s is the surface area, ε is emissivity, and σ is the Stefan-Boltzmann constant (5.567×10^{-8} W/m²–K⁴). Equation 18.29 can be rewritten as

$$\dot{q}_{rad} = 4A_s \varepsilon \sigma (T_{N,j}^2 + T_{\infty,j}^2)(T_{N,j} + T_{\infty,j})(T_{N,j} - T_{\infty,j}) \quad (18.30)$$

where the coefficient of $(T_{N,j} - T_{\infty,j})$ can be approximated by the $j - 1$ terms given Δt is relatively small. This gives

$$\begin{aligned} &4A_s \varepsilon \sigma (T_{N,j}^2 + T_{\infty,j}^2)(T_{N,j} + T_{\infty,j})(T_{N,j} - T_{\infty,j}) \\ &\approx 4A_s \varepsilon \sigma (T_{N,j-1}^2 + T_{\infty,j-1}^2)(T_{N,j-1} + T_{\infty,j-1})(T_{N,j} - T_{\infty,j}) \end{aligned} \quad (18.31)$$

Labeling this coefficient h_{rad} gives

$$\dot{q}_{rad} \approx h_{rad}(T_{N,j} - T_{\infty,j}) \quad (18.32)$$

where h_{rad} is calculated at each time step based on the previous values. This approximation makes the radiation term linear, allowing it to be solved using matrix math without an iterative approach. Some accuracy is lost with this approximation, but given a small enough time step Δt , there should not be large jumps in temperature.

The MATLAB script used to conduct both the trajectory- and thermal analysis can be seen in Appendix C.7. The analysis was done using a time step of 0.0025 s resulting in 1.3 million temporal nodes and used 11 spatial nodes throughout the wall thickness to see the extent of ablation. The kick stage and STD tank thermal analyses were conducted using the C_D - and C_L -values that provided the longest trajectory. Through testing, it was found that these trajectories resulted in the lowest \dot{q}_{max} -values. Despite the massive mesh size, the MATLAB code runs in just under 45 s. This is the benefit of using a package like MATLAB where matrix math is highly optimized. To give context, preliminary attempts at conducting explicit (forward time step) transient responses had run times upwards of 15 minutes with only 600 thousand temporal nodes and 11 spatial nodes—and even then—the solutions were diverging due to insufficiently small time steps!

Figure 18.13 shows the temperature distribution in the kick stage tank over time while Figure 18.14 shows the temperature at the inner and outer nodes over time. For this analysis, ablation is considered to have occurred when the nodal temperature reaches the melting point of Ti64 assumed to be 1,943 K [129].

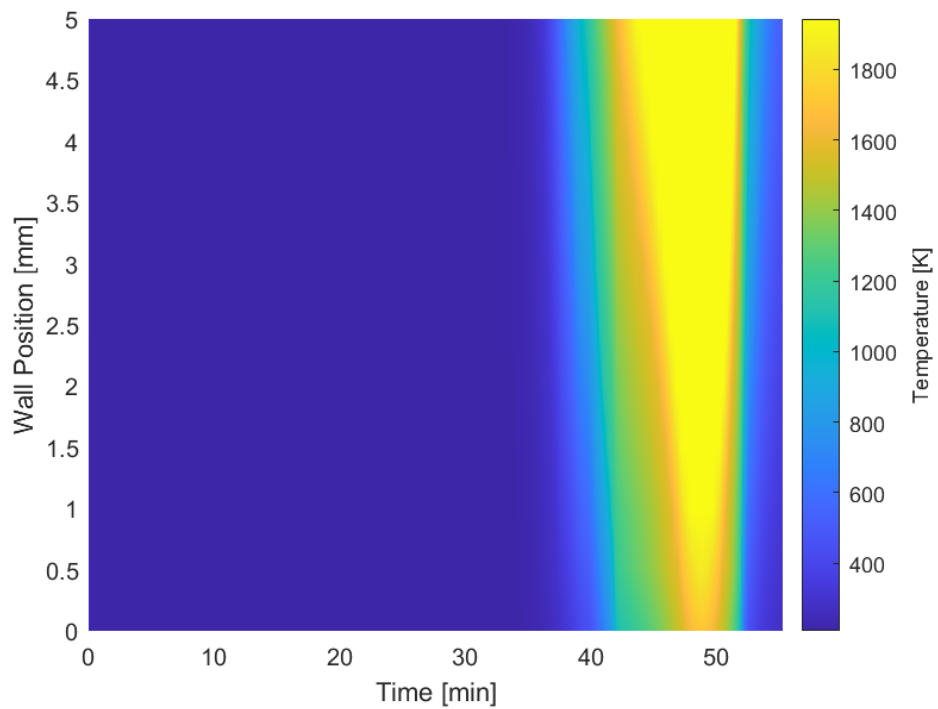


Figure 18.13: Temperature distribution in kick stage tank wall vs. time.

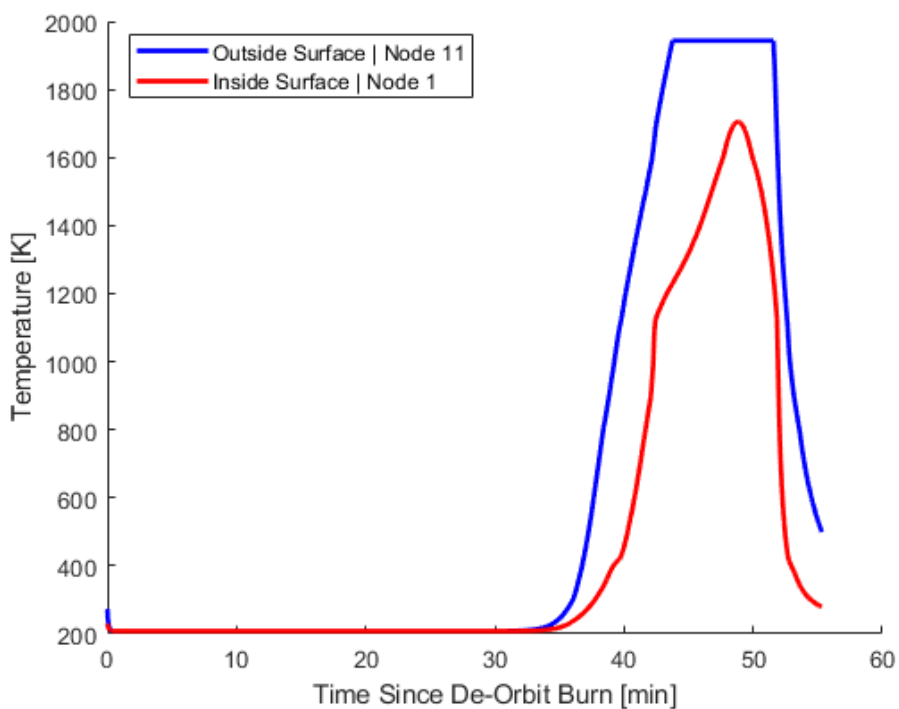


Figure 18.14: Inner and outer nodal temperature in kick stage tank wall vs. time.

From the results in Figures 18.13 and 18.14, the kick stage tanks will ablate away 4 mm of

the 5 mm tank. The analysis did not account for displacement of melted material or the change in temperature of the hydrazine. It can not be assumed that the kick stage tank will burn up fully and thus should have its landing specified over a safe area.

Figure 18.15 shows the temperature distribution in the STD tank over time while Figure 18.16 shows the temperature at the inner and outer nodes over time.

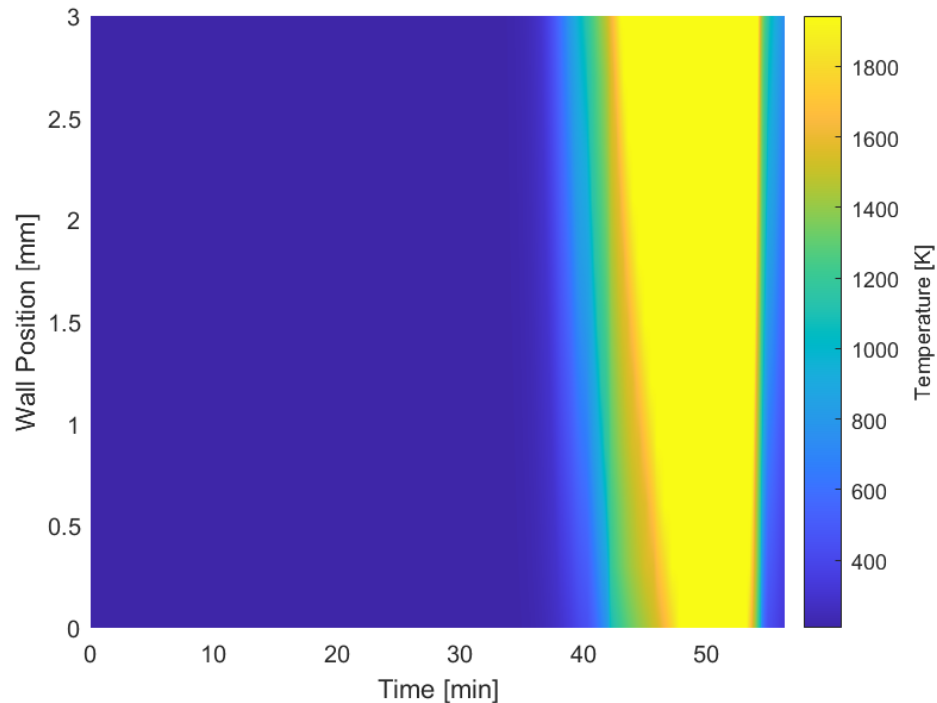


Figure 18.15: Temperature distribution in STD tank wall vs. time.

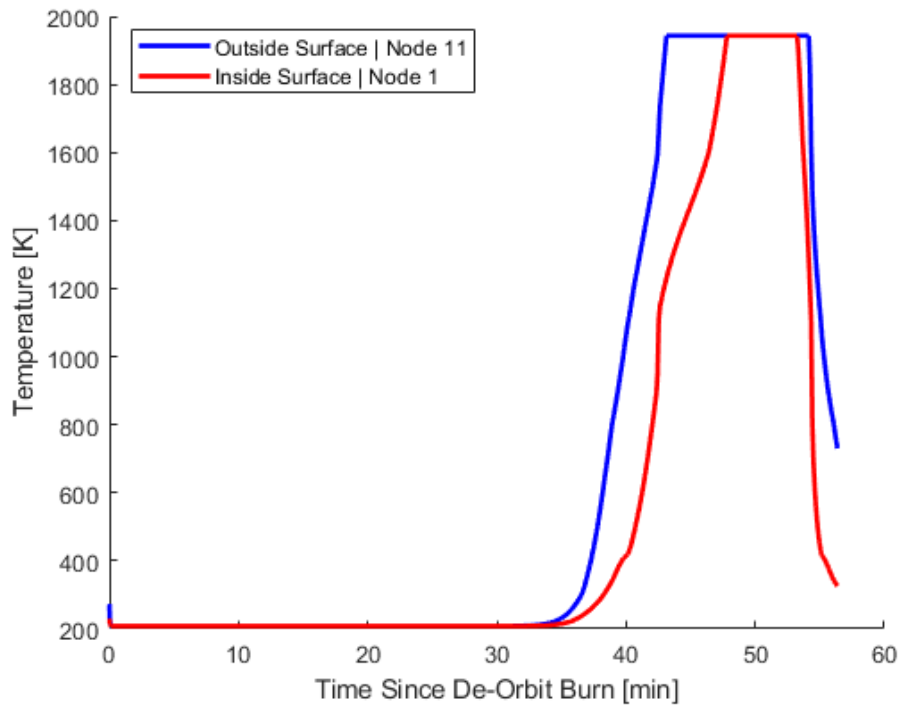


Figure 18.16: Inner and outer nodal temperature in STD tank wall vs. time.

From the results in Figures 18.15 and 18.16, the STD tank will fully ablate during re-entry. With these results, the STDs could, in theory, be de-orbited anywhere on Earth, but it is best to specify the trajectory using the results from Section 18. The kick stage, however, should have its landing site specified such that it will burn-up over an ocean or unpopulated areas.

19 Design

19.1 Kick Stage

The kick stage serves as the carrier and deployment platform for the STDs, delivering them to their designated orbital altitudes and inclinations. After separation from the Falcon 9 launch vehicle, the kick stage executes a series of maneuvers to release the STDs in their target orbits before performing its controlled de-orbit. The kick stage is designed to operate autonomously in orbit, providing propulsion, structural support, and payload deployment functionality.

This section details the major subsystems of the kick stage design, including the structural configuration, propellant and pressurant tanks, propulsion system, and payload integration features. Each component is engineered to ensure mission reliability while minimizing overall mass.

19.1.1 Mounting Frame

The upper frame of the kick stage provides the primary load path between the kick stage and the STDs. It is designed to transfer vertical loads up to 6 g and lateral loads up to 3.5 g into the lower lattice and ultimately to the payload adapter interface [[spacexrideshare](#)]. During on-orbit propulsion operations, the frame also transmits thrust forces from the engine mount through the entire stage structure.

The frame is constructed using welded 6061-T6 aluminum square tubing to balance structural rigidity with mass efficiency. Aerospace-grade TIG welding is employed to achieve strong, fatigue-resistant joints compliant with NASA-STD-6016 workmanship standards [17]. All frame members are designed to efficiently carry both axial and bending loads under dynamic conditions.

The interior of the frame accommodates the nitrogen pressurant tanks, which are mounted via welded brackets directly attached to the frame's bottom ring, shown in Figure 19.1. The mounting layout is optimized to maintain a centralized center of gravity throughout the mission, minimizing torque requirements for attitude control.

Finite Element Analysis (FEA) confirmed positive margins of safety against yield and ultimate failure modes under both static and vibrational loads, using design factors specified in NASA-STD-5001B [19].

A CAD rendering of the kick stage frame is shown in Figure 19.1.

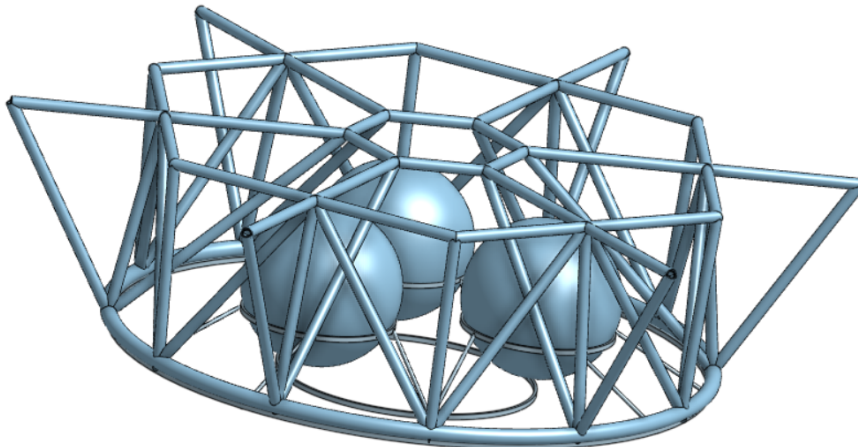


Figure 19.1: Kick Stage Upper Frame Assembly for Payload and Nitrogen Tank Support.

19.1.2 Lattice Structure

The cylindrical lattice structure below the frame supports the bipropellant tanks and forms the structural backbone of the kick stage. Its primary functions are to:

- Provide discrete bays for mounting the 2100L and 1450L propellant tanks.
- Transfer axial and lateral loads from the tanks to the launch vehicle interface.
- Prevent buckling under launch accelerations by reducing unsupported span lengths.

The lattice is fabricated from welded aluminum tubular members arranged in a diagonal truss pattern to minimize mass while maximizing stiffness.

The lattice is welded to the propellant tank mounts, the kick stage frame above, and the thrust puck below. This integration ensures that propulsion thrust loads are carried directly into the primary structural paths without overloading any single member.

Figure 19.2 shows the cylindrical lattice structure supporting the propellant tank assembly.

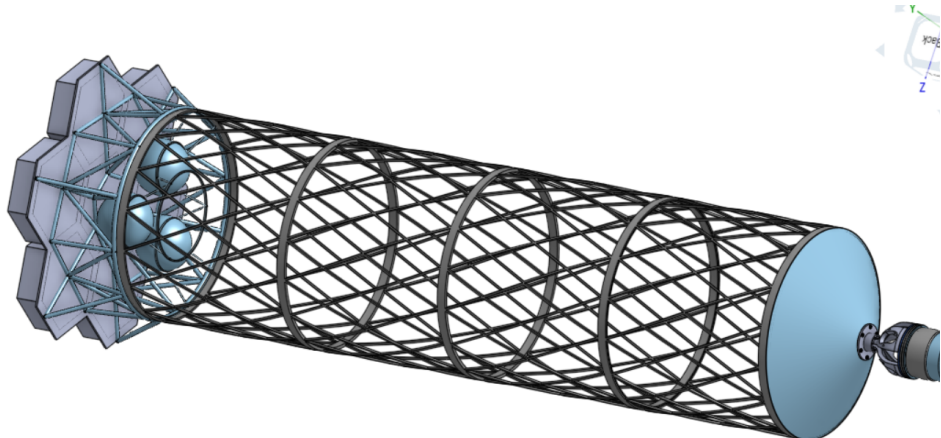


Figure 19.2: Kick Stage Cylindrical Lattice Structure.

19.1.3 Tanks

The kick stage tank system is designed to store and deliver the monomethylhydrazine and dinitrogen tetroxide, and the nitrogen pressurant required for propulsion operations. The tank system must support mission needs across multiple burns, maintain high reliability throughout storage and operation in orbit, and meet structural requirements during launch and thrust phases.

The tanks have been outsourced from the approved pressure vessel manufacturer, Ariane-Group [49]. Two specific tanks are selected for the kick stage:

- **2100L Bipropellant Tank MPCV ESM:** This tank provides 2,100 liters of storage capacity and was originally developed for the European Service Module (ESM) of the Orion spacecraft. It is optimized for high-reliability storage and delivery of hypergolic propellants, with titanium construction to resist corrosion and fatigue [49].
- **1450L Bipropellant Tank OST 26-X:** This smaller 1,450-liter bipropellant tank complements the primary tank, enabling modular propellant storage and better mass distribution within the kick stage structure. It also features a titanium construction and is qualified in space environments [49].

Each tank is equipped with internal diaphragms to ensure positive expulsion of propellant without ullage gas ingestion, enhancing reliability for multiple engine restarts across the mission profile. The tanks are secured within the cylindrical lattice structure of the kick stage, and are interfaced through rigid titanium rings to fix the tanks to the lattice structure.

Pressurization for the propellant tanks is provided by independent nitrogen storage tanks. These nitrogen tanks are similarly sourced from Ariane Group off-the-shelf hardware. Mounting brackets, welded to the lower ring of the kick stage frame, house the nitrogen tanks and prevent relative motion during launch vibrations.

Figure 19.3 illustrates the arrangement of the tanks within the kick stage assembly.

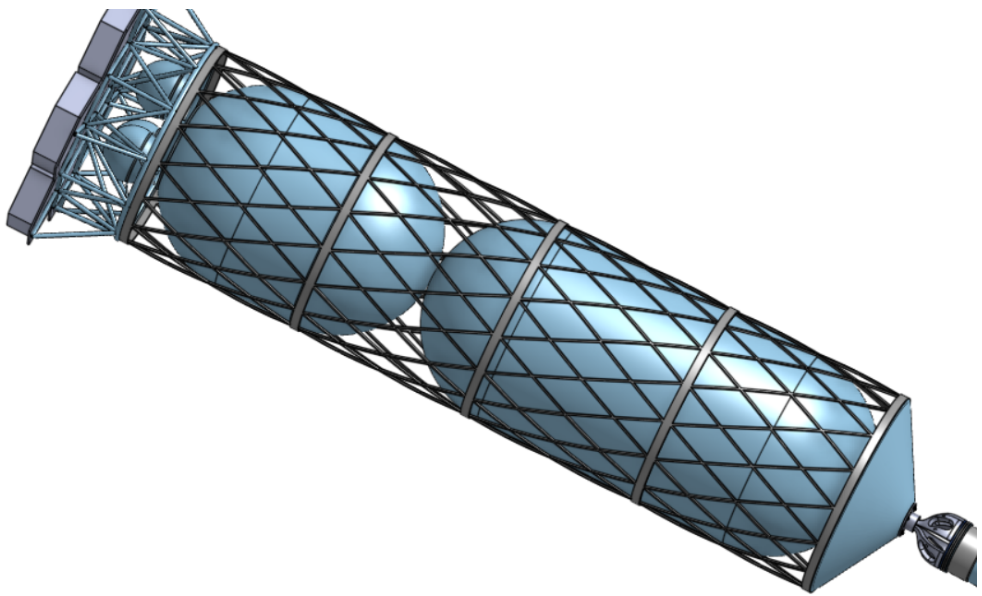


Figure 19.3: CAD model of tanks integrated into the kick stage.

19.2 STD

The Space Trash De-orbiter (STD) is the individual, autonomous spacecraft responsible for the rendezvous, capture, and de-orbiting of a single target Starlink satellite. Seven STDs are carried and deployed by the kick stage. Each STD is a self-contained system designed for high reliability during its relatively short mission duration (approximately one week from deployment to re-entry burn-up), with a target fueled mass of approximately 415 kg.

19.2.1 Structural Design

The structural architecture of the STD is centered around a lightweight, rigid frame designed to endure the harsh mechanical demands of launch and orbital operations while providing sufficient internal volume for subsystems. The core of the STD's structure comprises three thin-walled hexagonal prism segments fabricated from welded titanium alloy tubing, as shown in Figure 19.4. This hexagonal configuration enables efficient packing within the kick stage and aligns with the modular design philosophy of the overall system, facilitating the stacking of multiple STDs during deployment.

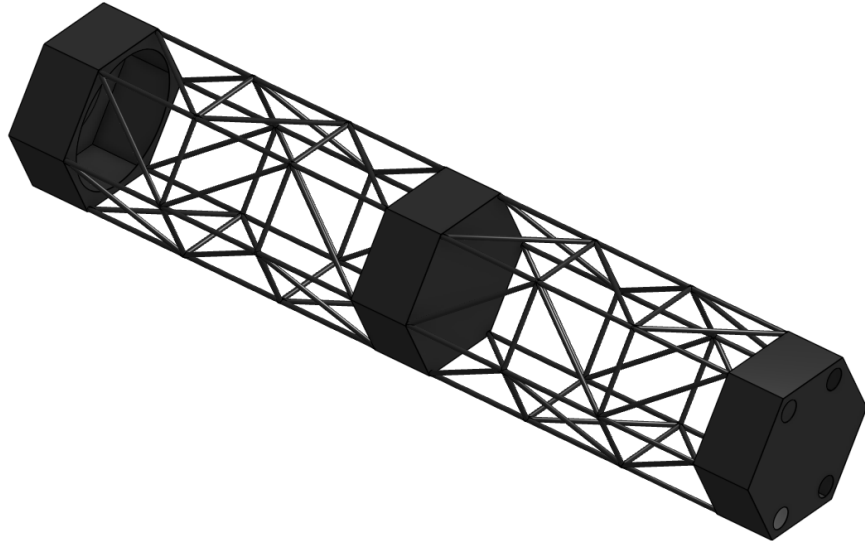


Figure 19.4: CAD of the STD structure

Two of the prism segments are modified with circular cut-outs to securely house the cylindrical fuel tank, minimizing wasted internal volume while preserving structural integrity. Additional cut-outs are included to accommodate the capturing mechanism interface, the rear-mounted main engine, attitude control thrusters, and ports for the Reaction Control System (RCS). Adequate internal clearance is maintained to allow for sensor integration, avionics modules, battery packs, and actuator wiring, ensuring compatibility with future control and autonomy upgrades.

The structure is engineered to withstand maximum expected launch loads of 6g in the axial direction and 3.5g laterally, in accordance with Falcon 9 rideshare envelope specifications. It is also rated for in-orbit thrust loads of up to 3,100 N, generated by the main propulsion

system during active orbital maneuvers, as well as contact forces incurred during docking and debris capture events. Finite Element Analysis (FEA), outlined in Section 15.5, confirms that the frame maintains elastic behavior under these load scenarios.

Internally, the STD houses the monopropellant hydrazine tank (approximately 215 kg capacity), propulsion feed lines, the main engine, electronics stack, and RCS plumbing within its prism bays. The fuel tank is secured using custom fixtures clamped to the primary beam structure of the STD, as depicted in Figure 19.5. These fixtures isolate the tank from load paths during acceleration and thermal cycling.

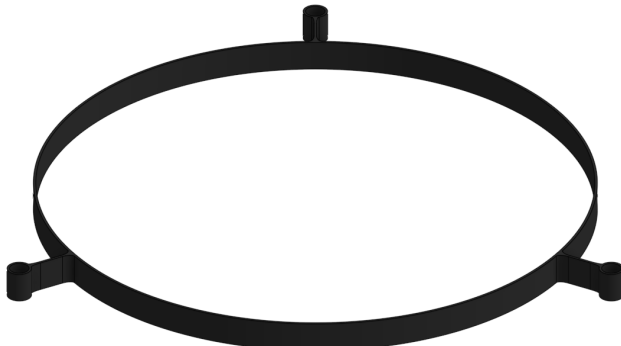


Figure 19.5: Fuel tank mounting fixture to clamp the fuel tank to the STD frame.

Figures 19.6 and 19.7 show front and rear CAD perspectives of the complete STD assembly. Mounting flanges at both ends of the hexagonal prisms permit direct mechanical interfacing with the kick stage and other deployed STDs, supporting mission scalability and integration simplicity.

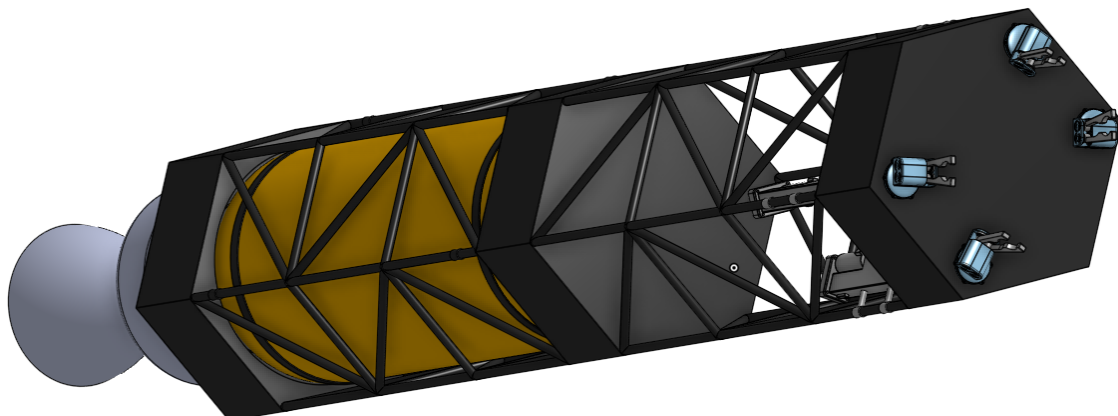


Figure 19.6: Front view of the full STD assembly.

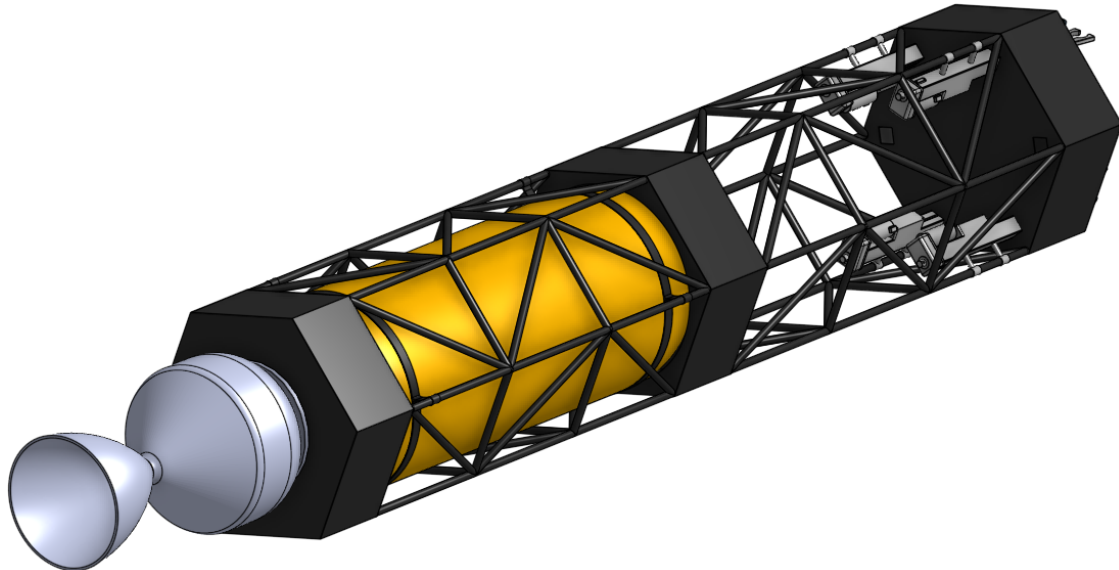


Figure 19.7: Rear view of the full STD assembly.

The total estimated wet mass of the STD is approximately 415 kg. This value includes the structural mass, internal subsystems, avionics, and the full propellant load. This mass budget is compatible with multi-unit rideshare deployments on medium-lift launch vehicles such as the Falcon 9 or Rocket Lab's Neutron, ensuring low-cost access to orbit for multi-capture missions.

19.2.2 Propulsion System

A single monopropellant hydrazine (N_2H_4) engine provides the primary de-orbit thrust of 3100 N with a specific impulse (I_{sp}) of 220 s (Section 8.1, 9.2). This allows for rapid de-orbit maneuvers post-capture while maintaining efficiency and weight savings. The nozzle, along with the combustion chamber, are formed as a singular part. A view of the nozzle is seen in Figure 19.8.

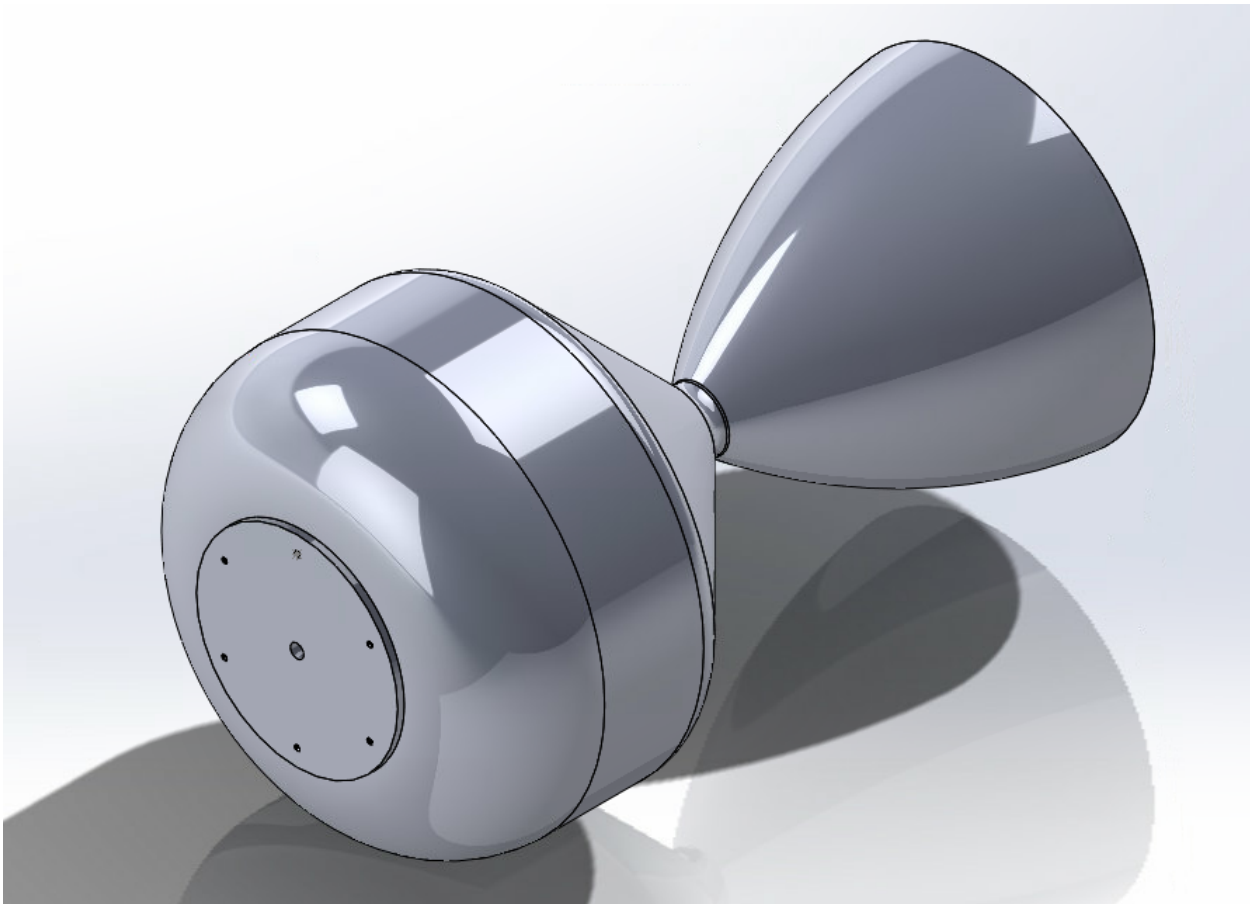


Figure 19.8: An isometric view of the nozzle

From this, a threaded endplate is attached to the nozzle using six M3.5x0.6 screws, then to the STD structure using six M12x1.5 screws. An isometric view of the full subassembly is shown in 19.9

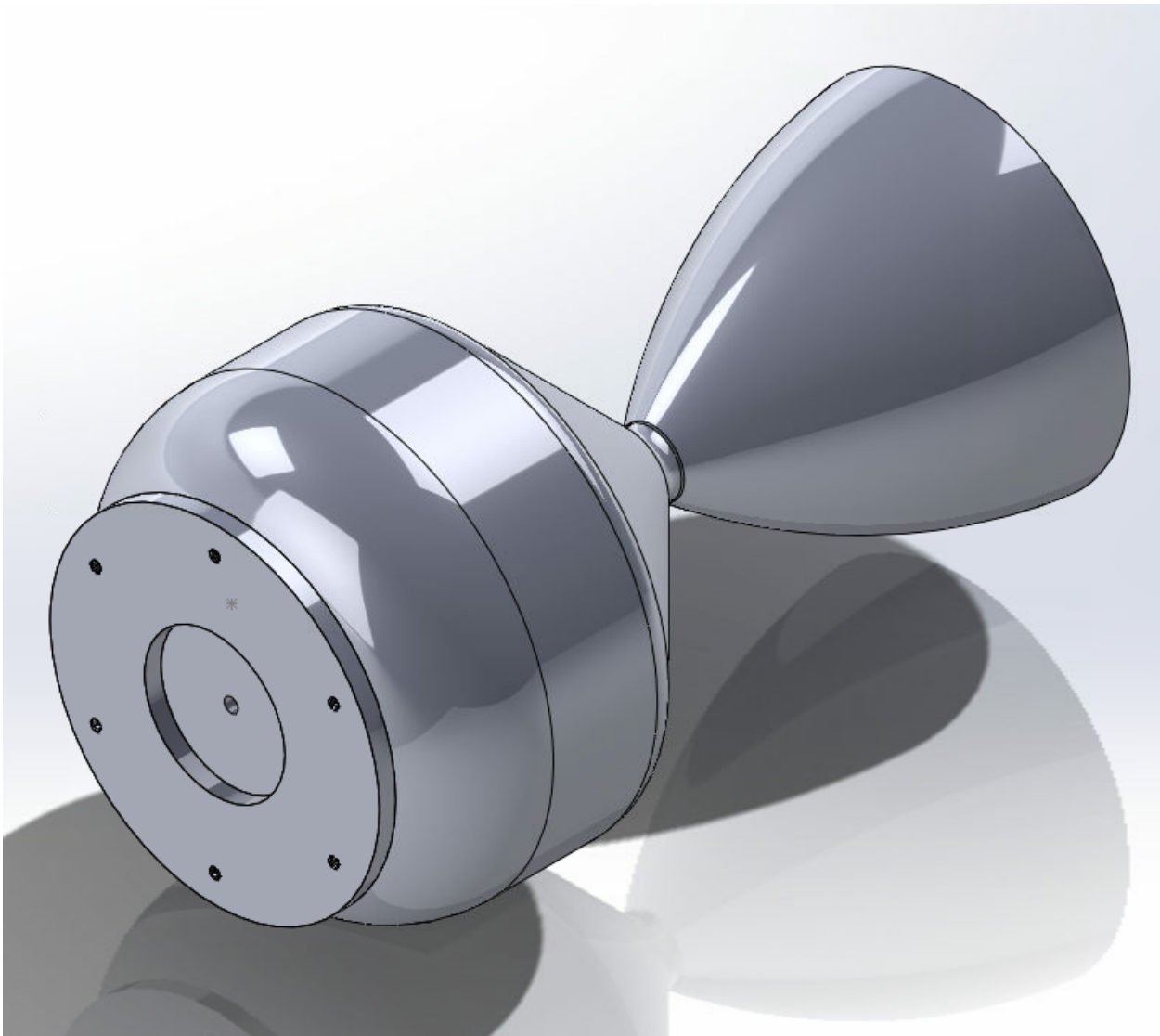


Figure 19.9: An isometric view of the nozzle and thrust plate subassembly

A network of 32 hydrazine Reaction Control System (RCS) thrusters (IHI AeroSpace 5N models or similar, Section 8.3, 9.4.2) provides attitude control and fine maneuvering capability for rendezvous and docking.

A central cylindrical Ti-6Al-4V tank with hemispherical end caps stores approximately 215 kg of hydrazine (Sections 8.1, 9.1). Nominal dimensions are 0.48 m diameter and 1.34 m height (Section 9.1.1). A 5 kg reserve is allocated for RCS (Section 8.1).

19.2.3 Attitude Determination and Control System

Attitude is determined using a combination of a VectorNav VN-100 Inertial Measurement Unit (IMU), an ST200 Star Tracker, and a NovAtel OEM719 GNSS receiver (Sections 8.4, 8.6, 8.7). Control is achieved using four Honeywell HR14-25 reaction wheels (25 Nms capacity

each) for precise pointing and stabilization, supplemented by the 5N RCS thrusters for larger maneuvers and momentum dumping (Section 8.3, 9.4.1). The system is sized to handle target satellite tumble rates up to 10°/s (Section 8.3).

19.2.4 Guidance, Navigation, and Control

The LEON3FT flight computer (Section 8.5) runs the GNC algorithms for autonomous operation, while rendezvous and docking rely on relative navigation data from an SSBV FM CW Radar (100m range, Section 8.9) and a Benewake CE30-D LiDAR system (30m range, Section 8.10) for precision range and bearing measurements.

19.2.5 Docking Mechanism

A four-point armature gripping system is used for capture (Section 7.3.6, Figure 7.4 configuration c or d). Each point features a dual-clamp gripper actuated by a 1.5 Nm NEMA 23 Hybrid Stepper Motor via a 47.4:1 two-stage planetary gearbox (410 stainless steel gears) (Section 10, 17.1).

Each clamp is designed to exert 1550 N to securely hold the target during the 3100 N de-orbit burn (Section 10). The mechanism includes provisions for minor axial and rotational adjustments during final approach (Section 7.3.6).

19.2.6 Power System and Communications

Primary power is supplied by a Lithium-ion battery pack with an estimated capacity of 6.4 kWh and mass of 20 kg, sufficient for the short mission duration (Section 9.5). It powers all subsystems, meeting the peak operational load of approximately 136.5 W (Table 8.1). Solar panels are not utilized. For communication, an EnduroSat S-band transceiver supports telemetry downlink and command uplink at rates up to 1 Mbps (Section 8.8).

19.2.7 Thermal Control and Burn-up

Passive thermal control (coatings, insulation) manages temperature extremes (-150°C to 150°C) while the STD is in low-earth orbit (LEO). The STD is designed for complete atmospheric burn-up upon re-entry, adhering to NASA-STD 8719.14 (Section 4.2, 18.2). Material selection (e.g., aluminum structure, titanium tank) and the venting of residual hydrazine prior to re-entry facilitate demise. Thermal analysis confirms tank burn-up (Section 18.2.2).

The STD design integrates these subsystems into a capable and robust platform optimized for the specific task of autonomous single-target debris capture and de-orbit, meeting the mission's operational and safety requirements.

19.2.8 Gripping Mechanism

The STD employs a robust four-point armature gripping system to capture and secure the target Starlink satellite prior to de-orbit. Each of the four identical gripper assemblies comprises:

- **Dual-clamp jaws:** Two opposing stainless-steel fingers, driven synchronously to exert up to 1550 N of normal force each, providing redundancy and even load distribution.
- **Actuation gearbox:** A 25:1 two-stage planetary reduction couples the motor to the clamps, transforming motor torque into high clamping force.
- **Stepper motor:** A NEMA 23 hybrid stepper (1.5 N·m stall torque) provides precise, reversible control of the clamping action; full release under power ensures recovery from mis-dock events.
- **Compliant alignment stage:** A linear actuator with 12 in travel and a miniature through-shaft rotary bearing with $\pm 10^\circ$ of compliance allow fine axial and angular adjustment during final approach.
- **Location:** The grippers for docking will be placed at the forward end of the STD. This is a design change from an analysis to follow in Section 15.5. This location change was made for an advantage during docking. This advantage is that the STD will be able to use the main engine to provide a normal acceleration while circling the spinning Starlink. This relaxation on the demand of RCS thruster will become apparent in Section 9.4.2, where the only consideration for the approach is the input torques on the STD instead of torques and accelerations.

Each of the four grippers are mounted with two ring brackets which attach to the frame of the STD. These bracket along with all of the other subsystems that make up each gripping mechanism is shown in Figure 19.10.

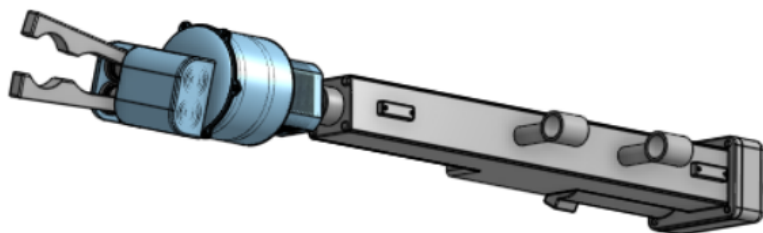


Figure 19.10: CAD of gripping mechanism installed with two brackets for STD mounting.

19.3 Final Assembly



Figure 19.11: Final Assembly with seven STDs mounted on top of the kick stage

20 Future Work

20.1 Orbital Mechanics

20.1.1 Momentum Loss

Section 6.2 outlines a scenario in which the kick stage traverses the orbits in ascending order, from lowest altitude to highest. One could imagine momentum changes from releasing STDs at varying altitudes and the effects it may have on the kick stage's velocity, slowing it down and dropping its orbit slightly. The effect can be approximated by a 1-D case of linear momentum, in the tangential direction, ignoring applied forces

$$m_k v_0 + \sum_{i=1}^N m_s v_0 = m_k v_1 + \sum_{i=1}^{N_{released}} m_s (v_0 + \Delta v_s) + \sum_{i=1}^{N-N_{released}} m_s v_1 \quad (20.1)$$

where m_s, m_k represent the STD's and kick stage's mass, v_0 and v_1 are the initial and final velocity of the kick stage, respectively. Equation 20.1 can be solved for final velocity of the kick stage

$$v_1 = \frac{m_k v_0 + (N - N_r) m_s v_0 - N_r m_s \Delta v_s}{m_k + (N - N_r) m_s} \quad (20.2)$$

Simplifying 20.2 further and solving for the change in velocity of the kick stage Δv_k , defined as

$$\Delta v_k = v_1 - v_0 \quad (20.3)$$

after the partial release of the STDs yields

$$\Delta v_k = -\frac{N_r m_s \Delta v_s}{m_k + (N - N_r) m_s} \quad (20.4)$$

Upon inspection of 20.4, releasing STDs will cause a Δv for the kick stage. The extent of this effect will need to be analyzed further to determine whether it can be used as a practical way to save fuel by a simple re-ordering of the target orbits or if altitude corrections in the kick stage are necessary after releasing STDs.

20.1.2 Continuous Burn Maneuvers

Another consideration that could be looked into is the use of continuous burn maneuvers. This would eliminate the need for the impulsive maneuver assumption and add realism to the mission while potentially allowing for more-complex maneuvers that could allow for longer de-orbit burns, potentially saving fuel.

20.1.3 Probabilistic Approach to Trajectory Analysis

To loosen up the $\pm 10^\circ$ assumption used in the re-entry trajectory analysis in Section 18, a probabilistic approach could be taken to ensure the range of a landing zone to a specific confidence level. If instead the angle of attack α is normally-distributed where $\alpha \sim N(\mu, \sigma^2)$

where μ is the mean and σ^2 is the variance, then one could specify a landing zone within a specific certainty using a confidence interval.

Another probabilistic approach that could yield promising results would be to use Monte Carlo simulation. If the angle of attack were initially be some value α_i , at each time step a random coin could be flipped (or dice rolled) to determine whether a small perturbation $\Delta\alpha$ could made to the angle of attack. The perturbation would need to be specified such that it is not too large, but this could simulate a re-entry with random disturbances. Several simulations could be done to get a better idea of where the landing zone could be, although this would need to be investigated fully to know whether the results are useful.

20.2 Kick Stage Propulsion

While the preliminary calculations in EES served a valuable purpose in validating the FEA model, making this a more sophisticated model could have proved worthwhile, since it is very closed to the steady-state FEA model and requires a lot less resources. The model could have been expanded into 2D as well as into a transient calculation using methods learned in [103].

Additionally, the film cooling correlation attempted yielded poor and likely unphysical results. At the present the root cause could not be determined since it is very similar to a working code used to analyze a different engine, but it is likely down to a small computation error that is throwing off the calculation.

Fluid system analysis would have been a great addition if time permitted, since analyzing all of the valves, fittings, and feed lines could offer excellent insight into pressure drops along the fluid system, fill time transients, and also allow for proper routing of fluid lines from the tanks to the propulsion system.

20.3 Kick Stage Structure

While preliminary static and launch load analyses demonstrate positive margins of safety for the kick stage frame and lattice structure, additional refinement of the structural design is recommended.

First, a detailed vibration analysis should be conducted to assess the dynamic response of the kick stage during launch. Although global launch accelerations were considered in static load cases, a full modal analysis and random vibration environment assessment are necessary to ensure that structural resonances do not align with significant excitation frequencies from the launch vehicle. Natural frequencies should be verified to remain above 35 Hz to comply with standard secondary payload rideshare requirements [20].

Second, further investigation into weld design at critical interfaces is needed. While all primary frame and lattice connections are assumed to be fully welded joints, a dedicated weld strength assessment based on AWS D17.1 spaceflight welding standards [131] should be performed. This analysis should account for local stress concentrations, thermal distortion effects during fabrication, and potential crack propagation at welded joints. Special attention

should be given to the welds connecting the frame to the cylindrical lattice structure and to the nitrogen tank mounting brackets, where local loads are expected to peak.

Incorporating these refinements will ensure a more robust structural design capable of withstanding both the quasi-static and dynamic loads experienced during the mission lifecycle.

20.4 Flight Computer

The demands of the docking maneuver have been defined and analyzed. A functional program that implements a combination of Model Predictive Control (MPC) in the early stages of the approach and Proportional-Integral-Derivative (PID) control in the final approach will be required. A switch to PID control is likely necessary for fast reaction adjustments at the time of docking, which requires lighter computation. These methods can be programmed and compiled in C++ to control the main engine, RCS thrusters, reaction wheels, and grabbing mechanism actuation in tandem with each other. This program will be simulated in MATLAB and other physics-based simulations to verify the controls.

20.5 Gripping Mechanism Refinement

It was determined at the end of the gear analysis that the sun gear in the second gear reduction would likely fail. This was due to an initial assumption that the shear stress at the root was negligible compared to the bending stress. This failed to be true. The gear sizes will need to be reevaluated for an increase in module of all the gears or an increase in the pitch diameter of the sun gear.

Furthermore, structural analysis should be conducted on the clamp and the shafts that the clamps rotate about. These components would be under high stress when the maximum force is applied during the de-orbit burn.

21 Conclusion

The escalating proliferation of space debris in Low-Earth Orbit (LEO) represents a significant and growing impediment to the safety and sustainability of current and future space operations. Addressing this challenge necessitates proactive and effective Active Debris Removal (ADR) solutions. This report details the successful conceptual design and feasibility analysis of the Dumpster Dynamics Space Trash De-Orbiter (STD) System, an innovative multi-target ADR mission conceived to mitigate the orbital debris threat, specifically targeting defunct Starlink satellites. The project has culminated in a comprehensive design framework, validated through rigorous analysis, demonstrating a viable and efficient approach to debris remediation.

The Dumpster Dynamics system employs a robust and efficient two-stage architecture. A dedicated kick stage, utilizing a high-performance MMH/NTO bipropellant system, acts as the carrier vehicle and deployment platform. Launched via a SpaceX Falcon 9 – selected for its proven reliability, payload capacity, and launch accessibility – the kick stage is designed to transport seven individual Space Trash De-orbiters (STDs) to multiple operational orbits within the 525-535 km altitude range. Detailed mission profiling confirmed the feasibility of this multi-deployment strategy, calculating the necessary delta-V for orbital transfers (including Hohmann transfers and optimized split-plane changes) totaling 3.02 km/s for the kick stage. Simulation using MATLAB's ode113 solver, chosen after careful convergence analysis, verified the orbital mechanics calculations.

Each STD is conceived as an autonomous unit equipped for rendezvous, capture, and de-orbit of a single target satellite. A reliable hydrazine monopropellant system (Isp 220 s, 3100 N thrust) was selected for the STDs, providing the calculated maximum required delta-V of 183 m/s for phasing maneuvers and final de-orbit burns. Sizing calculations based on the Tsiolkovsky rocket equation, component mass estimations (engine, tanks, structure, RCS, capture mechanism), and propellant density resulted in an estimated STD wet mass of approximately 415 kg, including 215 kg of hydrazine stored in a appropriately sized and structurally sound Ti-6Al-4V tank. The attitude control system, incorporating Honeywell reaction wheels (25 Nms) and a network of 5N hydrazine RCS thrusters, was sized to manage rendezvous dynamics and de-spin tumbling targets with angular velocities up to 10°/s, supported by detailed mass moment of inertia calculations for the combined STD-Starlink body.

A critical component of the STD is the capture mechanism. Following a comparative analysis of various gripping concepts (including snare, electroadhesive, and puncture methods), a four-point armature gripping system was selected based on criteria including compatibility, effectiveness, and cost. This system utilizes dual-clamp jaws driven by stepper motors via a two-stage planetary gearbox, designed to exert the 1550 N clamping force required to withstand the maximum anticipated loads during the 3100 N de-orbit burn. The design adheres to the principle of non-destructive capture, attaching to pre-defined hardpoints assumed on the target.

Structural integrity was a paramount concern throughout the design process. Both the kick stage mounting frame and lattice structure, as well as the STD frame, were subjected to rigorous analysis. Finite Element Analysis (FEA) using ANSYS confirmed that the selected designs (welded Al 6061-T6 tubing for the kick stage frame, Ti-6Al-4V for STD structures and tanks, CHS 16x1 beams for STD frame bars) can withstand the demanding launch accelerations specified by the Falcon 9 User Guide (up to 6g axial, 3.5g lateral) and operational thrust loads. Analyses incorporated appropriate material properties (Aluminum 6061-T6, Titanium Ti-6Al-4V, Inconel 718 for engine components) and adhered to NASA structural design and safety factors (e.g., 1.25 yield, 1.4 ultimate per NASA-STD-5001B), demonstrating positive margins against yield and buckling failures.

Safety and mission assurance were guided by relevant industry standards, including FCC regulations for communications, NASA-STD-6016 for materials selection, and critically, NASA-STD 8719.14 for orbital debris mitigation. A key design requirement derived from this standard is the complete atmospheric burn-up of both the STD and the captured debris upon re-entry. Thermal analysis of the STD hydrazine tank during re-entry, using atmospheric density models and stagnation point heat transfer calculations, confirmed that the Ti-6Al-4V tank will fully ablate. Trajectory analysis, incorporating lift and drag effects, established a predicted landing footprint variance, confirming that with proper timing, re-entry can be targeted over unpopulated ocean regions like Point Nemo, satisfying safety constraints. While the STD is predicted to demise fully, the re-entry analysis indicated the kick stage tanks may not fully ablate, necessitating targeted disposal over a safe zone. The system also meets the critical operational requirement of de-orbiting the target within one week of capture, minimizing orbital hazard duration.

Propulsion system analysis for both the kick stage (MMH/NTO) and STD (hydrazine) engines involved detailed design and analysis of key components. Chemical Equilibrium with Applications (CEA) calculations guided propellant selection and mixture ratio optimization (MR=1.5 for kick stage). Injector design focused on a like-impinging configuration for reliability, with orifice sizing determined based on required flow rates and pressure drops. Combustion chamber and nozzle (Rao parabolic approximation) geometry were defined based on characteristic length (L^*), thrust requirements (28 kN kick stage, 3.1 kN STD), expansion ratio (=150 for kick stage), and material thermal limits (Inconel 718, Haynes 25). Thermal analysis, including 1D approximations and FEA, assessed wall temperatures under convective and radiative loads, confirming the necessity and guiding the implementation of film cooling for the kick stage engine and verifying acceptable temperatures for the STD engine nozzle during its operational burns. Pressure analysis informed tank design and injector performance requirements.

In summary, the Dumpster Dynamics project has successfully established the conceptual design and demonstrated the feasibility of a novel, multi-target Space Trash De-Orbiter system. Through detailed analysis spanning orbital mechanics, propulsion, structures, thermal management, and systems integration, this report validates the core design choices and confirms the system's capability to meet its primary objectives: autonomously rendezvous with, capture, and rapidly de-orbit multiple defunct Starlink satellites, ensuring complete

atmospheric demise of the STD and its captured payload. The proposed two-stage architecture offers a scalable and cost-effective approach compared to single-target missions. While further refinement and analysis are warranted, as outlined in the Future Work section (including detailed vibration analysis, fluid system design, control algorithm development, and enhanced re-entry modeling), the Dumpster Dynamics STD System presents a robust and promising concept contributing to the vital effort of ensuring the long-term sustainability and safety of the LEO environment for continued exploration and technological advancement

22 References

- [1] Australian Space Academy. *Collision velocity in low Earth orbit*. URL: <https://www.spaceacademy.net.au/watch/debris/collvel.htm>. (visited: 03/02/2025).
- [2] Donald J. Kessler. *Critical Density of Spacecraft in Low Earth Orbit: Using Fragmentation Data to Evaluate the Stability of the Orbital Debris Environment*. Feb. 2000. URL: <https://aquareid.physics.uwo.ca/kessler/Critical%20Density-with%20Errata.pdf>. (visited: 03/02/2025).
- [3] Jonathan McDowell. *Starlink launch statistics*. URL: <https://planet4589.org/space/con/star/stats.html>. (visited: 11/02/2025).
- [4] S. Kawamoto, T. Hirai, S. Kitajima, S. Abe, T. Hanada. *Evaluation of Space Debris Mitigation Measures Using a Debris Evolutionary Model*. Accessed: 2025-02-25. 2017. URL: https://www.jstage.jst.go.jp/article/tastj/16/7/16_599/_pdf.
- [5] M. Bigdeli, R. Srivastava, M. Scaraggi. *Dynamics of space debris removal: A review*. Accessed: 2025-02-25. 2023. URL: <https://doi.org/10.48550/arXiv.2304.05709>.
- [6] New Space Economy. *The Growing Threat of Space Debris: Challenges and Potential Solutions*. Accessed: 2025-02-25. URL: <https://newspaceeconomy.ca/2024/04/15/the-growing-threat-of-space-debris-challenges-and-potential-solutions/>.
- [7] Pablo C. Budassi. *Space Sustainability*. 2023. URL: <https://pablocarlosbudassi.com/2021/02/space-sustainability.html>. (visited: 03/02/2025).
- [8] European Space Agency. *ClearSpace-1*. 2020. URL: https://www.esa.int/Space_Safety/_ClearSpace-1.
- [9] Robin B. et al. *The ClearSpace-1 Mission: ESA And ClearSpace Team Up To Remove Debris*. Accessed: 2025-04-03. URL: <https://conference.sdo.esoc.esa.int/proceedings/sdc8/paper/320/SDC8-paper320.pdf>.
- [10] NASA Technology Transfer Program. *Spacecraft to Remove Orbital Debris (MSC-TOPS-90)*. URL: <https://technology.nasa.gov/patent/MSC-TOPS-90>. (visited: 04/02/2025).
- [11] Astroscale. *ELSA-M*. URL: <https://astroscale.com/elsa-m/>. (visited: 04/02/2025).
- [12] eoPortal. *OneWeb Minisatellite Constellation for Global Internet Service*. Accessed: 2025-02-25. 2019. URL: <https://www.eoportal.org/satellite-missions/oneweb#spacecraft>.
- [13] Tereza Pultarova. *Astroscale's space debris removal demo mission funded for 2026 launch*. July 2024. URL: <https://www.space.com/astroscale-elsa-m-space-debris-removal-funding>. (visited: 06/02/2025).
- [14] FCC. *CFR-2015 Title 47, Volume 2, Part 25*. Tech. rep. Federal Communications Commision, 2015.
- [15] National Aeronautics and Space Administration. *Process for Limiting Orbital Debris*. Tech. rep. NASA-STD-8719.14C. National Aeronautics and Space Administration, Nov. 2021. URL: https://www.nasa.gov/wp-content/uploads/2018/01/process_for_limiting_orbital_debris.pdf.

- [16] National Aeronautics and Space Administration. *Load Analyses of Spacecraft and Payloads*. Tech. rep. NASA-STD-5002A. National Aeronautics and Space Administration, Sept. 2019. URL: <https://standards.nasa.gov/sites/default/files/standards/NASA/A/0/nasa-std-5002a.pdf>.
- [17] National Aeronautics and Space Administration. *STANDARD MATERIALS AND PROCESSES REQUIREMENTS FOR SPACECRAFT*. Tech. rep. NASA-STD-6016C. National Aeronautics and Space Administration, Nov. 2023. URL: https://standards.nasa.gov/sites/default/files/standards/NASA/C-w/Change-1/1/2023-11-15-NASA-STD-6016C-w-Chg-1-Final_0.pdf.
- [18] National Aeronautics and Space Administration. *NASA Space Mission Architecture Framework Handbook for Uncrewed Space Missions*. Tech. rep. NASA-HDBK-1005. National Aeronautics and Space Administration, Mar. 2021. URL: <https://standards.nasa.gov/standard/NASA/NASA-HDBK-1005>.
- [19] National Aeronautics and Space Administration. *Structural Design and Test Factors of Safety for Spaceflight Hardware*. Tech. rep. NASA-STD-5001B. National Aeronautics and Space Administration, Sept. 2014. URL: <https://standards.nasa.gov/sites/default/files/standards/NASA/B-w/CHANGE-2/2/Historical/nasa-std-5001b.pdf>.
- [20] LLC Space Exploration Holdings. *Falcon User's Guide*. Sept. 2021. URL: <https://www.spacex.com/media>.
- [21] John E. Prussing and Bruce A. Conway. *Orbital Mechanics*. Oxford University Press, 2012.
- [22] Mike Sracic. *Course Content from EMA 550: Astrodynamics, Spring 2024, University of Wisconsin-Madison*.
- [23] The MathWorks Inc. *MATLAB version: 24.1.0.2537033 (R2024a)*. Natick, Massachusetts, United States, 2024. URL: <https://www.mathworks.com>.
- [24] ai-solutions. *J2 Perturbations*. (accessed Feb. 4, 2025). URL: https://ai-solutions.com/_freeflyeruniversityguide/j2_perturbation.htm.
- [25] LLC Space Exploration Holdings. *Consolidated Opposition to Petitions and Response to Comments of Space Exploration Holdings, LLC*. Federal Communications Commission Filing. GN Docket No. 23-135, ICFS File No. SAT-MOD-20230207-00021. May 2023. URL: <https://www.fcc.gov/>.
- [26] Jonathan C. McDowell. "The edge of space: Revisiting the Karman Line". In: *Acta Astronautica* 151 (2018), pp. 668–677. ISSN: 0094-5765. DOI: <https://doi.org/10.1016/j.actaastro.2018.07.003>. URL: <https://www.sciencedirect.com/science/article/pii/S0094576518308221>.
- [27] NASA. *Earth Fact Sheet*. (accessed Feb. 2, 2025). URL: <https://nssdc.gsfc.nasa.gov/planetary/factsheet/earthfact.html>.
- [28] Space Opera. *Falcon 9 velocity/altitude values from webcast*. 2016. URL: <https://forum.nasaspacesflight.com/index.php?topic=40983.0>.
- [29] Konstantin Tsiolkovsky. *The Exploration of Cosmic Space by Means of Reaction Devices*. Translated from Russian, cited as the foundational work for the rocket equation. Cosmos, 1903.
- [30] SpaceX. *Starlink Updates*. Accessed: 2025-02-06. 2025. URL: <https://www.starlink.com/updates>.

- [31] National Aeronautics and Space Administration. *Assessment of MON-25/MMH Propellant System for Deep-Space Engines*. Tech. rep. M19-7648. National Aeronautics and Space Administration, Oct. 2019. URL: <https://ntrs.nasa.gov/api/citations/20190033304/downloads/20190033304.pdf>.
- [32] NASA Glenn Research Center. *Gridded Ion Thrusters - NEXT-C*. Accessed: 2025-02-27. 2024. URL: <https://www1.grc.nasa.gov/space/sep/gridded-ion-thrusters-next-c/>.
- [33] Jeff Bezos. *Everyday Astronaut Tour - BE-3U Engine Update*. Accessed: 2025-02-27, Jeff Bezos discusses the BE-3U engine thrust upgrade to 765 kN and specific impulse of 445 seconds. 2024. URL: <https://www.youtube.com/watch?v=rsuqSn7ifpU>.
- [34] NASA. *ORBITAL MANEUVERING SYSTEM DESIGN EVOLUTION*. Tech. rep. Accessed: 2025-02-06. NASA, 1985. URL: <https://ntrs.nasa.gov/api/citations/19850008634/downloads/19850008634.pdf>.
- [35] NASA. *Aerojet - AJ10-137 Apollo Service Module Engine*. Tech. rep. Accessed: 2025-02-06. NASA, 2010. URL: <https://ntrs.nasa.gov/citations/20100027319>.
- [36] Elliot W. Hawkes, Dillon L. Christensen, and Mark R. Cutkosky. “Hard-Soft Electroadhesion for Robotics”. In: *IEEE Robotics and Automation Letters* 5.2 (2020), pp. 2902–2909. DOI: [10.1109/LRA.2019.8946902](https://doi.org/10.1109/LRA.2019.8946902).
- [37] Honeywell. *HR14-25*. Accessed: 2025-02-20. URL: <https://www.satcatalog.com/component/hr14-25/>.
- [38] Rafael Advanced Defense Systems. *25N Monopropellant Hydrazine Thruster*. Accessed: 2025-02-20. URL: <https://www.satcatalog.com/component/25n-monopropellant-hydrazine-thruster/>.
- [39] VectorNav. *VN-100 IMU*. URL: <https://www.vectornav.com/products/detail/vn-100>. (visited: 04/29/2025).
- [40] Gaisler. *LEON3*. URL: <https://www.gaisler.com/products/leon3>. (visited: 04/29/2025).
- [41] NovAtel. *OEM719 MF GNSS*. URL: https://canalgeomatics.com/product/novatel-multi-frequency-oem719/?gad_source=1&gad_campaignid=22100553546&gbraid=0AAAAArA3PtXa5jAh3AWVk2Tu7gEbqJD6&gclid=Cj0KCQjw8cHABhC-ARIsAJnY12xaWgMe3Gf3rb3W3mTaf0LA_36ABoHLtV5PEjb93m0LejjssSwzyIHAaAmL7EALw_wcB. (visited: 04/29/2025).
- [42] CubeSat. *ST200 Star Tracker*. URL: <https://www.aac-clyde.space/what-we-do/space-products-components/adcs/st200>. (visited: 04/29/2025).
- [43] Endurosat. *s-band-transceiver*. URL: <https://www.endurosat.com/products/s-band-transceiver/>. (visited: 04/29/2025).
- [44] SSBV Aerospace Technology Group. *RADAR systems*. URL: <https://www.cubesatshop.com/vendor-information/newspace-systems/>. (visited: 04/29/2025).
- [45] benewake. *LiDAR Technology*. URL: https://en.benewake.com/IndustrialProduct/index.html?gad_source=1&gad_campaignid=20198862682&gbraid=0AAAAAC72aeTyQGHu9iM3FCQ6gWNQzcWQ1&gclid=Cj0KCQjw8cHABhC-

ARIsAJnY12zkvYnVzX2QFnlu1vwnYn8Yhy4cIDeSKyk1kurCnir0jLa50wZSPy8aAsTYEALw_wCB.
(visited: 04/29/2025).

- [46] National Aeronautics and Space Administration. *The Status of Monopropellant Hydrazine Technology*. Tech. rep. 32-722. National Aeronautics and Space Administration, Feb. 1968. URL: <https://ntrs.nasa.gov/api/citations/19680006875/downloads/19680006875.pdf>.

[47] K. Oakes. *Making satellites safer: the search for new propellants*. Accessed: 2025-02-25. 2020. URL: <https://projects.research-and-innovation.ec.europa.eu/en/horizon-magazine/making-satellites-safer-search-new-propellants#:~:~>.

[48] ArianeGroup GmbH. *Hydrazine Thrusters*. Accessed: 2025-02-25. URL: <https://www.space-propulsion.com/spacecraft-propulsion/hydrazine-thrusters/index.html>.

[49] ArianeGroup GmbH. *Hydrazine Propellant Tanks*. Accessed: 2025-02-25. URL: <https://www.space-propulsion.com/spacecraft-propulsion/hydrazine-tanks/index.html>.

[50] Robert Stengel. *Spacecraft Structures*. Accessed: 2025-02-25. 2016. URL: <https://stengel.mypanel.princeton.edu/MAE342Lecture9.pdf>.

[51] National Aeronautics and Space Administration. *In-Situ Analysis of Hydrazine Decomposition Products*. Tech. rep. AIAA-87-2122. National Aeronautics and Space Administration, June 1987. URL: <https://ntrs.nasa.gov/api/citations/19870014260/downloads/19870014260.pdf>.

[52] National Aeronautics and Space Administration. *Confidence Testing of Shell 405 and S-405 Catalysts in a Monopropellant Hydrazine Thruster*. Tech. rep. National Aeronautics and Space Administration, Feb. 2005. URL: <https://ntrs.nasa.gov/api/citations/20050205849/downloads/20050205849.pdf>.

[53] T. W. Price and D. D. Evans. *The Status of Monopropellant Hydrazine Technology*. Accessed: 2025-02-25. 1968. URL: <https://ntrs.nasa.gov/api/citations/19680006875/downloads/19680006875.pdf>.

[54] National Aeronautics and Space Administration. *Mars Science Laboratory: Entry, Descent, and Landing System Performance*. Tech. rep. 1467. National Aeronautics and Space Administration, Mar. 2006. URL: https://web.archive.org/web/20140225022544/https://ntrs.nasa.gov/archive/nasa/casi.ntrs.nasa.gov/20090007730_2009006430.pdf.

[55] Richard Garcia. *Making Correct Parabolic Nozzles*. Accessed: 2025-02-25. URL: <https://rrs.org/2023/01/28/making-correct-parabolic-nozzles/>.

[56] “Starlink Ad”. In: NA (2025).

[57] SpaceX. *For Modification of Authorization for the SpaceX Gen2 NGSO Satellite System to Add a Supplemental Coverage from Space System*. Tech. rep. SpaceX, 2023.

[58] Spectrolab. *Space Solar Panels*. Technical Report TR-2022-01. Spectrolab, 2022. URL: <https://www.spectrolab.com/DataSheets/Panel/panels.pdf> (visited on 04/18/2025).

[59] Jerry Ginsberg. *Engineering Dynamics*. 1st. Cambridge: Cambridge University Press, 2008.

[60] ZARM Technik AG. *MT400-2-L*. Accessed: 2025-02-20. URL: <https://www.satcatalog.com/component/mt400-2-1/>.

- [61] British Columbia/Yukon Pressbooks. *Torque on a Current Loop: Motors and Meters*. Accessed: 2025-04-03. URL:
<https://pressbooks.bccampus.ca/introductorygeneralphysics2phys1207/chapter/22-8-torque-on-a-current-loop-motors-and-meters/#:~:text=%CF%84%20%3D%20N%20I%20A%20B%20sin%CE%B8, on%20the%20loop%20is%20zero..>
- [62] Charles' Labs. *Reaction Wheel Attitude Control*. URL:
<https://charleslabs.fr/en/project-Reaction+Wheel+Attitude+Control>. (visited: 04/03/2025).
- [63] Research Gate. *Isp of cold gas propellant*. Accessed: 2025-04-03.
- [64] Dieter K. Huzel and David H. Huang. *Design of Liquid Propellant Rocket Engines, Second Edition*. Washington, DC: American Institute of Aeronautics and Astronautics (AIAA), 1992.
- [65] Daniel C. Krammer. *Satellite Dynamics*. EMA642. Accessed: April 26, 2025.
- [66] CAVU AEROSPACE. *OBC-Cube-Polar*. Accessed: 2025-02-25. URL:
<https://www.satcatalog.com/component/obc-cube-polar/>.
- [67] Cervos Space. *Line 1*. Accessed: 2025-02-25. URL:
<https://www.satcatalog.com/component/line-1/>.
- [68] CubeSpace. *Gen2: CubeStar*. Accessed: 2025-02-25. URL:
<https://www.satcatalog.com/component/gen2-cubestar/>.
- [69] Safran Sensing Technologies (Sensonor AS). *STIM380H*. Accessed: 2025-02-25. URL:
<https://www.satcatalog.com/component/stim380h/>.
- [70] Ecuadorian Space Agency. *GCA02*. Accessed: 2025-02-25. URL: <https://www.satcatalog.com/component/gca02-high-gain-11-gnss-active-patch-antenna/>.
- [71] Clean Energy Institute. *LITHIUM-ION BATTERY*. Accessed: 2025-02-25. URL:
<https://www.cei.washington.edu/research/energy-storage/lithium-ion-battery/#:~:text=They%20have%20some%20of%20the,kg%20for%20lead%2Dacid%20batteries..>
- [72] Thyssenkrupp. *Aerospace Grade Aluminium*. Accessed: 2025-02-24. URL:
<https://www.thyssenkrupp-materials.co.uk/aerospace-grade-aluminum>.
- [73] Matweb. *Aluminum 2024-T3*. Accessed: 2025-02-24. URL:
<https://asm.matweb.com/search/specifymaterial.asp?bassnum=ma2024t3>.
- [74] Marko V. Lubarda. *Intermediate Solid Mechanics*. Cambridge University Press, 2020.
- [75] Lin Engineering. *WO-4118L-07P*. Accessed: 2025-04-03. 2020. URL:
https://www.digikey.com/en/products/detail/lin-engineering/WO-4118L-07P/11564408?gclidcpc=gclsrc=aw.ds&utm_adgroup=&utm_source=google&utm_medium=cpc&utm_campaign=PMax%20Shopping_Product_Low%20R0AS%20Categories&utm_term=&utm_content=&utm_id=go_cmp-20243063506_adg-_ad__dev-c_ext-_prd-11564408_sig-CjwKCAjw47i_BhBTEiwAaJfPplioNuXI0qgcWx3s1oHYD7Sn7Ge-4NsQuhOE1EIbJdS1xMprdb7tlxoC69EQAvD_BwE&gad_source=1&gclid=CjwKCAjw47i_BhBTEiwAaJfPplioNuXI0qgcWx3s1oHYD7Sn7Ge-4NsQuhOE1EIbJdS1xMprdb7tlxoC69EQAvD_BwE&gclsrc=aw.ds.
- [76] George P. Sutton and Oscar Biblarz. *Rocket Propulsion Elements, Ninth Edition*. Hoboken, NJ: Wiley, 2016.
- [77] ArianeGroup. *2100 L Biprop Tank - MPCV ESM*. Accessed: 2025-03-31. 2025. URL:
<https://www.satcatalog.com/component/2100-l-biprop-tank-mpcv-esm/>.

- [78] MT Aerospace AG. *PVG-50 - Helium, Nitrogen Tank*. Accessed: 2025-03-31. 2025. URL: <https://www.satcatalog.com/component/pvg-50/>.
- [79] ASM MatWeb. *Titanium Ti-6Al-4V (Grade 5), Annealed*. Accessed: 2025-02-25. URL: <https://asm.matweb.com/search/specifymaterial.asp?bassnum=mtp641>.
- [80] NASA Engineering and Safety Center (NESC). *Material Compatibility of Common Aerospace Metals in MMH/MON-3*. Accessed: 2025-02-25. 2023. URL: <https://www.nasa.gov/centers-and-facilities/nesc/material-compatibility-of-common-aerospace-metals-in-mmh-mon-3/>.
- [81] Nickel Institute. *High-Temperature Characteristics of Stainless Steel*. Tech. rep. 9004. Originally published by the American Iron and Steel Institute in 1979; republished by the Nickel Institute in 2020. Accessed: 2025-03-31. Nickel Institute, 2020. URL: https://nickelinstitute.org/media/1699/high_temperaturecharacteristicsofstainlesssteel_9004_.pdf.
- [82] Special Metals Corporation. *INCONEL® Alloy 718*. Tech. rep. Accessed: 2025-03-31. Special Metals Corporation, 2007. URL: <https://www.specialmetals.com/documents/technical-bulletins/inconel/inconel-alloy-718.pdf>.
- [83] M. Li and S. J. Zinkle. “Physical and Mechanical Properties of Copper and Copper Alloys”. In: *Comprehensive Nuclear Materials*. Ed. by R. J. M. Konings. Vol. 4. Accessed: 2025-03-31. Elsevier, 2012, pp. 667–690. URL: https://digital.library.unt.edu/ark:/67531/metadc829254/m2/1/high_res_d/1036615.pdf.
- [84] NASA Glenn Research Center. *Chemical Equilibrium with Applications (CEA)*. Accessed: 2025-03-31. 2025. URL: <https://www.grc.nasa.gov/www/CEAWeb/>.
- [85] Riccardo Bonazza. *Course Content from EMA 524: Rocket Propulsion, Fall 2024, University of Wisconsin-Madison*.
- [86] Charlie Taylor. *RocketCEA Documentation*. Accessed: 2025-03-31. 2025. URL: <https://rocketcea.readthedocs.io/en/latest/>.
- [87] ASM International. *Inconel 718 - Material Data*. Accessed: 2025-03-31. 2025. URL: <https://asm.matweb.com/search/specifymaterial.asp?bassnum=ninc34>.
- [88] Chris Bergin. *SpaceX’s Propulsion Evolution: The Raptor Engine*. Accessed: 2025-03-31. 2016. URL: <https://www.nasaspacesflight.com/2016/10/its-propulsion-evolution-raptor-engine/>.
- [89] Frank M. White. *Fluid Mechanics*. 7th ed. McGraw-Hill, 2011. ISBN: 9780073529349.
- [90] Everyday Astronaut. *Elon Musk Explains SpaceX’s Merlin Engine!* Accessed: 2025-03-31. 2023. URL: <https://youtu.be/hIPLmZK3C1Y?si=uLzVWL1ev0lbDv1W>.
- [91] Erik M. Betts. *A Historical Systems Study of Liquid Rocket Engine Throttling Methods*. Tech. rep. NASA/TM-2010-216668. Accessed: 2025-03-31. NASA, 2010. URL: <https://ntrs.nasa.gov/api/citations/20100033271/downloads/20100033271.pdf>.
- [92] G. S. Gill and W. H. Nurick. *Liquid Rocket Engine Injectors*. Tech. rep. NASA-SP-8089. Accessed: 2025-03-31. NASA, 1976. URL: <https://ntrs.nasa.gov/citations/19760023196>.
- [93] Trebor International. *Chemical Resistance Chart / PFA / PTFE*. Accessed: 2025-03-31. 2025. URL: <https://treborintl.com/chemical-resistance-chart/>.

- [94] Parker Hannifin Corporation. *Parker O-Ring Selector / Calculator*. Accessed: 2025-03-31. 2025. URL: <https://divapps.parker.com/divapps/oring/ORingSelector/?LangID=EN&lang=en&cntry=us/17061&LangSrcType=local>.
- [95] High Temp Metals, Inc. *Inconel 718 Technical Data*. Accessed: 2025-03-31. 2025. URL: <https://www.hightempmetals.com/techdata/hitempInconel718data.php>.
- [96] Michal Malek. *Design of a Small Liquid Rocket Engine*. (visited: 2025-04-29). 2021. URL: https://dspace.cvut.cz/bitstream/handle/10467/96995/F2-DP-2021-Malek-Michal-DP_Michal_Malek_2021.pdf.
- [97] Bolt Depot, Inc. *Bolt Grade Markings and Strength Chart*. Accessed: 2025-03-31. 2025. URL: <https://boltdepot.com/Fastener-Information/Materials-and-Grades/Bolt-Grade-Chart>.
- [98] The Engineering ToolBox. *Metric Bolt Strength: Minimum, Ultimate Tensile & Proof Loads*. Accessed: 2025-03-31. 2025. URL: https://www.engineeringtoolbox.com/metric-bolts-minimum-ultimate-tensile-proof-loads-d_2026.html.
- [99] Franklin D. Jones et al. *Machinery's Handbook*. 27th ed. Industrial Press, Inc., 2004. ISBN: 9780831127008.
- [100] C&W Seals. *Graphite Gaskets*. Accessed: 2025-03-31. 2025. URL: <https://candwseals.co.uk/products/graphite-gaskets/>.
- [101] Wevolver. *Merlin Engine (Merlin 1D) - Falcon 9 / Falcon Heavy*. Accessed: 2025-03-31. 2025. URL: <https://www.wevolver.com/specs/merlin-engine-merlin-1d-falcon-9-falcon-heavy>.
- [102] Rao and Shmyglevsky. *The Thrust Optimised Parabolic Nozzle*. Accessed: 2025-03-31. 1950s. URL: <http://www.aspirespace.org.uk/downloads/Thrust%20optimised%20parabolic%20nozzle.pdf>.
- [103] G.F. Nellis and S.A. Klein. *Introduction to Engineering Heat Transfer*. 1st. Cambridge University Press, 2020.
- [104] Robert Lea. *How cold is space? Physics behind the temperature of the universe*. Accessed: 2025-03-31. 2022. URL: <https://www.space.com/how-cold-is-space>.
- [105] Vitor Dias da Silva. *Mechanics and Strength of Materials*. 1st ed. Department of Civil Engineering, University of Coimbra, 2006. ISBN: 9783540251316.
- [106] MechaniCalc. *Column Buckling*. Accessed: 2025-04-03. URL: <https://mechanicalc.com/reference/column-buckling>.
- [107] Fidelis. *What Is Buckling? - How Do We Calculate It? - And Why Is It So Important?* Accessed: 2025-04-03. URL: <https://www.fidelisfea.com/post/what-is-buckling-how-do-we-calculate-it-and-why-is-it-so-important>.
- [108] MechaniCalc. *Stresses Deflections in Beams*. Accessed: 2025-04-03. URL: <https://mechanicalc.com/reference/beam-analysis>.
- [109] Mississippi State University. *Section III.3 Flexural Shear Stress and Shear Flow*. <https://www.ae.msstate.edu/tupas/SA2/chA14.6text.html>. Accessed: 2025-04-03.
- [110] Boston University. *Mechanics of Materials: Torsion*. Accessed: April 26, 2025. URL: <https://www.bu.edu/moss/mechanics-of-materials-torsion/>.
- [111] Engineers Edge. *Von Mises Criterion (Maximum Distortion Energy Criterion) Strength (Mechanics) of Materials*. Accessed: 2025-04-03. URL: https://www.engineersedge.com/material_science/von_mises.htm.

- [112] National Aeronautics and Space Administration. *HYDRAZINE CATALYST PRODUCTION - SUSTAINING S-405 TECHNOLOGY*. Accessed: 2025-04-03. 2003. URL:
<https://ntrs.nasa.gov/api/citations/20030066232/downloads/20030066232.pdf>.
- [113] Haynes International. *HAYNES® 25*. Accessed: 2025-04-03. 2025. URL: <https://haynesintl.com/en/alloys/alloy-portfolio/high-temperature-alloys/haynes-25/>.
- [114] Robert J. Santoro and Sibthosh P. *Experimental Studies of the Heat Transfer to RBCC Rocket Nozzles for CFD Application to Design Methodologies*. Accessed: 2025-04-03. 1999. URL:
<https://ntrs.nasa.gov/api/citations/19990025912/downloads/19990025912.pdf>.
- [115] D. R. Bartz. *A Simple Equation for Rapid Estimation of Rocket Nozzle Convective Heat Transfer Coefficients*. Accessed: 2025-04-03. 1957. URL: <https://pdfcoffee.com/a-simple-equation-for-rapid-estimation-of-h-bartz-pdf-free.html>.
- [116] M. Balat-Pichelin et al. *Oxidation induced emissivity variations of the Haynes 25 alloy at high temperatures*. 2023. URL:
<https://www.sciencedirect.com/science/article/pii/S1350449523003882>.
- [117] Lechler USA. *Full Cone Nozzles*. Accessed: 2025-04-03. URL:
www.lechlerusa.com/fileadmin/media-usa/Literature/Catalog/05_Full_Cone_Nozzles.pdf.
- [118] W.H. Dornfeld. *Gear Tooth Strength Analysis*. 1st. Fairfiled University, 2006.
- [119] ASM. *ASM Material Data Sheet*. URL:
<https://asm.matweb.com/search/specifymaterial.asp?bassnum=mq304a>. (visited: 04/03/2025).
- [120] *Densiy of Air*. URL: https://en.wikipedia.org/wiki/Density_of_air.
- [121] W. de Vries. *Cubesat Drag Calculations*. Sept. 2010. URL:
<https://www.osti.gov/servlets/purl/1124870>.
- [122] H. Elmore Blanton Anna Muzyka. *Optimum Earth Re-entry Corridors*. Mar. 1966.
- [123] European Space Agency. *Reentry and Collision Avoidance*. Accessed: 2025-03-29. n.d. URL:
https://www.esa.int/Space_Safety/Space_Debris/Reentry_and_collision_avoidance.
- [124] Geography Realm. *What is Point Nemo?* [Online; accessed 28-April-2025]. 2016. URL: <https://www.geographyrealm.com/where-is-point-nemo/>.
- [125] Federal Aviation Administration. *Returning from Space: Re-entry*. Accessed: 2025-03-25. Federal Aviation Administration. n.d. URL:
https://www.faa.gov/sites/faa.gov/files/about/office_org/headquarters_offices/avs/III.4.1.7_Returning_from_Space.pdf.
- [126] D. E. Klett R. K. Irey. *Methods of Determining Thermal Accommodation Coefficients from Free Molecular Flow Heat Trans Molecular Flow Heat Transfer Data er Data*. Accessed: 2025-03-31. 1969. URL:
<https://commons.erau.edu/cgi/viewcontent.cgi?article=2932&context=space-congress-proceedings>.
- [127] National Aeronautics and Space Administration. *NASA White Paper*. Accessed: 2025-03-29. 2008. URL:
https://thebulletin.org/wp-content/uploads/2008/08/NASA_White_Paper.pdf.

- [128] Jeannette Plante and Brandon Lee. *Environmental Conditions for Space Flight Hardware - A Survey*. Tech. rep. For the NASA Electronic Parts and Packaging (NEPP) Program. Dynamic Range Corporation, 2004.
- [129] F-Chart Software. *Engineering Equation Solver (EES)*. 2025. URL: <https://www.fchart.com>.
- [130] Gregory Nellis and Sanford Klein. *Heat Transfer*. 1st. Cambridge: Cambridge University Press, 2011.
- [131] American Welding Society. *AWS D17.1/D17.1M: Specification for Fusion Welding for Aerospace Applications*. Accessed April 2025. 2017. URL: <https://pubs.aws.org/p/1190/aws-d171d171m2017-specification-for-fusion-welding-for-aerospace-applications>.
- [132] Keith Fratus. *The Two-Body Problem*. 2015. URL: <https://web.physics.ucsb.edu/~fratus/phys103/LN/TBP.pdf>. (visited: 2/25/2025).
- [133] J. D. Anderson. *Fundamentals of Aerodynamics, Sixth Edition*. New York, NY: McGraw-Hill Education, 2017.
- [134] Federal Communications Commission. *Streamlining Licensing Procedures for Small Satellites*. Tech. rep. FCC 19-81. Federal Communications Commission, Aug. 2019. URL: <https://www.fcc.gov/document/streamlining-licensing-procedures-small-satellites-1>.
- [135] Creative Technology Co. *What is an Electrostatic Chuck (ESC)*? Accessed: 2025-02-06. URL: <https://creative-technology.co.jp/esc-e/>.
- [136] Jianglong Guo, Jinsong Leng, and Jonathan Rossiter. “Electroadhesion Technologies for Robotics: A Comprehensive Review”. In: *IEEE Transactions on Robotics* 36.2 (2020), pp. 313–327. DOI: [10.1109/TRO.2019.2956869](https://doi.org/10.1109/TRO.2019.2956869).
- [137] Ecuadorian Space Agency. *Gen2: CubeSense Sun*. Accessed: 2025-02-25. URL: <https://www.satcatalog.com/component/gen2-cubesense-sun/>.

A Product Design Specification (PDS)

EMA 469
Product Design Specification

Product **Dumpster Dynamics Space Trash Deorbiters**

Date **1/28/2025**

Revision **1.0**

Group Members **Kyle Adler, Dom Morand-Rivers, Gavin Day, Bryce Quinton, Martin Du Jardin**

Guidelines	Specification Element	Team Design	Competition
<p>The performance demanded or likely to be demanded should be fully defined.</p> <p>Is the performance demanded attainable in an economic manner? A common failure in specifying performance is to ask for the ultimate, rather than that which is obtainable.</p>	Performance	<p>Debris altitude: LEO 525-535km (1-10 years to deorbit naturally)</p> <p>Starlink V3 roughly 1900kg [source]</p> <p>Kick stage: bring each of the S.T.D.'s to destination orbit altitude, inclination, eccentricity</p> <p>S.T.D.: Deorbit debris within 6 months, the lower the better. Initial estimates of 500 lbf thrust, 120 second burn (deltav/burntime*combined mass = thrust)</p> <p>Example:</p>	<p>RL-10 Aerojet AJ10 and variations</p> <p>ClearSpace-1: LEO (660-8000 km) 112 kg 1 year Uncontrolled re-entry 2m diameter</p>

All aspects of the product's likely environment should be considered and investigated: <ul style="list-style-type: none"> Temperature range. Pressure range (altitude). Humidity. Shock loading (gravity forces). Dirty or dusty? How dirty? Corrosion from fluids. Noise levels. Insects. Vibration 	Environment	For LEO, temperatures typically range from -65°C to 125°C [NASA]. Intense solar UV radiation Ionizing radiation Pressure in LEO $\sim 10^{-10}$ Torr (~ 0 psi).	For LEO, temperatures typically range from -65°C to 125°C [NASA]. Intense solar UV radiation Ionizing radiation Pressure in LEO $\sim 10^{-10}$ Torr (~ 0 psi).
Is regular maintenance available or desirable? Will designing a maintenance-free product be too expensive to buy in the first place? Does the company, or indeed the market into which the product will ultimately go, have a definitive maintenance policy? Is the market used to maintaining equipment once it is purchased? <ul style="list-style-type: none"> Specify ease of access to the parts that are likely to require maintenance. It is no good calling for regular maintenance if it takes 10 days to reach the part. What is the maintenance and spares philosophy of the company and market? What is the likely need and desirability of special tools for maintenance? 	Maintenance	STDs will be single-use due to the satellite and STD burning up on reentry. No maintenance will be required after launch.	Current satellites, if defunct, just decay down and burn up.
Are there any restrictions on the size of the product? Size constraints should be specified	Size	Full design (kick stage + STDs) must fit within	ClearSpace-1 is targeting VESPA which is the upper

initially. Does the product size and shape make it difficult to handle?		Falcon 9 payload volume capabilities . Depending on the final size of individual STDs, the Smallsat Rideshare Program may be viable on Falcon 9/Heavy.	part of a payload adapter from PROBA-1. Vespa is a 2 m diameter, conical-shaped object.
What is the desirable weight? Should the design be modular to assist in the size/weight area? Should lifting points be provided and how many people are required to move it?	Weight	Heaviest payload placed into LEO with the Falcon 9 has been confirmed at 17.4 metric tons . ~100-200kg per STD	ClearSpace-1 is targeting VESPA that is 112 kg
Think about materials that are used in similar applications or by competitor's products. What manufacturing methods will be used (welding, forming, molding)? Does your product operate in a corrosive environment? Specific materials should be specified by quoting the appropriate standard.	Materials	Aluminum 2024-T4 is widely used in aerospace applications due to its high strength to weight ratio . Design of Liquid Propellant Rocket Engines (Huang, et. al) outlines common materials used in engines themselves, pages 59-62. These include low-alloy steels like AISI 4130, 4140, and 4340; aluminum alloys, namely alloys that are only cold-workable (1100,	Competition deorbiters are most likely composed of Aluminum Alloys, Titanium and Composites. Similar to those being used for the STD

		3003, 3004, etc.) and heat-treatment capable (2011, 2014, 2017, 2024!) Hypergolic propellants and propulsion components will require careful material selection. https://ntrs.nasa.gov/citations/19720019028	
Some indication of the life of a product as a marketable entity should be sought. Is it likely to remain in production for two years or 20 years? The answer is crucial as it can affect the design approach and interacts with the market and competition, tooling policy, manufacturing facility and the like.	Product Life Span	Single-use: capable of maintaining operations (main limiting factor being electricity) for several years, from transfer to debris to deorbit burn.	ClearSpace-1 is also single-use and designed specifically for VESPA
Is the product to be designed to current international and/or US standards? If so, then these should be specified and copies obtained. Cross-correlation of such standards should be carried out prior to commencement of the design. It is difficult, costly, time consuming and inefficient to attempt retrospective matching of designs already finalized to such standards.	Standards and Specifications	Check out this NASA document for lots of info on this stuff SpaceX's Falcon Users Guide Orbital Debris Mitigation Standard	Orbital Debris Mitigation Standard
All products have to some degree a man-machine interface. What height, reach, forces and operating torques are acceptable to	Ergonomics and Human Factors	No passengers, therefore no user requirements.	ClearSpace-1 is also not a manned vehicle.

the user? Consult with potential users of the product.		Will meet human safety standards at the launch site.	
Who is buying / using your product? How many units can you sell in a year? It is essential to obtain first-hand information on customer likes, dislikes, preferences and prejudices.	Customer / Market	Our customers would mainly be government agencies or private defense/space contractors. SpaceX contracts to mitigate debris caused by Starlink.	ClearSpace-1 is designed by ESA for an ESA satellite.
Most products require some form of testing after manufacture, either in the factory, on site or both. Do we sample test one in ten, one in a hundred, or what? Do we need a new test facility? How can we be sure that the product is designed to have rapid engagement with and detachment from the test rig? Data collection and product history are needed to answer these questions. An initial test specification should be written at this stage.	Testing	Check out this NASA document for potential testing info. - Test all units - Hypergolic thrusters - Vibration equivalent to takeoff specs - Pressure test for cold gas thrusters - Mechanical testing for docking	Information is proprietary, but likely followed similar testing as state to the left.
The safety aspects of the proposed design and its place in the market must be considered. • OSHA standards for workplace safety	Safety, Public Health, and Human Welfare	- Deorbits will need to guarantee burnup. If deorbit does not result in burnups it will need to	ClearSpace-1 will burn up on reentry as the STD intends as well.

<ul style="list-style-type: none"> User safety: sharp edges, pinch points, potential misuse. Public safety: are there potential dangers to those in or around the area the product is being used? Human Welfare: Does your product benefit those in need? 		<p>have their landing areas specified</p> <p>- Dangers arise from returning debris to the surface. Miscalculations could potentially put lives in danger.</p>	
<p>Economic, Social and cultural factors affecting business/products include belief systems and practices, customs, traditions and behaviours of all people in given country, and market activities influencing actions and decisions.</p> <p>Consider the following in assessing your product</p> <ul style="list-style-type: none"> social classes & influence on the society disposable income level and wealth of your customers economic inequalities level and access to education level and access to health-care health consciousness in society buying habits and consumer preferences conflicts within society 	Economic, Cultural, Social Factors	<p>The product will be for commercial/government contracts.</p> <p>Minimize cost due to single-use and to allow for large production</p>	<p>Government agencies, defense, and space companies.</p>
<p>Discuss environmental cost/benefit of your product. Think about the full product life cycle including manufacturing, transportation, use, and disposal.</p> <ul style="list-style-type: none"> Product end-of-life. Is it recyclable? Does it contain hazardous chemicals? 	Environmental Impact	<p>Removing space debris from Earth's orbit will help ensure humans do not face the Kessler effect.</p>	<p>ClearSpace-1 contributes to the effort of removing space debris and improving the space environment.</p>

<ul style="list-style-type: none"> ● Is there an environmental impact from the mining of raw materials used on your product? ● Does your product help the environment? Clean energy, carbon-free transportation, clean pollution ● Impact on global warming / carbon footprint ● Eco-friendly materials ● See these tips: https://business.vic.gov.au/business-information/sustainability/design-sustainable-products 		<p>The product's end-of-life will be a burnup in the upper atmosphere.</p>		
--	--	--	--	--

B STD fuel tank sizing code

```
clear all; close all; %clc

% Inputs
m_capture = 15; % mass of capturing mechanism [kg]
m_engine = 25; % mass of engine [kg]
m_tank = 25; % mass of fuel tank [kg]
m_propsys = 35; % mass of propulsion system [kg]
m_RCS = 30; % mass of RCS [kg]
m_structural = 50; % other structural mass [kg]
m_fuel = 215; % propellant mass [kg]
hd_ratio = 2.8; % height to diameter ratio of tanks
SF = 1.15; % safety factor

% Hydrazine inputs
I_sp = 220; % [s] (Hydrazine)
rho = 1004.5; % [kg/m^3]

% Fixed inputs
m_starlink = 1900; % [kg]
g_e = 9.81; % [m/s^2] (Earth)

m_l = m_starlink; % payload mass
[m]
m_s = m_capture+m_engine+m_tank+m_propsys+m_RCS+m_structural; % structural mass [kg]
m_p = m_fuel*Sf; % propellant
[m]
m_0 = m_l + m_s + m_p; % total mass [kg]

epsilon = m_s/(m_p + m_s); % structural coefficient
lambda = m_l/(m_0 - m_l); % payload ratio

R = (1+lambda)/(epsilon+lambda);

u_eq = I_sp * g_e; % equivalent exhaust velocity [
[m/s]
delta_v = u_eq * log(R); % [m/s]
```

```

volume_fuel = m_fuel/rho;                                % [m^3]
volume_fuel_liter = volume_fuel * 10^3;                  % [L]

% Cylindrical body with hemispherical end caps
syms diameter
soln = vpasolve(volume_fuel == pi*diameter^2/4*(hd_ratio*
    diameter-diameter)+4/3*pi*diameter^3/8);
diameter = double(soln(1));                               % [m]
height = hd_ratio*diameter;                            % [m]
length = height-diameter;                            % [m]

% Display final results
disp('Results-----')
disp(['delta-V = ', num2str(delta_v), ' m/s (Req. 183 m/s)']);
disp(['volume = ', num2str(volume_fuel), ' m^3 = ', num2str(
    volume_fuel_liter), ' L']);
disp(['diameter = ', num2str(diameter), ' m'])
disp(['height = ', num2str(height), ' m'])
disp(['length of cylinder = ', num2str(length), ' m'])
disp(['dry mass = ', num2str(m_s), ' kg'])
disp(['liquid mass = ', num2str(m_fuel), ' kg (Safety Factor ',
    num2str(SF), ')'])
disp(['epsilon = ', num2str(epsilon)])
disp(['lambda = ', num2str(lambda)])
disp(['R = ', num2str(R)])

```

C Orbital Mechanics Calculations

Appendix C has all of the MATLAB scripts for the orbital mechanics calculations. Each subsection of this appendix will explain the code.

C.1 Hohmann Transfer

This code first, computes the Δv required for the Hohmann transfers, and then simulates the maneuver using a 2-DOF solver. This code was used to compute the kick stage Δv as well as generate Figure 6.5.

```
%% Hohmann Transfer
% Written by Dom

clc; clear; close all;

r_e = 6378.137;

alt_initial = 100;
alt_target = 4000;

r_a = alt_initial + r_e;
r_b = alt_target + r_e;

mu_e = 0.39860e6;
v_a = sqrt(mu_e/r_a);

e_transfer1 = (r_b-r_a)/(r_b+r_a);
a_transfer1 = (r_a+r_b)/2;
v_end_t1 = sqrt(mu_e*(2/r_b - 1/a_transfer1));
delta_v1 = abs(sqrt(mu_e*(2/r_a - 1/a_transfer1)) - v_a );

% Start and end on left-hand side of body
R_a = [r_a; 0];
V_a = [0; v_a + delta_v1];
y01 = [R_a;V_a];

n_t1 = sqrt(mu_e/a_transfer1^3);
tf1 = (pi-e_transfer1*sin(pi))/n_t1;

function ydot = rates(t,y)
mu_e = 0.39860e6;
R = [y(1); y(2)];
V = [y(3); y(4)];
```

```

r = norm(R);
A = -mu_e*R/r^3;

ydot = [V;A];
end

opts = odeset('RelTol',1e-5);
[t1,y1] = ode45(@(t,y) rates(t,y),[0 tf1],y01,opts);

X1 = y1(:,1);
Y1 = y1(:,2);

figure;
hold on;
plot(X1,Y1,'-r','DisplayName','Transfer Ellipse','LineWidth',2)
plot(r_a*cos(0:0.001:2*pi),r_a*sin(0:0.001:2*pi),'-k','
    DisplayName',...
    'Initial Orbit','LineWidth',2)
plot(r_b*cos(0:0.001:2*pi),r_b*sin(0:0.001:2*pi),'-b','
    DisplayName',...
    'Target Orbit','LineWidth',2)
plot(r_a,0,'xk','DisplayName','Burn #1','MarkerSize',12,'
    LineWidth',2);
plot(-r_b,0,'xb','DisplayName','Burn #2','MarkerSize',12,'
    LineWidth',2);

axis('equal')
legend('show','Location','best')
fontsize(22,"points");
set(gca,'XColor','none','YColor','none','color','none')
movegui

```

C.2 Split-plane Change

This code solves for the optimal inclination splits for the split-plane changes used by the kick stage.

```

%% Split-Plane Change
% Written by Dom

clear; clc; close all;

mu = 0.3986e6;
r_e = 6378;

```

```

% Initial Altitude
alt_i = 525;

% Destination Altitude
alt_f = 530;

% Inclination Change
delta = 10 * pi/180;

r_t1 = r_e + alt_i;
r_t2 = r_e + alt_f;
a_t = (r_t1+r_t2)/2;

v_i = sqrt(mu/r_t1);
v_t1 = sqrt(mu*(2/r_t1-1/a_t) );
v_t2 = sqrt(mu*(2/r_t2-1/a_t) );
v_f = sqrt(mu/r_t2);

syms a1

dV_1 = sqrt( v_t1^2 + v_i^2 - 2*v_t1*v_i*cos(a1) );
dV_2 = sqrt( v_t2^2 + v_f^2 - 2*v_t2*v_f*cos(delta-a1) );

dV_tot = dV_1 + dV_2;

a1_opt = vpasolve(diff(dV_tot)==0,a1);

clc;

dV_1_opt = sqrt( v_t1^2 + v_i^2 - 2*v_t1*v_i*cos(a1_opt) );
dV_2_opt = sqrt( v_t2^2 + v_f^2 - 2*v_t2*v_f*cos(delta-a1_opt) );
dV_tot_opt = dV_2_opt + dV_1_opt;

a1_deg = a1_opt*180/pi;
a2_deg = (delta - a1_opt)*180/pi;
fprintf(['Inclination Change: %.3f\ndV1 = %.3f\nndV1 = %.3f\nndV
= %.3f\na1...'\ ...
' = %.3f\na2 = %.3f\n'],delta*180/pi,dV_1_opt,dV_2_opt,
dV_tot_opt, ...
a1_deg,a2_deg);

```

C.3 Phasing

This script computes the phasing Δv needed for the individual STDs and plots the maneuver.

```
%% Phasing
% Written by Dom

clear; clc; close all;

mu = 3.986004418e5;
r_e = 6378;

r0 = r_e + 525;
a0 = r0;
v0 = sqrt(mu/a0);
T0 = 2*pi*sqrt(a0^3/mu);
n0 = sqrt(a0^3/mu);
Tp = 15000;

%t_phasing_vec = 0:50:1e5;
t_phasing_vec = 86400*5 + T0;

for i=1:length(t_phasing_vec)

    t_phasing = t_phasing_vec(i);
    dTheta = 1.89*pi;
    m = 0;
    residual = 100;

    % Number of orbits around the original orbit
    while residual>0
        m = m + 1;

        if dTheta<0
            t_lag = n0*( abs(dTheta) );
            N = dTheta/(2*pi) + m;
        else
            t_lag = n0*( 2*pi - abs(dTheta) );
            N = (2*pi - abs(dTheta))/(2*pi) + m;
        end

        residual = t_phasing - N*T0;
    end

    t_phase = t_lag + m*T0;
    a_phase = ((t_phase/(2*pi))^2*mu)^(1/3);
```

```

%dV = sqrt(mu*(2/r0 - 1/a_phase)) - sqrt(mu/r0);

dV = -sign(dTheta)*dTheta/(2*pi)*mu/(3*a0*v0*N);
dV_tot = 2*abs(dV)*1000;

v1 = v0 + dV;
a1 = (2/r0 - (v1^2/mu))^(-1);
T1 = 2*pi*sqrt(a1^3/mu);

dV_param(i) = dV_tot;
end

if length(dV_param)>1
plot(t_phasing_vec,dV_param,'.-b');
end

%% Simulate

R_a = [r0; 0];
V_a = [0; v0 + dV];
y01 = [R_a; V_a];

R_b = [r0*cos(dTheta); r0*sin(dTheta)];
V_b = [-v0*sin(dTheta); v0*cos(dTheta)];
y02 = [R_b; V_b];

function ydot = rates(t,y)
mu_e = 3.986004418e5;
R = [y(1); y(2)];
V = [y(3); y(4)];

r = norm(R);
A = -mu_e*R/r^3;

ydot = [V; A];
end

opts = odeset('RelTol',1e-10);

t_vec = linspace(0,t_phase,1000);

t_vec1 = linspace(0,T1,100);
t_vec2 = linspace(0,T0,100);

```

```

[t,Orbit1] = ode45(@(t,y) rates(t,y),t_vec1,y01,opts);
[t,Orbit2] = ode45(@(t,y) rates(t,y),t_vec2,y02,opts);

[t1,Y1] = ode45(@(t,y) rates(t,y),t_vec,y01,opts);
[t2,Y2] = ode45(@(t,y) rates(t,y),t_vec,y02,opts);

x1 = Y1(:,1);
y1 = Y1(:,2);

x2 = Y2(:,1);
y2 = Y2(:,2);

figure; hold on;
plot(Orbit1(:,1),Orbit1(:,2), '--r');
plot(Orbit2(:,1),Orbit2(:,2), '--b');

plot(x1(end),y1(end), 'or')
plot(x2(end),y2(end), 'ob')
plot(x1(1),y1(1), 'xr')
plot(x2(1),y2(1), 'xb')

axis('equal')

%{
figure; hold on;
for i=1:length(t_vec)
clf;
plot(-2*r0,-2*r0,2*r0,2*r0,-2*r0,2*r0,2*r0,-2*r0,x1(i),y1(i), 'or', x2(i),y2(i), 'ob', Orbit1(:,1),Orbit1(:,2), '-r', Orbit2(:,1),Orbit2(:,2), '-b');
axis('equal')
drawnow
end
%}

```

C.4 De-orbit

This code just computes the de-orbit Δv needed for the STDs as well as the kick stage (at the end of the mission). This is just solving for what Δv will put the STD/kick stage on a elliptical orbit that will intercept the Karman line at perigee.

```

%% De-orbit
clear; clc; close all;

mu = 0.3986e6;

```

```

r_e = 6378;

% Initial Altitude
alt_i = 525;

% Destination Altitude
alt_f = 100;

a = ((r_e + alt_i)+(r_e+alt_f))/2;

r1 = r_e + alt_i;
V1 = sqrt(mu/r1);

V2 = sqrt(mu*(2/r1 - 1/a) );

dV = V2 - V1;

```

C.5 Satellite Orbit Figures

This script was used to automatically generate Figures 6.1, 6.2, and 6.3. This was done so that they appear uniform and professional.

```

%% Satellite Orbit Figures
clear; clc; close all;

N = 20;
r = 6378 + 520;

theta = linspace(-pi,pi,1000);
theta_satellites = linspace(2*pi/N,2*pi+2*pi/N,N);

OrbitTag = 'Orbit B';
defunct_numbers = [2,14,9,17,8,11,18];

% A
% [2,14]

% B
% [9,17]

% C
% [8,11,18]

theta_defunct = theta_satellites(defunct_numbers);
theta_A = theta_satellites(defunct_numbers);

```

```

r_vec = linspace(0,r,1000);

f = figure;
hold on;

% Named plot elements
plot(r.*cos(theta),r.*sin(theta), '-k','LineWidth',1);
%plot(r.*cos(theta_satellites),r.*sin(theta_satellites), 'xk','
    LineWidth',2,'MarkerSize',10);
plot(r.*cos(theta_defunct),r.*sin(theta_defunct), 'xr','
    LineWidth',3,'MarkerSize',10);
plot(r,0,'ob','LineWidth',3,'MarkerSize',7,'MarkerFaceColor','b
');

% Unnamed plot elements
for i=1:length(theta_defunct)
t = theta_defunct(i);
r_angle = r/(5-i);
if t > pi
    t_line = 2*pi-t;
    t_vec = linspace(0,-t_line,100);
else
    t_vec = linspace(0,t,100);
end
dtheta = t_vec(end);
plot(r_angle*cos(t_vec),r_angle*sin(t_vec), '-k','LineWidth',2)
plot(r_vec.*cos(t),r_vec.*sin(t), '--r','LineWidth',2)
x_txt = 1.3*r_angle*cos(t_vec(50));
y_txt = 1.3*r_angle*sin(t_vec(50));
text(x_txt,y_txt,['\Delta\theta_',...
    num2str(i)],'FontSize',20)

end
plot(r_vec,r_vec.*sin(0), '--b','LineWidth',2)

% Axis
k = 1.2;
axis('equal')

% Legend
legend('show','Location','best')

```

```

legend(OrbitTag , 'Defunct Satellites' , 'Kick Stage')
fontsize(16 , "points");
set(gca , 'XColor' , 'none' , 'YColor' , 'none' , 'color' , 'none')
movegui

%%
mu = 0.3986e6;
r_e = 6378;

r0 = r_e + 525;
a0 = r0;
v0 = sqrt(mu/a0);
T0 = 2*pi*sqrt(a0^3/mu);

Tp = 86400 * 6;

dTheta = theta_satellites(defunct_numbers);
for i=1:length(dTheta)
if dTheta(i) > pi
dTheta(i) = -(2*pi - dTheta(i));
end
end

dV = abs(-sign(dTheta).*dTheta/(2*pi) * mu/(3*a0*v0*N))

```

C.6 Convergence Analysis

The following code conducts the convergence analysis for the two-body problem.

```

clear; clc; close all;

r_e = 6378;

tolerances = [1e-5 1e-6 1e-7 1e-8 1e-9 1e-10 1e-11 1e-12];
errors = zeros(1,length(tolerances));
R_expected = r_e + 525;

a = R_expected;
e = 0;
theta = 0;
i = 0;
Omega = 0;
omega = 0;

N = 10000;

```

```

t = linspace(0,86400*6,N);

[R0, V0] = getECI(a, e, theta, i, Omega, omega);
Y0 = [R0;V0];

for i=1:length(errors)
tolerance = tolerances(i);
opts = odeset('AbsTol',tolerance);

[t,y] = ode113(@(t,y) rates(t,y),t,Y0,opts);
x1 = y(:,1);
y1 = y(:,2);
z1 = y(:,3);

Rf = norm([x1(end),y1(end),z1(end)]);
errors(i) = double(100*(Rf - R_expected)/R_expected);
end

plot(log10(tolerances),errors,'-or','LineWidth',2,'MarkerSize'
,10);
set(gca, 'xdir', 'reverse')
xlabel('log_10 Absolute Tolerance')
ylabel('Percent Error')
grid on;

%{
for i=1:1:N
clf;
hold on;
set(gcf, 'Color', 'k');
set(gca, 'Color', 'k', 'XColor', 'k', 'YColor', 'k', 'ZColor',
'k');

plot3(x1(i),y1(i),z1(i),'om',x1(:),y1(:),z1(:),'--w');

axis equal;
view(3)
drawnow;
end
%}

%% dy/dt vector
function ydot = rates(t,y)

```

```

mu = 3.986004418e5;
R = [y(1); y(2); y(3)];
V = [y(4); y(5); y(6)];

r = norm(R);
A = -mu*R/r^3;

ydot = [V;A];
end

%% Earth Centered Inertia C-SYS Function
% Modified Classic Set --> ECI Cartesian (R, V)

function [R, V] = getECI(a, e, theta, i, Omega, omega)

% To get from MCS, I will get into a perifocal reference frame
% then into ECI Cartesian.

% angle inputs should be in degrees
deg2rad = pi/180;
mu_s = 3.986004418e5;

r = a*(1-e^2)/(1+e*cos(theta*deg2rad));

rp = r*cos(theta*deg2rad);
rq = r*sin(theta*deg2rad);

R_pqw = [rp; rq; 0];

vp = -sqrt( sqrt(mu_s/(a*(1-e^2)))^2 )*sin(theta*deg2rad);
vq = sqrt( sqrt(mu_s/(a*(1-e^2)))^2 )*(e+cos(theta*deg2rad));
V_pqw = [vp; vq; 0];

R_3 = @(x) [ cos(x*deg2rad) sin(x*deg2rad) 0; ...
             -sin(x*deg2rad) cos(x*deg2rad) 0; ...
                         0                      1];

R_1 = @(x) [1 0 0; ...
            0 cos(x*deg2rad) sin(x*deg2rad); ...
            0 -sin(x*deg2rad) cos(x*deg2rad)];;

R = R_3(-Omega)*R_1(-i)*R_3(-omega)*R_pqw;
V = R_3(-Omega)*R_1(-i)*R_3(-omega)*V_pqw;

```

```
end
```

C.7 Re-entry Analysis

The following code runs both the trajectory- and thermal analysis as they are coupled analyses.

```
%% Orbital Re-entry Analysis

% Written by Dominic Morand-Rivers
% EMA 569: Senior Design

%% Re-entry Trajectory:
tic; clc; clear all;

showPlots = true;
runHeatTX = true;

% Gravitaional Parameter:
mu = 3.986004418e5;
r_e = 6378;

% Time Step of Analysis:
dt = 0.01; % sec%

% Comes in on elliptical de-orbit burn to 100 km
alta = 535;
rA = 6378 + alta;
rB = 6378 + 100;
aT = (rA + rB)/2;
v0 = sqrt(mu*(2/rA - 1/aT));

a = aT;
e = 1- rB/aT;
theta = 0;
i = 0;
Omega = 0;
omega = 0;
set = [a,e,theta,i,Omega,omega];

R0 = [rA; 0; 0]; V0 = [0; v0; 0]; Y0 = [R0;V0];

% Surface Area and Mass:
ship = "std";
% kick stage:
```

```

if ship=="ks"
As = 5 * (1/1000)^2; m = 5000;
xf = 0.5;
th = 5e-3;
elseif ship=="std"
% STDs:
As = 1 * (1/1000)^2; m = 2000;
xf = 0.25;
th = 3e-3;
end

% Normal Trajectory (a):
CD = 0; CL = 0;
[t_vec,R_vec.a,V_vec.a] = re_entry_function(Y0, set, dt, CD, CL
, As, m);
for i = 1:length(t_vec)
H_vec.a(i) = norm(R_vec.a(i,:)) - r_e;
end

CD_vec = [1.8 1.6];
CL_vec = [-0.4 0.4];

% CD_vec = [1.6 1.8];
% CL_vec = [0.4 -0.4];

figure; hold on;
for j=1:length(CD_vec)

% Drag and Lift Model Trajectory (b):
CD = CD_vec(j); CL = CL_vec(j);

[t_vec,R_vec.b,V_vec.b] = re_entry_function(Y0, set, dt, CD, CL
, As, m);
for i = 1:length(t_vec)
H_vec.b(i) = norm(R_vec.b(i,:)) - r_e;
end

% Find time craft would be at surface if not burnt up:
[H_surf,T_surf] = min(abs(H_vec.b));

x.a = R_vec.a(:,1);
y.a = R_vec.a(:,2);

x.b = R_vec.b(1:T_surf,1);
y.b = R_vec.b(1:T_surf,2);

```

```

theta_crash(j) = mod(atan2(y.b(end),x.b(end)),2*pi)*180/pi;

disp(ship)
fprintf('CD = %.1f | CL = %.1f | theta = %.1f\n',CD,CL,
theta_crash(j));

% theta_crash:
%{

% Kick Stage:
CD      CL          theta (deg from start)
1.8     0.4          191.3
1.8     0             177.3
1.8    -0.4          170.9 MIN
1.6     0.4          195.0 MAX
1.6     0             178.3
1.6    -0.4          171.3

theta range = [170.9, 195.0]
24 degree range

% STD:
CD      CL          theta (deg from start)
1.8     0.4          199.4
1.8     0             183.9
1.8    -0.4          176.6 MIN
1.6     0.4          203.8 MAX
1.6     0             185.2
1.6    -0.4          177.1

theta range = [176.6, 203.8]
27.2 degree range

%}

% Extract Useful Solution (dropping subscript a,b)
% These are for the drag/lift model
t = t_vec(1:T_surf);
V = V_vec.b(1:T_surf);
H = H_vec.b(1:T_surf);
max_V = max(V);

% Find when the solutions diverge from each other <95% similar
(for plotting)

```

```

for i=1:length(t)
diff(i) = abs(abs(H_vec.a(i)-H_vec.b(i))/H_vec.a(i) - 0.95);
end
[h_diverge,i_diverge] = min(diff(:));
t_diverge = i_diverge*dt;

% Orbital Plots
% if showPlots
% % Orbital Mechanics Trajectory around Earth:
% figure; hold on;
% plot(x.b,y.b,'-r','DisplayName','Re-entry Model','LineWidth
% ',2);
% plot(x.a,y.a,'--b','DisplayName',[Transfer Orbit e =
% num2str(e)],'LineWidth',1);
% plot(r_e*cos(0:0.01:2*pi),r_e*sin(0:0.01:2*pi),'-g','
% DisplayName','Earth Surface','LineWidth',2);
% plot(x.b(end),y.b(end),'xk','DisplayName',[End Position:
% theta = ,num2str(theta_crash)],'LineWidth',1)
% axis("equal")
% axis off
% legend()

% Altitude vs Time
p1(j) = plot(t(:)/60,H(:));
% plot(t(:)/60,H(:),'-r','DisplayName',[C_D =
% num2str(CD),
% | C_L = ,num2str(CL), | \theta = ,num2str(theta_crash)
% ],'LineWidth',2);
p2(j) = plot(t(end)/60,H(end),'xk','LineWidth',1);
% plot(t(end)/60,H(end),'xk','DisplayName',[End Position:
% theta = ,num2str(theta_crash)],'LineWidth',1)

% Altitude vs Velocity
% figure; hold on;
% p1 = plot(H(1:T_surf),V(1:T_surf),'-r','DisplayName',
% Velocity with Atmosphere','LineWidth',2);
% %p3 = plot(H_vec.a(1:T_surf),V_vec.a(1:T_surf),'--b','
% DisplayName','Velocity without Atmosphere','LineWidth',2);
% p2 = plot(H(1:T_surf),max_V*ones(1,T_surf),'--k','DisplayName
% ',[V_m_a_x = ,num2str(max(max_V)), ' km/s']);
% legend("Location","best");
% xlabel('Altitude (km)');
% ylabel('Velocity (km/s)')
% clear gca;
% ax = gca; % Get current axis handle

```

```

% ax.XDir = 'reverse'; % Reverse the x-axis direction
% axis([0 alta 0 9]);
end

if showPlots
p3 = plot(t(:)/60,H_vec.a(1:T_surf),'--b','DisplayName','De-
orbit Transfer without Atmosphere','LineWidth',1.5);
p4 = plot(t(:)/60,zeros(1,length(t)),'-g','DisplayName','Earth
Surface','LineWidth',1);
p5 = plot(t(:)/60,100*ones(1,length(t)),'--k','DisplayName',
'Karman Line','LineWidth',1);
xlabel('Time Since De-orbit Burn (min)');
ylabel('Altitude (km)')
%legend([p1(1),p1(2)],{['C_D = ',num2str(CD_vec(1)), ' | C_L =
',num2str(CL_vec(1)), ' | \theta = 176.6'], ['C_D = ',num2str
(CD_vec(2)), ' | C_L = ',num2str(CL_vec(2)), ' | \theta =
203.8']})
legend([p1(1),p1(2),p3,p4,p5],{sprintf('C_D = %g, C_L = %g, \\
theta = %.1f', CD_vec(1), CL_vec(1),theta_crash(1)), ...
sprintf('C_D = %g, C_L = %g, \\\theta =
%.1f', CD_vec(2), CL_vec(2),
theta_crash(2)),...
sprintf('De-orbit Transfer without
Atmosphere'), ...
sprintf('Earth Surface'),...
sprintf('Karman Line'))});
p1(1).Color='r'; p1(1).LineStyle='-.'; p1(1).LineWidth=2;
p1(2).Color='r'; p1(2).LineStyle='--'; p1(2).LineWidth=2;
hold off;
end
runTime_orbit = round(toc);
disp(['Orbital mechanics analysis done in ',num2str(
runTime_orbit), ' s']);

%% Heat Transfer Effects
if runHeatTX
r_nose = 0.5; % m
Hn = 10.4; % km
rho0 = 1.225; % kg/m^3

% Exponential Model for Air Density
rho = rho0.*exp(-H/Hn);

% q_dot_entry for re-entry vehicle
%q_dot_entry = 1.83e-4*(V*1000).^3.*sqrt(rho./r_nose);

```

```

q_dot_entry = 0.7*rho.* (V*1000).^3/2;

[q_max,I_q_max] = max(q_dot_entry);
V_q_max = V(I_q_max);
H_max_q = H(I_q_max);

% Determine convection heat transfer coef:
Pr = 0.7;
D = 2*r_nose;
mu_air = 47.8802687*4e-7;
Re_D = rho.*V*(1000)*D/mu_air;

% Nusselt Number Correlation: Heat Transfer Cambridge p. 619
Nu_D = 2 + ( 0.4*Re_D.^0.5 + 0.06*Re_D.^2/3 ).*Pr.^0.4;
k_air = 50e-3;
h_conv = Nu_D*k_air/D;
%figure; plot(t,h_bar,'-k');

if showPlots
figure; hold on;
plot(q_dot_entry,H,'-r','LineWidth',2);
p2 = plot(q_dot_entry,H_max_q.*ones(1,T_surf),'--k','
DisplayName',['Hq_m_a_x = ',num2str(H_max_q),' km']);
legend(p2,['Alt_q_/_m_a_x = ',num2str(H_max_q),' km']);
xlabel('q_e_n_t_r_y [ W/m^2 ]')
ylabel('Altitude [km]')

figure; hold on;
plot(q_dot_entry,V,'-r','LineWidth',2);
p2 = plot(q_dot_entry,V_q_max.*ones(1,T_surf),'--k','
DisplayName',['Vq_m_a_x = ',num2str(V_q_max),' km/s']);
legend(p2,['Vq_m_a_x = ',num2str(V_q_max),' km/s']);
xlabel('q_e_n_t_r_y [ W/m^2 ]')
ylabel('Velocity [km/s]')

figure; hold on;
yyaxis left;
p2 = plot(t/60,V,'-r','LineWidth',2);
p3 = plot(t/60,max_V*ones(1,T_surf),'--r','LineWidth',1);
ax = gca;
ax.YColor='r';
axis auto;
ylabel('Re-entry Speed [km/s]')

```

```

yyaxis right;
p4 = plot(t/60,H,'-b','LineWidth',2);
ax = gca;
ax.YColor='b';
ylabel('Altitude [km]')
xlabel('Time [min]')
hold off;
%legend(p3,sprintf('V_m_a_x = %.2f km/s\n',max_V),'location','best')

figure; hold on;
plot(t/60,q_dot_entry,'-r','LineWidth',2)
xlabel('Time [min]')
ylabel('q_e_n_t_r_y [ W/m^2 ]')

end

%% Crank-Nicolson Method

% Spatial Discretization
nx = 11;
%th = 5e-3;
xi = xf-th;
dx = (xf-xi)/(nx-1);
x = linspace(0,th,nx);

% Temporal Discretization
nt = T_surf;
tf = t_vec(T_surf);
dt = tf/(nt-1);
time = t;

% Parameter Functions:

% Titanium Specific Heat Capacity:
Cp_vs_T = readmatrix("Cp_vs_K.csv");
Cp_vs_T_x = Cp_vs_T(:,2);
Cp_vs_T_y = Cp_vs_T(:,1);
Cp_T = @(T) interp1(Cp_vs_T_x,Cp_vs_T_y,T,'linear','extrap');
if showPlots
figure; hold on;
plot(Cp_vs_T_x,Cp_vs_T_y,'.-k');
xlabel('Temperature [K]');
ylabel('C_p [J/kg-K]');
end

```

```

% Titanium Conduction k
K_vs_T = readmatrix("K_vs_T.csv");
K_vs_T_x = K_vs_T(:,2);
K_vs_T_y = K_vs_T(:,1);
k_T = @(T) interp1(K_vs_T_x,K_vs_T_y,T,'linear','extrap');
if showPlots
figure; hold on;
plot(K_vs_T_x,K_vs_T_y,'.-k')
xlabel('Temperature [K]')
ylabel('K [W/m-K]')
end

% Atmospheric Temperature vs Altitude:
Alt_vs_Temp = readmatrix('Altitude_vs_Temperature.csv');
Alt_vs_Temp_x = unique(Alt_vs_Temp(:,2));
Alt_vs_Temp_y = unique(Alt_vs_Temp(:,1));
temperatureFunc = @(h) interp1(Alt_vs_Temp_x,Alt_vs_Temp_y,h,
    'linear','extrap');
if showPlots
figure; hold on;
plot(Alt_vs_Temp_x,Alt_vs_Temp_y,'.-k')
xlabel('Altitude [km]')
ylabel('Temperature [K]')
end

% T_infinity = T_atmosphere at altitude for each time step!
%T_inf = 273*ones(1,nt);

% Heat Transfer Coef (convection)

% Initialize Matrix and Vector
A = zeros(nx,nx);
T = zeros(nx,nt);
d = zeros(nx,1);

% Initial Conditions
T(:,1) = linspace(230,273,nx);

% Constant Parameters:
rho_T = 4437;
k_h = 2.4;
Cp_h = 1559.45;
rho_h = 1025.3;
alpha_h = k_h/Cp_h/rho_h;

```

```

% Radiation Terms:
% Stefan-Boltzmann Constant
sigma = 5.670374419e-8;
As_out = xf^2*4*pi;
epsilon = 0.45;

% Constant Hydrazine Temp
%T_H = 230;
%T_H = linspace(200,300,nt);
vol_h = 4*pi/3*xi^3;
R = alpha_h*4*pi/(1/0.4 - 1/xi)/vol_h;

%%%
tic;

% Constant Material Parameters:
%
% Hydrazine Temp:
%T_H = zeros(1,nt);
T_H = 200;

% Atmosphere Temp:
T_inf = 208.15*ones(1,nt);
%T_inf = temperatureFunc(H(:));

% Titanium Parameters:
alpha_T = 3.5e-6; % average alpha for T = 200K to 1943K for
    Titanium
cp = 916; % average from 200K to 1943K

ai = -alpha_T/(2*dx^2);
bi = (1/dt) + (alpha_T/dx^2);
ci = -alpha_T/(2*dx^2);

main_diag = bi*ones(1,nx);
up_diag = ci*ones(1,nx-1);
low_diag = ai*ones(1,nx-1);
A = diag(main_diag) + diag(up_diag,1) + diag(low_diag,-1);

% Convection & Radiation (linear approx)
h = h_conv(1) + As_out*epsilon*sigma*(T(nx,1)^2 + T_inf(1)^2)*(
    T(nx,1) + T_inf(1));
%h = -h;

```

```

%h = (mean(h_conv) + mean(4*As_out*epsilon*sigma*((200:1943).^2
    + (200:1943).^2).*(200:1943 + 200:1943))) ;
%h = h_conv(1) ;

% BCs
A(1,1) = 2/dt + alpha_T/dx^2 + k_h/cp/rho_T/dx^2;
A(1,2) = -alpha_T/dx^2;

A(nx,nx-1) = -alpha_T/dx^2;
A(nx,nx) = 2/dt + h/rho_T/cp/dx + alpha_T/dx^2;

for j=2:nt

    % Convection + Radiation (linear approx)
    h = h_conv(j) + 4*As_out*epsilon*sigma*(T(nx,j-1)^2 + T_inf(j-1)^2)*(T(nx,j-1) + T_inf(j-1));
    % Inside Wall:
    d(1) = ( 2*T_H )*k_h/cp/rho_T/dx^2 + T(2,j-1)*alpha_T/dx^2 + T(1,j-1)*( 2/dt - alpha_T/dx^2 - k_h/cp/rho_T/dx^2 );

    % Generate interior d vector
    for i=2:nx-1
        % ai = -alpha_T/(2*dx^2);
        % bi = (1/dt) + (alpha_T/dx^2);
        % ci = -alpha_T/(2*dx^2);
        d(i)=(1/dt)*T(i,j-1)-ai*T(i-1,j-1)+(ai+ci)*T(i,j-1)-ci*T(i+1,j-1);
    end

    % Outer Wall BC:
    A(nx,nx) = 2/dt + h/rho_T/cp/dx + alpha_T/dx^2;
    d(nx) = T(nx-1,j-1)*(alpha_T/dx^2) + T(nx,j-1)*(-h/(rho_T*cp*dx) - alpha_T/dx^2 + 2/dt) + (T_inf(j-1)+T_inf(j))*( h/(rho_T*cp*dx) ) + ( q_dot_entry(j) + q_dot_entry(j-1) )/( rho_T*cp*dx );

    T(:,j) = A\d;
end
%}

runTime_heatTx = toc;
disp(['Heat transfer analysis done in ',num2str(round(
    runTime_heatTx*1000)), ' ms']);

N_30min = round(30*60/dt);

```

```

% Get Realistic Temperatures
T_mask1 = (T<1943).*1;
T_mask2 = (T>=1943).*1943;
T = (T.*T_mask1) + (T*T_mask2);
index_plot = 1:nt;
%max(max(T))

if true
figure; hold on;
plot(x,T(:,1), 'b', 'DisplayName', 'Initial')
plot(x,T(:,end), 'r', 'DisplayName', 'Final')
legend();
end

figure; hold on;
plot(time(index_plot)/60,T(nx,index_plot), 'b', 'DisplayName', [
    'Outside Surface | Node ', num2str(nx)], 'LineWidth', 2)
% for i=1:3
% plot(time(index_plot)/60,T(nx-i,index_plot), 'k', 'DisplayName
%     ', ['Node ', num2str(nx-i)]);
% end
% plot(time(index_plot)/60,T(7,index_plot), 'g', 'DisplayName', 'Node 7');
plot(time(index_plot)/60,T(1,index_plot), 'r', 'DisplayName', 'Inside Surface | Node 1', 'LineWidth', 2);
xlabel('Time Since De-Orbit Burn [min]')
ylabel('Temperature [K]');
legend('Location','best');
axis('auto')

if showPlots
figure; hold on;
[X,Y] = meshgrid(x*1000,t/60);
surf(Y,X,transpose(T));
ylabel('Position (mm)')
xlabel('Time (min)')
shading interp;
view(2);
axis("tight")
colorbar;
end

end
% end if runHeatTX

```

```

%% Re-entry Trajectory Function

function [t,R_t,V_t] = re_entry_function(Y0, set, dt, C_D, C_L,
    As, m)

% Inputs:
% Y0 - Initial Conditions of Re-entry
% set - Modified Classic Set parameters
% dt - Time Step of Trajectory
% CD - Coef. of Drag
% CL - Coef. of Lift

% Outputs:
% t - Time vector of re-entry trajectory
% H_t - vector of altitude
% V_t - vector of speed

% ode113 error
opts = odeset('RelTol',1e-12,'AbsTol',1e-12);

% Earth Gravitational Parameter
mu = 3.986004418e5;

% Rotation Matrices
deg2rad = pi/180;

R_1 = @(x) [1 0 0; ...
            0 cos(x*deg2rad) sin(x*deg2rad); ...
            0 -sin(x*deg2rad) cos(x*deg2rad)]; ...

R_3 = @(x) [cos(x*deg2rad) sin(x*deg2rad) 0; ...
            -sin(x*deg2rad) cos(x*deg2rad) 0; ...
            0 0 1]; ...

% Initial Orbit Elements:
a = set(1);
e = set(2);
theta = set(3);
i = set(4);
Omega = set(5);
omega = set(6);

% Read in Parameters
R = Y0(1:3);

```

```

V = Y0(4:6);

% Rotate into perifocal reference frame:
R0 = R_3(omega)*R_1(i)*R_3(Omega)*R;
V0 = R_3(omega)*R_1(i)*R_3(Omega)*V;

% Initial Position for 2-DOF (x,y) solver
y0 = [R0(1:2);V0(1:2)];

% Properties
rho0 = 1.225 * (1000)^3; % kg km^3 - sea level density of air
Hn = 10.4; % km
% As = pi*(0.5)^2 * (1/1000)^2; % Surface Area of Lift/Drag
% Surfaces
% m = 5000; % kg

% 2-DOF Re-entry Equation of Motion:
function ydot = rates(t,y)

% Altitude (km)
h = (norm([y(1) y(2)]) - 6378);
rho = rho0*exp(-h/Hn);

% Read in position and velocity
R = [y(1); y(2)];
V = [y(3); y(4)];

% Polar
r_hat = R./norm(R);
theta_hat = V./norm(V);

% Body-fixed-reference
x_hat = V./norm(V);
y_hat = [cos(pi/2) sin(pi/2); -sin(pi/2) cos(pi/2)]*x_hat;

% Gravity Term
mu = 3.986004418e5;
r = norm(R);
Fg = mu/r^2;
Fg_vec = -Fg*r_hat;

% Drag Inclusion
Vx = V(1);
Vy = V(2);
v = sqrt(Vx^2 + Vy^2);

```

```

% Lift & Drag
L = 0.5*rho*v^2*As*C_L;
D = 0.5*rho*v^2*As*C_D;

% Accel Vector
A = L*y_hat/m - D*x_hat/m + Fg_vec;

ydot = [V;A];
end

n0 = sqrt(a^3/mu);
T_final = 2*pi*n0;
t = 0:dt:T_final;

[t,y] = ode113(@(t,y) rates(t,y),t,y0,opts);

R_t = y(:,1:2);
for i=1:length(t)
V_t(i) = norm(y(i,3:4));
end

end

```

D Nozzle Geometry and State Calculations

Appendix D contains the MATLAB script used to define and plot the geometry for all engine nozzles, as well as finding temperatures using the Bartz correlation.

```
% Rao Parabolic Nozzle
% Tooling Constants

Re = 0.15; % Exit radius ( MAIN VARIABLE )
eps = 44; % Expansion ratio
Rt = sqrt ( Re ^2 / eps ) ; % Throat radius
Rdt = 0.382* Rt ; % Downrange throat curve radius
Rut = 1.5* Rt ; % Uprange throat curve radius
theta_a = deg2rad(38); % Initial nozzle slope
theta_e = deg2rad(13); % Final nozzle slope
theta_s = deg2rad(45); % Chamber Slope

% Geometric Constants
xco = Rdt * sin ( theta_a ) ; % Crossover x
Rco = Rt + Rdt *(1 - cos ( theta_a ) ) ; % Crossover radius
xs = - sin ( theta_s ) * Rut ; % Combustion chamber ending x
rc = - sqrt ( Rut ^2 - xs ^2) + Rt + Rut ; % Combustion chamber
    crossover radius
r0 = 0.372/2; % Combustion chamber final radius

% System of Equation Constants
a = ( xco ^2 * tan ( theta_a ) ^2 - 4* Rco * Re + 4* Rco ^2 -
    4* Rco * xco * tan ( theta_a ) + 4* Re * xco * tan ( theta_a
    ) ) / (4* Rco - 4* Re ) ;
b = ( - tan ( theta_a ) * (2* Re - 2* Rco + xco * tan ( theta_a
    ) ) ) / (2*(Rco - Re ) ) ;
c = tan ( theta_a ) ^2 / (4* Rco - 4* Re ) ;
xe = (2* Re - 2* Rco + xco * cos ( theta_a ) - Re * sin (
    theta_e ) ) / tan (theta_a ) ;
xb = rc + xs - r0;

% Piecewise Setup
x4 = linspace(-2, xb, 100);
x0 = linspace(xb, xs, 100);
x1 = linspace(xs, 0, 100);
x2 = linspace(0, xco, 5);
x3 = linspace(xco ,xe ,100) ;
f4 = r0 * ones(length(x4));
f0 = rc - x0 + xs;
f1 = -sqrt (Rut ^2 - x1.^2) + Rt + Rut ;
```

```

f2 = -sqrt (Rdt ^2 - x2.^2) + Rdt + Rt ;
f3 = a + b*x3 + c*x3.^2;

figure
hold on
xlim ([-0.3 , xe+0.05]) ;
ylim ([0 , 0.3]) ;
plot(x4, f4, 'LineWidth', 1);
plot(x0, f0, 'LineWidth', 1);
plot(x1, f1, 'LineWidth', 1);
plot(x2, f2, 'LineWidth', 1);
plot(x3, f3, 'LineWidth', 1);

r_x = [f2, f3];
xnew = [x2, x3];
A_x = pi .* r_x.^2;
A_t = Rt^2 * pi;
A_As = A_x ./ A_t;

gamma = 1.4;
isentropic_func = @(M, A_Astar) (1./M) .* ((2./(gamma+1) .* (1
+ (gamma - 1)/2 .* M.^2)) .^ ((gamma+1)/(2*(gamma-1)))) -
A_Astar;

Msub = zeros(size(A_As));
Msup = zeros(size(A_As));

for i = 1:length(A_As)
    A_val = A_As(i);
    Msup(i) = fzero(@(M) isentropic_func(M, A_val), [1, 100]);
end

Psup_P0 = zeros(size(A_As));
Tsup_T0 = zeros(size(A_As));

for i = 1:length(Msup)
    Mval = Msup(i);
    Psup_P0(i) = (1 + ((gamma - 1) / 2)*Mval^2)^(gamma / (1 -
gamma));
    Tsup_T0(i) = (1 + ((gamma - 1) / 2) * Mval^2)^(-1);
end

P0 = 730000; %Pa
Psup = Psup_P0 .* P0;
Psup = Psup';

```

```

PsupDist = [xnew '+0.37586, -Psup];

T0 = 1136; % K
Tsup = Tsup_T0 .* T0;

figure;
plot(xnew, r_x);
xlabel('x (m)')
ylabel('Radius (m)')

figure;
plot(xnew, Msup)
xlabel('x (m)')
ylabel('Mach Number')
title('Mach Number vs Distance from Throat')

figure;
semilogy(xnew, Psup, 'LineWidth', 1.5, 'Color', 'k')
xlabel('x (m)')
ylabel('Pressure (Pa)')
title('Pressure vs Distance from Throat')

%% Heat Transfer
A_s = 0.31415 * 2*pi; % Surface area available to convect to/
radiate from

Tw_guess = (293 + Tsup) ./ 2; % Wall temp guess for avg. heat
transfer coeff.
mu_0 = 3.178 * 10^-5; % Dynamic viscosity, appx. as air
dt = Rt * 2;
Pr_0 = 0.7368; % Prandtl number
Cp = 2375; % J/kgK
Cstar = 1282.3; % Characteristic velocity
omega = 0.6; % Assumption for diatomic gases, valid for general
use cases

% Bartz coeff.
sigma = ((0.5 .* (Tw_guess ./ T0) .* (1 + ((gamma - 1) / 2) .*%
Msup.^2)+0.5).^(0.8 - 0.2*omega).*((1 + ((gamma - 1)/2) .*%
Msup.^2).^(0.2*omega))).^(-1);

hg = ((0.026 / (dt^0.2))*(Cp * ((mu_0^0.2) / (Pr_0^0.6)))*(P0 / %
Cstar)^0.8*(dt / Rut)^0.1 .* (1 ./ A_As).^0.9 .* sigma;
hbar = mean(hg); % Mean heat transfer coefficient for thermal
analysis

```

```

epsilon = 0.2; % See bookmarked source
T_initial = 293; % Wall initially at 293 K
tspan_pre = [0 8435+(7*24*3600)]; %Pre-burn time
tspan = [0 120]; % 2 minute burn time
sigma_b = 5.67e-8; % Stefan-Boltzmann constant
rho_h25 = 9070; %Density of haynes-25, kg/m^3
th = 5.62 * 10^-3; % Thickness of nozzle wall
T_inf = 3; %K, space temp
T_bar = max(Tsup); % Max gas temp (@ Throat)
ch25 = 582; %J/kgC, Spec. heat of Haynes 25 @ 800C

% Biot number, hL/k, gives absolute maximum of 0.1185 at room
% temp. Lumped
% Capacitance is valid
dTdt = @(t, T) (hbar * (T_bar - T) + epsilon*sigma_b*(T_inf^4 -
T^4)) / (rho_h25 * th * ch25);

dTdt_pre = @(t, T) (epsilon*sigma_b*(T_inf^4 - T^4)) / (rho_h25
* th * ch25); % dTdt for pre-burn temp

[t_pre, Twall_pre] = ode45(dTdt_pre, tspan_pre, T_initial);

figure;
plot(t_pre/3600, Twall_pre - 273.15, 'LineWidth', 1.5)
xlabel('Time since Payload Fairing Deployment (hr)')
ylabel('Nozzle Temperature (C)')
title('Pre-Burn Wall Temperature vs Time')

disp(['Initial Pre-Burn Wall Temperature: ' num2str(Twall_pre(
end)-273.15) ' C']);

T_initial_new = Twall_pre(end);

[t, Twall] = ode45(dTdt, tspan, T_initial_new);

figure;
plot(t, Twall - 273.15, 'LineWidth', 1.5)
xlabel('Burn Time (s)')
ylabel('Nozzle Temperature (C)')
title('Nozzle Wall Temperature vs Burn Time')

T_max = max(Twall);

```

```
disp(['Ending Throat Wall Temperature: ' num2str(T_max-273.15)
      ' C'])
```

E Attitude Control Calculations

Appendix C has all of the MATLAB scripts for the sizing of attitude control system.

```
% Moments of Inertia
m_tot = 2000; % starlink mass
n_solar = 2; % number of solar arrays
Solar Arrays
m_perc = 0.2; % percentage of satellite mass by the solar
    arrays
m_solar = m_tot*m_perc/n_solar; % mass of one solar array
a = 20.2;
b = 6.36;
c = 0.1;
I_solar = rectprism_MOI(a, b, c, m_solar);
% Bus
m_bus = m_tot*(1-m_perc);
a = 2.7
b = 10.1;
c = 0.2;
I_bus = rectprism_MOI(a,b,c,m_bus);
% STD MOI:
R = 0.5; % side length of cubic model of STD
L = 2;
turn = pi; % magnitude of turn
m_STD = 400; % mass of STD
I_STD_lat = (1/12)*m_STD*(3*R^2+L^2);
I_STD_rad = (1/2)*m_STD*R^2;
I_STD_cyl = diag([I_STD_lat,I_STD_lat,I_STD_rad]);
Parallel Axis Theorem
r_array = [10.7,0,0.4];
I_gsolar = parallel_axis_moi(I_solar,m_solar,r_array);

r_STD = [0,0,-0.6];
I_gSTD = parallel_axis_moi(I_STD_cyl,m_STD,r_STD);

r_bus = [0,0,0.4];
I_gBus = parallel_axis_moi(I_solar,m_bus,r_bus);

I_SL = 2*I_gsolar + I_gBus + I_gSTD

% Momentum:
I_max = max(I_SL(:));
omega_max = deg2rad(10);
H_SL = omega_max * I_max
```

```

% Magnetorquers:
mag_dipole = 400;
B_mag = 2.5*10^-5;
torque_mag = mag_dipole*B_mag;
alpha_mag = torque_mag/I_max;
t_slow = omega_max/alpha_mag;
t_slow_days = t_slow/(60*60*24);
disp("Number of Days to slow using magnetorquers: " +
      t_slow_days)

% Thrusters:
% First Turn:
t_turn = 30; % time to orient for burn
omega_turn = turn/(t_turn/2);
alpha_turn = omega_turn/(t_turn/2);
torque_turn = max(I_STD_cyl(:))*alpha_turn;
disp("Contstant torque for first turn: " + torque_turn + " N-m
      ")
STD_arm = 0.5;
F_turn = torque_turn/STD_arm
% Slow Starlink:
omega_max = deg2rad(10); % max initial angular speed of the
                           starlink
t_max = 600;% max allowable time to slow the starlink
arm_torque = 1.5;
impulse = H_SL/arm_torque
alpha_ave = omega_max/t_max;
torque_ave = I_max*alpha_ave;
disp("Average Torque to slow the angular momentum of Starlink
      in " + t_max + " seconds: " + torque_ave + " N-m")
F_slow = torque_ave/arm_torque

% Second Turn:
t_turn2 = 5*60; % time to orient for burn
omega_turn2 = turn/(t_turn2/2);
alpha_turn2 = omega_turn2/(t_turn2/2);
torque_turn2 = I_max*alpha_turn2;
disp("Contstant torque for second turn: " + torque_turn2 + " N-
      m");
F_turn2 = torque_turn2/arm_torque

% Mass Required:
N2:
Isp_N2 = 60;
g0 = 9.81;

```

```

v_N2 = Isp_N2 * g0
m_turn_N2 = (F_turn/v_N2)*t_turn;
m_slow_N2 = impulse/(Isp_N2*g0)
m_turn2_N2 = (F_turn2/v_N2)*t_turn2
m_dock_N2 = 10*m_turn_N2;

m_tot_N2 = m_turn_N2 + m_slow_N2 + m_turn2_N2 + m_dock_N2

R_N2 = 296.8; % Gas constant for N2
T_N2 = 300; % temperature of N2 in tank
P_bar = 75; % bar pressure
P_N2 = P_bar*100000;
V_N2 = m_tot_N2*R_N2*T_N2/P_N2
% Hyrdazine:
Isp_hz = 210;
v_hz = Isp_hz * g0;
m_turn_hz = (F_turn/v_hz)*t_turn;
m_slow_hz = impulse/(Isp_hz*g0);
m_turn2_hz = (F_turn2/v_hz)*t_turn2;
m_dock_hz = 10*m_turn_hz;

m_tot_hz = m_turn_hz + m_slow_hz + m_turn2_hz + m_dock_hz

rho_hz = 1004;
V_hz = m_tot_hz/rho_hz

% Reaction Wheel:

t_turn_wheel = 60;
omega_turn_wheel = pi/t_turn_wheel;
H_STD_wheel = omega_turn_wheel * max(I_STD_cyl(:));
H_wheel = 2*H_STD_wheel

% Functions:
function I = rectprism_MOI(a, b, c, m)
    % This function calculates the moment of inertia for a
    % rectangular prism.
    % a, b, c are the dimensions of the rectangular prism
    % m is the mass of the rectangular prism

    % Moment of inertia about the x-axis (through the center)
    I_x = (1/12) * m * (b^2 + c^2);

    % Moment of inertia about the y-axis (through the center)

```

```

I_y = (1/12) * m * (a^2 + c^2);

% Moment of inertia about the z-axis (through the center)
I_z = (1/12) * m * (a^2 + b^2);

% Output the moment of inertia tensor as a diagonal matrix
I = diag([I_x, I_y, I_z]);
end

function I_new = parallel_axis_moi(I_orig, m, d)
%PARALLEL_AXIS_MOI Applies the parallel axis theorem to
    % shift a MOI matrix.
%
%   I_new = parallel_axis_moi(I_orig, m, d) returns the new
%   3x3 moment of
%   inertia matrix I_new after shifting the reference point
%   by the displacement
%   vector d, given the mass m and the original moment of
%   inertia matrix I_orig.
%
%   The parallel axis theorem for a moment of inertia
%   matrix is given by:
%
%       I_new = I_orig + m * (||d||^2*I - d*d')
%
%   where ||d||^2 is the squared norm of the displacement
%   vector, I is the
%   3x3 identity matrix, and d*d' is the outer product of d
%   with itself.
%
%   Inputs:
%       I_orig - 3x3 original moment of inertia matrix (
%               about the center of mass)
%       m      - Mass of the object
%       d      - Displacement vector [dx, dy, dz] (can be a
%               row or column vector)
%
%   Output:
%       I_new - 3x3 moment of inertia matrix about the new
%               reference point

% Ensure d is a column vector
d = d(:);

% Calculate the squared norm of d

```

```
d_squared = sum(d.^2);  
  
% Outer product of d with itself (3x3 matrix)  
ddT = d * d';  
  
% 3x3 identity matrix  
I_identity = eye(3);  
  
% Apply the parallel axis theorem  
I_new = I_orig + m * (d_squared * I_identity - ddT);  
end
```

F Kick Stage Propulsion Python Code

F.1 CEA

```
from rocketcea.cea_obj import CEA_Obj

pcL = [ 750., 500., 250.]

tempObj = CEA_Obj(propName=' ', oxName='N2O4', fuelName="MMH")

for Pc in pcL:
    tempArr = []
    MR = 0.5
    mrArr = []
    while MR < 4.0:
        tempArr.append((5/9)*tempObj.get_Temperatures( Pc=Pc, MR=MR, eps=5)[1])
        mrArr.append(MR)
        MR += 0.05
    plt.plot(mrArr, tempArr, label='Pc=%g_psia %Pc')
plt.plot([0.5, 4.0], [1700, 1700], label='Melting_point_of_Inconel_718')
plt.legend(loc='best')
plt.grid(True)
plt.title( tempObj.desc )
plt.xlabel( 'Mixture_Ratio' )
plt.ylabel( 'Throat_temperature_(K)' )
plt.savefig('cea_throat_temp_plot.png', dpi=120)
plt.show()

from rocketcea.cea_obj import CEA_Obj
import matplotlib.pyplot as plt

pcL = [750., 500., 250.] # Chamber pressures in psia
tempObj = CEA_Obj(propName=' ', oxName='N2O4', fuelName="MMH")

for Pc in pcL:
    ispArr = []
    mrArr = []
    MR = 0.5
    while MR < 4.0:
        ispArr.append(tempObj.get_Isp(Pc=Pc, MR=MR, eps=60)) # Get ISP at P
        mrArr.append(MR)
        MR += 0.05
    plt.plot(mrArr, ispArr, label='Pc=%g_psia %Pc')

plt.yticks(np.arange(int(min(ispArr)), max(ispArr) + 5, 5)) # Set y-axis ticks
```

```

plt.legend(loc='best')
plt.grid(True)
plt.title(tempObj.desc)
plt.xlabel('Mixture_Ratio_(O/F)')
plt.ylabel('Isp_(s)')
plt.savefig('cea_isp_plot.png', dpi=120)
plt.show()

```

F.2 Kick stage propulsion sizing

```

m_structure = 400 # kg
m_press = 150 # kg
m_tanks = 350 # kg, iterated with below code to converge on 225 kg
m_rcs = 25 # kg
m_prop = 100 # kg
m_std = 400 # kg

m_b1 = m_structure + m_tanks + m_rcs + m_prop + m_press + m_std*7

u_e = 2900 # m/s, MMH-NTO from NASA CEA

delta_v1 = 246 # m/s, from Dom calculations
m_b2 = m_structure + m_tanks + m_rcs + m_prop + m_press + m_std*5
delta_v2 = 1324 # m/s, from Dom calculations
m_b3 = m_structure + m_tanks + m_rcs + m_prop + m_press + m_std*3
delta_v3 = 1324 # m/s, from Dom calculations
m_b4 = m_structure + m_tanks + m_rcs + m_prop + m_press
delta_v4 = 124 # m/s, from Dom calculations

m_f1 = (math.exp(delta_v1/(u_e)) - 1)*m_b1
m_f2 = (math.exp(delta_v2/(u_e)) - 1)*m_b2
m_f3 = (math.exp(delta_v3/(u_e)) - 1)*m_b3
m_f4 = (math.exp(delta_v4/(u_e)) - 1)*m_b4

print(f"m_b1={m_b1}kg", f"m_b2={m_b2}kg", f"m_b3={m_b3}kg", f"m_b4={m_b4}kg")

print(f"m_f1={m_f1}kg", f"m_f2={m_f2}kg", f"m_f3={m_f3}kg", f"m_f4={m_f4}kg")

m_f = (m_f1 + m_f2 + m_f3 + m_f4)*1.25 # 25% margin

print(f"m_f={m_f}kg")

rho_mmh = 880 # kg/m^3
rho_nto = 1442 # kg/m^3

```

```
MR = 2 #NTO to MMH
```

```
rho_weighted_average = (rho_mmh + MR*rho_nto)/(1+MR)
print(rho_weighted_average)
```

```
V_f = m_f/rho_weighted_average*1.5
print(f"V_f={V_f} m^3")
```

```
m_liftoff = m_b1 + m_f
print(m_liftoff)
```

```
# get volume of propellant to find tanks to update tank mass, use mixture rate
```

```
m_b1 = 3825 kg m_b2 = 3025 kg m_b3 = 2225 kg m_b4 = 1025 kg
m_f1 = 338.62485187901524 kg m_f2 = 1750.328730375449 kg m_f3 = 1287.4318760612807 kg m_f
= 4276.454433841335 kg
1254.6666666666667
V_f = 5.11265806383794 m^3
8101.454433841335
vol_prop = 5.11
```

```
# equation in notes
diameter = 1.8
```

```
height = vol_prop/(math.pi*diameter**2/4)
```

```
# surface area of tank
area = math.pi*diameter*height + 2*math.pi*(diameter/2)**2
```

```
# thickness of tank
# sigma = p*r/t
sigma = 0.75*880*10**6 # (75% of 880 MPa)
p = 500*6894.76 # Psi to Pa
r = diameter/2
t = max(p*r/(sigma),0.002)
```

```
tank_wall_volume = area*t
rho_Ti6Al4V = 4430 # kg/m^3
m_tank = tank_wall_volume*rho_Ti6Al4V
print(f"m_tank={m_tank} kg")
print(f"tank_diameter={diameter} m, height={height} m, thickness={t} m")
print(area)
```

```
m_tank = 342.47086947738205 kg
```

```

tank diameter = 1.8 m, height = 2.0081031091347783 m, thickness = 0.004700972727272728 m
16.444935654371022

# look at expansion ratio improvements

from rocketcea.cea_obj import CEA_Obj
import matplotlib.pyplot as plt

Pc = 250
#pcL = [750., 500., 250.] # Chamber pressures in psia
MRL = np.arange(0.5, 2, .15) # Mixture ratios
tempObj = CEA_Obj(propName=' ', oxName='N2O4', fuelName="MMH")

for MR in MRL:
    ispArr = []
    epsArr = []
    eps = 5
    while eps < 100:
        ispArr.append(tempObj.get_Isp(Pc=Pc, MR=MR, eps=eps)) # Get ISP at P
        epsArr.append(eps)
        eps += 1
    plt.plot(epsArr, ispArr, label='MR=%g' % MR)

plt.yticks(np.arange(230, 360, 10)) # Set y-axis ticks every 5

plt.legend(loc='best')
plt.grid(True)
plt.title(tempObj.desc)
plt.xlabel('Expansion_Ratio_(eps)')
plt.ylabel('Isp_(s)')
plt.savefig('cea_isp_eps_plot.png', dpi=120)
plt.show()

# full CEA

# rough input values
Pc = 185 # chamber pressure in psia
MR = 1.5 # mixture ratio
#PcOvPe = 1000 # chamber pressure over exit pressure
eps = 150 # expansion ratio
#subar = 3 # subsonic area ratio
CR = (125**2)/(61.237**2)

from rocketcea.cea_obj import CEA_Obj

# Define CEA object for the specified propellant combination

```

```

ispObj = CEA_Obj(propName=' ', oxName='N2O4', fuelName='MMH')

# Get equilibrium results
sol_eq = ispObj.get_full_cea_output(
    Pc=Pc,
    MR=MR,
    eps=eps,
    short_output=0,
    pc_units='psia',
    output='siunits',
    fac_CR=CR # Finite area combustor contraction ratio (if needed)
)

# Get frozen flow results
sol_fr = ispObj.get_full_cea_output(
    Pc=Pc,
    MR=MR,
    eps=eps,
    short_output=0,
    pc_units='psia',
    output='siunits',
    frozen=1, # Setting frozen flow condition
    fac_CR=CR # Finite area combustor contraction ratio (if needed)
)

# Print results
#print("Equilibrium Results:\n", sol_eq)
print("\nFrozen Flow Results:\n", sol_fr)

```

Frozen Flow Results:

NASA-GLENN CHEMICAL EQUILIBRIUM PROGRAM CEA, OCTOBER 18, 2002
 BY BONNIE MCBRIDE AND SANFORD GORDON
 REFS: NASA RP-1311, PART I, 1994 AND NASA RP-1311, PART II, 1996

```

reac
fuel CH6N2(L)  C 1      H 6      N 2      wt% = 100.00
h,cal=12900.0    t(k)=298.15   rho=.874

```

oxid N2O4(L) N 2 O 4 wt% = 100.00
h,cal=-4676.0 t(k)=298.15

prob case=RocketCEA,
rocket frozen nfz=1 p,psia=185.000000, supar=150.000000,
fac ac/at=4.166700,
o/f=1.500000,

output siunits transport
end

OPTIONS: TP=F HP=F SP=F TV=F UV=F SV=F DETN=F SHOCK=F REFL=F INCD=F
RKT=T FROZ=T EQL=T IONS=F SIUNIT=T DEBUGF=F SHKDBG=F DETDBG=F TRNSPT=T

TRACE= 0.00E+00 S/R= 0.000000E+00 H/R= 0.000000E+00 U/R= 0.000000E+00

Pc,BAR = 12.755251

Pc/P =

SUBSONIC AREA RATIOS =

SUPERSONIC AREA RATIOS = 150.0000

NFZ= 1 Mdot/Ac= 0.000000E+00 Ac/At= 4.166700E+00

REACTANT	WT.FRAC	(ENERGY/R),K	TEMP,K	DENSITY
EXPLODED FORMULA				
F: CH ₆ N ₂ (L)	1.000000	0.649149E+04	298.15	0.8740
C	1.000000	H 6.000000	N 2.00000	
O: N ₂ O ₄ (L)	1.000000	-0.235304E+04	298.15	0.0000
	N 2.000000	O 4.00000		

SPECIES BEING CONSIDERED IN THIS SYSTEM
(CONDENSED PHASE MAY HAVE NAME LISTED SEVERAL TIMES)
LAST thermo.inp UPDATE: 9/09/04

g 7/97 *C	tpis79 *CH	g 4/02 CH2
g 4/02 CH3	g11/00 CH2OH	g 7/00 CH3O
g 8/99 CH4	g 7/00 CH3OH	srd 01 CH3OOH
g 8/99 *CN	g12/99 CNN	tpis79 *CO
g 9/99 *C02	tpis91 COOH	tpis91 *C2
g 6/01 C2H	g 1/91 C2H ₂ ,acetylene	g 5/01 C2H ₂ ,vinylidene
g 4/02 CH2C0,ketene	g 3/02 O(CH)20	srd 01 HO(CO)20H

g 7/01	C2H3,vinyl	g 9/00	CH3CN	g 6/96	CH3CO,acetyl
g 1/00	C2H4	g 8/88	C2H40,ethylen-o	g 8/88	CH3CHO,ethanal
g 6/00	CH3C0OH	srd 01	0HCH2C0OH	g 7/00	C2H5
g 7/00	C2H6	g 8/88	CH3N2CH3	g 8/88	C2H5OH
g 7/00	CH3OCH3	srd 01	CH3O2CH3	g 7/00	CCN
tpis91	CNC	srd 01	OCCN	tpis79	C2N2
g 8/00	C2O	tpis79	*C3	n 4/98	C3H3,1-propynl
n 4/98	C3H3,2-propynl	g 2/00	C3H4,allene	g 1/00	C3H4,propyne
g 5/90	C3H4,cyclo-	g 3/01	C3H5,allyl	g 2/00	C3H6,propylene
g 1/00	C3H6,cyclo-	g 6/01	C3H6O,propylox	g 6/97	C3H6O,acetone
g 1/02	C3H6O,propanal	g 7/01	C3H7,n-propyl	g 9/85	C3H7,i-propyl
g 2/00	C3H8	g 2/00	C3H8O,1propanol	g 2/00	C3H8O,2propanol
srd 01	CNCOCN	g 7/88	C3O2	g tpis	*C4
g 7/01	C4H2,butadiyne	g 8/00	C4H4,1,3-cyclo-	n10/92	C4H6,butadiene
n10/93	C4H6,1butyne	n10/93	C4H6,2butyne	g 8/00	C4H6,cyclo-
n 4/88	C4H8,1-butene	n 4/88	C4H8,cis2-buten	n 4/88	C4H8,tr2-butene
n 4/88	C4H8,isobutene	g 8/00	C4H8,cyclo-	g10/00	(CH3COOH)2
n10/84	C4H9,n-butyl	n10/84	C4H9,i-butyl	g 1/93	C4H9,s-butyl
g 1/93	C4H9,t-butyl	g12/00	C4H10,n-butane	g 8/00	C4H10,isobutane
g 6/01	C4N2	g 8/00	*C5	g 5/90	C5H6,1,3cyclo-
g 1/93	C5H8,cyclo-	n 4/87	C5H10,1-pentene	g 2/01	C5H10,cyclo-
n10/84	C5H11,pentyl	g 1/93	C5H11,t-pentyl	n10/85	C5H12,n-pentane
n10/85	C5H12,i-pentane	n10/85	CH3C(CH3)2CH3	g 2/93	C6H2
g11/00	C6H5,phenyl	g 8/00	C6H5O,phenoxy	g 8/00	C6H6
g 8/00	C6H5OH,phenol	g 1/93	C6H10,cyclo-	n 4/87	C6H12,1-hexene
g 6/90	C6H12,cyclo-	n10/83	C6H13,n-hexyl	g 6/01	C6H14,n-hexane
g 7/01	C7H7,benzyl	g 1/93	C7H8	g12/00	C7H8O,cresol-mx
n 4/87	C7H14,1-heptene	n10/83	C7H15,n-heptyl	n10/85	C7H16,n-heptane
n10/85	C7H16,2-methylh	n 4/89	C8H8,styrene	n10/86	C8H10,ethylbenz
n 4/87	C8H16,1-octene	n10/83	C8H17,n-octyl	n 4/85	C8H18,n-octane
n 4/85	C8H18,isoctane	n10/83	C9H19,n-nonyl	g 3/01	C10H8,naphthale
n10/83	C10H21,n-decyl	g 8/00	C12H9,o-bipheny	g 8/00	C12H10,biphenyl
g 6/97	*H	g 6/01	HCN	g 1/01	HCO
tpis89	HCCN	g 6/01	HCCO	g 6/01	HNC
g 7/00	HNCO	g10/01	HNO	tpis89	HN02
g 5/99	HN03	g 4/02	H02	tpis78	*H2
g 5/01	HCHO,formaldehy	g 6/01	HCOOH	g 8/89	H2O
g 6/99	H2O2	g 6/01	(HCOOH)2	g 5/97	*N
g 6/01	NCO	g 4/99	*NH	g 3/01	NH2
tpis89	NH3	tpis89	NH2OH	tpis89	*NO
g 4/99	N02	j12/64	N03	tpis78	*N2
g 6/01	NCN	g 5/99	N2H2	tpis89	NH2N02
g 4/99	N2H4	g 4/99	N2O	g 4/99	N2O3
tpis89	N2O4	g 4/99	N2O5	tpis89	N3
g 4/99	N3H	g 5/97	*O	g 4/02	*OH

tpis89 *02	g 8/01 03	n 4/83 C(gr)
n 4/83 C(gr)	n 4/83 C(gr)	g11/99 H2O(cr)
g 8/01 H2O(L)	g 8/01 H2O(L)	

SPECIES WITH TRANSPORT PROPERTIES

PURE SPECIES

C	CH4	CH3OH	CO
CO2	C2H2, acetylene		
C2H4	C2H6	C2H5OH	C2N2
H	HCN		
H2	H2O	N	NH3
NO	NO2		
N2	N2O	N2O4	O
OH	O2		

BINARY INTERACTIONS

C	O
CH4	O2
CO	CO2
CO	N2
CO	O2
CO2	H2
CO2	H2O
CO2	N2
CO2	O2
H	H2
H	N
H	N2
H	O
H2	H2O
H2	N2
H2	O2
H2O	N2
H2O	O2
N	NO
N	N2
N	O
N	O2
NO	O
N2	O
N2	O2
O	O2

O/F = 1.500000

ENTHALPY (KG-MOL) (K)/KG	EFFECTIVE FUEL h(2)/R 0.14089971E+03	EFFECTIVE OXIDANT h(1)/R -0.25573476E+02	MIXTURE h0/R 0.41015800E+02
-----------------------------	--	--	-----------------------------------

KG-FORM.WT./KG	bi(2)	bi(1)	b0i
*C	0.21705280E-01	0.00000000E+00	0.86821119E-02
*H	0.13023168E+00	0.00000000E+00	0.52092671E-01
*N	0.43410559E-01	0.21736532E-01	0.30406143E-01
*O	0.00000000E+00	0.43473063E-01	0.26083838E-01

POINT	ITN	T	C	H	N	O
1	22	2972.296	-15.101	-9.943	-13.504	-17.904
2	2	2970.087	-15.134	-9.961	-13.523	-17.910

Pinf/Pt = 1.755931

3	4	2743.245	-15.096	-10.095	-13.654	-18.594
---	---	----------	---------	---------	---------	---------

Pinf/Pt = 1.765400

3	2	2741.055	-15.095	-10.097	-13.655	-18.601
---	---	----------	---------	---------	---------	---------

Pinf/Pt = 1.765502

3	1	2741.032	-15.095	-10.097	-13.655	-18.601
4	2	2965.401	-15.134	-9.964	-13.525	-17.923
4	2	2965.203	-15.134	-9.964	-13.526	-17.924
4	1	2965.199	-15.134	-9.964	-13.526	-17.924
2	2	2971.623	-15.111	-9.948	-13.510	-17.906

Pinf/Pt = 1.756134

3	4	2744.113	-15.071	-10.082	-13.641	-18.591
---	---	----------	---------	---------	---------	---------

Pinf/Pt = 1.765614

3	2	2741.916	-15.070	-10.084	-13.642	-18.598
---	---	----------	---------	---------	---------	---------

Pinf/Pt = 1.765716

3	1	2741.892	-15.070	-10.084	-13.642	-18.598
---	---	----------	---------	---------	---------	---------

4	2	2966.923	-15.111	-9.951	-13.513	-17.918
4	2	2966.724	-15.111	-9.951	-13.513	-17.919
4	1	2966.720	-15.111	-9.951	-13.513	-17.919

END OF CHAMBER ITERATIONS

WARNING!! ASSIGNED pip = 0.00000 IS NOT PERMITTED
TO BE LESS THAN Pinj/Pc = 1.02451. POINT OMITTED (ROCKET)

4	12	636.328	-2.096	-11.662	-15.347	-53.316
4	3	649.490	-2.324	-11.605	-15.295	-52.408
4	2	649.565	-2.325	-11.605	-15.295	-52.403

THEORETICAL ROCKET PERFORMANCE ASSUMING EQUILIBRIUM

COMPOSITION DURING EXPANSION FROM FINITE AREA COMBUSTOR

Pinj = 185.0 PSIA

Ac/At = 4.1667 Pinj/Pinf = 1.012042

CASE = RocketCEA,

	REACTANT	WT FRACTION (SEE NOTE)	ENERGY KJ/KG-MOL	TEMP K
FUEL	CH6N2(L)	1.0000000	53973.600	298.150
OXIDANT	N2O4(L)	1.0000000	-19564.384	298.150

O/F= 1.50000 %FUEL= 40.000000 R,EQ.RATIO= 1.664270 PHI,EQ.RATIO= 1.664270

	INJECTOR	COMB END	THROAT	EXIT
Pinj/P	1.0000	1.0245	1.7870	3194.92
P, BAR	12.755	12.450	7.1379	0.00399
T, K	2972.30	2966.72	2741.89	649.57
RHO, KG/CU M	1.0179 0	9.9556-1	6.2170-1	1.4892-3
H, KJ/KG	341.03	325.70	-341.41	-4944.87
U, KJ/KG	-912.03	-924.87	-1489.54	-5212.96
G, KJ/KG	-37728.5	-37687.4	-35473.8	-13267.9

S, KJ/(KG)(K)	12.8081	12.8132	12.8132	12.8132
M, (1/n)	19.722	19.725	19.856	20.146
(dLV/dLP)t	-1.00796	-1.00790	-1.00440	-1.01001
(dLV/dLT)p	1.1628	1.1619	1.0962	1.1808
Cp, KJ/(KG)(K)	3.6352	3.6284	3.0833	3.3213
GAMMAS	1.1749	1.1750	1.1888	1.1951
SON VEL,M/SEC	1213.3	1212.2	1168.3	566.0
MACH NUMBER	0.000	0.144	1.000	5.744

TRANSPORT PROPERTIES (GASES ONLY)
CONDUCTIVITY IN UNITS OF MILLIWATTS/(CM)(K)

VISC,MILLIPOISE 0.92288 0.92167 0.87218 0.31656

WITH EQUILIBRIUM REACTIONS

Cp, KJ/(KG)(K)	3.6352	3.6284	3.0833	3.3213
CONDUCTIVITY	8.1347	8.1086	6.1772	1.6340
PRANDTL NUMBER	0.4124	0.4124	0.4353	0.6435

WITH FROZEN REACTIONS

Cp, KJ/(KG)(K)	2.2019	2.2014	2.1786	1.7006
CONDUCTIVITY	3.3337	3.3279	3.0877	0.9754
PRANDTL NUMBER	0.6096	0.6097	0.6154	0.5519

PERFORMANCE PARAMETERS

Ae/At	4.1667	1.0000	150.00
CSTAR, M/SEC	1735.3	1735.3	1735.3
CF	0.1009	0.6733	1.8737
Ivac, M/SEC	7317.4	2151.0	3333.9
Isp, M/SEC	175.1	1168.3	3251.4

MOLE FRACTIONS

CH4	0.00000	0.00000	0.00000	0.00296
*CO	0.14178	0.14176	0.14077	0.01617
*CO2	0.02944	0.02949	0.03162	0.15578
*H	0.01808	0.01799	0.01116	0.00000
*H2	0.19793	0.19797	0.20098	0.32105
H2O	0.30186	0.30197	0.30812	0.19775
NH3	0.00000	0.00000	0.00000	0.00001

*NO	0.00108	0.00106	0.00045	0.00000
*N2	0.29929	0.29934	0.30165	0.30628
*O	0.00050	0.00049	0.00016	0.00000
*OH	0.00971	0.00962	0.00498	0.00000
*O2	0.00030	0.00030	0.00010	0.00000

* THERMODYNAMIC PROPERTIES FITTED TO 20000.K

PRODUCTS WHICH WERE CONSIDERED BUT WHOSE MOLE FRACTIONS
WERE LESS THAN 5.000000E-06 FOR ALL ASSIGNED CONDITIONS

*C	*CH	CH2	CH3	CH2OH
CH3O	CH3OH	CH3OOH	*CN	CNN
COOH	*C2	C2H	C2H2,acetylene	C2H2,vinylidene
CH2CO,ketene	O(CH)2O	HO(CO)2OH	C2H3,vinyl	CH3CN
CH3CO,acetyl	C2H4	C2H4O,ethylen-o	CH3CHO,ethanal	CH3COOH
OHCH2COOH	C2H5	C2H6	CH3N2CH3	C2H5OH
CH3OCH3	CH3O2CH3	CCN	CNC	OCCN
C2N2	C2O	*C3	C3H3,1-propynl	C3H3,2-propynl
C3H4,allene	C3H4,propyne	C3H4,cyclo-	C3H5,allyl	C3H6,propylene
C3H6,cyclo-	C3H6O,propylox	C3H6O,acetone	C3H6O,propanal	C3H7,n-propyl
C3H7,i-propyl	C3H8	C3H8O,1propanol	C3H8O,2propanol	CNCOCN
C3O2	*C4	C4H2,butadiyne	C4H4,1,3-cyclo-	C4H6,butadiene
C4H6,1butyne	C4H6,2butyne	C4H6,cyclo-	C4H8,1-butene	C4H8,cis2-buten
C4H8,tr2-butene	C4H8,isobutene	C4H8,cyclo-	(CH3COOH)2	C4H9,n-butyl
C4H9,i-butyl	C4H9,s-butyl	C4H9,t-butyl	C4H10,n-butane	C4H10,isobutane
C4N2	*C5	C5H6,1,3cyclo-	C5H8,cyclo-	C5H10,1-pentene
C5H10,cyclo-	C5H11,pentyl	C5H11,t-pentyl	C5H12,n-pentane	C5H12,i-pentane
CH3C(CH3)2CH3	C6H2	C6H5,phenyl	C6H5O,phenoxy	C6H6
C6H5OH,phenol	C6H10,cyclo-	C6H12,1-hexene	C6H12,cyclo-	C6H13,n-hexyl
C6H14,n-hexane	C7H7,benzyl	C7H8	C7H8O,cresol-mx	C7H14,1-heptene
C7H15,n-heptyl	C7H16,n-heptane	C7H16,2-methylh	C8H8,styrene	C8H10,ethylbenz
C8H16,1-octene	C8H17,n-octyl	C8H18,n-octane	C8H18,isoctane	C9H19,n-nonyl
C10H8,naphthale	C10H21,n-decyl	C12H9,o-bipheny	C12H10,biphenyl	HCN
HCO	HCCN	HCCO	HNC	HNCO
HNO	HN02	HN03	HO2	HCHO,formaldehy
HCOOH	H2O2	(HCOOH)2	*N	NCO
*NH	NH2	NH2OH	NO2	NO3
NCN	N2H2	NH2NO2	N2H4	N2O
N2O3	N2O4	N2O5	N3	N3H
O3	C(gr)	H2O(cr)	H2O(L)	

NOTE. WEIGHT FRACTION OF FUEL IN TOTAL FUELS AND OF OXIDANT IN TOTAL OXIDANTS

WARNING!! DIFFICULTY IN LOCATING THROAT (ROCKET)

THEORETICAL ROCKET PERFORMANCE ASSUMING FROZEN COMPOSITION

Pinj = 185.0 PSIA

Ac/At = 4.1667 Pinj/Pinf = 1.012042

CASE = RocketCEA,

	REACTANT	WT FRACTION (SEE NOTE)	ENERGY KJ/KG-MOL	TEMP K
FUEL	CH6N2(L)	1.0000000	53973.600	298.150
OXIDANT	N2O4(L)	1.0000000	-19564.384	298.150

O/F= 1.50000 %FUEL= 40.000000 R,EQ.RATIO= 1.664270 PHI,EQ.RATIO= 1.664270

	INJECTOR	COMB END	THROAT	EXIT
Pinj/P	1.0000	1.7774	1.7971	4263.32
P, BAR	12.755	7.1762	7.0979	0.00299
T, K	2972.30	2660.23	2654.56	448.51
RHO, KG/CU M	1.0179 0	6.3988-1	6.3424-1	1.5823-3
H, KJ/KG	341.03	-341.26	-353.55	-4618.53
U, KJ/KG	-912.03	-1462.75	-1472.66	-4807.61
G, KJ/KG	-37728.5	-34413.8	-34353.5	-10363.1
S, KJ/(KG)(K)	12.8081	12.8081	12.8081	12.8081
M, (1/n)	19.722	19.722	19.722	19.722
Cp, KJ/(KG)(K)	2.2019	2.1696	2.1690	1.5832
GAMMAS	1.2368	1.2412	1.2413	1.3629
SON VEL,M/SEC	1244.9	1179.8	1178.6	507.6
MACH NUMBER	0.000	0.990	1.000	6.204

TRANSPORT PROPERTIES (GASES ONLY)

CONDUCTIVITY IN UNITS OF MILLIWATTS/(CM)(K)

VISC,MILLIPOISE 0.92288 0.92167 0.85219 0.22510

WITH FROZEN REACTIONS

Cp, KJ/(KG)(K)	2.2019	2.2014	2.1690	1.5832
CONDUCTIVITY	3.3337	3.3279	3.0136	0.5997
PRANDTL NUMBER	0.6096	0.6097	0.6133	0.5943

PERFORMANCE PARAMETERS

Ae/At	4.1667	1.0000	150.00	
CSTAR, M/SEC	1686.0	1686.0	1686.0	
CF	0.6929	0.6991	1.8680	
Ivac, M/SEC	2128.2	2128.1	3209.5	
Isp, M/SEC	1168.1	1178.6	3149.5	

MOLE FRACTIONS

*CO	0.14178	*CO2	0.02944	*H	0.01808
*H2	0.19793	H2O	0.30186	*NO	0.00108
*N2	0.29929	*O	0.00050	*OH	0.00971
*O2	0.00030				

* THERMODYNAMIC PROPERTIES FITTED TO 20000.K

PRODUCTS WHICH WERE CONSIDERED BUT WHOSE MOLE FRACTIONS
WERE LESS THAN 5.000000E-06 FOR ALL ASSIGNED CONDITIONS

*C	*CH	CH2	CH3	CH2OH
CH3O	CH3OH	CH3OOH	*CN	CNN
COOH	*C2	C2H	C2H2, acetylene	C2H2, vinylidene
CH2CO, ketene	O(CH)2O	HO(CO)2OH	C2H3, vinyl	CH3CN
CH3CO, acetyl	C2H4	C2H4O, ethylen-o	CH3CHO, ethanal	CH3COOH
OHCH2COOH	C2H5	C2H6	CH3N2CH3	C2H5OH
CH3OCH3	CH3O2CH3	CCN	CNC	OCCN
C2N2	C2O	*C3	C3H3, 1-propynl	C3H3, 2-propynl
C3H4, allene	C3H4, propyne	C3H4, cyclo-	C3H5, allyl	C3H6, propylene
C3H6, cyclo-	C3H6O, propylox	C3H6O, acetone	C3H6O, propanal	C3H7, n-propyl
C3H7, i-propyl	C3H8	C3H8O, 1propanol	C3H8O, 2propanol	CNCOCN
C3O2	*C4	C4H2, butadiyne	C4H4, 1,3-cyclo-	C4H6, butadiene
C4H6, 1butyne	C4H6, 2butyne	C4H6, cyclo-	C4H8, 1-butene	C4H8, cis2-buten
C4H8, tr2-butene	C4H8, isobutene	C4H8, cyclo-	(CH3COOH)2	C4H9, n-butyl
C4H9, i-butyl	C4H9, s-butyl	C4H9, t-butyl	C4H10, n-butane	C4H10, isobutane
C4N2	*C5	C5H6, 1,3cyclo-	C5H8, cyclo-	C5H10, 1-pentene
C5H10, cyclo-	C5H11, pentyl	C5H11, t-pentyl	C5H12, n-pentane	C5H12, i-pentane
CH3C(CH3)2CH3	C6H2	C6H5, phenyl	C6H5O, phenoxy	C6H6
C6H5OH, phenol	C6H10, cyclo-	C6H12, 1-hexene	C6H12, cyclo-	C6H13, n-hexyl
C6H14, n-hexane	C7H7, benzyl	C7H8	C7H8O, cresol-mx	C7H14, 1-heptene
C7H15, n-heptyl	C7H16, n-heptane	C7H16, 2-methylh	C8H8, styrene	C8H10, ethylbenz
C8H16, 1-octene	C8H17, n-octyl	C8H18, n-octane	C8H18, isoocetane	C9H19, n-nonyl
C10H8, naphthale	C10H21, n-decyl	C12H9, o-bipheny	C12H10, biphenyl	HCN
HCO	HCCN	HCCO	HNC	HNCO
HNO	HN02	HN03	H02	HCHO, formaldehy

HCOOH	H2O2	(HCOOH)2	*N	NCO
*NH	NH2	NH2OH	N02	N03
NCN	N2H2	NH2NO2	N2H4	N2O
N2O3	N2O4	N2O5	N3	N3H
O3	C(gr)	H2O(cr)	H2O(L)	

NOTE. WEIGHT FRACTION OF FUEL IN TOTAL FUELS AND OF OXIDANT IN TOTAL OXIDANTS

Engine sizing

thrust = 28000 # N, keeps longest maneuver under 3 minutes

D_e = 1.5 # m, diameter of engine

A_e = math.pi*D_e**2/4 # m^2, area of engine

eps = 150 # expansion ratio

A_t = A_e/eps # throat area

D_t = (4*A_t/math.pi)**(1/2) # throat diameter

print(f"throat_diameter={D_t}m")

Cf = 1.8737 # thrust coefficient from CEA

P_c = thrust/(Cf*A_t)

print(f"chamber_pressure={P_c}Pa, {P_c/6894.76}psi")

#from rocketcea.cea_obj import CEA_Obj

#ispObj = CEA_Obj(propName='', oxName='N2O4', fuelName='MMH')

Define input parameters

Pc = 183.0 # Chamber pressure in psi

MR = 1.5 # Mixture ratio

Pamb = 0.000000000145 # Ambient pressure in psi (sea level)

Calculate thrust coefficient

CF, CF_amb, mode = ispObj.get_PambCf(Pc=Pc, MR=MR, eps=eps, Pamb=Pamb)

Print results

print(f"Thrust Coefficient (CF): {CF}")

print(f"Thrust Coefficient at Ambient Pressure (CF_amb): {CF_amb}")

print(f"Nozzle Operating Mode: {mode}")

T = m_dot*u_e + (P_e - P_amb)*A_e # thrust equation

P_e = 0.00402 # bar

P_e = P_e*100000 # Pa

```

u_e = 3251.4 # m/s, from CEA
m_dot = (thrust - (P_e*math.pi*D_e**2/4))/u_e
print(f"u_e={u_e} m/s, m_dot={m_dot} kg/s")
m_dot_fuel = m_dot/(1+MR)
m_dot_ox = m_dot - m_dot_fuel

print(f"m_dot_fuel={m_dot_fuel} kg/s, m_dot_ox={m_dot_ox} kg/s")

A_cc_cooled = math.pi*250*213.36 # mm^2
print(f"A_cc_cooled={A_cc_cooled} mm^2")

# injector
deltaP = 0.2*P_c # Pa
print(f"rho_mmh={rho_mmh} kg/m^3, rho_nto={rho_nto} kg/m^3")
print(f"deltaP={deltaP} Pa")
A_fuel = m_dot_fuel/(0.65*(2*rho_mmh*deltaP)**0.5)
A_fuel_mm2 = A_fuel*10**6
print(f"A_fuel={A_fuel} m^2, {A_fuel_mm2} mm^2")
A_ox = m_dot_ox/(0.65*(2*rho_nto*deltaP)**0.5)
A_ox_mm2 = A_ox*10**6
print(f"A_ox={A_ox} m^2, {A_ox_mm2} mm^2")

A_inj = math.pi*(0.125)**2
F_inj = deltaP*A_inj

print(f"A_inj={A_inj} m^2, F_inj={F_inj} N")
numbolts = 8
Fperbolt = F_inj/numbolts
print(f"Fperbolt={Fperbolt} N")

throat diameter = 0.1224744871391589 m
chamber pressure = 1268460.168030619 Pa, 183.97452094498124 psi
u_e = 3251.4 m/s, m_dot = 8.39318673839177 kg/s
m_dot_fuel = 3.3572746953567085 kg/s, m_dot_ox = 5.035912043035062 kg/s
A_cc_cooled = 167572.55214247957 mm^2
rho_mmh = 880 kg/m^3, rho_nto = 1442 kg/m^3
deltaP = 253692.0336061238 Pa
A_fuel = 0.00024443521395303496 m^2, 244.43521395303497 mm^2
A_ox = 0.0002864268564232964 m^2, 286.4268564232964 mm^2
A_inj = 0.04908738521234052 m^2, F_inj = 12453.078578925835 N
Fperbolt = 1556.6348223657294 N

import math

def conical_nozzle_length(exit_diameter, expansion_ratio, half_angle_deg=15):

```

```
"""
```

```
Calculate the length of a conical rocket nozzle.
```

```
Parameters:
```

```
exit_diameter (float): Exit diameter of the nozzle (m)
```

```
expansion_ratio (float): Nozzle expansion ratio ( $A_e / A_t$ )
```

```
half_angle_deg (float): Half-angle of the conical nozzle (default = 15 degrees)
```

```
Returns:
```

```
float: Nozzle length (m)
```

```
"""
```

```
# Convert half-angle to radians
```

```
half_angle_rad = math.radians(half_angle_deg)
```

```
# Calculate throat diameter
```

```
throat_diameter = exit_diameter / math.sqrt(expansion_ratio)
```

```
# Calculate nozzle length
```

```
nozzle_length = (exit_diameter - throat_diameter) / (2 * math.tan(half_angle_rad))
```

```
return nozzle_length
```

```
# Example Inputs
```

```
exit_diameter = 1.5 # meters
```

```
expansion_ratio = 150 # Example: 50:1 expansion ratio
```

```
# Calculate nozzle length
```

```
length = conical_nozzle_length(exit_diameter, expansion_ratio)
```

```
print(f"Nozzle Length: {length:.4f} meters")
```

```
# this equation is also in RPE on p.77
```

G Kick Stage Propulsion EES Code

G.1 Initial Approximation

```
$UNITSYS SI J K kPa kJ mass rad

// 1D convection

// T_flame --- h_bar --- Twall ---- conduction --- radiative
// bartz?

T_flame = 2972.3 [K] // from cea
// T_wall = ?
T_infty = 2.7 [K] // space

h = 1500 [W/m^2-K] // estimate of convective HTC
k = 16.3 [W/m-k] // 316SS thermal conductivity
th_w = 10 [mm]*Convert(mm, m) // wall thickness
epsilon = 0.5 [-] // surface emissivity

// equations
q_dprime_conv = h*(T_flame-T_wall) // convection
q_dprime_cond = k/th_w*(T_wall-T_outer) // conduction
q_dprime_rad = epsilon*sigma#*(T_outer^4 - T_infty^4) // radiation

// e-bal, no gen no stored so IN=OUT
q_dprime_conv = q_dprime_cond
q_dprime_cond = q_dprime_rad
```

G.2 Film Cooling and Bartz Model

```
$UNITSYS SI K kPa kJ mass rad
"Input parameters"
D_cc = 250 [mm]*Convert(mm,m) // chamber diameter
Pc = 1268460 [Pa] // Chamber pressure, 185psi
A_cc_cooled = 167572.552 [mm^2]*Convert(mm^2,m^2) // Cooled chamber area, same as total
g = 9.81 [m/s^2] // gravity
molWT = 46.073 [g/mol]*Convert(g,kg) // molecular weight of coolant
m_dot_total = 8.3932 [kg/s] // total mass flow rate of engine

"Calculate required mass flow rate of film coolant for desired temperature"
"Liquid film cooling equation: Zucrow and Sellers, eq. 4-33 in Huzel & Huang"
//m_dot_film = 1 [kg/s] // GUESS VALUE
G_c = m_dot_film*g/A_cc_cooled // film coolant weight flow per unit area of cooled chamber
G_g = m_dot_total*g/A_cc_cooled // combustion gas weight flow per unit area of chamber p
```

```

eta_c = 0.3 // film cooling efficiency, ranges 0.3-0.7 due to losses
H = C_pvc*(T_aw - T_wg) / ( C_plc*(T_wg - T_co) + DELTAH_vc) // film coolant enthalpy
C_plc_mol = 134.93 [J/mol-K] // NIST source
C_plc = C_plc_mol/molWT
C_pvc = 0.5*C_plc // estimate since no data available
C_pg_inj = 3.6352 [kJ/kg-K] // Cp of combustion gases from CEA at injector
T_aw = 2972.3 [K] // adiabatic wall temp at injector
T_wg = 1000 [K] // gas side wall temp and film temp, this is the allowable wall temp bas
T_co = 273.15 [K] // coolant bulk temperature at manifold, 0C for this
DELTAH_vc_mol = 41.8 [kJ/mol]*Convert(kJ,J) // enthalpy of vaporization of coolant, from
DELTAH_vc = DELTAH_vc_mol/molWT

"Fluid velocities and things"
"CEA Values"
M_cc = 0.144 // mach number at CC end
a_cc = 1212.2 [m/s] // sonic velocity at CC end
u_max = M_cc*a_cc // max velocity of combustion gases
rho_g = 0.99556 [kg/m^3] // combustion gas density at CC end
mu_g = 0.92167*0.0001 [Pa-s] // dynamic viscosity in mP at CC end
Pr_g = 0.4124 [-] // Prandtl number
Cp_g = 3.6284 [kJ/kg-K]*Convert(kJ,J)

//nu = mu/rho // kinematic viscosity

epsilon = 1.6e-6 [m] // estimate for machined steel 1.6um
epsilonoverd = epsilon/D_cc // relative surface roughness
//Re = rho*u_max*D_cc/mu // Reynolds number

Re = rho_g*u_avg*D_cc/mu_g // Reynolds number
f = 0.014 [-] // Moody chart iteration

u_edge = u_max*(1-1.3*Sqrt(f)) // White viscous fluid flow
u_avg/u_max = (1+1.3*Sqrt(f))^-1 // White viscous fluid flow

V_g = u_max // axial stream velocity of combustion gases at centerline of thrust chamber
V_d = u_edge // axial stream velocity of combustion gases at edge of boundary layer
V_m = u_avg // average axial lstream velocity of combustion gases

Re_tp = (G_c+G_g)*D_cc/mu_g // Reynolds number for homogenous two phase flow
f_tp = 0.079*Re_tp^(-0.25) // friction coefficient for two-phase flow between combustion
a = 2*V_d/(V_m*f_tp) // a constant in 4-33
b = (V_g/V_d)-1 // b constant in 4-33

gas_ratio = 1/eta_c * H / (a*(1+b^(C_pvc/C_pg_inj)))
gas_ratio = G_c/G_g

```

```

film_ratio = m_dot_film/m_dot_total

"Bartz correlation for convection coefficient"
h_g = (0.026/D_cc^0.2) * (Cp_g*mu_g^0.2/Pr_g^0.6) * (rho_g*u_max)^0.8 * (rho_am/rho_prime)
"subscripts: 0: stagnation/chamber combustion temp. am: arithmetic mean temperature of f
"v is gas velocity"

T_am = (T_aw+T_wg)/2 // mean temp
rho_am = rho_g*T_aw/T_am // approximate using ideal gas law
mu_am = mu_g*(T_am/T_aw)^(3/2) // approximate behaviour of viscosity
rho_prime = rho_g // ????

h_film = h_g*(1-eta_c) // correct bartz for film cooling

```

H STD Simple Model APDL Code

```
finish                                ! exit processor
/clear,start                           ! clear database

/filnam, STD_structure                ! set filename
/title, Simple STD Model
/prep7                                 ! enter preprocessor

! inputs
w=0.289
h=0.35
r=0.011

g=9.81
a1=3.5
a2=2

m_capture=15/6                         ! mass of capturing
  mechanism [kg]
m_engine=25/6                          ! mass of engine [kg]
m_tank=25/6                            ! mass of fuel tank [kg]
m_propsys=35/6                          ! mass of propulsion
  system [kg]
m_RCS=30/6                            ! mass of RCS [kg]
m_structural=50/6                      ! other structural mass
  [kg]
m_fuel=215/6                           ! propellant mass [kg]

! Ti-6Al-4V inputs
E=113.8e9
rho=4430
nu=0.342

! elements
et,1,beam188
et,2,mass21,,,2

! material properties
mp,ex,1,E                               ! modulus of elasticity
mp,dens,1,rho                            ! density [kg/m^3]
mp,prxy,1,nu                             ! poisson ratio
```

```

!real constants
sectype,1,beam,csolid
secdat,r
real,2
r,2,m_capture ! Define mass for capture mechanism
real,3
r,3,m_engine ! Define mass for engine
real,4
r,4,m_tank ! Define mass for fuel tank
real,5
r,5,m_propsys ! Define mass for propulsion system
real,6
r,6,m_RCS ! Define mass for RCS
real,7
r,7,m_structural ! Define mass for structural components
real,8
r,8,m_fuel ! Define mass for fuel

!important locations
x0=0
x1=w/2
x2=w
y0=0
y1=h

!create keypoints
k,1,x0,y0
k,2,x0,y1
k,3,x0,2*y1
k,4,x0,3*y1
k,5,x2,y0
k,6,x2,y1
k,7,x2,2*y1
k,8,x2,3*y1

k,9,x0,4*y1
k,10,x0,5*y1
k,11,x0,6*y1
k,12,x2,4*y1
k,13,x2,5*y1
k,14,x2,6*y1

!create lines
l,1,2
l,2,3

```

```

1,3,4
1,5,6
1,6,7
1,7,8
1,1,5
1,2,6
1,3,7
1,4,8
1,2,5
1,2,7
1,4,7

1,4,9
1,9,10
1,10,11
1,8,12
1,12,13
1,13,14
1,9,12
1,10,13
1,11,14
1,4,12
1,12,10
1,10,14

num_div=4
lesize,all,,,num_div

! create elements
mat,1
secnum,1
type,1
lmesh,all

! Add mass elements at force nodes
type,2
real,2
en,101,37 ! MASS21 for capturing mechanism MIDDLE

real,3
en,102,79 ! MASS21 for engine TOP

real,4
en,103,85 ! MASS21 for fuel tank TOP MIDDME

```

```

real ,5
en ,104 ,85      ! MASS21 for propulsion system TOP MIDDLE

real ,6
en ,105 ,43      ! MASS21 for RCS BOTTOM MIDDLE

real ,7
en ,106 ,37      ! MASS21 for structural components MIDDLE

real ,8
en ,107 ,85      ! MASS21 for fuel mass TOP MIDDLE

! boundary conditions
nsel,s,loc,y,y0
d,all,all,0

allsel

acel,-a2*g,a1*g,0,gravity

allsel

finish

/solu
autots,on           ! autotimestepping
deltim,1e-2          ! initial timestep
antype,static        !
solve
save

finish

/post1               ! start the post processor

allsel
FSUM
PRRSOL

```

I STD Engine Pressure Distribution

Table I.1: Complete Nozzle Pressure Distribution

Axial Pressure Profile	
Axial Distance from Injector (m)	Pressure (Pa)
0.00000	-1.23×10^6
0.10740	-1.23×10^6
0.18740	-7.30×10^5
0.37586	-3.86×10^5
0.37719	-3.39×10^5
0.37852	-2.92×10^5
0.37985	-2.47×10^5
0.38118	-2.02×10^5
0.38399	-1.37×10^5
0.38680	-1.01×10^5
0.38961	-7.71×10^4
0.39242	-6.09×10^4
0.39523	-4.93×10^4
0.39804	-4.06×10^4
0.40085	-3.40×10^4
0.40366	-2.88×10^4
0.40648	-2.47×10^4
0.40929	-2.14×10^4
0.41210	-1.87×10^4
0.41491	-1.65×10^4
0.41772	-1.46×10^4
0.42053	-1.30×10^4
0.42334	-1.17×10^4
0.42615	-1.05×10^4
0.42896	-9.53×10^3
0.43177	-8.67×10^3
0.43458	-7.92×10^3
0.43739	-7.27×10^3
0.44020	-6.69×10^3
0.44301	-6.17×10^3
0.44583	-5.72×10^3
0.44864	-5.31×10^3
0.45145	-4.94×10^3
0.45426	-4.62×10^3
0.45707	-4.32×10^3
0.45988	-4.05×10^3

Continued on next page

Axial Distance from Injector (m)	Pressure (Pa)
0.46269	-3.81×10^3
0.46550	-3.59×10^3
0.46831	-3.39×10^3
0.47112	-3.20×10^3
0.47393	-3.03×10^3
0.47674	-2.88×10^3
0.47955	-2.73×10^3
0.48237	-2.60×10^3
0.48518	-2.48×10^3
0.48799	-2.37×10^3
0.49080	-2.26×10^3
0.49361	-2.17×10^3
0.49642	-2.08×10^3
0.49923	-1.99×10^3
0.50204	-1.91×10^3
0.50485	-1.84×10^3
0.50766	-1.77×10^3
0.51047	-1.71×10^3
0.51328	-1.65×10^3
0.51609	-1.59×10^3
0.51891	-1.54×10^3
0.52172	-1.49×10^3
0.52453	-1.44×10^3
0.52734	-1.39×10^3
0.53015	-1.35×10^3
0.53296	-1.31×10^3
0.53577	-1.27×10^3
0.53858	-1.24×10^3
0.54139	-1.21×10^3
0.54420	-1.17×10^3
0.54701	-1.14×10^3
0.54982	-1.12×10^3
0.55263	-1.09×10^3
0.55544	-1.06×10^3
0.55826	-1.04×10^3
0.56107	-1.01×10^3
0.56388	-9.93×10^2
0.56669	-9.72×10^2
0.56950	-9.51×10^2
0.57231	-9.32×10^2
0.57512	-9.14×10^2

Continued on next page

Axial Distance from Injector (m)	Pressure (Pa)
0.57793	-8.97×10^2
0.58074	-8.80×10^2
0.58355	-8.65×10^2
0.58636	-8.50×10^2
0.58917	-8.35×10^2
0.59198	-8.22×10^2
0.59480	-8.09×10^2
0.59761	-7.96×10^2
0.60042	-7.85×10^2
0.60323	-7.73×10^2
0.60604	-7.62×10^2
0.60885	-7.52×10^2
0.61166	-7.42×10^2
0.61447	-7.33×10^2
0.61728	-7.24×10^2
0.62009	-7.16×10^2
0.62290	-7.08×10^2
0.62571	-7.00×10^2
0.62852	-6.93×10^2
0.63134	-6.86×10^2
0.63415	-6.80×10^2
0.63696	-6.73×10^2
0.63977	-6.67×10^2
0.64258	-6.62×10^2
0.64539	-6.57×10^2
0.64820	-6.52×10^2
0.65101	-6.47×10^2
0.65382	-6.43×10^2
0.65663	-6.39×10^2
0.65944	-6.35×10^2

J Orbital Mechanics Calculations

Appendix J has all of the MATLAB scripts for the maximum torque required by the STD during docking. Each subsection of this appendix will explain the code.

J.1 Main Script

This script sets various initial conditions for the equations of motion of the Starlink satellite with a fixed initial velocity magnitude. Script then calls function files for equations of motion of both the Starlink satellite and STD to determine the required STD torque. This script was written by Bryce Quinton.

```
% fixed angular velocity magnitude
wI = 0.1745;

% number of samples in nutation and spin
nTheta = 40;
nPhi = 40;

% create vectors of sample angles
thetaList = linspace(0, pi, nTheta);
phiList = linspace(0, 2*pi, nPhi);

% preallocate list of initial omegas
numDirs = nTheta * nPhi;
omega0List = zeros(numDirs, 3);
idx = 0;

for i = 1:nTheta
    theta = thetaList(i);
    for j = 1:nPhi
        phi = phiList(j);
        idx = idx + 1;
        % direction on unit sphere
        dir = [ sin(theta)*sin(phi), ...
                 sin(theta)*cos(phi), ...
                 cos(theta) ];
        % scale to magnitude w
        omega0List(idx, :) = w* dir;
    end
end

% sweep through each direction and record peak torque
peakTorque = zeros(numDirs,1);
```

```

for k = 1:numDirs
    omega0 = omega0List(k, :);
    % run your simulation function
    [~, ~, ~, ~, tauB] = tauSTD(omega0);
    % compute instantaneous torque magnitude
    mag = sqrt(sum(tauB.^2, 2));
    peakTorque(k) = max(mag);
end

% find the worst case direction
[~, worstIdx] = max(peakTorque);
worstOmega0 = omega0List(worstIdx, :);
worstTau = peakTorque(worstIdx);

fprintf('Worst case omega0 = [% .4f, %.4f, %.4f] rad/s\n',
       worstOmega0);
fprintf('Peak torque needed = %.4f N m\n', worstTau);

```

J.2 tauSTD.m

This function calls the Starlink satellite equation of motion function and then determines angular accelerations throughout the ensuing motion to determine the input torque required from the STD to have the same angular velocities across the simulation time. This function file was written by Bryce Quinton.

```

function [t, bt, omt, alphaB, tauB] = tauSTD(omega0)
%--- set up initial quaternions + ode options as before ---
bet0 = [1,0,0,0];
xQ0 = [bet0, omega0];
odeOpts = odeset('RelTol',1e-10, 'AbsTol',1e-10, 'MaxStep',1e
                 -2);
tend = 200;
[t, qout] = ode45('eom_satquat', [0,tend], xQ0, odeOpts);
bt = qout(:,1:4);
omt = qout(:,5:7);

%--- compute body accel and torque as before ---
alphaB = zeros(size(omt));
for k=1:3
    alphaB(:,k) = gradient(omt(:,k), t);
end

I1 = 182; I3 = 13; I = diag([I1,I1,I3]);
tauB = zeros(size(omt));

```

```

for i=1:size(omt,1)
    w = omt(i,:)';
    tauB(i,:) = (I*alphaB(i,:))' + cross(w, I*w);
end
end

```

J.3 eom_{satquat.m}

This function defines the equations of motion for the Starlink satellite given an initial condition and a time-frame to integrate across. This function outputs values of ω and $\dot{\omega}$ required to calculate torque for the STD. This function file was written by Mike Sracic.

```

function [xdot] = eom_satquat(t,x)

I1=14364; I2=85767; I3=100131;

momentMag = 0;

% matlab passes in values of x at time t
% x=[bet0,bet1,bet2,bet3,om1,om2,om3].'
b0=x(1); b1=x(2); b2=x(3); b3=x(4); om1=x(5); om2=x(6); om3=x
(7);

% applied Moment
M=zeros(3,1);
if t<=1;
    M(1,1)=momentMag*(1-cos(t*pi)); % smooth ramp up to maximum
    moment
    % Vector - about x- axis only
else
    M(1,1)=momentMag;
end

% Equations of Motion. Note, these EOM are identical for any
% system, so
% this part of the function could be used to integrate any
% system.
xdot(1:4,1)=(1/2)*[0, -om1, -om2, -om3;
    om1, 0, om3, -om2;
    om2, -om3, 0, om1;
    om3, om2, -om1, 0]*x(1:4); % [b1; b2; b3; b4]
xdot(5:7,1)=[M(1)/I1+(I2-I3)*om2*om3/I1;
    M(2)/I2+(I3-I1)*om1*om3/I2;
    M(3)/I3+(I1-I2)*om1*om2/I3];
end

```